Final Project

Sensitivity Analysis of MIRAS/SMOS Instrument Calibration Parameters

Author:

Miriam Pablos Hernández

Advisors:

Verónica González Gambau

Dr. Núria Duffo Úbeda

[veronica.gonzalez, duffo]@tsc.upc.edu

Department of Signal Theory and Communications

Universitat Politècnica de Catalunya

Barcelona, September 2010

ACKNOWLEDGMENTS

The time spent during this Final Project has changed my life personally and professionally. I have become more mature and responsible and have acquired a strong technical background on remote sensing. It has given me an overview of what scientific research means.

I would like, first of all, to express my gratitude to one of my advisors, Dr. Núria Duffo, for her support and suggestions during the performance of this project.

I would also like to thank Prof. Francesc Torres and Prof. Ignasi Corbella, for their valuable comments, for making me feel part of the Remote Sensing Laboratory group and support my suggestions.

My gratitude specially goes to my advisor Verónica González, who has provided me assistance and she has become a good friend and an exemplar model to follow.

Thanks to my workmates Israel Durán, Wu Lin and Ruben Dávila, which whom I have shared a lot of good moments.

Special thanks to my family, in particular to my parents. They have always supported and encouraged me to do my best in all matters of life.

And last but not least, I want to show my deepest gratitude to Marc, my partner, who has always been by my side, even during the more difficult moments.

CONTENTS

LIST OF FIGURES

LIST OF TABLES

LIST OF ACRONYMS

CAS	CAlibration Subsystem
CIP	Calibration Internal Plane
CCU	Correlator Control Unit
CMN	Control and Monitoring Node
CNES	Centre National d'Etudes Spatiales
DICOS	DIgital COrrelator System
DPGS	Data Processing Ground Segment
ESA	European Space Agency
ESAC	European Space Agency Centre
FWF	Fringe Washing Function
HAP	Horizontal Antenna Plane
IF	Intermediate Frequency
LICEF	Light-Weight Cost Effective Front-end
LO	Local Oscillator
LSS	Large Space Simulator
MIRAS	Microwave Imaging Radiometer with Aperture Synthesis
NDN	Noise Distribution Network
NIR	Noise Injection Radiometer
NS	Noise Source
PD	Power Divider
PMS	Power Measurement System
RF	Radio Frequency
SMOS	Soil Moisture Ocean Salinity
SMOS-BEC	SMOS-Barcelona Expert Centre
SOGS	Satellite Operations Ground Segment
TPR	Total Power Radiometer
TSC	Theory of Signal and Communications
UPC	Universitat Politècnica de Catalunya
VAP	Vertical Antenna Plane

CHAPTER 1

1. Introduction

This introduction is intended to describe the objectives within the scope in which the research has been developed and the organization of this Final Project.

1.1. Scope and objectives

The Final Project has been developed in the framework of the ESA's Soil Moisture and Ocean Salinity (SMOS) mission [1], during the development of Pre-Commissioning and Commissioning phases. The first steps of this work were in September 2009 with the Remote Sensing Laboratory group of TSC (Theory of Signal and Communications Department) at UPC [2].

One of the main objectives of any mission is to obtain and provide stable and accurate final products. So, a well-calibrated instrument provides the basis for stable and accurate measurements. The calibration of any Earth Observation sensor is a key stage which encompasses those tasks which are necessary to convert the raw measurement data into science data. The characterization of the instrument is a requirement for the development of the calibration activities. Characterization consists of the measurement of the typical behavior of instrument performances, including subsystems, which may affect the accuracy or quality of its response or derived data.

The aim of this Final Project is to perform a comprehensive temperature sensitivity analysis of the instrument that is the SMOS payload. To do this, it is necessary to characterize the Power Measurement System (PMS) included in each receiver over the physical temperature. Additionally, the correlation phase related to the Local Oscillator (LO) located in each segment of the instrument is also analyzed. PMS calibration parameters (*gain* and *offset*) and the correlation phase (*LO phase*) are planned to be periodically updated during the mission to account for possible instrumental drifts. These parameters are tracked, initially on-ground and after in orbit, during the measurement mode using their respective corrections to remove physical temperature drifts.

1.2. Organization of the project

The report of this project is divided in nine chapters. In this first chapter the goals and the scope of this work are exposed.

Chapter 2 is a brief introduction to the basic concepts of microwave radiometry needed to understand the development of this work.

Chapter 3 gives an overview of the SMOS mission and the MIRAS instrument in order to describe the context of the mission and the subsystems of the instrument.

Chapter 4 is devoted to present in detail the calibration procedures of the MIRAS radiometer.

Chapter 5 shows an analysis of the temperature drift experimented by some calibration parameters (PMS gain, PMS offset and the receiver noise temperature) giving the sensitivity values of these parameters to the physical temperature.

Chapter 6 illustrates the method to track the PMS offset in measurement mode using several techniques like the heater offset correction and the temperature correction.

Chapter 7 is devoted to assess different strategies of the PMS gain track as the temperature correction and alternative PMS gain track by periodic uncorrelated noise injection.

Chapter 8 analyzes several techniques to track the Local Oscillator phases, using the temperature correction and different methods based on interpolation.

Chapter 9 presents the conclusions reached with the completion of the Final Project and the future work which could be done.

Finally, the sensitivity values are presented in the first appendix. The heater offset correction values are summarized in the second appendix. This is completed by the list of publications as presented in the third appendix.

CHAPTER 2

2. Basic Concepts of Radiometry

Radiometry is a field of a science and engineering related to the measure of electromagnetic radiation, i.e. the energy that all bodies emit due to be at a physical temperature above 0 K or approximately -273.15 ºC.

The instrument MIRAS located in the satellite SMOS is a radiometer. That is, it is a passive instrument that collects the natural thermal emission of the Earth. In this sense, this chapter describes the basic concepts of radiometry to give a grasp on the fundamentals of its application to remote sensing [3] [4].

2.1. Brightness and power measured by the antenna

The power emitted by a body at a solid angle per unit area [$W \cdot sr^{-1} \cdot m^{-2}$] is called brightness. The definition of the brightness for an extended source of incoherent radiation area with a determined pattern is:

$$B(\theta,\phi) = \frac{F_t(\theta,\phi)}{A_t} \qquad \textit{Eq. 2.1}$$

where $B(\theta,\phi)$ is the brightness, A_t is the effective area that is radiating and $F_t(\theta,\phi)$ corresponds to the antenna pattern.

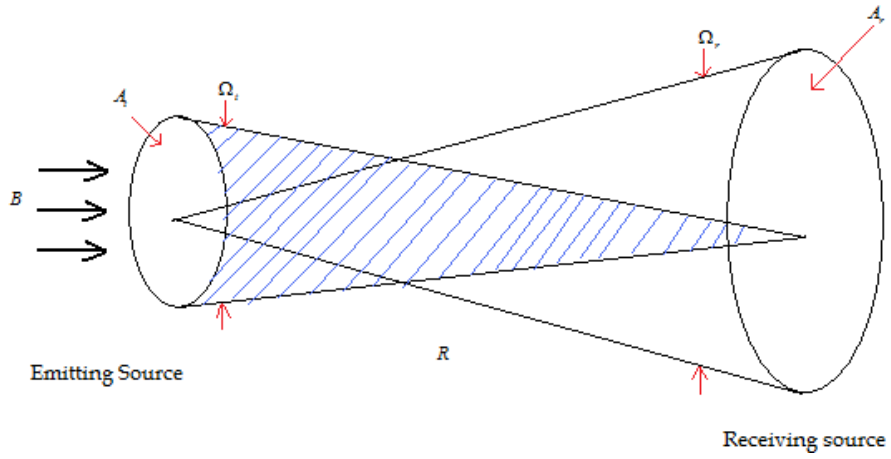

Fig. 2.1 Geometry for power received from an emitting source.

If it is considered the case shown in Fig. 2.1 of two lossless antennas separated a distance R, oriented in the direction of maximum directivity with an effective area A_t for the transmitting antenna and A_r for the receiving antenna, being R large enough to be considered constant power over a solid angle Ω_r, then the measured power by the receiver antenna (P_r) is described by the following equation:

$$P_r = S_t \cdot A_r \qquad \textit{Eq. 2.2}$$

In Eq. 2.2, S_t indicates the power density and can be defined as:

$$S_t = \frac{F_t}{R^2} \qquad \textit{Eq. 2.3}$$

Replacing Eq. 2.1 and Eq. 2.3 in Eq. 2.2, the power measured by the antenna depending on the brightness is:

$$P_r = B \cdot A_r \cdot \frac{A_t}{R^2} \qquad \textit{Eq. 2.4}$$

The solid angle subtended by the transmitting antenna (Ω_t) that it is observed by the receiver antenna corresponds to the following expression:

$$\Omega_t = \frac{A_t}{R^2} \qquad \textit{Eq. 2.5}$$

So, the power measured by the antenna can be expressed as:

$$P_r = B \cdot A_r \cdot \Omega_t \qquad \textit{Eq. 2.6}$$

If the emitting surface is not observed by the receiver antenna in the maximum direction of the radiation pattern, the diagram must be added:

$$dP = A_r \cdot B(\theta,\phi) \cdot \left|F_n(\theta,\phi)\right|^2 \qquad \textit{Eq. 2.7}$$

In addition, if the brightness is not constant with frequency, it is defined the spectral brightness density $B_f(\theta,\phi)$ with the units [$W \cdot sr^{-1} \cdot m^{-2} \cdot Hz^{-1}$]. The total power measured by the antenna can be obtained by integrating Eq. 2.7 in bandwidth and space system:

$$P = \frac{1}{2} A_r \int_{f}^{f+\Delta f} \iint_{4\pi} B_f(\theta,\phi) \left|F_n(\theta,\phi)\right|^2 d\Omega df \qquad \textit{Eq. 2.8}$$

The term $\frac{1}{2}$ in Eq. 2.8 takes into account that the antenna that presents a polarization determined, only measures half the thermal power emitted if the source emission is randomly polarized.

2.2. Thermal radiation

As mentioned before, all bodies that are at a higher temperature above 0 K, emit electromagnetic radiation.

According to quantum theory, each spectral line corresponds to the transition of an electron from an atomic energy level ε_1 to a lower energy level ε_2. Radiation occurs at a frequency (f) given by the Bohr's equation:

$$f = \frac{\varepsilon_1 - \varepsilon_2}{h} \qquad \textit{Eq. 2.9}$$

where the parameter h corresponds to Planck's constant.

Atomic emission is caused by a collision with another atom or particle. The probability of emission is higher for atomic and kinetic higher energy densities. According to Kirchhoff's law in thermodynamic equilibrium, all the energy absorbed is re-emitted.

In the case of a blackbody (opaque perfectly ideal body that absorbs all incident radiation of all frequencies) the radiated energy follows Planck's law, so radiates uniformly in all directions with a spectral brightness [$W \cdot sr^{-1} \cdot m^{-2} \cdot Hz^{-1}$] which corresponds to the following expression:

$$B_f = \frac{2hf^3}{c^2} \cdot \frac{1}{e^{\frac{h \cdot f}{k_B \cdot T_{ph}}} - 1} \qquad \textit{Eq. 2.10}$$

In Eq. 2.10, f corresponds to the frequency [Hz], k_B is the Boltzmann's constant ($1.38 \cdot 10^{-23}$ [$joules \cdot K^{-1}$]), T_{ph} is the absolute temperature [K] and c is the velocity of light ($3 \cdot 10^8$ [$m \cdot s^{-1}$]).

Stefan-Boltzmann obtains another expression for the total brightness by integrating Eq. 2.10 on the whole spectrum, so that the brightness of a blackbody responds to the expression:

$$B_{bb} = \int_0^\infty B_f \, df = \frac{\sigma \cdot T_{ph}^4}{\pi} \qquad \textit{Eq. 2.11}$$

where the parameter $\sigma = 5.673 \cdot 10^{-8}$ [$W \cdot sr^{-1} \cdot m^{-2} \cdot K^{-4}$] is the Stefan-Boltzmann's constant.

Fig. 2.2 shows the brightness spectral density versus frequency for different physical temperatures. The curves illustrate two variations of brightness with different wavelengths.

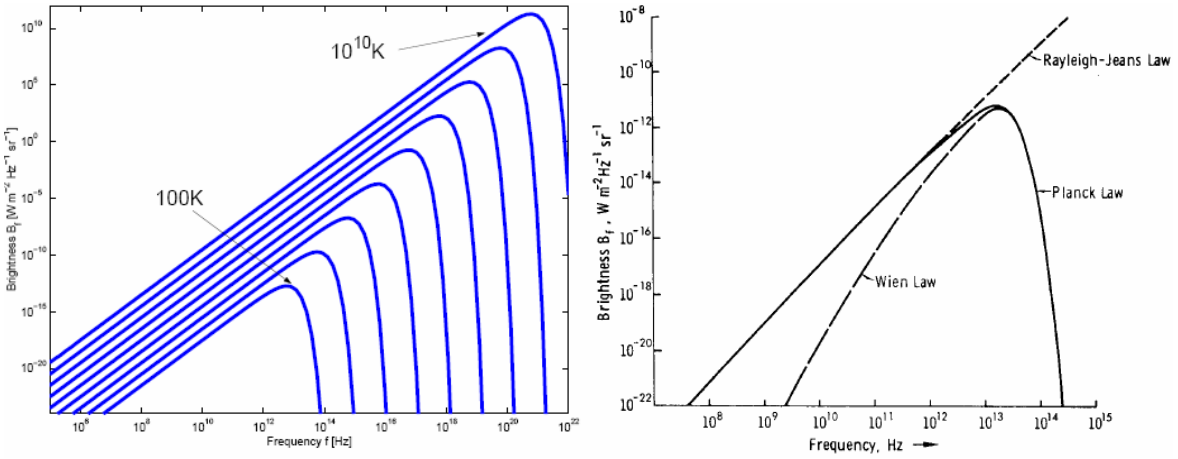

Fig. 2.2 Left: Brightness spectral density versus frequency for different physical temperatures. Right: Approaches the Planck's radiation law: the law of Rayleigh-Jeans (low frequencies) and Wien's law (high frequencies) approximations at 300 K.

For high frequencies, Eq. 2.10 is reduced to the Wien's law as follows:

$$B_f = \frac{2h}{c^2} \cdot f^3 \cdot e^{\frac{h \cdot f}{k_B \cdot T_{ph}}} \qquad \text{Eq. 2.12}$$

In the case of low frequencies the function approaches the Rayleigh-Jeans law. As shown in Eq. 2.13, there is a linear relationship between spectral brightness density and physical temperature:

$$B_f = \frac{2 f^2 k_B T_{ph}}{c^2} = \frac{2 k_B T_{ph}}{\lambda^2} \qquad \text{Eq. 2.13}$$

2.3. Non-blackbody radiation. Brightness temperature and emissivity

A blackbody, in thermal equilibrium, radiates all the energy it has absorbed and therefore emits as much energy to a specific physical temperature. A blackbody is a perfect absorber.

On the other hand, real materials (also called grey bodies) emit less power than a blackbody because they do not necessarily absorb the entire energy incident on them.

In the case of a grey body, the brightness emitted depends on the direction $B(\theta,\phi)$ and can be expressed as follows:

$$B(\theta,\phi) = 2 \cdot \frac{k_B}{\lambda^2} \cdot T_B(\theta,\phi) \cdot \Delta f \qquad \text{Eq. 2.14}$$

where T_B is the brightness temperature and Δf is the bandwidth.

The relationship between brightness of a material ($B(\theta,\phi)$) and the brightness of a blackbody (B_{bb}) that is on the same physical temperature is called emissivity ($e(\theta,\phi)$):

$$e(\theta,\phi) = \frac{B(\theta,\phi)}{B_{bb}} = \frac{T_B(\theta,\phi)}{T_{ph}} \qquad \textit{Eq. 2.15}$$

where $B(\theta,\phi) \le B_{bb}$ and $0 \le e(\theta,\phi) \le 1$.

The brightness temperature of a grey body expresses its emission properties (angular dependent) compared with that of a blackbody. Since the brightness temperature of a grey body is less than of a blackbody, the brightness temperature of a material is always smaller or equal to its physical temperature. Therefore, the emissivity has value 0 for a fully reflective material and has value 1 for a perfect absorber (blackbody).

2.4. Apparent temperature

The incident radiation upon an antenna from any specific direction may contain components originating from several different sources: the radiation emitted by the ground (T_B), the radiation emitted by the atmosphere and the radiation emitted by the atmosphere that falls on the ground and that is reflected.

Apparent radiometric temperature ($T_{AP}(\theta,\phi)$) is the blackbody equivalent temperature distribution representing the brightness distribution ($B_i(\theta,\phi)$) of the energy incident upon the antenna.

$$B_i(\theta,\phi) = \frac{2k_B}{\lambda^2} \cdot T_{AP}(\theta,\phi) \cdot \Delta f \qquad \textit{Eq. 2.16}$$

The brightness temperature ($T_B(\theta,\phi)$) is related to the radiation received on a surface or volume, while the apparent temperature ($T_{AP}(\theta,\phi)$) is related to the incident energy received by the antenna. Only in the case where the losses of the atmosphere can be considered negligible, the apparent temperature coincides with the brightness temperature ($T_{AP} = T_B$) since the only contribution to the apparent temperature is the radiation emitted by the surface.

As seen, the brightness's distribution of a grey body can be expressed in terms of the apparent temperature. Thus, taking into account the previous theory and Eq. 2.8 the power received by the antenna can be expressed as follows:

$$P = \frac{1}{2} \cdot A_r \cdot \iint_{4\pi} \frac{2k}{\lambda^2} \cdot T_{AP}(\theta,\phi) \cdot \Delta f \cdot F_n(\theta,\phi) \cdot d\Omega \qquad \textit{Eq. 2.17}$$

When computing the transfer function of the receiver, measuring the output voltage as a function of physical temperature of a load placed at the receiver input, it is possible to obtain the noise power (P_n) which is proportional to physical temperature. If the correspondence is done with the power supplied by the antenna to the receiver, it is called radiometric antenna temperature (T_A) such as an equivalent resistance to deliver the same power:

$$P_n = P = k \cdot T_A \cdot \Delta f \qquad \textit{Eq. 2.18}$$

Therefore, the antenna temperature can be expressed in terms of the normalized radiation diagram of the antenna ($F_n(\theta,\phi)$) and its effective area (A_r) as follows:

$$T_A = \frac{A_r}{\lambda^2} \cdot \iint_{4\pi} T_{AP}(\theta,\phi) \cdot F_n(\theta,\phi) \cdot d\Omega \qquad \textit{Eq. 2.19}$$

A passive radiometer is an instrument that measures the spontaneous electromagnetic emission. This radiation is normally associated with thermal effect: the brightness temperature.

Unlike other receivers, such as radar receivers that consider the radiometric antenna temperature is a noise contribution, the radiometers obtain from this signal information on the emission characteristics of the scene being viewed.

The next sections explain the main features of two different types of radiometers: real aperture radiometers and interferometric radiometer by aperture synthesis.

This Final Project presents a study of how the temperature drifts affect different calibration parameters of the first 2D interferometric radiometer by aperture synthesis on board a satellite within the SMOS mission of the European Space Agency for the observation of geophysical parameters of Earth.

2.5. Total Power Radiometer

So far, all microwave radiometers used for Earth observation have been real aperture radiometers. The more simplified version of this type of radiometers is the Total Power Radiometer (TPR).

A total power radiometer consists of an antenna connected to a superheterodyne receiver with bandwidth Δf and total gain G, followed by a power detector and a low-pass filter (Fig. 2.3). The power delivered by the antenna is usually broadband noise higher than the range of the receiver. The antenna receives the radiofrequency (RF)

power emitted by the material observed and an RF amplifier (low noise) increases the noise power of the signal acquired. The band-pass filter selects the desired frequency band which is converted in the mixer. The signal is amplified before passing through the power detector. Finally, it is necessary to use a low pass filter to average the obtained voltage. In a total power radiometer, the output voltage is proportional to the noise temperature of the system and can be written as:

$$V_{out} = k \cdot T_{sys} \cdot \Delta f \qquad \textit{Eq. 2.20}$$

where $T_{sys} = T_A + T_R$ is the system noise temperature, T_A is the equivalent noise temperature measured by the antenna, T_R corresponds to the equivalent noise temperature of the receiver and Δf is the bandwidth.

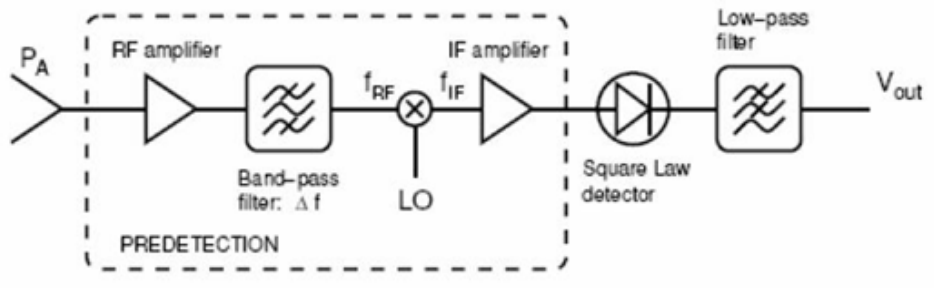

Fig. 2.3 Block diagram of a Power Total Radiometer.

In order to calibrate a total power radiometer is enough to measure the output voltage corresponding to two noise temperatures at the input (cold load and hot load). So, a TPR requires only external calibration (Fig. 2.4).

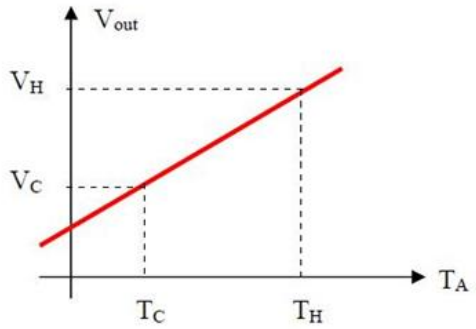

Fig. 2.4 Total Power Radiometer calibration using cold load and hot load.

Two important parameters that characterize the radiometric measurement are the sensitivity or radiometric resolution and the accuracy. The absolute accuracy, that it is the closeness of the agreement between the result of a brightness temperature measurement and the true value, depends of the calibration strategies and the stability of

the instrument. In contrast, the sensitivity or radiometric resolution of the measure can be defined as the smallest change in temperature of antenna that can be detected at the output of the radiometer. The desired sensitivity value is typically on the order of 1K.

The spatial resolution that can reach a radiometer is limited by the size of its antenna. Measuring geophysical parameters such as soil moisture and ocean salinity (L-band) requires high spatial resolution, and therefore the size of the antenna of a real aperture radiometer to allow such resolution is not technologically viable.

2.6. Interferometric Radiometer with Aperture Synthesis

As mentioned above, the radiometry is concerned with measuring the radiation power emitted by the materials. Interferometry is also addressing the measurement of the phase information of this radiation. However, the spatial resolution requirements needed by the scientific community would force to use radiometers with large antennas.

The interferometric called aperture synthesis is a technique in which the cross-correlation between signals acquired from two or more antennas are measured. Substantial reductions in the antenna aperture needed for a given spatial resolution can be achieved with this technique. As a result, aperture synthesis has been the solution that has improved spatial resolution with respect to the actual opening passive microwave remote sensing instruments in space to obtain geophysical parameters as soil moisture and ocean salinity which require observations at long wavelengths and, therefore, large antennas.

An interferometric radiometer consists of an array of antennas. The output voltages of different pairs of antennas are correlated and return the visibility function. From the samples of this function, using image inversion algorithms, the image is reconstructed obtaining brightness temperature maps of the scene. This type of radiometers require a previous correction of the visibility samples before to external calibration as explained in total power radiometers, since the interferometric radiometer by aperture synthesis do not measure the distribution of brightness temperature but the samples of its Fourier transform.

The American hybrid real and synthetic aperture radiometer ESTAR (Electronically Steered Thinned Array Radiometer) on board an aircraft demonstrates the validity of the 1D aperture synthesis – 1D real aperture principle. The experiments indicate that a valid image reconstruction and calibration have been obtained for this remote sensing technique. In the nowadays, a European 2D interferometric radiometer by aperture synthesis called MIRAS (Microwave Imaging Radiometer using Aperture Synthesis) is used for the implementation of these measures within the SMOS mission.

CHAPTER 3

3. SMOS mission and MIRAS instrument

This chapter is devoted to explain the importance of the Soil Moisture and Ocean Salinity (SMOS) mission and how it has been designed. The mission will demonstrate a new technology in the Earth observation from space. A brief description of some important parts of the instrument on board of SMOS satellite is presented.

3.1. SMOS mission

SMOS mission is the second Earth Explorer Opportunity mission selected in the framework of the ESA's Living Planet Programme [1]. This programme comprises a science and research element, including different Earth explorer missions and an Earth watch element. It has been designed to facilitate the delivery of Earth observation data for use in operational services.

In the SMOS mission, the main objectives are to globally observe soil moisture over the Earth's landmasses and salinity over the oceans for a period of 3-5 years with an innovate technology on board a satellite, a Microwave Imaging Radiometer by Aperture Synthesis (MIRAS). This is possible because both the moisture and salinity affect the electrical properties of matter and the emissivity of any material based on these properties. The MIRAS instrument is based on the moisture and salinity decrease the emissivity of soil and seawater, respectively.

The goal of monitoring the continental areas is providing global measurements on soil moisture in appropriate temporal-spatial accuracy and assiduity, controlling the percentages of rainfall running the surface, filtering the land and evaporating and thus becoming part of the atmosphere to carry out climatic, meteorological and hydrological studies on a large scale. The objective in observing the marine areas of the planet is to monitor oceanic circulation on a global scale, since the tracking of salinity allows determining the course of water masses, and particularly, the circulation that depends on density changes in water masses. Ultimately, the soil moisture and the ocean salinity are key parameters in the characterization of atmospheric, oceanographic and hydrological predictive models.

The SMOS satellite had been launched the 2nd of November 2009 at 02:50 CET hour (01:50 GMT hour) together with the PROBA-2 satellite (Fig. 3.1) using the Rockot launch vehicle from the Plesetsk Cosmodrome in northern Russia [5], to a nearly sun-synchronous orbit of 763 km, forcing an orbital period of about 100 minutes. This means that the satellite will go around our planet 14.4 times per day and the revisit time in any point on the Earth is guaranteed to be 3 days.

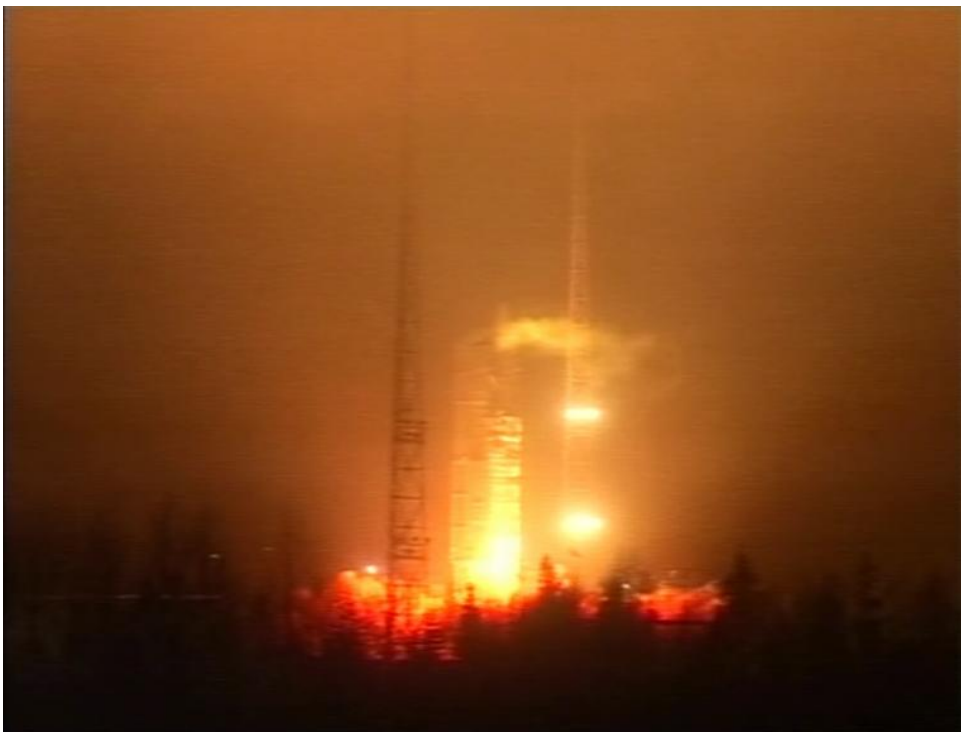

Fig. 3.1 The SMOS and Proba-2 at the moment liftoff (Credits: ESA).

The theoretical design of the SMOS instrument and its subsystems has been commissioned by different European universities, like the Aalto University School of Science and Technology (TKK), in Helsinki, Findland, and the Universitat Politècnica de Catalunya (UPC), Spain, by the Remote Sensing Laboratory Group (RSLab) from the Theory and Signal Communication department (TSC) [2]. The receivers have been manufactured by the Spanish company MIER Communications and the integration of the different elements has been carried out by EADS-CASA Espacio.

The mission is being developed under the management of ESA in two areas: the Satellite Operations Ground Segment (SOGS) and the Data Processing Ground Segment (DPGS). The Centre National d'Etudes Spatiales (CNES) located in Toulouse, France, is in charge of the spacecraft operations via an S-band station in Kiruna, Sweden. The European Space Astronomy Centre (ESAC) is ESA's centre for space science. It is located in Villanueva de la Cañada, close to Madrid in Spain, and hosts the science operation centers for all ESA astronomy and planetary missions together with their scientific archives. It is in charge of the data processing, where the payload data are received via X-band. A consortium formed by different Spanish companies, like EADS-CASA Espacio, GMV Aerospace and Defense and INDRA Espacio, and a Portuguese company Deimos Space, performs data processing and validation. European Universities and other institutions, among them the SMOS Barcelona Expert Centre on Radiometric Calibration and Ocean Salinity (SMOS-BEC) [6] are also involved in the data processing.

3.2. MIRAS instrument

In this section the instrument architecture, the operating principle, the observation modes and a description of some subsystems of the instrument involved to this project are exposed.

3.2.1. Instrument architecture

The Microwave Imaging Radiometer using Aperture Synthesis (MIRAS) instrument [7] is the single payload in the SMOS mission. It is a 2D interferometric radiometer with aperture synthesis which is capable of measuring thermal radiation around 1.4 GHz (L-band). This type of instrument has never been used before on board of a satellite.

The structure (Fig. 3.2 and Fig. 3.3) contains three deployable arms that form angles of 120º to each other forming a Y-shape, joined by a central nucleus or hub. The hub measures 1.3 m in diameter being the dimensions with the three arms completely extended up to 8 m in diameter. The satellite weights around 680 kg. Each arm contains three segments and each segment contains 6 antennas distributed at equivalent intervals, forming the 54 antennas. The hub has 15 antennas in a star configuration, making a total of 69 antennas.

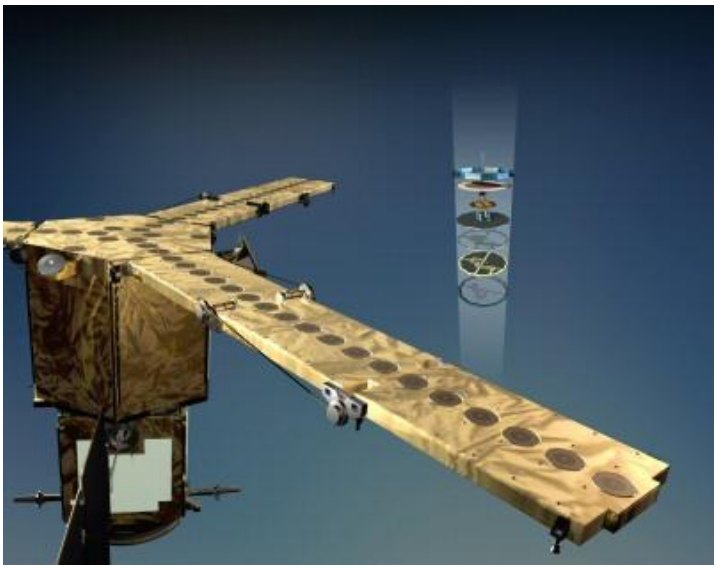

Fig. 3.2 Global vision of the MIRAS instrument (Credits: ESA).

The receiver known as LICEF (Lightweight Cost Effective Front-end) has a patch-type antenna, with a beam width of approximately 70º. There are 3 elements named NIR (Noise Injection Radiometer) that contain one antenna with two polarizations and two special receivers, one for each polarization. The rest contains one antenna with also two polarizations but only one receiver. In conclusion, there are a total of 72 receivers that measure the Earth radiation emitted at L-band on the horizontal and vertical polarizations.

The acquired signal is then transmitted to a central correlator unit, which performs interferometry cross-correlation of the signals collected by each receiver pairs, giving

the samples of the visibility function. From these samples of visibility maps, the brightness temperature of the land and the oceans can be produced using a Fourier Synthesis technique.

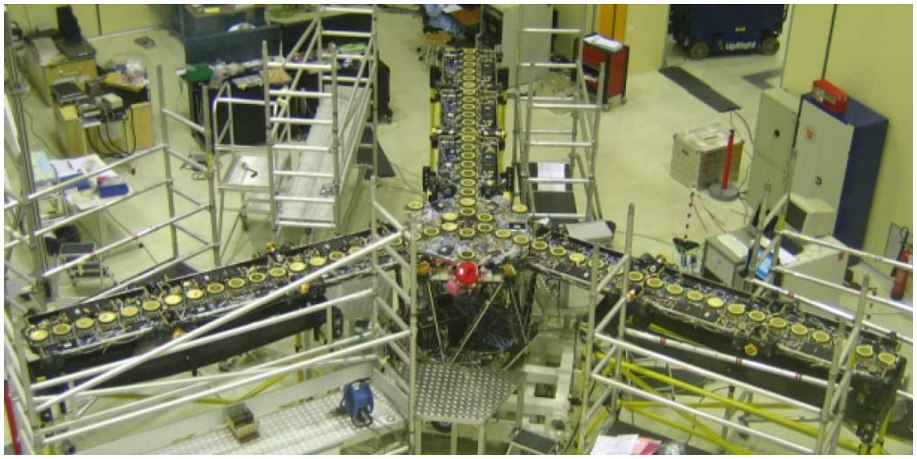

Fig. 3.3 Flight-model photograph in the clean room of EADS-CASA Espacio (Credits: ESA)

3.2.2. Operating principle

The operating principle of the MIRAS is the baseline [8][9] that is formed by two antennas, two receivers and a complex correlator, as shown in Fig. 3.4:

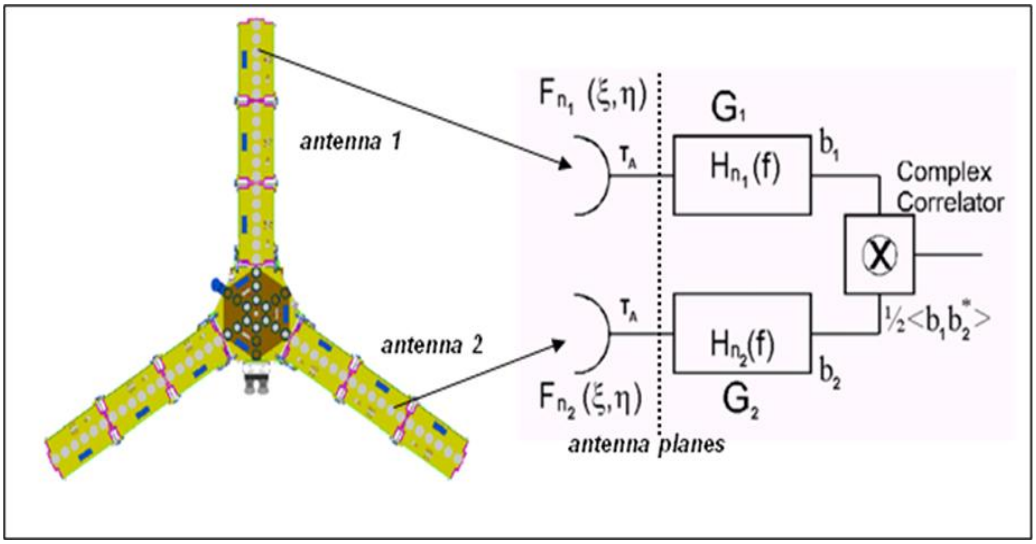

Fig. 3.4 Outline of a baseline in the interferometric radiometer.

where G_k and G_j are the available power gains of the channels, $H_{nk}(f)$ and $H_{nj}(f)$ their frequency response, $F_{nk}(\theta,\phi)$ and $F_{nj}(\theta,\phi)$ the normalized antenna patterns and $b_k(t)$ and $b_j(t)$ are the analytical signal extracted for each pair of receivers.

The antennas are situated in the plane XY and near the coordinate origin. The polar coordinates (r, θ, ϕ) and the direction cosines ($\xi = sin\theta \cdot \cos\phi$, $\eta = sin\theta \cdot \sin\phi$) are defined.

The autocorrelation and the cross-correlations of the signal at the receivers output can be expressed as follow:

$$\frac{1}{2}\left\langle \left|b_k(t)\right|^2 \right\rangle = k_B \cdot B_k \cdot G_k \cdot (T_{A_k} + T_{R_k}) \qquad \textit{Eq. 3.1}$$

$$\frac{1}{2}\left\langle \left|b_j(t)\right|^2 \right\rangle = k_B \cdot B_j \cdot G_j \cdot (T_{A_j} + T_{R_j}) \qquad \textit{Eq. 3.2}$$

$$\frac{1}{2}\left\langle b_k(t) \cdot b_j^*(t) \right\rangle = k_B \cdot V_{kj} \cdot \sqrt{B_k \cdot B_j} \cdot \sqrt{G_k \cdot G_j} \qquad \textit{Eq. 3.3}$$

being k_B the Boltzmann constant, T_{R_k} and T_{R_j} the equivalent noise temperature of the receivers k and j respectively, B_k and B_j the equivalent noise bandwidth ($B_k = \int_0^{+\infty} \left|H_{nk}(f)\right|^2 df$), T_{A_k} and T_{A_j} the equivalent antenna temperature and V_{kj} is the visibility function.

The visibility function V_{kj} is related to the distribution of brightness temperature T_B of the source in this way:

$$V(u_{kj}, v_{kj}) = \frac{1}{\sqrt{\Omega_k \cdot \Omega_j}} \iint_{\xi^2+\eta^2 \le 1} \frac{T_B(\xi,\eta) - T_{ph}}{\sqrt{1-\xi^2-\eta^2}} \cdot F_{nk}(\xi,\eta) \cdot F_{nj}^*(\xi,\eta) \cdot \tilde{r}_{kj}\left(-\frac{u_{kj}\cdot\xi + v_{kj}\cdot\eta}{f_0}\right) \cdot e^{-j2\pi(u_{kj}\cdot\xi + v_{kj}\cdot\eta)} d\xi d\eta \qquad \textit{Eq. 3.4}$$

In Eq. 3.4, Ω_k and Ω_j are the equivalent solid angle of the antennas, $u_{kj} = \frac{x_k - x_j}{\lambda_0}$ and $v_{kj} = \frac{y_k - y_j}{\lambda_0}$ are the set of spatial frequencies, where the visibility function is sampled (corresponding to the projections at X and Y axis of the distance between antennas normalized at wavelength), $F_{nk}(\xi,\eta)$ and $F_{nj}(\xi,\eta)$ are the normalize antenna patterns and $\tilde{r}_{kj}\left(-\frac{u_{kj}\cdot\xi + v_{kj}\cdot\eta}{f_0}\right)$ corresponds to the *Fringe – washing* function term. This term is related to the differences in the frequency response of the filters in the two receivers within the baseline.

In the ideal case, the antenna radiation patterns are identical. The effect of the spatial decorrelation (*Fringe – washing* function term) is negligible and there are not errors in the antennas situation. Therefore, the expression of the visibility function is modified to the following:

$$V(u,v) = F\left[\frac{\left|F_{nk}(\xi,\eta)\right|^2}{\Omega_k} \cdot \frac{T_B(\xi,\eta) - T_{ph}}{\sqrt{1-\xi^2-\eta^2}}\right] \qquad \textit{Eq. 3.5}$$

Now the visibility function is a special 2-Dimensional Fourier Transform of the brightness temperature.

3.2.3. Observation modes

The MIRAS has two main operation modes [8]: the measurement mode, which performs measurements of the instrument to compute, in final term, the brightness temperature; and the calibration mode where various parameters are monitored and corrected if necessary. The calibration procedures will be explained in detail in chapter 4. The instrument has two measurement modes depending on the antenna polarization: dual-pol and full pol.

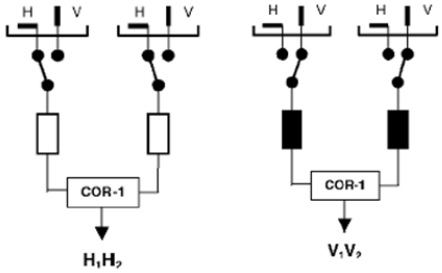

Fig. 3.5 Measurement mode dual-pol. Left: horizontal-horizontal. Right: vertical-vertical.

In the dual-pol mode, the LICEFs measure alternately in different polarization. Each LICEF has a switch that allows changing the polarization of its antenna. Nevertheless, each NIR has only one polarization (actually, it has one antenna with two polarizations but two separate receivers for each polarization). First, the two LICEFs are in horizontal except the vertical NIRs, and after this, the LICEFs are in vertical mode (Fig. 3.5) except the horizontal NIRs. This produces 2346 baselines from the receivers in the same polarization (HH or VV), with an additional three measurements from the NIR receivers in the opposite polarization. In both cases the integration time is 1.2 seconds.

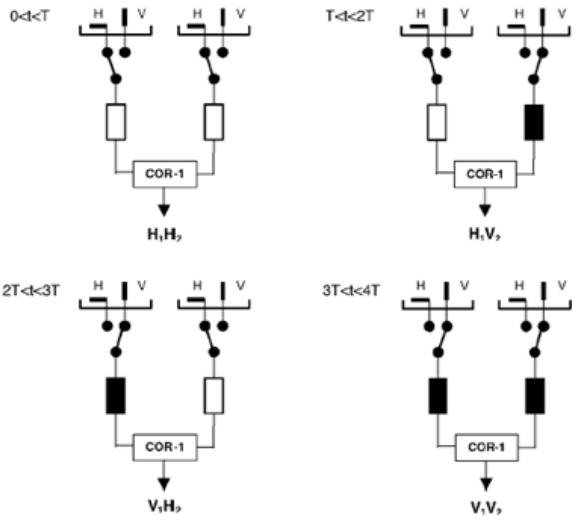

Fig. 3.6 Measurement mode full-pol. Left top: horizontal-horizontal. Right top: horizontal-vertical. Left bottom: vertical-horizontal. Right bottom: vertical-vertical.

Using the full-pol mode, the timing cycle is based on an alternating four-epochs sequence that was devised to measure all cross-correlations, including the correlations between horizontal and vertical polarization as shown in Fig. 3.6. There are 8 steps in the full-pol mode, because the instrument has three arms (HHH, HVV, VHV, VVH, VVV, VHH, HVH, HHV). Of course, the NIRs keep their polarization in the 8 steps.

3.2.4. MIRAS description

In the following section different parts of the instruments will be described for better understanding the MIRAS instrument operation [7][9][10].

3.2.4.1. Antennas

The LICEF antenna provides best performance in terms of gain, bandwidth and differentiation of horizontal and vertical polarization components of incoming microwaves. It consists of four probes implemented as pairs, which are rotated 90 degrees to each other to acquire the two different signal polarizations.

Multi-layer 'microstrip' technology has been chosen for the circuit configuration. Each layer is dedicated to one polarization. Each antenna weighs 190 g, is 165 mm in diameter and is 19 mm high. The different layers are described in Fig. 3.7:

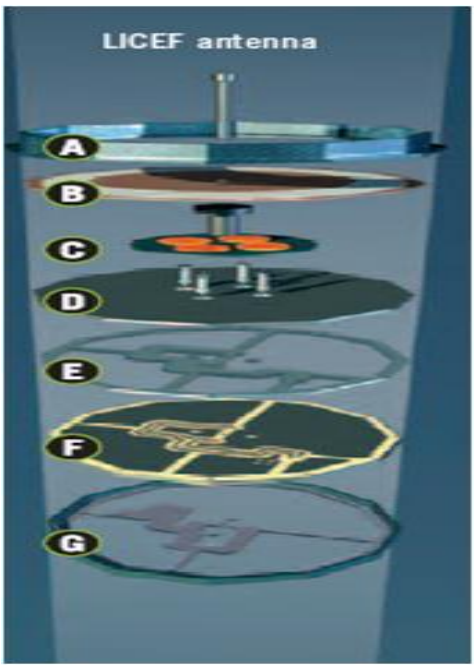

a) Carbon-fibre structure
b) Patch antenna
c) Feeding discs
d) Cavity floor to patch antenna
e) Alumninum spacer
f) Feed circuits (Multilayer microstrips on both sides of the grounding plane)
g) Aluminium spacer

Fig. 3.7 Different layers in the LICEF antennas.

The operating wavelength is determined by the increase in the sensitivity of the brightness temperature to soil moisture (ground) and to salinity (ocean) as the observation frequency decreases. L-band (1400-1427 MHz) is used because it is the lowest frequency with a protected band.

3.2.4.2. LICEF receivers

The function of the LICEFs is to measure the antenna radiometric temperature which represents the radiation noise power delivered by the antenna to the receiver. It generates 1-bit digital signal as detailed in Fig. 3.8 and this signal is transmitted to a DICOS (Digital correlator system). A photograph of the LICEF is shown in Fig. 3.9.

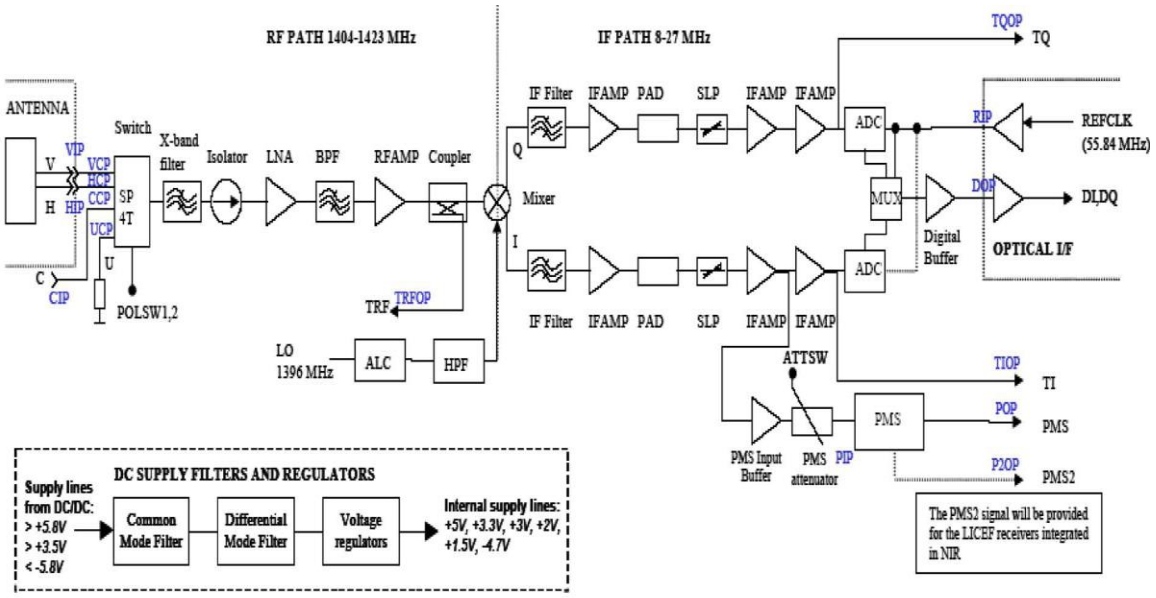

Fig. 3.8 LICEF block diagram (Credits: ESA).

The radiofrequency (RF) section is designed to minimize the noise figure and leakage between receivers and to filter out any signal outside the protected radio astronomy band between 1400 and 1427 MHz. Each LICEF has four possible inputs, the horizontal and vertical antenna inputs (H and V), the calibration input for correlated noise (C) and the input with the load for uncorrelated noise (U). The switch allows selecting one of these inputs. An X-band filter is used to prevent interference from the satellite data transmitter and undesired intermodulation products within the low noise amplifier, and an isolator absorbs any backward noise generated by the low noise amplifier. A bandpass filter achieves the required out-of-band rejection, particularly the image band. A RF amplifier amplifies the filter output to drive the mixing stage.

The mixer, using a local oscillator (LO) frequency of 1396 MHz, shifts the RF band down to between 8 and 27 MHz intermediate frequency (IF) band. A high-pass filter at the LO input has been included to improve the mixer isolation from the LO port to IF port in the intermediate frequencies and to reject thermal noise coming from the LO input to avoid a nonsymmetrical noise figure in the I and Q branches. A band pass filter

at the mixer output in I and Q removes out-of-band spurious signals of the downconversion. An automatic level control circuit at the LO input ensures that the power level of the LO at the input of the mixter remains constant.

A low-noise IF amplifier increases the voltage signal after the mixer. Also it reduces the noise figure contribution of the IF chain. This is followed by a variable attenuator and a slope corrector. The variable atenuator circuit is used for reducing the gain of the receiver, for compensating gain variations with temperature if needed, for compensating amplitude imbalances between I and Q channel of each individual receiver and also for correcting amplitude deviations between the receivers. The slope corrector circuit modifies potential severe deviations in the slope of the receiver response, thus improving the amplitude similarity between receivers. Two additional IF amplifiers condition the signal for the analog-to-digital converter that converts the analog signals to 1-bit digital signal, detecting only the sign of the signal and outputs a low or high digital level. Both digital signals are time-multiplexed before they enter to an electrical-optical converter that sends them to the correlator.

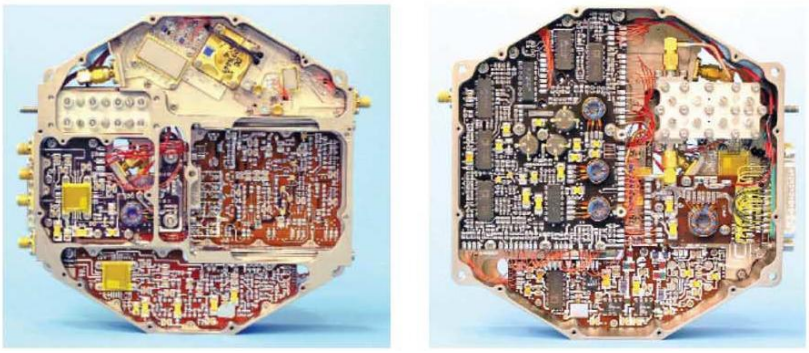

Fig. 3.9 Photograf of LICEF antennna side (left) and bottom side (right) (Credits: ESA).

3.2.4.3. NIR receivers

The NIR is a polarimetric noise injection rediometer in L-band. There are three NIR units situated in the hub, the central part of the MIRAS instrument. Photographs of one of the NIR units are shown in Fig. 3.10.

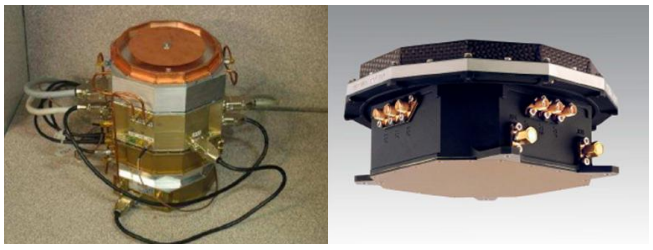

Fig. 3.10 Photograf of a NIR unit (left) and NIR controller unit (right).

The main purposes of the NIRs is to measure the full polarimetric antenna noise temperature to provide a precise measurement of the average brightness temperature scene and to measure the amplitude of the noise temperature level of the reference noise source of the calibration system (CAS). Thus, NIR is the absolute amplitude reference

of MIRAS. Furthermore, NIR incorporates operational modes that allow it to form interferometric baselines (so-called mixed baselines) with other receivers.

Each NIR consists of one NIR controller unit, two LICEF receivers, one for vertical and one for horizontal polarization, and phase stable RF cables that connect the controller to the receivers, as shown in Fig. 3.11. The controller incorporates an antenna that receives the target noise. The receivers of NIR are almost identical to the other receivers of MIRAS. Also, the antenna is identical to those of the other antennas of MIRAS.

The functions of the controller are to inject reference noise into the two receiver chains, regulate the amount of the injected noise to keep the system balanced with antenna temperature or with the calibration noise from CAS, and control the Dicke switches of NIR according to the selected operation mode.

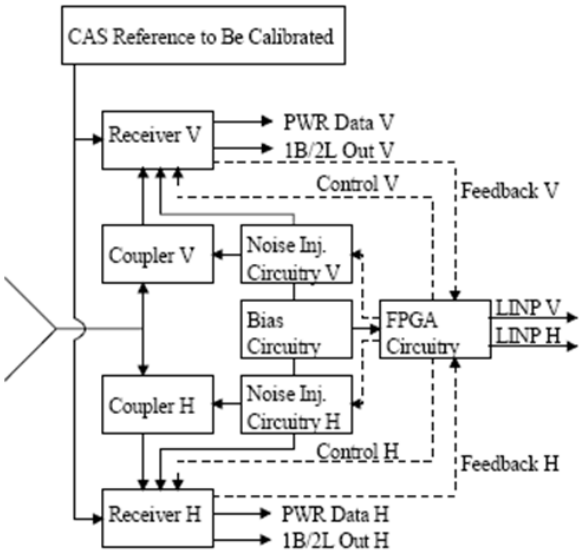

Fig. 3.11 Block diagram of the NIR units.

The NIR have different operation modes. The most important modes are: NIR-A mode in which the average brightness temperature of the scene is measured, NIR-R mode in which the NIR measures the two levels of CAS noise temperature and NIR-AR mode that is used to calibrate the instrument looking to the cold sky.

3.2.4.4. Calibration subsystem and noise sources

The calibration subsystem (CAS) is based on a noise distributed network (NDN) that provides a correlated noise source (NS) reference to calibrate the noise temperature and the relative phase characteristics between the receivers. The NDN (Fig. 3.12) contains three NS for each arm and one NS source in the hub that generate the two different reference noise levels (hot and warm). The amplitude of the noise generated is periodically calibrated in flight using the NIR receivers. All NS are duplicated (it have the nominal one or the redundant one) in case of failure.

In the arms, a NS is located at each segment. Each one drives a one-to-twelve network (1:2 x 1:6) for distributing the noise using power dividers (PD) for a set of 12 LICEFs

with an overlap of 6 LICEFs so that every receiver can receive noise from two adjacent sources, one at a time, except for the third section in each arm that only receives noise from one source.

In the hub there is a one-to-eighteen network (1:3 x 1:6) for distributing the noise generated by a single source simultaneously to all hub receivers. This noise is also sent to the NIRs for accurate measurement of the noise temperature being injected.

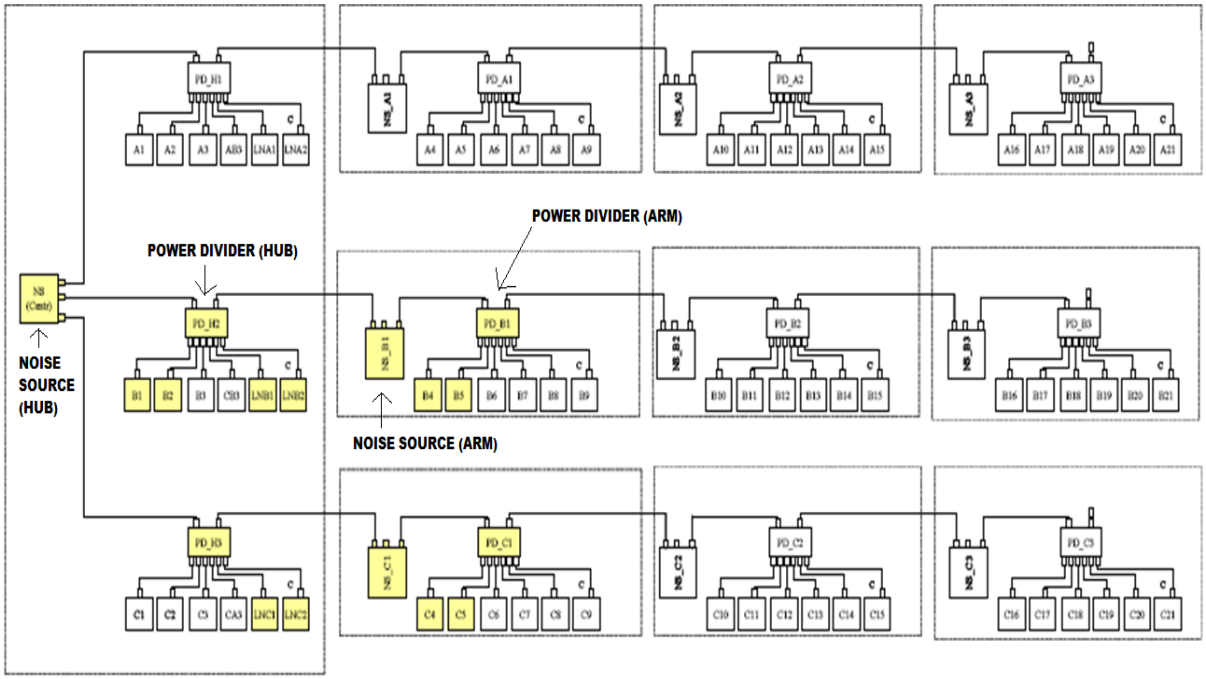

Fig. 3.12 Distributed CAS system for arms and hub.

To determine the passive network characterization, it has been necessary measuring, over the physical temperature, the generated noise level, the S-parameters of all individual NS, the S-parameters of the PD, cables, etc, and combining the results in a mathematical model to simulate the behaviour of the integrated network. Depending on the physical temperature measured by the thermistors during calibration the S-parameters will have to be linearly interpolated in temperature using the two closest temperature values characterized on-ground. A photograph of the noise sources and power dividers are below in Fig. 3.13.

Fig. 3.13 Noise source (left) and power divider (right) (Credits: ESA).

3.2.4.5. Digital Correlator System

The digital signal produced by each receiver is transmitted by a dedicated optical link to the digital correlator system (DICOS) whose function is to correlate the signals produced by all the receivers.

Each DICOS is a XNOR gate whose the output only is 1 if the two inputs are equal, as shown in Fig. 3.14. The correlation is measured accumuling its output during the integration time at a given clock frequency of 55.84 MHz. At the end, the correlator counts are read and the accumulator is reseated for the next integration. The correlator counts (N_C) means the number of coincident bits in the pair of receivers that form a baseline. There are different combinations in phase and quadrature of each pair of receivers and for each position of the switch. The correlations are performed at punctual delays during measurement, and, in addition, at early and late delay lags during calibration intervals.

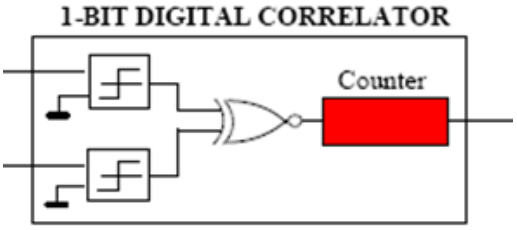

Fig. 3.14 Digital correlator scheme.

There are $N_{rec} \cdot \frac{(N_{rec}-1)}{2}$ baselines. MIRAS has 72 receivers and therefore the number of baselines is 2556, although only 612 baselines have a common noise source. $N_{C_{\max}}$ is the maximum number of counts, which is a function of the sliding window of the DICOS and the integration time used. For dual polarization the values is 65437 while for full polarization mode it is 43625. The correlation units (c.u.) are defined as normalized values multiplied by 10^4, so their maximum value is 10^4 c.u.

In Fig. 3.15 a Correlator Control Unit (CCU) that comprises the instrument central computer unit and the correlator units is shown.

Fig. 3.15 Photograph of Correlator Control Unit (Credits: ESA).

3.2.4.6. Control and Monitoring Node and Local Oscillators

The Control and Monitoring Node (CMN) acts as a remote terminal of the CCU. Each of the three arms contains three segments of six receivers. In each segment, there is one CMN responsible of the control and monitoring of the signals. The hub is divided in three sectors with a CMN in each sector. There are a total of 12 CMN's in the instrument.

The main functions of the CMN's are the reception of commands from and sending to the CCU, the acquisition of the physical temperature readings of the thermistors, the acquisition of the voltages, the control of the LICEF polarization switch, the control of the noise injection, the distribution of the thermal control actuations and the generation and distribution of the Local Oscillator (LO) signals.

In each CMN is synthesized the frequency of 1396 MHz because there are one LO phase-locked to a reference clock of 55.84 MHz as shown in Fig. 3.16. The design is based on a sampling phase detector block in which the 25^{th} harmonic of the reference is compared to a 1396 MHz LO provided by a Colpitts oscillator. It generates no clock harmonics in the pass band of the instrument, which could fatally degrade its performance.

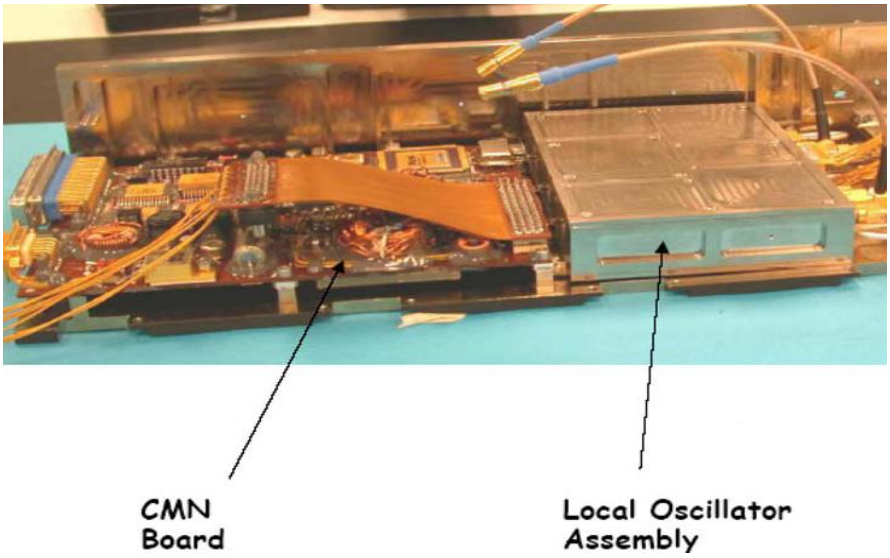

Fig. 3.16 Photograph of CMN and LO (Credits: ESA).

3.2.4.7. Power Measurement System

Each LICEF has a Power Measurement System (PMS) to perform the power to voltage conversion of the received signal.

The PMS circuit consists in a quadratic power detector based on a tunnel diode and a low pass filter as integrator, as shown in Fig. 3.17. Its operation is equivalent to a total power radiometer. It also incorporates a switch that selects between two reference voltages (attenuated or non-attenuated).

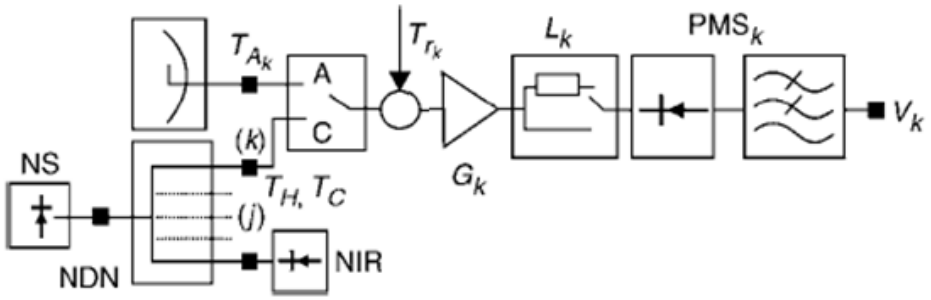

Fig. 3.17 Block diagram of the PMS.

In the scheme of Fig. 3.17, v_k is the output voltage for each *k*-LICEF and it can be approximated as follows:

$$v_k = G_k^A \cdot (T_{A_k} + T_{r_k}^A) + v_{off_k} \qquad \textit{Eq. 3.6}$$

where v_{off_k} is the PMS offset [V], G_k^A is the PMS gain [V/K], T_{A_k} is the antenna temperature [K] and $T_{r_k}^A$ is the receiver noise temperature [K]. Both the gain and offset are parameters that are estimated in the PMS calibration which will be explained in detail in chapter 4.

The system temperature (T_{sys_k}) in antenna is defined below:

$$T_{sys_k}^A = T_{A_k} + T_{r_k}^A \qquad \textit{Eq. 3.7}$$

The visibility samples are normalized to the system temperature, and therefore, it is necessary to know the value of that parameter. For this reason, the calibrated PMS gain and offset are required.

$$T_{sys_k}^C = \frac{v_k - v_{off_k}}{G_k^C} \qquad \textit{Eq. 3.8}$$

Although the PMS design could, at its simplest, be a single diode, considerable effort has been invested in designing a PMS that is highly stable over a wide temperature and dynamic range. Anyway, from different tests on ground and in flight, some thermal drift in the PMS parameters has been detected, so it was decided to monitor this drift to make a more accurate estimation of these parameters, as seen in chapter 5.

3.2.4.8. Thermal control system

The thermal environment will vary around the orbit and it is important to understand both the intra-orbit and inter-orbit variations. The thermal control system [11] has been designed to minimize the temperature differences between all receivers.

The different temperature sensors distributed along the instrument acquire the physical temperatures that are sent to the CMNs to switch on or off the heaters. Each heater is controlled by their associated CMN. There are 12 heaters, one in each section of the three arms and three more in the hub.

In this way the receivers shall be controlled at 22 +/- 0.25 ºC in order to achieve the maximum gradient specified of 6ºC during the measurement modes. After examining the measurements in flight, it was observed that the maximum gradient is around the 3.5ºC, so it is within the range expected.

CHAPTER 4

4. Calibration of MIRAS instrument

This chapter is devoted to explain the calibration procedures in the MIRAS instrument to accomplish the scientific requirements set out in the SMOS mission. Since some of the system performances of the instrument can change over time and with the temperature drifts, MIRAS has to be calibrated in order to achieve the desired accuracy in the SMOS final data products.

The MIRAS instrument is based on 2D-interferometry thus gets the brightness temperatures from the visibility samples by means of Fourier synthesis technique. These visibility samples are previously denormalized and corrected from instrumental errors according the following expression:

$$V_{kj}^{A} = \frac{\sqrt{T_{sys_k}^{A} \cdot T_{sys_j}^{A}}}{G_{kj}^{A}} \cdot M_{kj} \qquad \textit{Eq. 4.1}$$

where M_{kj} is the normalized complex correlations computed from the correlations counts after the self-calibration procedure. $T_{sys_k}^{A}$ and $T_{sys_j}^{A}$ are the system temperatures referred to the antenna plane of LICEF k and LICEF j, respectively. G_{kj}^{A} is the Fringe Wash function term also referred to the antenna plane.

To correct the visibility samples it is necessary the calibration of the instrument both in amplitude and phase [12] [13] [14].

4.1. Amplitude calibration

When the amplitude calibration is mentioned, we refer to the $T_{sys_k}^{A}$ and $T_{sys_j}^{A}$ measured by means of a PMS and $\left|G_{kj}^{A}\right|$, the modulus of the fringe-washing term evaluated at the origin. In this project, only the amplitude calibration of the PMS has been studied.

4.1.1. PMS calibration

The main objective is to calibrate the PMS in terms of gain (G_{PMS}) and offset ($v_{off_{PMS}}$). For a better understanding of the calibration procedure, a block diagram of a baseline and the calibration system is shown in Fig. 4.1. Note that the calibration internal plane (CIP), the antenna plane that includes the horizontal antenna plane (HAP) and the vertical antenna plane (VAP) and the NIR plane are also shown in the scheme.

There are three types of calibration of the PMS: the internal calibration using the correlated noise injection, the external calibration based on looking at a constant and known target and the one-point calibration that it is a combination of the internal and external signals. In both, the calibration is based on a lineal model of the PMS. The

performance of the PMS used to denormalize the digital correlations in interferometric radiometers is degraded due to its non-linear behavior. This effect in the PMS has been studied and corrected [15].

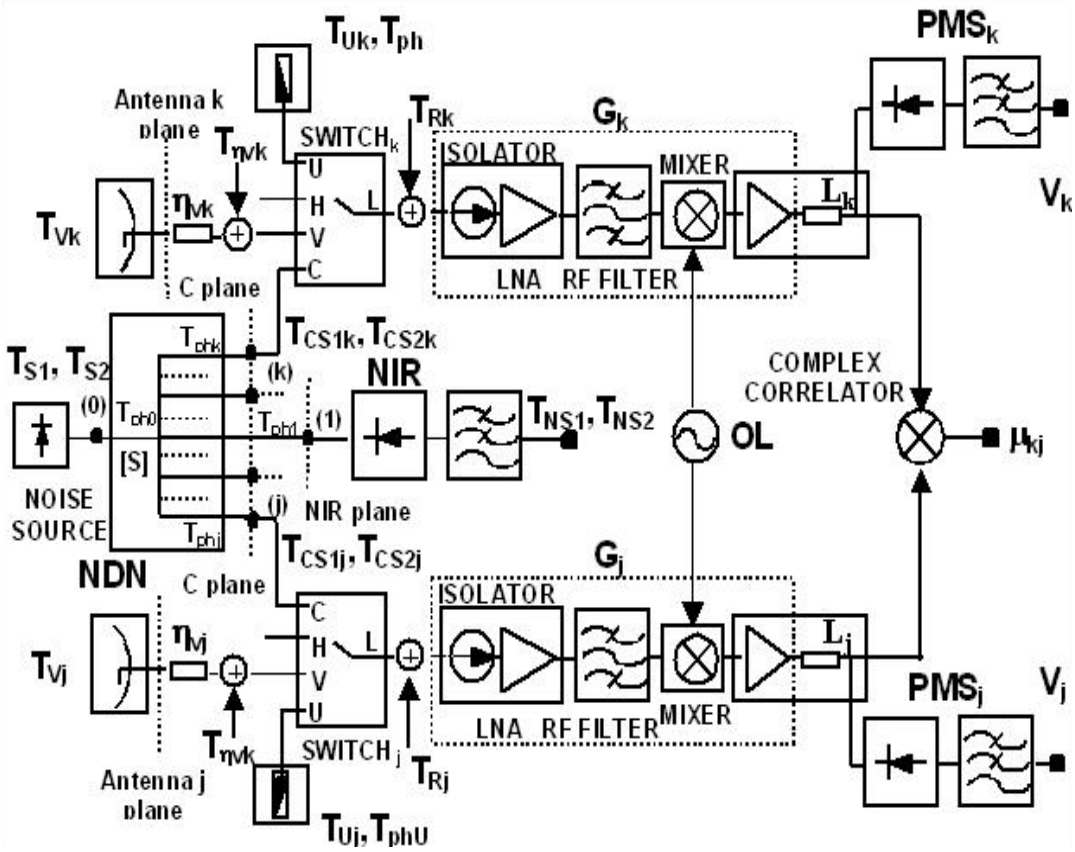

Fig. 4.1 Block diagram of a single baseline

4.1.1.1. Internal calibration

The internal calibration of the PMS, also called ***4-points calibration method*** [14] [16], occurs when correlated noise from the NS is injected through the NDN in the "C" port of the switch. Hence, for each *k*-receiver and taking into accounts that all equations are referred to the C plane (Fig. 4.1), the measured output voltage of the PMS (v_k), when an equivalent system temperature (T_{sys_k}) is presented at system input, is given by:

$$v_k = G_k^C \cdot T_{sys_k}^C + v_{off_k} \qquad \textit{Eq. 4.2}$$

where $T_{sys_k}^C$ can be split into two terms relating the equivalent system noise temperature $T_{r_k}^C$ and the external temperature T_{ext_k}, being $T_{sys_k}^C = T_{r_k}^C + T_{ext_k}$.

If $T_{sys_k}^C$ is the desired magnitude to be estimated, then only the gain (G_k^C) and offset (v_{off_k}) are required, so it is necessary to have previously calibrated PMS because the output voltage (v_k) can be measured:

$$T_{sys_k}^C = \frac{v_k - v_{off_k}}{G_k^C} \qquad \textit{Eq. 4.3}$$

Note that in such cases where only differential knowledge of T_{ext} is required, the T_r^C term is irrelevant since $T_{sys_2}^C - T_{sys_1}^C = (T_{ext_2} + T_r^C) - (T_{ext_1} + T_r^C) = T_{ext_2} - T_{ext_1}$. Now, let's have two known external temperatures T_{CS_1} and T_{CS_2} where $T_{CS_1} < T_{CS_2}$. Hence T_{CS_1} is so-called warm temperature because corresponds to a low level of correlated noise and T_{CS_2} the so-called hot temperature because corresponds to a high level of correlated noise. Now the overall system can be switched between two values of gain in the "C" port: G_k^C (without attenuator) and G_k^C / L_k (with attenuator) by means of a suitable attenuator placed in the signal path at a point that it can be considered noiseless. Then, the four PMS voltage measurements PMS are given by the following set of equations:

$$v_{1_k} = v_{off_k} + G_k^C \cdot (T_{CS_{1_k}} + T_{r_k}^C) \qquad \text{Noise source = WARM and attenuator = OFF} \qquad \textit{Eq. 4.4}$$

$$v_{2_k} = v_{off_k} + G_k^C \cdot (T_{CS_{2_k}} + T_{r_k}^C) \qquad \text{Noise source = HOT and attenuator = OFF} \qquad \textit{Eq. 4.5}$$

$$v_{3_k} = v_{off_k} + \frac{G_k^C}{L_k} \cdot (T_{CS_{1_k}} + T_{r_k}^C) \qquad \text{Noise source = WARM and attenuator = ON} \qquad \textit{Eq. 4.6}$$

$$v_{4_k} = v_{off_k} + \frac{G_k^C}{L_k} \cdot (T_{CS_{2_k}} + T_{r_k}^C) \qquad \text{Noise source = HOT and attenuator = ON} \qquad \textit{Eq. 4.7}$$

The desired parameters can be obtained as follows:

$$G_k^C = \frac{v_{2_k} - v_{1_k}}{T_{CS_{2_k}} - T_{CS_{1_k}}} \qquad \textit{Eq. 4.8}$$

$$v_{off_k} = \frac{v_{2_k} \cdot v_{3_k} - v_{1_k} \cdot v_{4_k}}{v_{2_k} - v_{4_k} - v_{1_k} + v_{3_k}} \qquad \textit{Eq. 4.9}$$

Note that in Fig. 4.1 the two equivalent noise temperatures T_{S_1} (warm) and T_{S_2} (hot) are synthesized by the common external NS and delivered to the port "0" to be injected to each LICEF through the NDN.

The equivalent external temperatures at the calibration plane of the LICEF units (ports "k" and "j") are $T_{CS_{2_k}}$, $T_{CS_{2_j}}$, $T_{CS_{1_k}}$ and $T_{CS_{1_j}}$, related to the temperatures in the port "0" and the S-parameters of the NDN (S_{k0}), and a term of noise related to the physical temperature (T_{ph_k}), only expressed in Eq. 4.10 and Eq. 4.11 for the port "k" (similar for the port "j"):

$$T_{CS_{1_k}} = |S_{k0}|^2 \cdot T_{S_1} + (1 - |S_{k0}|^2) \cdot T_{ph_k} \qquad \textit{Eq. 4.10}$$

$$T_{CS_{2_k}} = |S_{k0}|^2 \cdot T_{S_2} + (1 - |S_{k0}|^2) \cdot T_{ph_k} \qquad \textit{Eq. 4.11}$$

These temperatures are measured by the NIR; giving the equivalent external temperatures at NIR plane T_{NS_1} and T_{NS_2} from the S-parameters between the port "0" and the NIR port "1" of the NDN (S_{10}), introducing a term of noise in relation with the physical temperature (T_{ph_1}) too:

$$T_{NS_1} = |S_{10}|^2 \cdot T_{S_1} + (1 - |S_{10}|^2) \cdot T_{ph_1} \qquad \textit{Eq. 4.12}$$

$$T_{NS_2} = |S_{10}|^2 \cdot T_{S_2} + (1 - |S_{10}|^2) \cdot T_{ph_1} \qquad \textit{Eq. 4.13}$$

Using the expressions Eq. 4.10, Eq. 4.11, Eq. 4.12 and Eq. 4.13, the differences between both equivalent external temperatures can be expressed as:

$$T_{CS_{2_k}} - T_{CS_{1_k}} = \frac{|S_{k0}|^2}{|S_{10}|^2} \cdot (T_{NS_2} - T_{NS_1}) \qquad \textit{Eq. 4.14}$$

Now combining the expressions Eq. 4.3, Eq. 4.8 and Eq. 4.14, the resulting system temperature at the calibration plane is:

$$T_{sys_k}^C = \frac{v_k - v_{off_k}}{v_{2_k} - v_{1_k}} \cdot \frac{|S_{k0}|^2}{|S_{10}|^2} \cdot (T_{NS_2} - T_{NS_1}) \qquad \textit{Eq. 4.15}$$

To obtain the system temperatures at the antenna plane, only is necessary a transformation plane using the S-parameters corresponding to the switch (S_{LC_k}, S_{LH_k}, S_{LV_k}) and the antenna efficiency (η_{H_k}, η_{V_k}):

$$T_{sys_k}^{H} = T_{sys_k}^{C} \cdot \frac{\left|S_{LC_k}\right|^2}{\left|S_{LH_k}\right|^2 \cdot \eta_{H_k}} \qquad \textit{Eq. 4.16}$$

$$T_{sys_k}^{V} = T_{sys_k}^{C} \cdot \frac{\left|S_{LC_k}\right|^2}{\left|S_{LV_k}\right|^2 \cdot \eta_{V_k}} \qquad \textit{Eq. 4.17}$$

As it has mentioned before, it is necessary to know the gain and the offset to get the system temperatures (Eq. 4.3). The PMS parameters have been computed in two steps: centralized calibration and distributed calibration, which are explained in detail in the next sections. Using the internal calibration, the correlated noise is injected to the receivers first with the so-called "even" noise sources and then using the "odd" noise sources (Fig. 4.2).

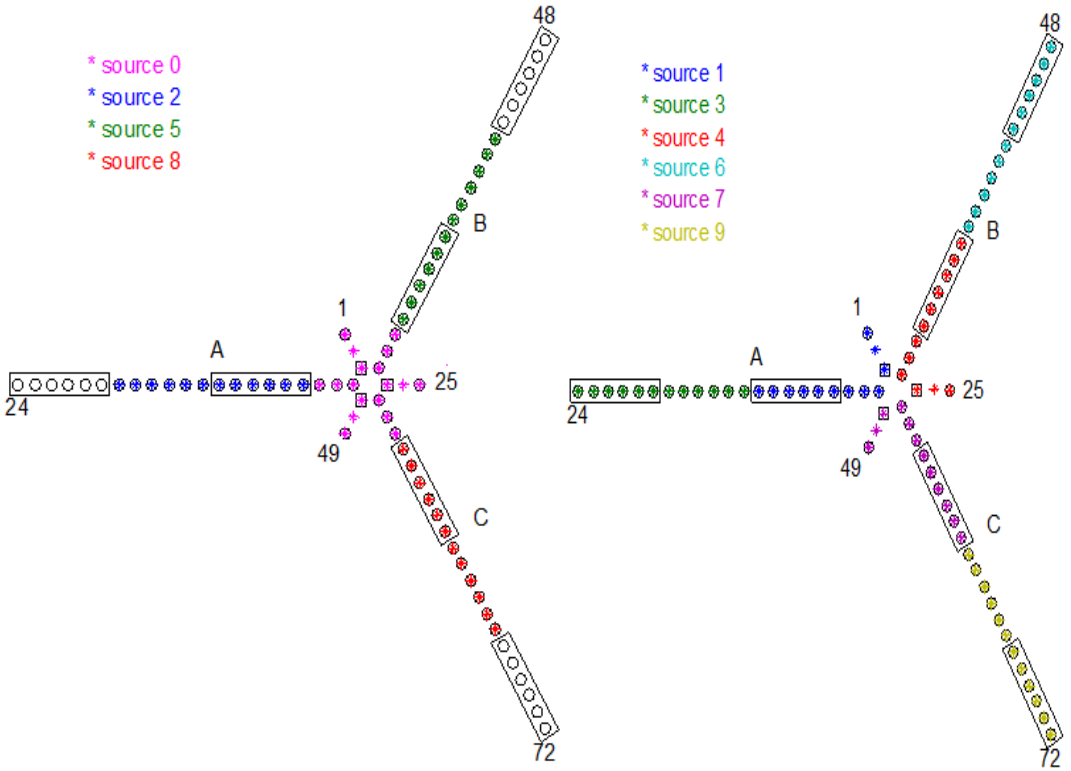

Fig. 4.2 Noise source scheme for even sources (left) and odd sources (right).

- ***Centralized calibration***

The centralized calibration has been used for receivers in the hub except for those acting as NIR (because the NIR is in the mode NIR_R and the PMS voltage measurement is wrong). The offset for the *k*-LICEF into the hub has been computed using this formula:

$$v_{off_k}^h = \frac{v_{2k}^h v_{3k}^h - v_{1k}^h v_{4k}^h}{v_{2k}^h - v_{4k}^h - v_{1k}^h + v_{3k}^h} \qquad \textit{Eq. 4.18}$$

with v_{1k}^h being the voltage for warm NS and no attenuator, v_{2k}^h is the voltage for hot NS and no attenuator, v_{3k}^h is the voltage for warm NS with attenuator and v_{4k}^h is the voltage for hot NS with attenuator.

The gain at C-plane for the *k*-LICEF in the hub has been computed as:

$$G_k^{hC} = \frac{v_{2k}^h - v_{1k}^h}{\frac{|S_{k0}|^2}{6}\sum_{N=1}^{6}\frac{(T_{sys_N}^{hC_2C} - T_{sys_N}^{hC_1C})}{|S_{N0}|^2}} \qquad \textit{Eq. 4.19}$$

where v_{2k}^h is the voltage for hot NS and no attenuator, v_{1k}^h is the voltage for warm NS and no attenuator, S_{k0} are the S-parameters between port "*0*" and port "*k*", S_{N0} are the S-parameters between port "*0*" and NIR port "*N*", $T_{sys_N}^{hC_2C}$ are the noise injection temperature measured by NIR when the switch are in the position hot and even source, and finally, $T_{sys_N}^{hC_1C}$ are the noise injection temperature measured by NIR when the switch are in the position warm and even source. The number "6" appears in the denominator of the expression because is an average of the 6 NIR channels located in the hub.

- ***Distributed calibration***

For the others receivers, the distributed calibration has been used as shown in Table 4.1. The offset voltage can be computed independently for each case. Its final value for those receivers driven twice noise source (even and odd) is the average of both:

$$\begin{aligned} v_{off_k}^e &= \frac{v_{2k}^e v_{3k}^e - v_{1k}^e v_{4k}^e}{v_{2k}^e - v_{4k}^e - v_{1k}^e + v_{3k}^e} \\ v_{off_k}^o &= \frac{v_{2k}^o v_{3k}^o - v_{1k}^o v_{4k}^o}{v_{2k}^o - v_{4k}^o - v_{1k}^o + v_{3k}^o} \\ v_{off_k} &= \frac{1}{2}\left[v_{off_k}^e + v_{off_k}^o \right] \end{aligned} \qquad \textit{Eq. 4.20}$$

The gain from measurements with odd noise sources for receivers in first section *l*-LICEF and NIR receivers can be calculated as:

$$T_{sys_h}^{C} = \frac{v_h - v_{off_h}}{G_h^{C}}$$

$$G_l^{C} = \frac{v_{2l} - v_{1l}}{\frac{|S_{l0}|^2}{4}\sum_{h=1}^{4}\frac{(T_{sys_h}^{C_2C} - T_{sys_h}^{C_1C})}{|S_{h0}|^2}} \qquad \textit{Eq. 4.21}$$

where $T_{sys_h}^{C}$ is the system temperature at C-plane, v_h is the voltage, v_{off_h} corresponds to the offset voltage and G_h^{C} is the gain of *h*-LICEFs with calibrated PMS. The number "4" appears in the denominator of the expression because is an average of the 4 LICEF already calibrated in the hub (all the receivers in the section which are not NIR).

Source number	HUB	ARM A			ARM B			ARM C		
	0	1	2	3	4	5	6	7	8	9
Receiver number	1	1	7	13	25	31	37	49	55	61
	2*	2*	8	14	26*	32	38	50*	56	62
	3**	3**	9	15	27**	33	39	51**	57	63
	4	4	10	16	28	34	40	52	58	64
	5	5	11	17	29	35	41	53	59	65
	6	6	12	18	30	36	42	54	60	66
	25	7	13	19	31	37	43	55	61	67
	26*	8	14	20	32	38	44	56	62	68
	27**	9	15	21	33	39	45	57	63	69
	28	10	16	22	34	40	46	58	64	70
	29	11	17	23	35	41	47	59	65	71
	30	12	18	24	36	42	48	60	66	72
	49	*l*	*m*	*n*	*l*	*m*	*n*	*l*	*m*	*n*
	50*									
	51**									
	52									
	53									
	54									
	h									

* NIR-LICEF H input
** NIR-LICEF V input

Table 4.1 Distributed noise injection.

The gain from measurements with even NS for receivers in second section *m*-LICEF is calculated as follows:

$$T_{sys_l}^{C} = \frac{v_l - v_{off_l}}{G_l^C}$$

$$G_m^C = \frac{v_{2m} - v_{1m}}{\frac{|S_{m0}|^2}{6}\sum_{l=1}^{6}\frac{(T_{sys_l}^{C_2C} - T_{sys_l}^{C_1C})}{|S_{l0}|^2}} \qquad \textit{Eq. 4.22}$$

with $T_{sys_l}^{C}$ being the system temperature at C-plane of *l*-LICEF in the second section of each arm, v_l is the PMS voltage and v_{off_l} is the offset voltage of *l*-LICEF with calibrated PMS. The number "6" appears in the denominator of the expression because is an average of the 6 LICEF already calibrated.

The gain from measurements with odd NS for receivers in third section *n*-LICEF can be calculated now:

$$T_{sys_m}^{C} = \frac{v_m - v_{off_m}}{G_m^C}$$

$$G_n^C = \frac{v_{2n} - v_{1n}}{\frac{|S_{n0}|^2}{6}\sum_{m=1}^{6}\frac{(T_{sys_m}^{C_2C} - T_{sys_m}^{C_1C})}{|S_{m0}|^2}} \qquad \textit{Eq. 4.23}$$

with $T_{sys_m}^{C}$ being the system temperature at C-plane of *m*-LICEF in the third section of each arm, v_m is the PMS voltage and v_{off_m} is the offset voltage of *m*-LICEF with calibrated PMS.

It must be pointed out that all receivers in the hub and in the first and second sections of each arm are driven twice (for even and odd NS), while the receivers in the third section are only driven once.

4.1.1.2. External calibration

The external calibration [17][18], so-called the ***absolute calibration*** is performed using the deep-sky view. The galactic-noise brightness temperature is essentially constant in both time and space with a value of about 3.6 K, comprising the 2.7 K for the cosmic background and 0.9 K for the galactic background radiation. Therefore, the attitude of the satellite is changed so that the instrument points toward the desired target. The change in orientation is performed using a pitch rotation to obtain the inertial pointing.

Accordingly, the payload executes a periodic pointing to the deep sky in order to calibrate the NIRs that act as reference radiometers in the internal calibration. During these cold sky views the PMS unit is also switched between antenna (cold noise) and

the port "U" to the 50 Ω load (warm noise). If the front end is in thermal equilibrium and perfectly matched, injecting uncorrelated noise by means of matched load is equivalent to place a perfect absorber in front of the antenna at the same temperature (Fig. 4.3):

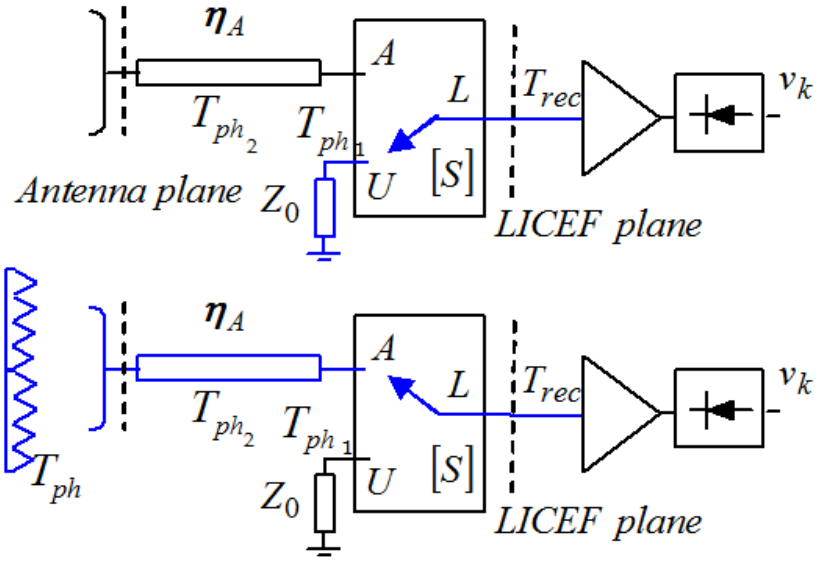

Fig. 4.3 LICEF/PMS front end scheme to illustrate the external calibration equivalence between measuring by antenna with a perfect absorber (bottom) or measuring by the U-load (top).

When the switch is in the U-port (warm noise according to the top of Fig. 4.3), the equivalent system temperature at C-plane using the Friis formula:

$$T_{sys_{WARM}}^{C} = T_{ph_1} + \frac{1-|S_{LU}|^2}{|S_{LU}|^2} \cdot T_{ph_1} + \frac{T_{rec}}{|S_{LU}|^2} = \frac{T_{ph_1} + T_{rec}}{|S_{LU}|^2} \qquad \text{Eq. 4.24}$$

being T_{ph_1} the physical temperature at the input of the U-port, T_{rec} corresponds to the noise temperature of the receiver in the LICEF plane and S_{LU} is the S-parameter between the port "U" and the output port of the switch.

To express the system temperature in the antenna plane only a plane translation is necessary, taking into account the antenna efficiency (η_A) and the S-parameters of the switch :

$$T_{sys_{WARM}}^{A} = T_{sys_{WARM}}^{C} \cdot \frac{|S_{LU}|^2}{|S_{LA}|^2 \cdot \eta_A} = \frac{T_{ph_1} + T_{rec}}{|S_{LA}|^2 \cdot \eta_A} \qquad \text{Eq. 4.25}$$

where S_{LU} is the S-parameter between the port "U" and the output port and S_{LA} is the S-parameter between the antenna port and the output port of the switch.

Similarly, when the switch is connected to the antenna port (cold noise according to the bottom of Fig. 4.3), the equivalent system temperature at the antenna plane is:

$$T_{sys_{COLD}}^{A} = T_{sky} + \frac{1-\eta_A}{\eta_A} \cdot T_{ph_2} + \frac{1-|S_{LA}|^2}{\eta_A \cdot |S_{LA}|^2} \cdot T_{ph_1} + \frac{T_{rec}}{\eta_A \cdot |S_{LA}|^2} \qquad \textit{Eq. 4.26}$$

with T_{sky} corresponding to the sky temperature and T_{ph_2} is the physical temperature at the input of the antenna port.

If the warm and cold PMS voltages reading are written as:

$$\begin{aligned} v_{COLD} &= G_k^A \cdot T_{sys_{COLD}}^A + v_{off} \\ v_{WARM} &= G_k^A \cdot T_{sys_{WARM}}^A + v_{off} \end{aligned} \qquad \textit{Eq. 4.27}$$

the PMS gain can be expressed for each *k*-receiver:

$$G_k^A = \frac{v_{WARM} - v_{COLD}}{T_{sys_{WARM}}^A - T_{sys_{COLD}}^A} \qquad \textit{Eq. 4.28}$$

The difference between the system temperatures at the antenna plane can be obtained as follows:

$$T_{sys_{WARM}}^A - T_{sys_{COLD}}^A = \frac{T_{ph1} - T_{ph_2}}{\eta_A} + T_{ph_2} - T_{sky} \qquad \textit{Eq. 4.29}$$

In the case that the radiometer front end is at a constant temperature, both the antenna and the switch are at the same physical temperature ($T_{ph_1} = T_{ph_2} = T_{ph}$), the difference can be simplified as:

$$T_{sys_{WARM}}^A - T_{sys_{COLD}}^A = T_{ph} - T_{sky} \qquad \textit{Eq. 4.30}$$

Based on this assumption, the PMS gain at the antenna plane results:

$$G_k^A = \frac{v_{WARM} - v_{COLD}}{T_{ph} - T_{sky}} \qquad \textit{Eq. 4.31}$$

This result has very important implications in the design of the calibration procedure because it is far much simpler to place an internal matched load than design another target with good return loss and constant temperature distribution.

Moreover, the receiver noise temperature can also be computed in the antenna plane as:

$$T_R^A = \frac{v_{COLD}' \cdot T_{ph} - v_{WARM}' \cdot T_{sky}}{v_{COLD} - v_{WARM}} \qquad \textit{Eq. 4.32}$$

where the v_{COLD}' and v_{WARM}' are the voltages with the offset subtracted.

- ***One-point calibration***

Looking at the deep sky is a special maneuver and it is difficult to execute very often for the satellite. Basing on some measurement of internal calibration and one measurement of external calibration, we can obtain the PMS gain using, as in the previous case, the measurements of PMS voltages when the switch are matched to the "U" port without looking at the deep sky.

This method use the measurement of the PMS offset from the internal calibration and the computation of the receiver noise temperature calibrated during the external views at the deep sky. In this way, it is possible to obtain the PMS gain at the antenna plane for each *k*-receiver as follows:

$$G_{1P_k}^{A} = \frac{v_{U_k} - v_{off_k}(T_{ph_k})}{T_{R_k}^A(T_{ph_k}) + T_{ph_k}} \qquad \textit{Eq. 4.33}$$

where v_{U_k} is the PMS voltage when the U-noise is injected, $v_{off_k}(T_{ph_k})$ is the offset from the internal calibration, once a temperature correction has been applied (explained in detail in the chapter 5), $T_{R_k}^A(T_{ph_k})$ corresponds to the receiver noise temperature in the antenna plane also corrected in temperature and T_{ph_k} is the physical temperature of the receiver.

4.2. Phase calibration

Phase calibration refers to the phase of the normalized complex correlation term M_{kj} and the phase of the fringe-washing term G_{kj}. In this project, only the fringe-washing phase term has been analyzed.

4.2.1. Fringe-Washing term

The fringe-washing term evaluated at the origin is related to the differences between the frequency responses of the filters of the two receivers forming the baseline (spatial decorrelation effect). It can be measured by injecting two levels of correlated noise for those 612 baselines formed by the receivers having a common noise source. For the rest, to complete the 2556 baselines, an estimation of this term must be performed [19].

First, this term is obtained at the calibration plane from the injection of hot and warm noise:

$$G_{kj}^{C} = \frac{\sqrt{T_{sys_k}^{C_2C} \cdot T_{sys_j}^{C_2C}} \cdot M_{kj}^{C_2} - \sqrt{T_{sys_k}^{C_1C} \cdot T_{sys_j}^{C_1C}} \cdot M_{kj}^{C_1}}{S_{k0} \cdot S_{j0}^{*} \cdot (T_{S_2} - T_{S_1})} \qquad \textit{Eq. 4.34}$$

being $T_{sys_k}^{C_2C}$ and $T_{sys_j}^{C_2C}$ the system temperatures at C-plane with hot correlated noise injection, $T_{sys_k}^{C_1C}$ and $T_{sys_j}^{C_1C}$ the system temperatures at C-plane with warm correlated noise injection, $M_{kj}^{C_2}$ and $M_{kj}^{C_1}$ correspond to the normalized complex correlation with hot and warm noise, respectively, S_{k0} and S_{j0}^{*} are the S-parameters between the port "k" or "j" and the port "0", in the second case complex conjugate, and T_{S_2} and T_{S_1} are the equivalent temperature at the output of the NS for level hot and level warm, respectively.

Substituting the expressions for the system temperature when hot and warm correlated noise are injected (calculated from the PMS measurements) and the expression of the external temperature difference (measured by the NIR), the final expression of G_{kj}^{C} term at the origin yields:

$$G_{kj}^{C} = \frac{M_{kj}^{C_2C} \cdot \sqrt{(v_{2_k} - v_{off_k}) \cdot (v_{2_j} - v_{off_j})} - M_{kj}^{C_1C} \cdot \sqrt{(v_{1_k} - v_{off_k}) \cdot (v_{1_j} - v_{off_j})}}{\sqrt{(v_{2_k} - v_{1_k}) \cdot (v_{2_j} - v_{1_j})}} \cdot \frac{|S_{k0}|}{S_{k0}} \cdot \frac{|S_{j0}|}{S_{j0}^{*}} \qquad \textit{Eq. 4.35}$$

This factor only depends on the quadrature corrected normalized correlation, the linearity of the PMS and phase unbalance of the noise distribution (the amplitude and phase of the CAS S-parameters are required).

A translation plane must be performed in order to have this term at the antenna. The factor that takes into account this translation depends on the phase of S-parameters of the switch, $\bar{S}_{LH_k} = \frac{S_{LH_k}}{|S_{LH_k}|}, \bar{S}_{LV_k} = \frac{S_{LV_k}}{|S_{LV_k}|}, \bar{S}_{LC_k} = \frac{S_{LC_k}}{|S_{LC_k}|}$ and the phase of the antenna in both polarizations (measured on ground, ϕ_{H_k}, ϕ_{V_k}):

$$G_{kj}^{H} = G_{kj}^{C} \cdot \frac{\bar{S}_{LH_k}}{\bar{S}_{LC_k}} \cdot \frac{\bar{S}_{LH_j}^{*}}{\bar{S}_{LC_j}^{*}} \cdot e^{j \cdot (\phi_{H_k} - \phi_{H_j})}$$

$$G_{kj}^{V} = G_{kj}^{C} \cdot \frac{\bar{S}_{LV_k}}{\bar{S}_{LC_k}} \cdot \frac{\bar{S}_{LV_j}^{*}}{\bar{S}_{LC_j}^{*}} \cdot e^{j \cdot (\phi_{V_k} - \phi_{V_j})} \qquad \textit{Eq. 4.36}$$

4.2.1.1. Phases in the Fringe-Washing term

If the frequency response of the receivers is very similar, as in SMOS, the term G_{kj} in the calibration plane can be approximated by the product of two separable terms:

$$G_{kj}^{C} \approx g_j e^{ja_j} g_k e^{ja_k} \qquad \textit{Eq. 4.37}$$

where g_j, g_k correspond to the amplitude term of each receiver and α_j, α_k are the corresponding phases.

The baseline phases (α_{kj}) have been extracted computing the angle of Fringe Wash term:

$$\alpha_{kj} = \arg(G_{kj}^{C}) \qquad \textit{Eq. 4.38}$$

The separable phases (α_k and α_j) have been estimated for each one of the calibration sequences by applying matrix pseudo-inverse:

$$\begin{cases} \alpha_{21} = \alpha_1 - \alpha_2 \\ \alpha_{31} = \alpha_1 - \alpha_3 \\ \dots \\ \alpha_{72\,71} = \alpha_{71} - \alpha_{72} \end{cases} \Rightarrow \begin{pmatrix} \alpha_{21} \\ \alpha_{31} \\ \\ \vdots \\ \\ \\ \alpha_{72\,71} \end{pmatrix} = \begin{pmatrix} 1 & -1 & 0 & 0 & \dots & 0 \\ 1 & 0 & -1 & 0 & \dots & 0 \\ 1 & 0 & 0 & -1 & \dots & 0 \\ \vdots & & \ddots & & & \\ & & & \ddots & & \vdots \\ 0 & 0 & 0 & \dots & 1 & -1 \end{pmatrix} \cdot \begin{pmatrix} \alpha_1 \\ \alpha_2 \\ \alpha_3 \\ \vdots \\ \\ \alpha_{72} \end{pmatrix} \qquad \textit{Eq. 4.39}$$

The matrix of this system has 612 rows (one for each baseline available- those formed by receivers sharing at the noise source-) and 72 columns (one for each LICEF). The left-hand side is a column vector that includes all the measured baseline phases. The system is solved after an iterative procedure to deal with the phase wrapping in the measurements α_{kj}. It must be taken into account that the rank of the system is 71 since a constant phase term can be added to each single phase.

Therefore, when the absolute phases are estimated by computing the pseudo-inverse of the matrix, the set of baseline phases always includes an arbitrary constant phase term. From these results, memory track between consecutive calibrations is needed in order to remove the remaining phase jumps. Once this change is introduced in the resolution, the phase jumps disappear and the G_{kj} phase presents a smooth behavior between calibrations as shown in Fig. 4.4.

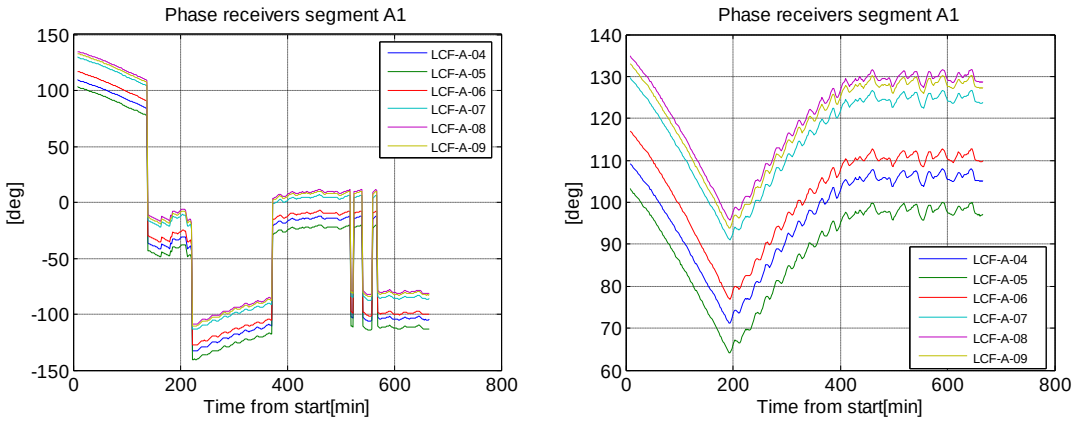

Fig. 4.4 Phase drift segment A1 receivers solving directly the system of equations (left) after applying memory track between consecutive calibrations (right).

Once the phases assigned to each receiver are known, the baseline phases can also be estimated using a difference of the separable phases:

$$\hat{\alpha}_{kj} \approx \alpha_j - \alpha_k \qquad \textit{Eq. 4.40}$$

A detailed study about the local oscillator phases track is done in chapter 8 due this calibration parameter has a very important impact in the visibility phases and therefore in the imaging reconstruction.

CHAPTER 5

5. Sensitivity analysis

In this chapter the temperature drift experimented by some calibration parameters will be study like the PMS gain, PMS offset and the receiver noise temperature.

The objective of computing the sensitivity of these parameters over the physical temperature is intended to achieve more accurate estimations in instants of time during which the instrument has not a measurement of these ones.

5.1. General concepts of sensitivity

The temperature behavior of any parameter, let's say A, has been modeled as a second order polynomial in the case to take into account the non-linearity of the sensitivity:

$$A(T_{ph}) = a + b \cdot T_{ph} + c \cdot T_{ph}^2 \qquad \textit{Eq. 5.1}$$

Hence, the sensitivity versus the physical temperature is a first order polynomial because is the derivate of parameter A as a function of temperature. The sensitivity is expressed around 21ºC reference in this way:

$$S_A(T_{ph}) = \alpha_A + \beta_A \cdot \left(T_{ph} - 21\right) \qquad \textit{Eq. 5.2}$$

where the coefficients are: $\alpha_A = b + 21 \cdot 2 \cdot c$ and $\beta_A = 2c$.

The rationale behind this modeling is based on two assumptions: the absolute value of A may have an error due to imperfect calibration and the sensitivity of A versus temperature is independent of the exact value of A.

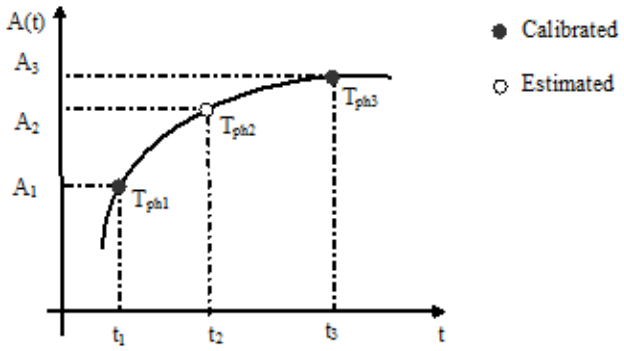

Fig. 5.1 Estimation of parameter A at physical temperature T_{ph_2} at instant t_2.

Now, let's assume that in Fig. 5.1 there are two calibrations of A at instants t_1 and t_3, where the associated physical temperature is T_{ph_1} and T_{ph_3} respectively, yielding the

values A_1 and A_3 respectively too. In order to estimate the value of A for an intermediate instant t_2 at physical temperature T_{ph_2} there are some possible approaches to take into account with the assumption of small temperature swings.

5.1.1. Case 1: The sensitivity is taken at 21°C

In this case, the coefficient β_A is neglected and the sensitivity is taken constant and equal to its value at 21°C:

$$\begin{aligned} &S_A(21^oC) = \alpha_A \\ &A\left(T_{ph_2}\right) = A\left(T_{ph_1}\right) + \alpha_A \cdot \left(T_{ph_2} - T_{ph_1}\right) \end{aligned} \qquad \textit{Eq. 5.3}$$

5.1.2. Case 2: The sensitivity is not taken at 21°C

In this case, parameter sensitivity is computed at the calibration temperature. Different methods can be used.

- ***Simple estimation***

If the calibration temperature is T_{ph_1}:

$$\begin{aligned} &S_A(T_{ph_1}) = \alpha_A + \beta_A \cdot \left(T_{ph_1} - 21\right) \\ &A\left(T_{ph_2}\right) = A\left(T_{ph_1}\right) + S_A\left(T_{ph_1}\right) \cdot \left(T_{ph_2} - T_{ph_1}\right) \end{aligned} \qquad \textit{Eq. 5.4}$$

Instead of that, if the calibration temperature is T_{ph_3}:

$$\begin{aligned} &S_A(T_{ph_3}) = \alpha_A + \beta_A \cdot \left(T_{ph_3} - 21\right) \\ &A\left(T_{ph_2}\right) = A\left(T_{ph_3}\right) + S_A\left(T_{ph_3}\right) \cdot \left(T_{ph_2} - T_{ph_3}\right) \end{aligned} \qquad \textit{Eq. 5.5}$$

- ***Estimation at the middle physical temperature***

If the calibration temperature is T_{ph_1}, the sensitivity is computed in the middle point between T_{ph_1} and T_{ph_2}:

$$\begin{aligned} &T_{ph_{12}} = \frac{T_{ph_1} + T_{ph_2}}{2} \\ &S_A(T_{ph_{12}}) = \alpha_A + \beta_A \cdot \left(T_{ph_{12}} - 21\right) \\ &A\left(T_{ph_2}\right) = A\left(T_{ph_1}\right) + S_A\left(T_{ph_{12}}\right) \cdot \left(T_{ph_2} - T_{ph_1}\right) \end{aligned} \qquad \textit{Eq. 5.6}$$

Similarly, if instead of T_{ph_1}, T_{ph_3} is the calibration temperature:

$$T_{ph_{32}} = \frac{T_{ph_3} + T_{ph_2}}{2}$$
$$S_A(T_{ph_{32}}) = \alpha_A + \beta_A \cdot \left(T_{ph_{32}} - 21\right) \qquad \text{Eq. 5.7}$$
$$A\left(T_{ph_2}\right) = A\left(T_{ph_3}\right) + S_A\left(T_{ph_{32}}\right) \cdot \left(T_{ph_2} - T_{ph_3}\right)$$

- ***Estimation by weighted average time***

In this case the sensitivity is computed at the temperatures related to the adjacent calibrations in order to perform the weighted average time as shown:

$$A\left(T_{ph_2}\right) = \frac{\left[A\left(T_{ph_1}\right) + S_A\left(T_{ph_1}\right) \cdot \left(T_{ph_2} - T_{ph1}\right)\right] \cdot \left(t_3 - t_2\right) + \left[A\left(T_{ph_3}\right) + S_A\left(T_{ph_3}\right) \cdot \left(T_{ph_2} - T_{ph_3}\right)\right] \cdot \left(t_2 - t_1\right)}{t_3 - t_1} \qquad \text{Eq. 5.8}$$

5.2. Large Space Simulator measurements

This campaign was aimed at characterizing the variation of calibration parameters and overall performance with respect to changes in physical temperature (April 2007). In these tests the instrument was fully deployed inside the Large Space Simulator (LSS) that it is a vacuum chamber where temperature and pressure were varied and monitored (Fig. 5.2). Only measurements of injected noise were performed.

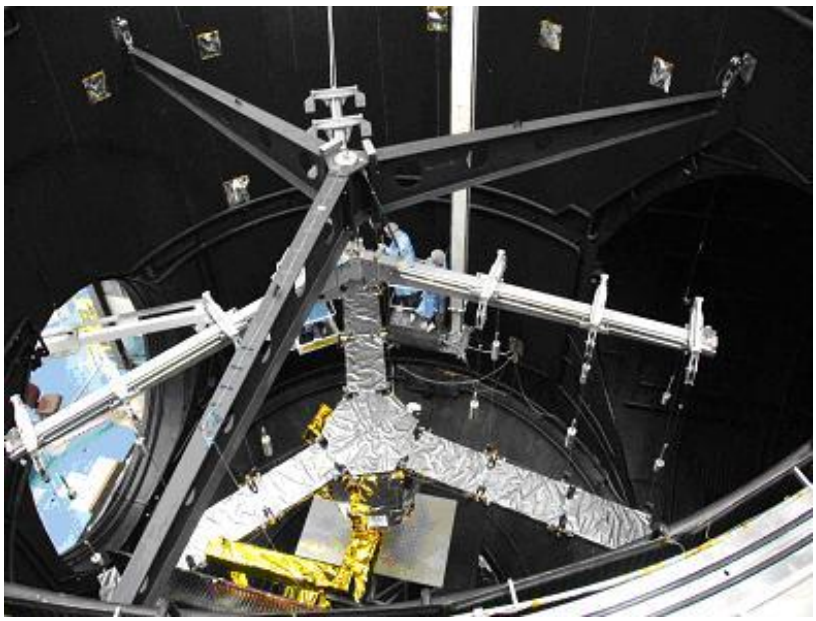

Fig. 5.2 The MIRAS payload at ESA-ESTEC Large Space Simulator during the thermal characterization of the instrument in spring 2007(Credits: EADS-CASA Espacio).

From the LSS, two on-ground datasets have been used to characterize the sensitivity of the calibration parameters:

- ***2007-04-23T12-47-25-PFM-TV*** (so-called ***COLD-FUNCTIONAL***)
  This dataset has been acquired when the instrument has been cycled approximately from 35ºC to 10ºC and then stabilized at this lower temperature using the thermal control system.

- ***2007-04-24T19-07-19_PFM_TV*** (so-called ***PFM-TV***)
  During the thermal test the instrument has been cycled from about 30ºC to 22ºC, and then stabilized at this lower temperature, using the thermal control system too.

The second dataset is the closest to the real conditions because both tests simulate the vacuum in space but only the *PFM-TV* simulates the physical temperature stabilization in-flight when the instrument will be in orbit.

5.3. PMS offset sensitivity

The PMS offset used to estimate the offset sensitivity has been computed by the *4-points calibration method* explained in detail in section 4.1.1.1 of this project.

The first estimation of the PMS offset sensitivity values has been provided by the Spanish company MIER Communications. A preliminary study about the offset sensitivity had been realized at UPC in 2007 using the LSS data [20].

5.3.1. First order correction

In February 2009, the offset sensitivity was estimated using the on-ground dataset *COLD-FUNCTIONAL*. It has been computed in two temperature ranges: between 20ºC to 30ºC and between 20ºC to 25ºC to compare and validate different temperature sensitivity estimations [21]. At that time it was not yet known exactly what temperature would be the instrument in flight and the temperature variation that is limited by the thermal control system.

In both estimations, the offset calibrations are considered as a first order polynomial. Following this assumption, the PMS offset sensitivity is defined as the slope of the regression line for the offset measurements of each calibration depending on the calibration temperature and for each *k*-receiver can be expressed as:

$$S_{voff_k} = \alpha_{v_{off_k}} = \frac{v_{off_k}(T_{ph_{1k}}) - v_{off_k}(T_{ph_{0k}})}{T_{ph_{1k}} - T_{ph_{0k}}} \qquad \textit{Eq. 5.9}$$

where S_{voff_k} is the offset sensitivity (unique value $\alpha_{v_{off_k}}$ [V/ºC] for the entire temperature range), v_{off_k} [V] is the PMS offset of the receiver , $T_{ph_{0k}}$ and $T_{ph_{1k}}$ are the physical temperatures [ºC].

Knowing the offset sensitivity and the offset at a calibration temperature, the offset at a measurement physical temperature can be expressed in this form:

$$v_{off_k}(T_{ph_{ik}}) = v_{off_k}(T_{ph_{0k}}) + S_{voff_k} \cdot (T_{ph_{ik}} - T_{ph_{0k}}) \qquad \textit{Eq. 5.10}$$

Being v_{off_k} the PMS offset voltage of *k*-receiver, $T_{ph_{0k}}$ the reference temperature, $T_{ph_{ik}}$ corresponds to the current measurement temperature and S_{voff_k} is the offset sensitivity.

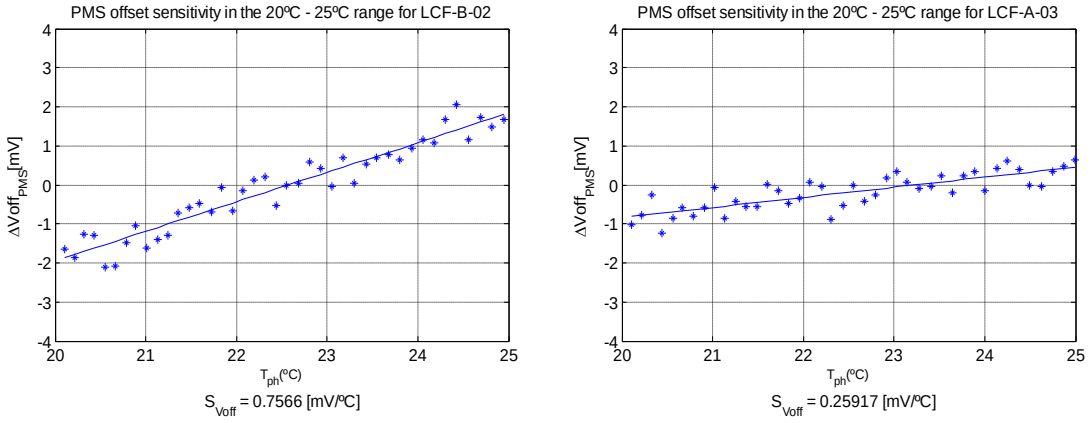

Fig. 5.3 Examples at the range 20ºC-25ºC of the linear regression in the PMS offset to compute the offset sensitivity. Both plots show a clear linear trend.

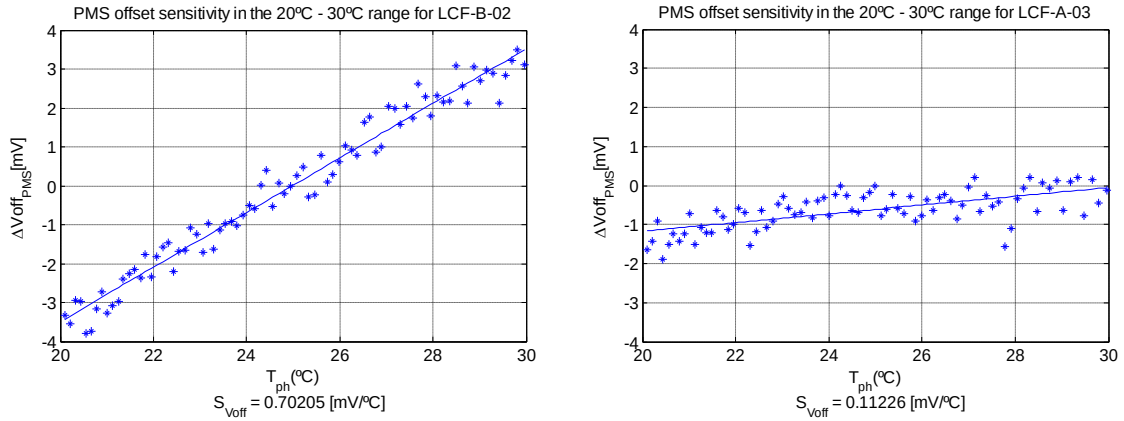

Fig. 5.4 Examples at the range 20ºC-30ºC of the linear regression in the PMS offset to compute the offset sensitivity. Left: LCF-B-02 with clear lineal trend. Right: LCF-A-03 with beginning of saturation.

Some results are exposed in Fig. 5.3 (temperature range 20ºC-25ºC) and Fig. 5.4 (temperature range 20ºC-30ºC). Observing the plots the conclusion is that the temperature interval to be taken into account is very important because if it is too wide, saturation and no-linearity errors are larger (Fig. 5.4 right compared to Fig. 5.3 right). On the other hand, if it is too narrow, there will not be sufficient measurements to compute the correct sensitivity value (Fig. 5.4 left compared with Fig. 5.3 left). Note that the plots are expressed in the units [mV/ºC].

5.3.2. Second order correction

To obtain better results, another estimation of the offset sensitivity has been computed in March 2009. In this case, the same dataset has been used but the temperature range taking into account is between the 14ºC to 30ºC [22].

If the PMS offset is estimated as a second order polynomial, the PMS offset sensitivity is the derivative of the PMS offset respect the physical temperature and it will be a first order polynomial, i.e., the sensitivity has a first order dependence with temperature. For the *k*-receiver, the PMS offset sensitivity can be expressed as follows:

$$S_{v_{off_k}}(T_{ph_{0k}}) = \beta_{v_{off_k}} \cdot (T_{ph_{0k}} - 21) + \alpha_{v_{off_k}} \qquad \textit{Eq. 5.11}$$

For each receiver, the coefficient $\beta_{v_{off}}$ [V/ºC^2] is the slope of physical temperature increment respect 21ºC and $\alpha_{v_{off}}$ [V/ºC] corresponds to the constant term.

Similarly as the previous, computing the offset sensitivity at $T_{ph_{0k}}$ and knowing the offset at a calibration temperature, the offset at a determined physical temperature can be expressed in this form:

$$v_{off_k}(T_{ph_{ik}}) = v_{off_k}(T_{ph_{0k}}) + S_{voff_k}(T_{ph_{0k}}) \cdot (T_{ph_{ik}} - T_{ph_{0k}}) \qquad \textit{Eq. 5.12}$$

Being v_{off_k} the PMS offset voltage of *k*-receiver, $T_{ph_{0k}}$ the reference temperature, $T_{ph_{ik}}$ corresponds to the current temperature and $S_{voff_k}(T_{ph_{0k}})$ is the offset sensitivity computed at the physical temperature $T_{ph_{0k}}$ (paragraph named *simple estimation* of section 5.1.2).

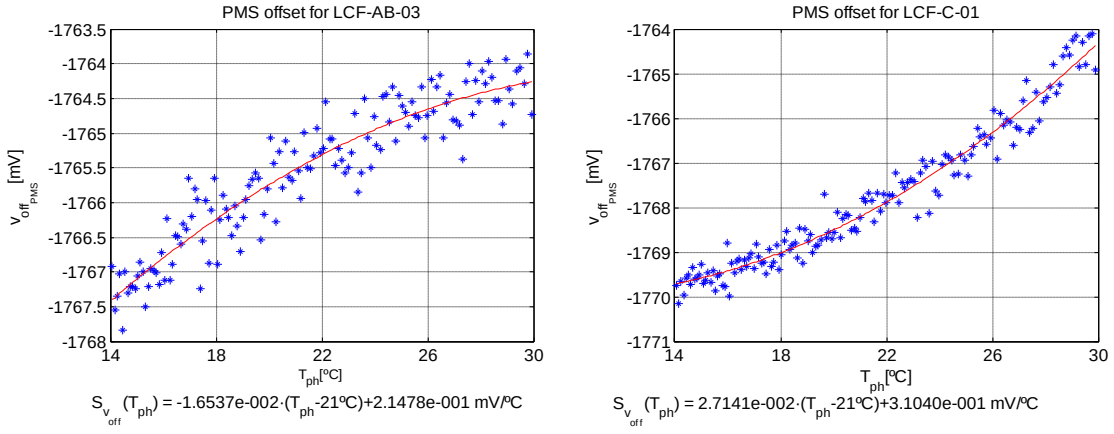

Fig. 5.5 Examples at the range 14ºC-30ºC of the second order regression in the PMS offset to compute the offset sensitivity. Left: LCF-AB-03. Right: LCF-C-01.

In Fig. 5.5 there are some graphics with examples. Observing the plots, the conclusion is that taking a wide temperature range it is necessary a second order correction of the offset with temperature.

From this offset sensitivity, an offset track has been intended to realize. The on-ground dataset used to track the offset is the *PFM-TV*. Fig. 5.6 shows the offset track in two receivers. In both, the offset sensitivity (in the stabilized zone) is unable to follow the offset calibrations. PMS offset calibrations have abrupt variations in the stabilized part of the tests whereas the physical temperature varies slightly around a nearly constant value.

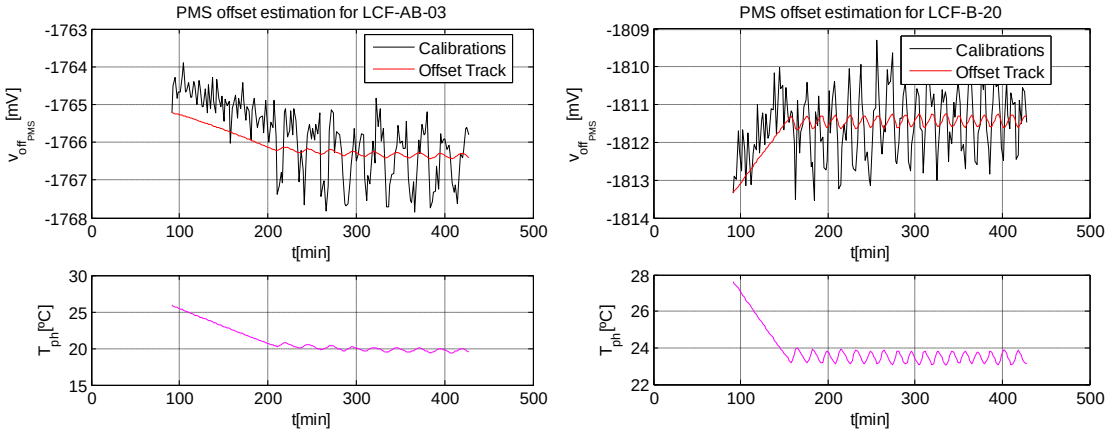

Fig. 5.6 Examples of offset track using the sensitivity of second order. Left: LCF-AB-03. Right: LCF-B-20.

The phenomenon mentioned above [23] can be observed in detail in Fig. 5.7.

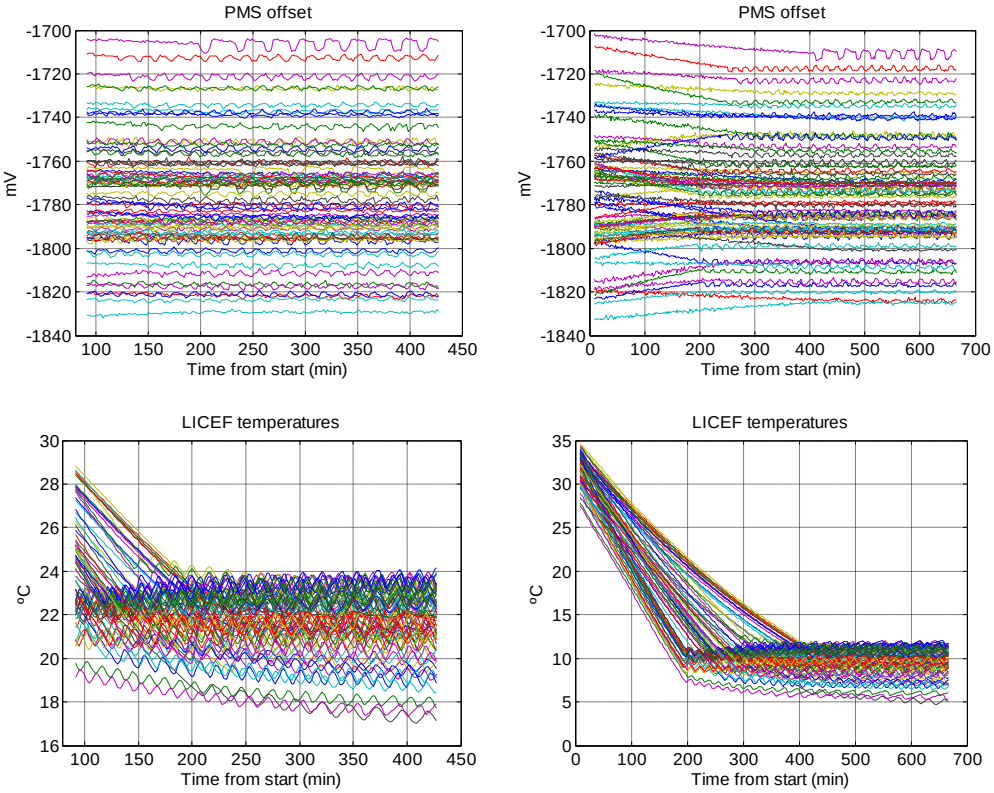

Fig. 5.7 PMS offset and LICEF physical temperature. Left: PFM-TV dataset. Right: COLD FUNCTIONAL dataset.

After this finding, the first idea was to think that the PMS offset sensitivity was not be computed correctly and recalculate the PMS offset sensitivity by other methods: Statistical method and using a Linear Regression in the part of the dataset stabilized in temperature.

5.3.3. Statistical method

The PMS offset sensitivity has been recalculated by the Statistical method to obtain other coefficients to track the offset in the stabilized part of the test *PFM-TV* (starting at minute 300 to the end). The absolute value of the offset sensitivity has been computed for each *k*-receiver as follows:

$$| S_{v_{off_{STD_k}}} | = | \alpha_{v_{off_{STD_k}}} | = \frac{\sigma(v_{off_k})}{\sigma(T_{ph_k})} \qquad \textit{Eq. 5.13}$$

where the $\sigma(v_{off_k})$ is the standard deviation for the PMS offset voltage from minute 300 to the end for the *k*-receiver and $\sigma(T_{ph_k})$ is the standard deviation for the physical temperature at the same time interval. The sign is given by the sign of the alpha term from the second order correction.

Fig. 5.8 shows the absolute value of the offset sensitivity comparison expressed in the units [mV/ºC] between MIER values, sensitivities of second order and the sensitivities computed using Eq. 5.13. Using the statistical method (equis in blue), the sensitivity increases considerably respect the Mier@21ºC (crosses in black) and the second order method (asterisks in red).

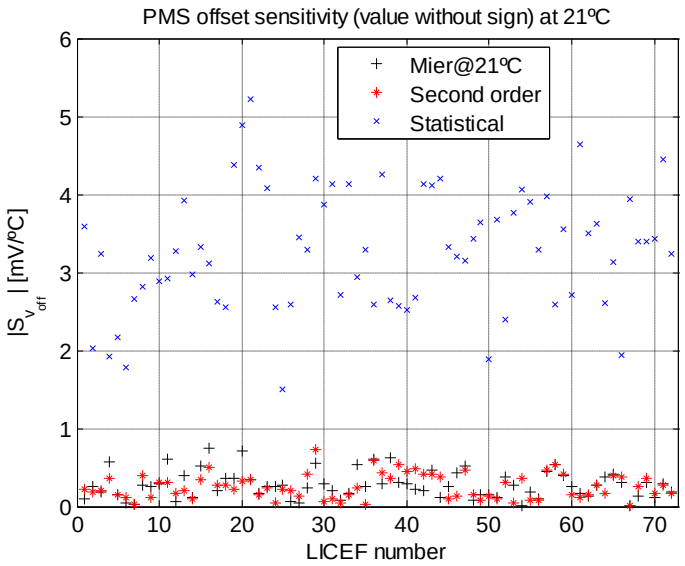

Fig. 5.8 PMS offset sensitivity absolute value comparison: the black crosses are measured by Mier at 21ºC, the red asterisks are the sensitivity from second order correction computed at 21ºC and the blue equis are the values computed by Statistical method.

5.3.4. Linear regression in stabilized part

The PMS offset sensitivity has been recalculated by the Linear Regression method to obtain other coefficients to track the offset in the stabilized part of the test *PFM-TV* (starting at minute 300 to the end). In this part the PMS offset sensitivity has been computed for each LICEF making the derivative of a linear regression of the offset as a function of the temperature, resulting only the alpha term in the units [V/ºC] that does not depend on the temperature:

$$S_{v_{off_{LR_k}}} = \alpha_{v_{off_{LR_k}}} \qquad \textit{Eq. 5.14}$$

Fig. 5.9 shows the absolute value of the offset sensitivity comparison expressed in the units [mV/ºC] between MIER values, sensitivities of second order and the sensitivities computed using Eq. 5.14. Using the Linear Regression in stabilized part (equis in green), the sensitivity increases considerably respect the Mier@21ºC (crosses in black) and the second order method (asterisks in red).

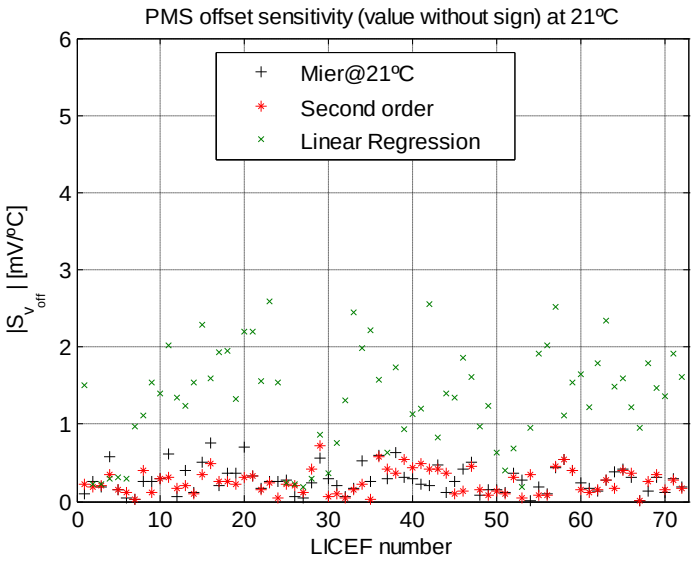

Fig. 5.9 PMS offset sensitivity absolute value comparison: the black crosses are measured by Mier at 21ºC, the red asterisks are the sensitivity from second order correction computed at 21ºC and the green equis are the values computed by Linear Regression in stabilized part.

Some examples are in Fig. 5.10. The values computed using the stabilized part of the dataset, are not reliable since there is some hysteresis. For a given temperature, there are until 4mV of difference in the PMS offset depending on whether the heaters are in state on or off, as shown in the top plots. While it may seem that the points cloud has a clear linear trend as it is shown in the bottom left plot, that does not happen for some receivers, for example in the top plots. The bottom right plot represents a receiver in which the temperature range is narrow (only 0.5 ºC). The point's cloud is sparse and do not has a defined slope, which is not known whether the sensitivity calculation is reliable.

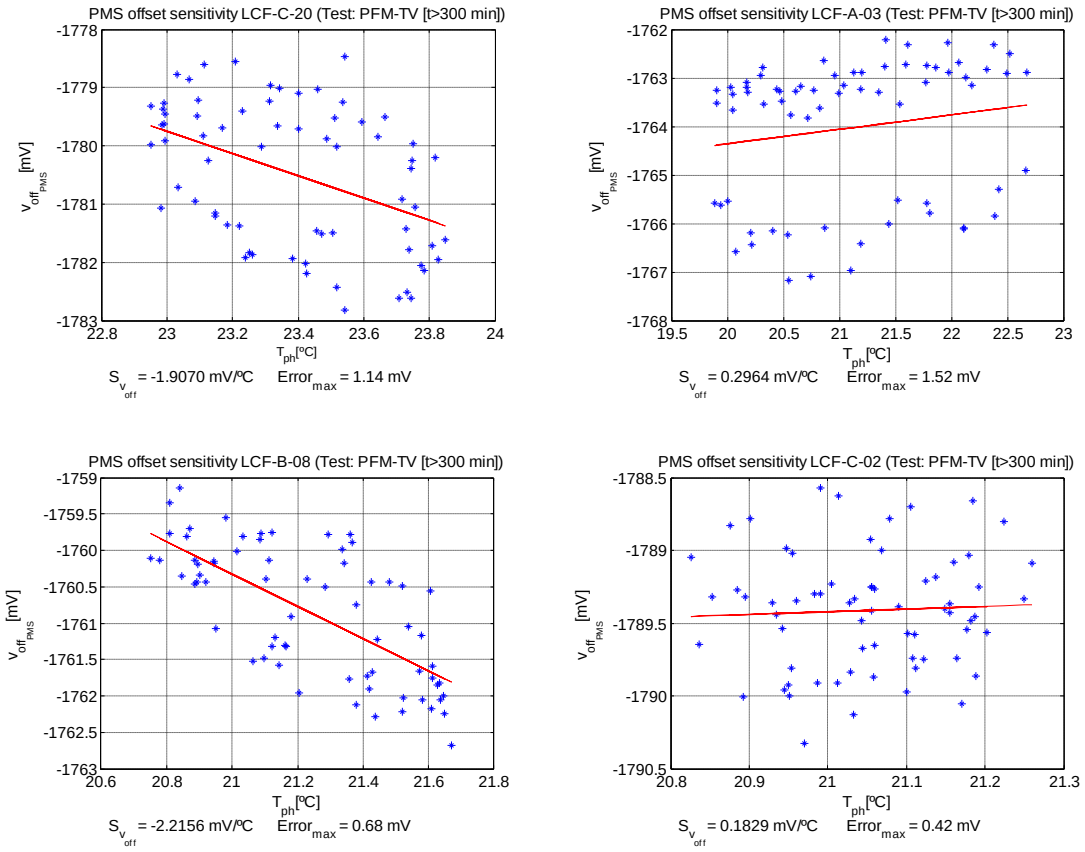

Fig. 5.10 Examples of Linear Regression method to compute the PMS offset sensitivity (S_{voff}) to the physical temperature.

To rule out the computation of the PMS sensitivity by Linear Regression method and Statistical method, an offset estimation has been represented in Fig. 5.11.

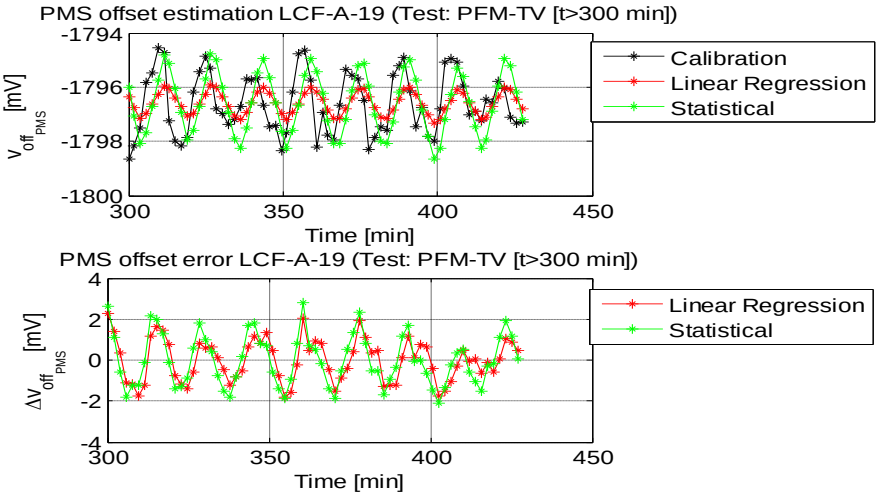

Fig. 5.11 PMS offset estimation (top) and PMS offset error (bottom) respect the calibration measurements (black) using the sensitivities computed by Linear Regression method (red) and Statistical method (green) for the test PFM_TV.

From both estimations it can be point out that the offset is not synchronized with the physical temperature variations because the estimations are delayed in time respect the calibration measurement. Moreover, the estimation by the Linear Regression method does not produce the same height jumps and although the estimation by Statistical method produces the same height jumps, the delay of the temperature respect to the offset makes a greater error.

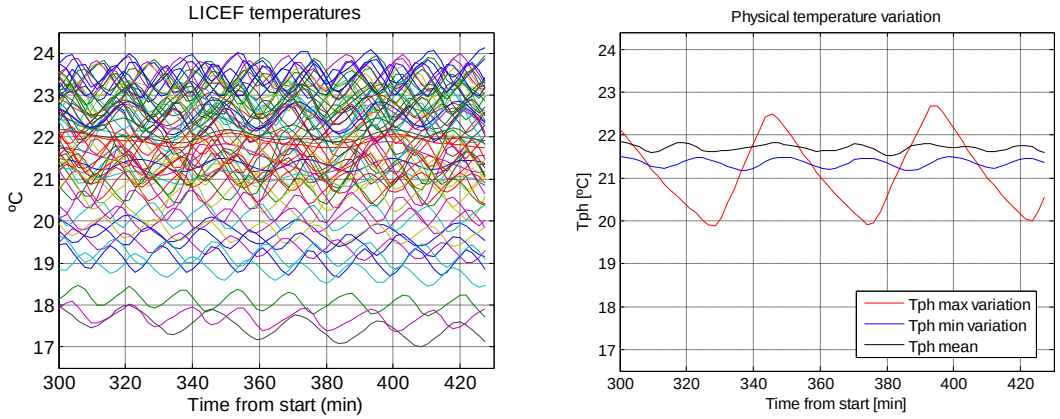

Fig. 5.12 LICEF temperatures (left) and temperature variation (right) in the stabilized part of test PFM_TV. In the right plot, the black line is LICEF average temperature, the red line is the maximum variation in temperature, approximately 2.5ºC (corresponding to LCF-A-03) and the blue line is the minimum variation on temperature, approximately 0.4ºC (corresponding to LCF-B-02).

PMS offset sensitivity computed by Statistical method apparently increases by a factor ~15 as shown in Fig. 5.8 and PMS offset sensitivity computed by Linear Regression method apparent increases by a factor ~8 as shown in Fig. 5.9. This increment is not real because the heaters in this part of the test are switching-on and switching-off and the physical temperature varies slightly as shown in Fig. 5.12. An extensive study about the heaters offset correction has been done in chapter 6.

5.3.5. First order correction in-flight

In 2010, after applying the *manual fine tuning adjustment* in the heater correction (see chapter 6 for more details), the PMS offset sensitivity has been recomputed in-orbit data using the dataset of *25th April 2010* for all receivers, except the NIRs [24]. If the physical temperature drift in an orbit is small enough (between 1ºC and 3ºC) and close to 21ºC to avoid having to approximate the offset with a second order polynomial, only a linear regression is necessary, resulting only the alpha term that not depends of the temperature in the units [V/ºC]:

$$S_{v_{offFLIGHT_k}} = \alpha_{v_{offFLIGHT_k}} \qquad \textit{Eq. 5.15}$$

Fig. 5.13 shows that the sensitivity values expressed in the units [mV/ºC] from the second order correction computed on-ground are distributed around zero to yield, approximately, a zero mean distribution. However, the sensitivity parameters estimated

from flight data on *25th April 2010* are biased to negative values. This fact can be clearly observed in the bottom plot where the difference between the sensitivities is negative for most of the receivers.

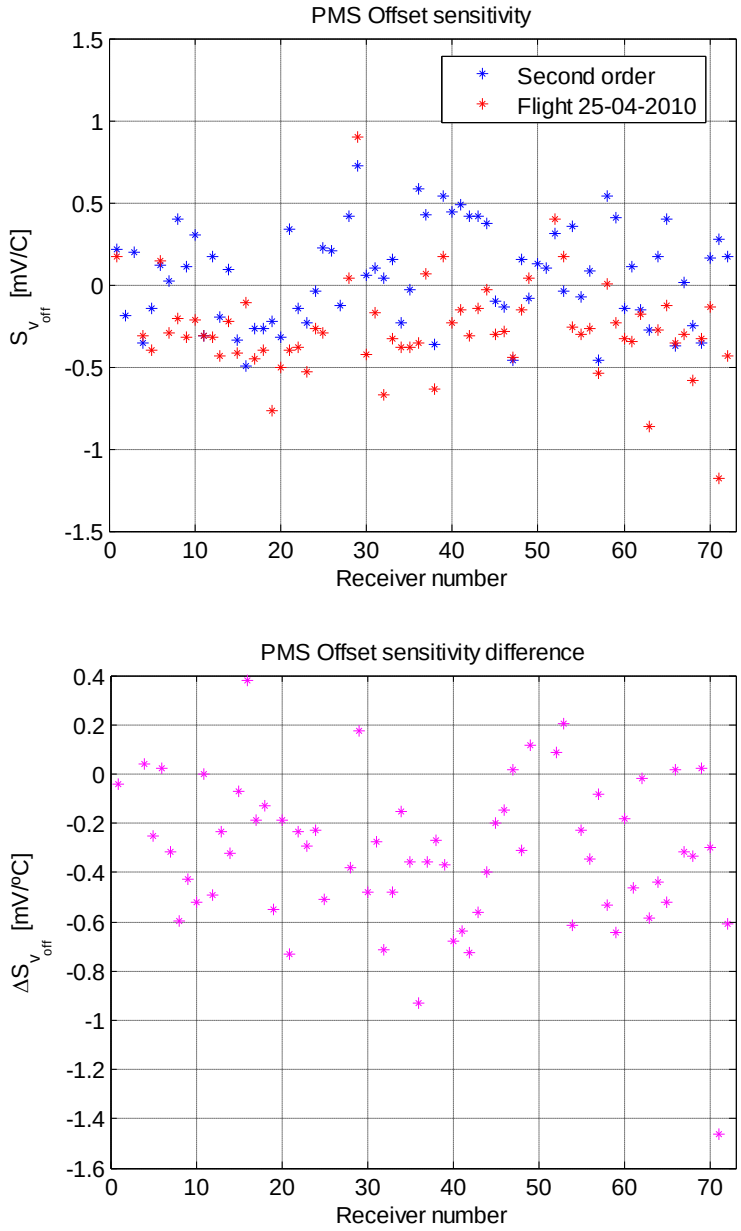

Fig. 5.13 Top: PMS offset sensitivity comparison between values of second order computed on ground (blue asterisks) and values computed in flight. Bottom: PMS offset sensitivity difference (values in-flight 25-04-2010 minus values second order correction on-ground).

The plots in Fig. 5.14 represent the offset as a function of the physical temperature and the linear regression computed on-ground with only alpha term of the second order method and in-flight with First order method. The slope of the regression lines is the PMS offset sensitivity. Note that some receivers, for example the LCF-B-03 (top) have a peculiar shape in the edges due to the transitions of the switching on-off or off-on in the heaters are not abrupt.

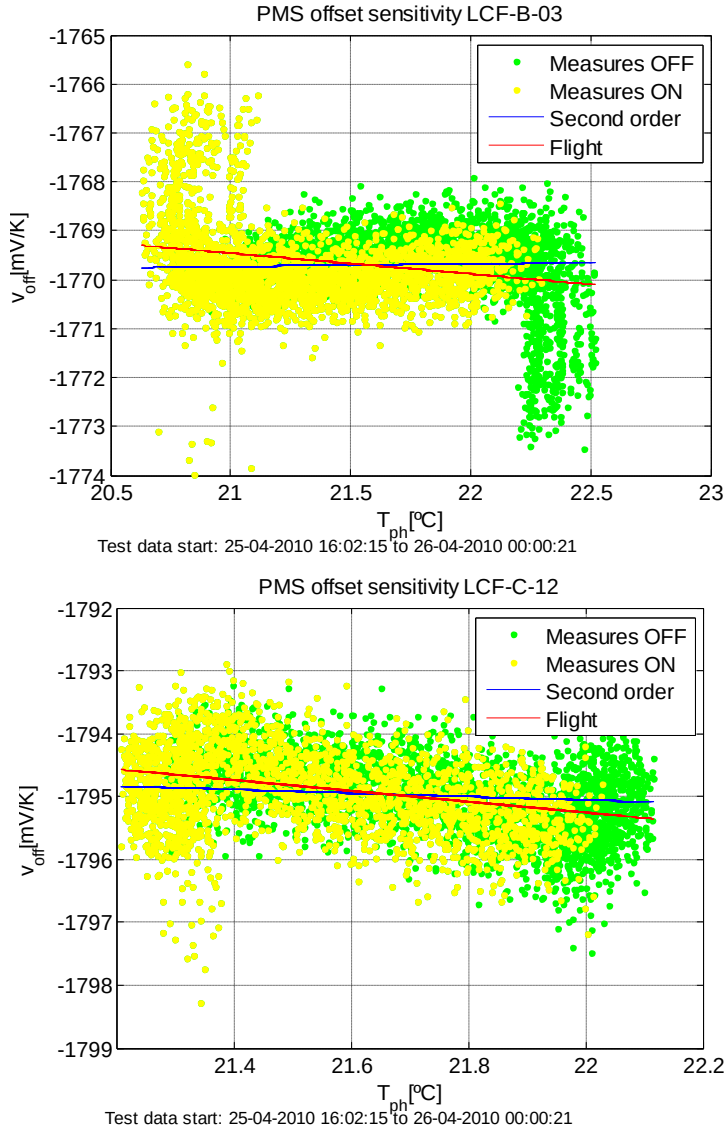

Fig. 5.14 Examples of the PMS offset as a function of the physical temperature and the linear regression computed on-ground with alpha term computed in the second order method (blue line) and in-flight with First order method (red line). The green points are the measurements when the heater associated is OFF and the yellow points are the measurements when the heater associated is in ON.

5.3.6. Conclusions of PMS offset sensitivity analysis

As a conclusion, **the PMS offset sensitivity to be used are the on-ground values from the second order correction, but only the alpha term that does not depend on the temperature because the physical temperature variation is really low and closed to 21ºC. The reason is that, in fact, it is the only estimation that is not affected by the heaters behavior and the computation is done with precision**. **For the moment these values, summarized in Appendix Table I (Appendix I: Sensitivity values) are considered to be the most accurate and are being used in the official SMOS Level 1 data processor.** Also, if more accuracy is required because the temperature variation increases or is away from 21ºC, it is possible to modify the software easily to include the use of the beta term in the estimation.

5.4. PMS gain sensitivity

The first estimation of the PMS gain sensitivity values has been provided by the Spanish company MIER Communications. A preliminary study about the gain sensitivity had been realized at UPC in 2007 using the LSS data [20].

5.4.1. First order correction

In February 2009, the gain sensitivity has been estimated in two temperature ranges: between 20ºC to 30ºC and between 20ºC to 25ºC using the on-ground dataset *COLD-FUNCTIONAL* [21]. At that time it was not yet known exactly what temperature would be the instrument in flight because the in orbit temperature variation is limited by the thermal control system.

The PMS gain sensitivity $S_{G_k}^C$ expressed in the units [(V/K)/ºC] is defined as the slope of the interpolation line for the PMS gain of each calibration depending on the physical temperature and for each k-receiver can be expressed as:

$$S_{G_k}^C = \alpha_G^C = \frac{G_{4P_k}^C(T_{ph_{1_k}}) - G_{4P_k}(T_{ph_{0_k}})}{T_{ph_{1_k}} - T_{ph_{0_k}}} \qquad \textit{Eq. 5.16}$$

where $G_{4P_k}^C$ [V/K] is the PMS gain at calibration plane computed by the *4-points calibration method* of the *k*-receiver, $T_{ph_{0_k}}$ and $T_{ph_{1_k}}$ [ºC] are the physical temperatures at two different calibrations. It is assumed that the gain is computed using the CAS (NDN+NIR) as reference and it is calibrated with an absolute error ΔG_{PMS}.

Knowing the gain sensitivity and the gain at a calibration temperature, the gain in measurement mode at a given physical temperature can be expressed in this form:

$$G_{4P_k}^C(T_{ph_{ik}}) = G_{4P_k}^C(T_{ph_{0k}}) + S_{G_k}^C \cdot (T_{ph_{ik}} - T_{ph_{0k}}) \qquad \textit{Eq. 5.17}$$

being $G_{4P_k}^C$ the PMS gain voltage of *k*-receiver computed using the *4-points calibration method*, $T_{ph_{0k}}$ the reference temperature, $T_{ph_{ik}}$ corresponds to the current temperature and $S_{G_k}^C$ is the gain sensitivity.

Two examples of the PMS gain sensitivities are shown in Fig. 5.15 and Fig. 5.16. Note that in those plots, the sensitivity is expressed in relative units [%/ºC] whereas in Eq. 5.17 the sensitivity is expressed in absolute units. The plots in Fig. 5.15 present more clear lineal trend than the receivers shown in Fig. 5.16 where the temperature range is wider and two effects appears: the non-linearity and the saturation in the edges.

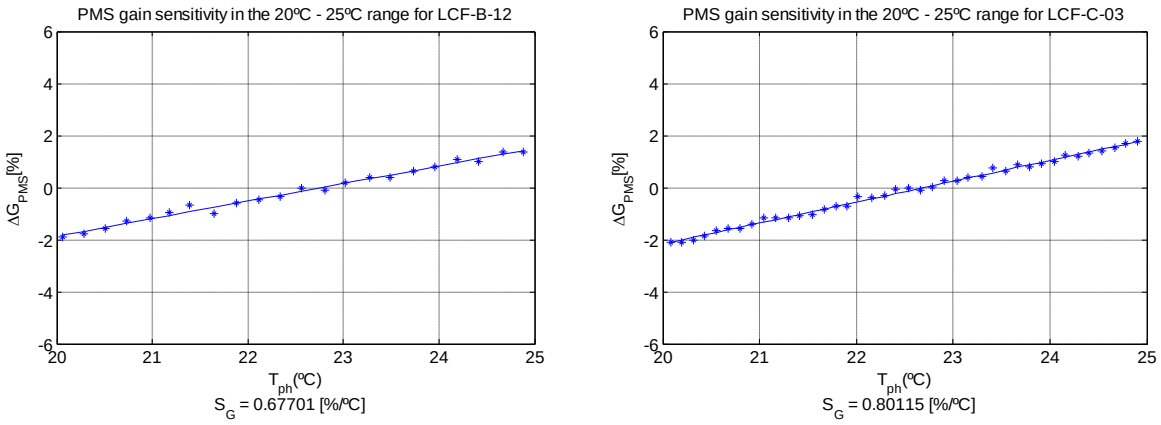

Fig. 5.15 Examples in the range 20ºC-25ºC of the first order regression in the PMS gain to compute the gain sensitivity at C-plane.

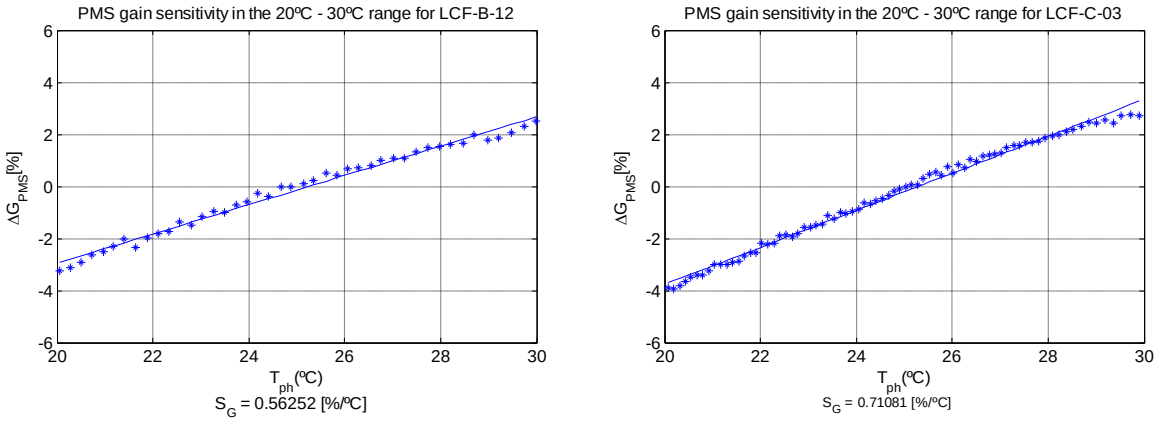

Fig. 5.16 Examples in the range 20ºC-25ºC of the first order regression in the PMS gain to compute the gain sensitivity at C-plane.

In summary, a second order correction is proposed to analyze the gain sensitivity from PMS gain values computed without the CAS influence.

5.4.2. Second order correction

In March 2009, another estimation of the gain sensitivity has been computed. In this case, the same dataset as before is used but the temperature range taken into account is between the 14ºC to 30ºC [22].

The PMS gain is computed by *one-point calibration method* at C-plane because this calculation is done without the intervention of the CAS and the errors associated:

$$G_{1P_k}^C = \frac{v_{U_k} - v_{off_k}}{T_{ph_k} + T_{R_k}^C} \qquad \textit{Eq. 5.18}$$

where v_{U_k} [V] is the PMS voltage when the U-noise is injected, v_{off_k} [V] is the PMS offset voltage, T_{ph_k} [K] is the physical temperature during the U-noise measurement and $T_{R_k}^C$ [K] is the receiver noise temperature at C-plane computed using MIER data at 21ºC and corrected for temperature using the receiver noise temperature sensitivity at CIP plane, also provided by MIER.

If the gain is estimated as a second order polynomial at C-plane for the *k*-receiver, the PMS gain sensitivity is the derivative of the PMS gain respect to the physical temperature and it will be a first order polynomial. For the *k*-receiver, the PMS gain sensitivity can be expressed as follows:

$$S_{G_k}^C(T_{ph_k}) = \beta_{G_k}^C \cdot (T_{ph_k} - 21) + \alpha_{G_k}^C \qquad \textit{Eq. 5.19}$$

where the coefficient β_G^C [(V/K)/ºC^2] is the slope of the increment of physical temperature respect 21ºC and the coefficient α_G^C [(V/K)/ºC] is the constant term. Note that the term α_G^C is the sensitivity around 21ºC, which is the case when the term β_G^C is neglected.

Computing the gain sensitivity at $T_{ph_{0k}}$ and knowing the gain at a calibration temperature, the gain at a given physical temperature can be expressed as:

$$G_{1P_k}^C(T_{ph_{ik}}) = G_{1P_k}^C(T_{ph_{0k}}) + S_{G_k}^C(T_{ph_{0k}}) \cdot (T_{ph_{ik}} - T_{ph_{0k}}) \qquad \textit{Eq. 5.20}$$

being $G_{1P_k}^C$ the PMS gain computed by the *one-point calibration method*, $T_{ph_{0k}}$ the reference temperature, $T_{ph_{ik}}$ corresponds to the current temperature in measurement mode and $S_{G_k}^C(T_{ph_{0k}})$ is the gain sensitivity computed at $T_{ph_{0k}}$.

In Fig. 5.17 there are two examples expressed in the units [(mV/K)/ºC]. Observing the plots it must pointed out that the second order correction becomes important if the physical temperature move away from 21 ºC and the gain sensitivity can vary depending on the temperature range.

To verify the maximum temperature drift that the instrument undergoes along an orbit, let's wait for the data in-flight. This is to check if it is really necessary to use the second order PMS gain sensitivity in the temperature correction.

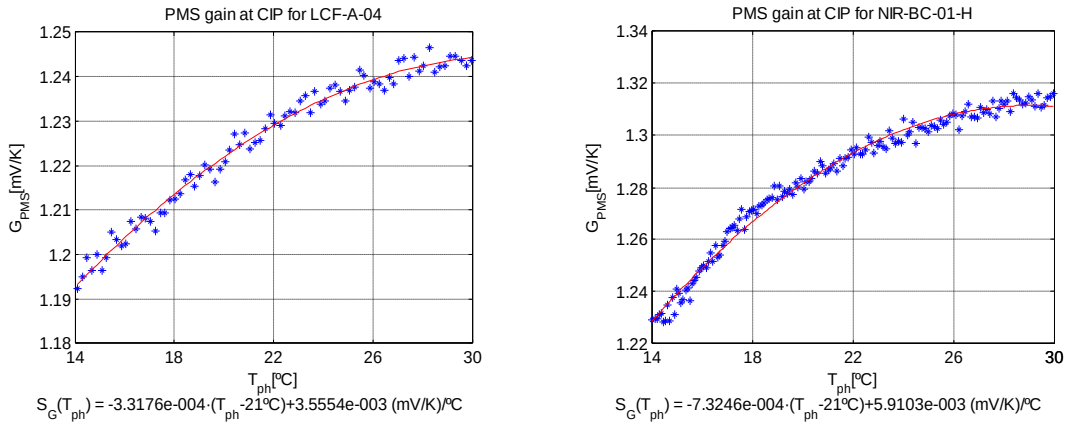

Fig. 5.17 Examples at the range 14ºC-30ºC of the second order regression in the PMS gain to compute the gain sensitivity at C-plane. Left: LCF-A-04. Right: NIR-BC-01-H.

5.4.3. First order correction in-flight

In 2010, using the gain computed by the *4-points calibration method* from the in-flight datasets with the CAS correction [25] and the heater offset correction applied, the PMS gain sensitivity has been estimated again. The physical temperature drift in an orbit is small enough (between 1ºC and 3ºC) and close to 21ºC to avoid having to approximate the gain with a second order polynomial.

If the PMS gain is estimated as a first order polynomial, the PMS gain sensitivity is the derivative of the PMS gain respect the physical temperature with the *09-02-2010 heater offset correction* (see chapter 6 for more details). For the *k*-receiver, the PMS gain sensitivity can be expressed as follows:

$$S_{G_k}^{C} = \alpha_{G_k}^{C} \qquad \textit{Eq. 5.21}$$

where the $\alpha_{G_k}^{C}$ [(V/K)/ºC] is a constant term that does not depend of the physical temperature.

The first dataset used starts the *24th of December 2009 at 00:00:25 to 27th of December 2009 at 07:56:29* [26]**.** The other dataset used starts the *20th of April 2010 at 06:00:25 to 23rd of April 2010 at 13:02:08* [27].

Fig. 5.18 shows two examples of the PMS gain sensitivity expressed in the units [(mV/K)/ºC]. Note that the differences between the gain sensitivity computed on-ground and in-flight are small. Also for some receivers, as the LCF-A-03, LCF-B-03 (Fig. 5.18 right) and LCF-C-03, the measurements of the gain have a peculiar behavior that produces a distribution showing memory effects (hysteresis) on the calibration measurement points. In these cases, the gain when the temperature is increasing is different to the gain when the temperature is decreasing. The PMS heaters correction modifies a little the gain sensitivity, but the differences are negligible in terms of gain and this correction is very important for the offset.

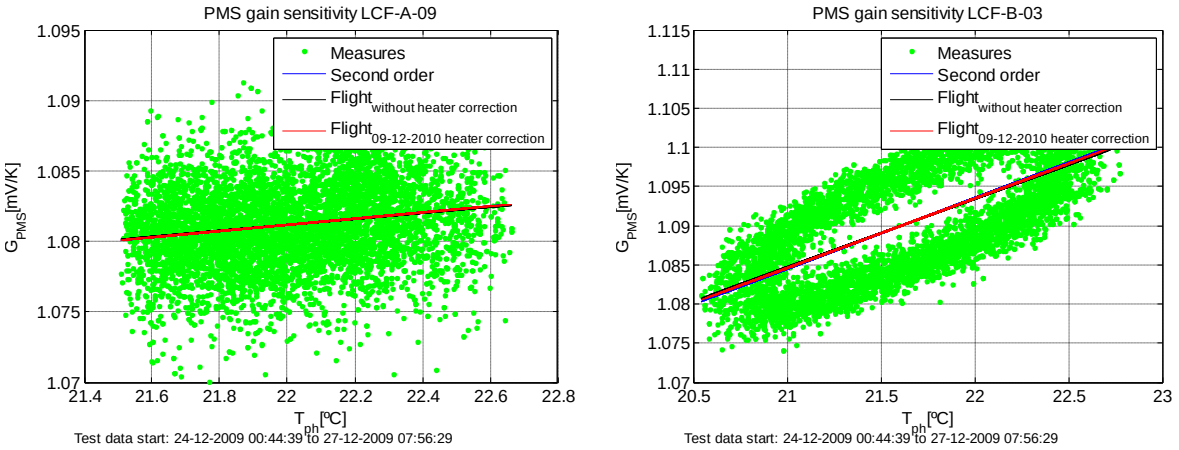

Fig. 5.18 Examples of the PMS gain as a function of the physical temperature (green points) and the linear regression computed on-ground with second order method using only alpha term (blue line) and in-flight with First order method (black line and red line, without and with heater offset correction, respectively).

In Fig. 5.19, the plots present two examples of the PMS gain sensitivity from both days in study. In this case, also the LCF-A-03, LCF-B-03 (Fig. 5.19 right) and LCF-C-03, the measurements of the gain have hysteresis.

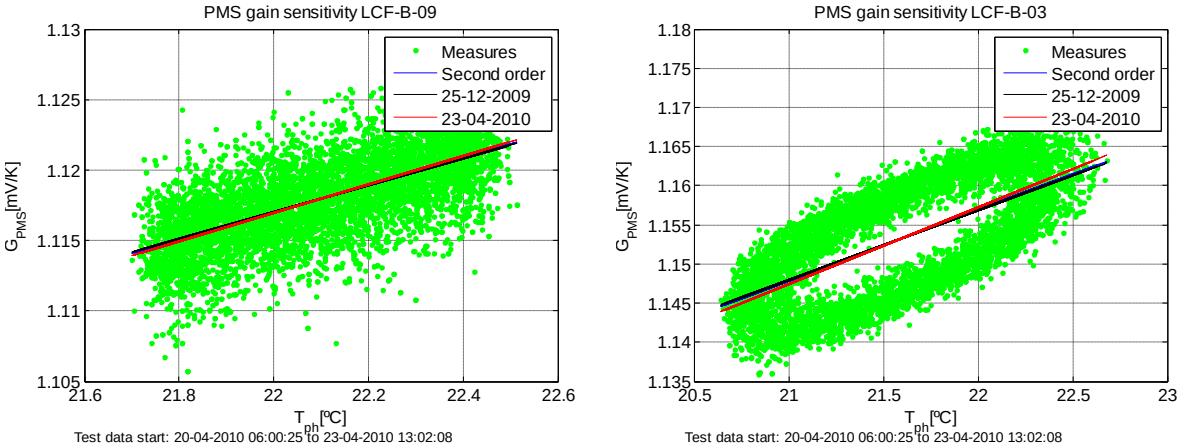

Fig. 5.19 Examples of the PMS gain as a function of the physical temperature (green points) and the linear regression computed on-ground with second order method using only alpha term (blue line) and in-flight with First order method (black line and red line, 25-12-2009 and 23-04-2010, respectively).

The Fig. 5.20 shows a comparison of the PMS gain sensitivity expressed in the units [(mV/K)/ºC]. The gain sensitivity computed in-flight does not have the same values as the sensitivity computed on ground (second order), but the difference in the values is small and random. Only in some receivers, as the LCF-B-07, LCF-C-17, LCF-C-18 and LCF-C-20, where the gain sensitivity is very small, the signal of the gain sensitivity in flight (positive) is different from the gain sensitivity of the second order (negative).

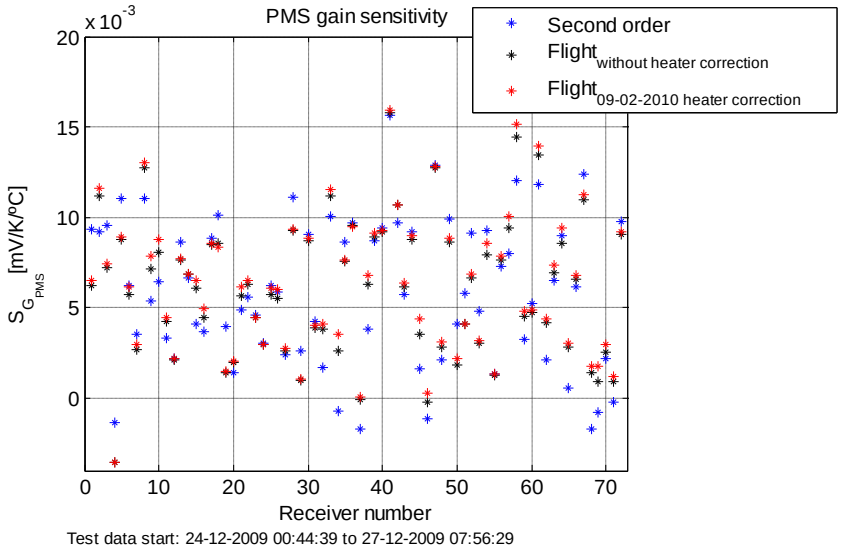

Fig. 5.20 Comparison of the PMS gain sensitivity. The asterisks in blue are the sensitivity of the second order (only the alpha term), the asterisks in black and red are the sensitivity of the First order from flight data 25-12-2009, applying or not applying the heater offset correction, respectively.

The Fig. 5.21 shows a comparison of the PMS gain sensitivity expressed in the units [(mV/K)/ºC]. Although the differences are very small, PMS gain sensitivities computed from the 23-04-2010 are systematically higher. These differences may be related to slightly different PMS gains due to the corrections in the software included since December 2009: different CAS coefficients (because the arm A of the instrument change the configuration) but same heater correction for the moment.

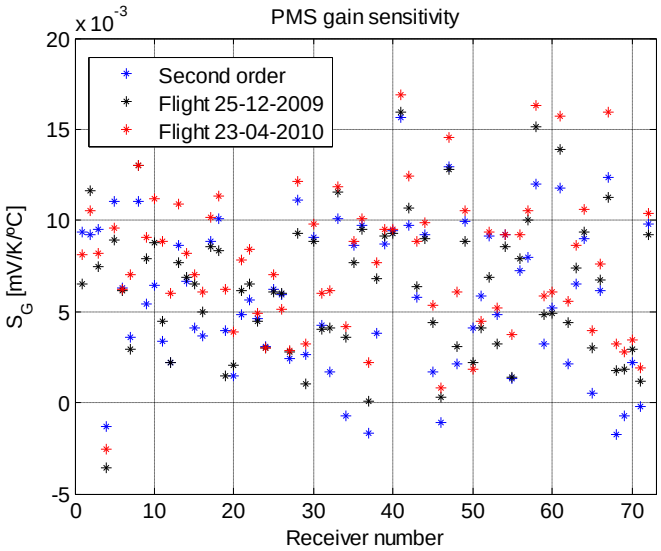

Fig. 5.21 Comparison of the PMS gain sensitivity. The asterisks in blue are the sensitivity of the second order (only the alpha term), the asterisks in black and red are the sensitivity from the First order in flight data 25-12-2009 and 23-04-2010, respectively.

5.4.4. Conclusions of PMS gain sensitivity analysis

PMS gain sensitivity computed from flight data on 23rd April of 2010 has been implemented because these values are summarized in Appendix Table I (Appendix I: Sensitivity values) are considered to be the most accurate and are used in the official SMOS Level 1 data processor.

To obtain the gain sensitivity at the antenna plane to apply the sensitivity directly at the antenna measurements, only it is necessary a transformation plain using the S-parameters corresponding to the switch (S_{LC_k}, S_{LH_k}, S_{LV_k}) and the antenna efficiency (η_{H_k}, η_{V_k}). Note that the temperature variation of the switch is considered negligible:

$$S_{G_k}^{H} = S_{G_k}^{C} \cdot \frac{\eta_{H_k} \cdot \left|S_{LH_k}\right|^2}{\left|S_{LC_k}\right|^2} \qquad \textit{Eq. 5.22}$$

$$S_{G_k}^{V} = S_{G_k}^{C} \cdot \frac{\eta_{V_k} \cdot \left|S_{LV_k}\right|^2}{\left|S_{LC_k}\right|^2} \qquad \textit{Eq. 5.23}$$

5.5. Receiver noise temperature sensitivity

Previously to explain how the receiver noise temperature sensitivity has been estimated a brief explanation about how the receiver noise temperature is computed it is presented next.

The receiver noise temperature has been computed for the *k*-receiver at C-plane using uncorrelated noise as follows:

$$T_{R_k}^{C} = \frac{v_{U_k} - v_{off_k}}{G_{PMS_k}^{C}} - T_{ph_k} \qquad \textit{Eq. 5.24}$$

where v_{U_k} [V] is the PMS voltage when the U-noise is injected, v_{off_k} [V] is the PMS offset voltage, T_{ph_k} [K] is the physical temperature and $G_{PMS_k}^{C}$ [V/K] is the PMS gain computed at calibration plane.

To obtain the receiver noise temperature at the antenna plane, a transformation plane only is necessary using the S-parameters corresponding to the switch (S_{LC_k}, S_{LH_k}, S_{LV_k}) and the antenna efficiency (η_{H_k}, η_{V_k}):

$$T_{R_k}^H = T_{ph_k} \cdot \left(\frac{\left|S_{LC_k}\right|^2}{\eta_{H_k} \cdot \left|S_{LH_k}\right|^2} - 1 \right) + T_{R_k}^C \cdot \frac{\left|S_{LC_k}\right|^2}{\eta_{H_k} \cdot \left|S_{LH_k}\right|^2} \qquad \textit{Eq. 5.25}$$

$$T_{R_k}^V = T_{ph_k} \cdot \left(\frac{\left|S_{LC_k}\right|^2}{\eta_{V_k} \cdot \left|S_{LV_k}\right|^2} - 1 \right) + T_{R_k}^C \cdot \frac{\left|S_{LC_k}\right|^2}{\eta_{V_k} \cdot \left|S_{LV_k}\right|^2} \qquad \textit{Eq. 5.26}$$

Another way to get the receiver noise temperature at the antenna plane is using the external calibration has been explained in detail in paragraph 4.1.1.2 of this project.

The first estimation of the receiver noise temperature sensitivity values at calibration plane has been provided by the Spanish company MIER Communications.

5.5.1. First order correction

The receiver noise temperature sensitivity $S_{T_R}^C$ is defined as the slope of the interpolation line for the measurements of the receiver noise temperature voltage of each calibration depending on the calibration temperature [21].

In 2009, using the on-ground dataset *COLD-FUNCTIONAL* the receiver noise temperature sensitivity has been estimated as follows:

$$S_{T_{R_k}}^C = \alpha_{T_{R_k}}^C = \frac{T_{R_k}^C(T_{ph_{1_k}}) - T_{R_k}^C(T_{ph_{0_k}})}{T_{ph_{1_k}} - T_{ph_{0_k}}} \qquad \textit{Eq. 5.27}$$

where $S_{T_R}^C$ [K/ºC] is the receiver noise temperature sensitivity at C-plane, $T_{R_k}^C$ [K] is the receiver noise temperature for each *k*-receiver, $T_{ph_{0_k}}$ and $T_{ph_{1_k}}$ [ºC] correspond to the physical temperatures at two different calibrations.

As a result, the receiver noise temperature at given physical temperature knowing the receiver noise temperature for other physical temperature can be expressed as:

$$T_{R_k}^C(T_{ph_{i_k}}) = T_{R_k}^C(T_{ph_{0_k}}) + S_{T_{R_k}}^C \cdot (T_{ph_{i_k}} - T_{ph_{0_k}}) \qquad \textit{Eq. 5.28}$$

being $T_{R_k}^C$ the receiver noise temperature, $T_{ph_{0_k}}$ is the reference temperature, $T_{ph_{i_k}}$ corresponds to the current temperature in measurement mode and $S_{T_R}^C$ is the receiver noise temperature sensitivity at calibration plane.

Fig. 5.22 shows an example of this estimation in the temperature ranges 20ºC-25ºC and 20ºC-30ºC. Note that the error in the receiver noise temperature sensitivity is high (distance between the regression line and the measurement points) because to compute

the receiver noise temperature it is necessary to know the gain at calibration plain. If this gain is computed using the *4-points calibration method* may have an absolute error in the gain that yields an absolute error in the receiver noise temperature.

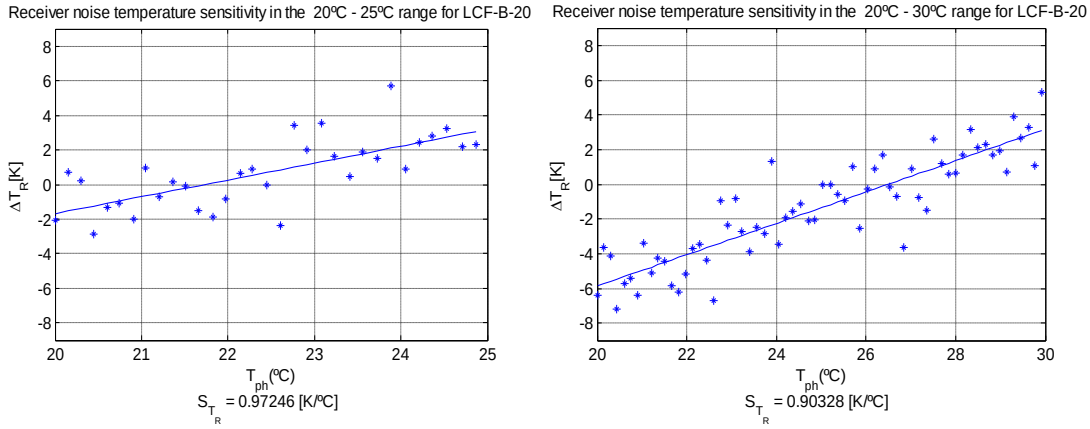

Fig. 5.22 Examples at the range 20ºC-25ºC (left) and at the range 20ºC-30ºC (right) of the receiver noise temperature first order regression to compute the sensitivity.

5.5.2. Conclusions of receiver noise temperature sensitivity analysis

It is assumed that the computation of the gain at calibration plane using the *4-points calibration method* may have errors caused by the CAS (NDN+NIR) and the influence of the S-parameters. In addition the *1-point calibration method* cannot be used because the gain in this method has been computed using the receiver noise temperature provided by MIER Communications [22].For all these reasons **it was decided not to estimate the receiver noise temperature sensitivity from the LSS measurements and take MIER Communications data as ground truth that is expressed by a unique constant value at calibration plane. These values are summarized in Appendix Table I (Appendix I: Sensitivity values) and are used in the official SMOS Level 1 data processor.**

To obtain the receiver noise temperature sensitivity at the antenna plane to apply the sensitivity directly at the antenna measurements, a transformation plain only it is necessary using the S-parameters corresponding to the switch (S_{LC_k}, S_{LH_k}, S_{LV_k}) and the antenna efficiency (η_{H_k}, η_{V_k}). Note that the temperature variation of the switch is considered negligible:

$$S_{T_{R_k}}^{H} = \frac{\left|S_{LC_k}\right|^2}{\eta_{H_k}\cdot\left|S_{LH_k}\right|^2} - 1 + S_{T_{R_k}}^{C}\cdot\frac{\left|S_{LC_k}\right|^2}{\eta_{H_k}\cdot\left|S_{LH_k}\right|^2} \qquad \textit{Eq. 5.29}$$

$$S_{T_{R_k}}^{V} = \frac{\left|S_{LC_k}\right|^2}{\eta_{V_k}\cdot\left|S_{LV_k}\right|^2} - 1 + S_{T_{R_k}}^{C}\cdot\frac{\left|S_{LC_k}\right|^2}{\eta_{V_k}\cdot\left|S_{LV_k}\right|^2} \qquad \textit{Eq. 5.30}$$

CHAPTER 6

6. PMS offset track

This chapter is devoted to analyze the PMS offset behavior with respect to the physical temperature and other factors such as the switching-on and switching-off of the heaters. The heater function is the thermal control of the instrument to hold the receiver temperatures around 22ºC when the satellite is in orbit.

6.1. Effect of thermal noise in the PMS offset

Fig. 6.1 shows the pk-to-pk and the standard deviation of two different datasets [23]. First datasets corresponds to stability measurements (test *STABILITY 4*) inside the Maxwell anechoic chamber. Second dataset is acquired in the LSS (test *PFM-TV*) with conditions of thermal vacuum.

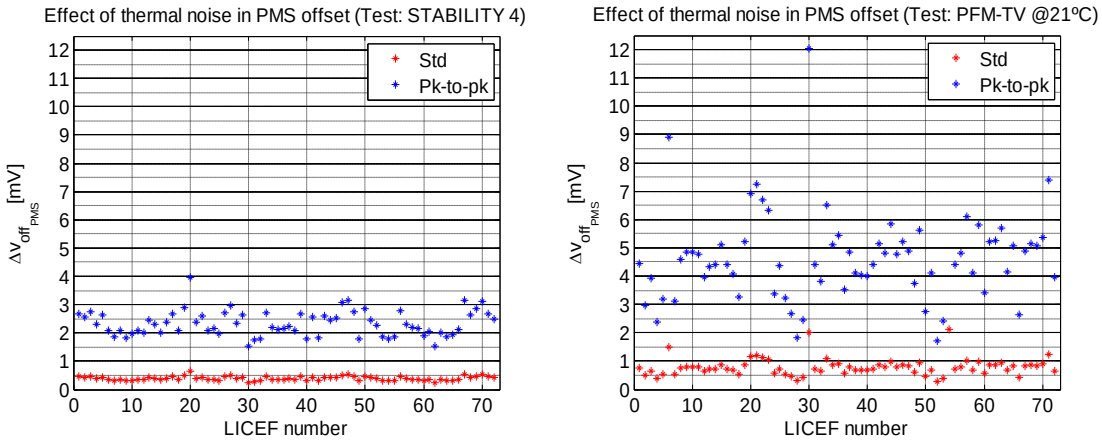

Fig. 6.1 Standard deviation (red asterisks) and pk-to-pk deviation (blue asterisks) of the PMS offset. Left: test STABILITY 4. Right: PFM_TV (stabilized part).

The PMS offset has a standard deviation around 0.4mV when the test data have been acquired inside the anechoic chamber (left plot). Instead, when the test data is a thermal vacuum (translated to 21ºC for avoid the oscillations in temperature) the standard deviation is slightly above around 0.7mV (right plot). Regarding to the pk-to-pk deviation, it is high in thermal vacuum (right plot) in comparison with the anechoic chamber (left plot).

Therefore, the consideration is that the thermal noise in the offset is lower than 1mV since in the thermal vacuum chamber is where you get an environment similar to the space conditions.

6.2. PMS offset track with temperature correction

Before the launch of the satellite, the PMS offset has been tracking using different sensitivity corrections [23] using the on-ground dataset *PFM-TV*.

6.2.1. Estimation with offset second order sensitivity

The sensitivity used to track the offset is computed using a second order polynomial (section 5.3.2) and estimated at the middle physical temperature (for more details see section 5.1.2).

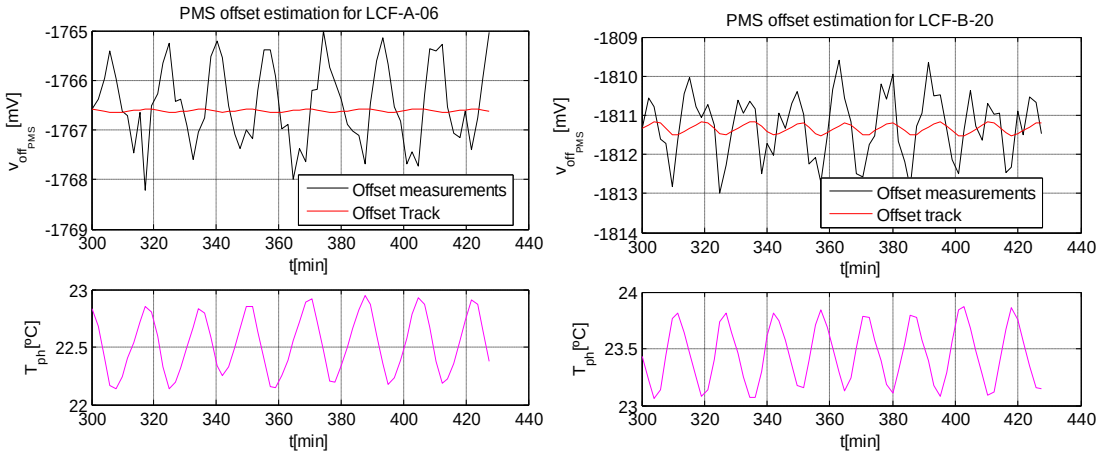

Fig. 6.2 Top: PMS offset tracking in the stabilized part of the test using the second order sensitivity. Bottom: physical temperature variation.

The results showing the stabilized part of the test, from the minute 300 to the end, are in Fig. 6.2. Note that the offset estimation with the sensitivity does not track the offset measurements in any case. The offset measurements variations are very abrupt and the offset track with sensitivity does not follow these jumps.

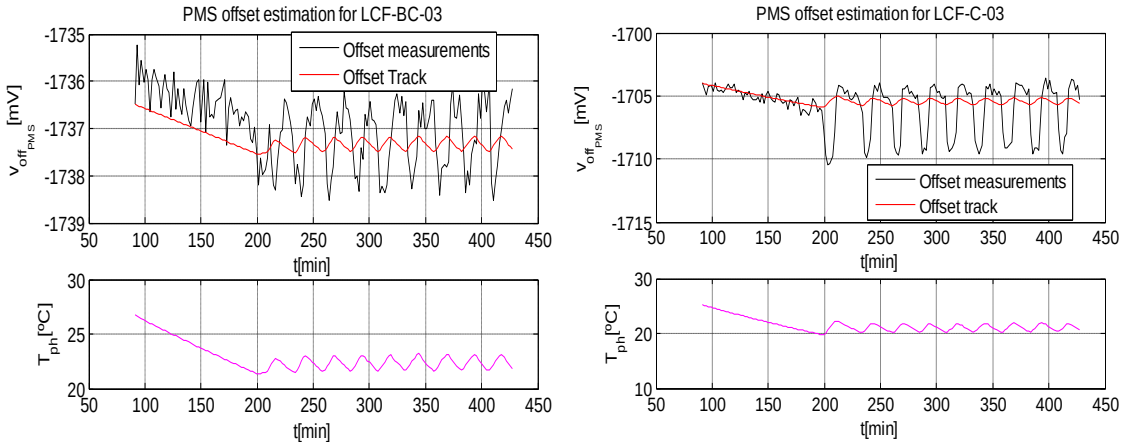

Fig. 6.3 Top: PMS offset tracking for the entire test using the second order sensitivity. Bottom: physical temperature variation.

For this reason, in Fig. 6.3, the plots show the entire test data to check if the sensitivity values are wrong. Note that in the initial part of the test, where the physical temperature has a high variation, the offset estimation can be tracking the measurements. Instead, it is not possible to track the offset in the stabilized part due the abrupt jumps using the offset dependence with the physical temperature.

From these results, it is not possible to make an offset estimation with the required accuracy (be within the limits of thermal noise), so other offset estimations have been tried in the stabilized part (1±2ºC physical temperature drift) because the instrument will has a similar behavior in orbit.

6.2.2. Estimation with offset Statistical method sensitivity

In this case the sensitivity used to estimate the offset is computed by the Statistical method (explained in section 5.3.3).

Some plots are shown in Fig. 6.4. It can be observed that once the offset has been corrected, the PMS offset estimation tracks well the magnitude of offset jumps but there is some misalignment between the offset calibrations and the offset estimation (top plots) that produces an error greater than the offset thermal noise (bottom plots). So, in conclusion it is not a good offset tracking.

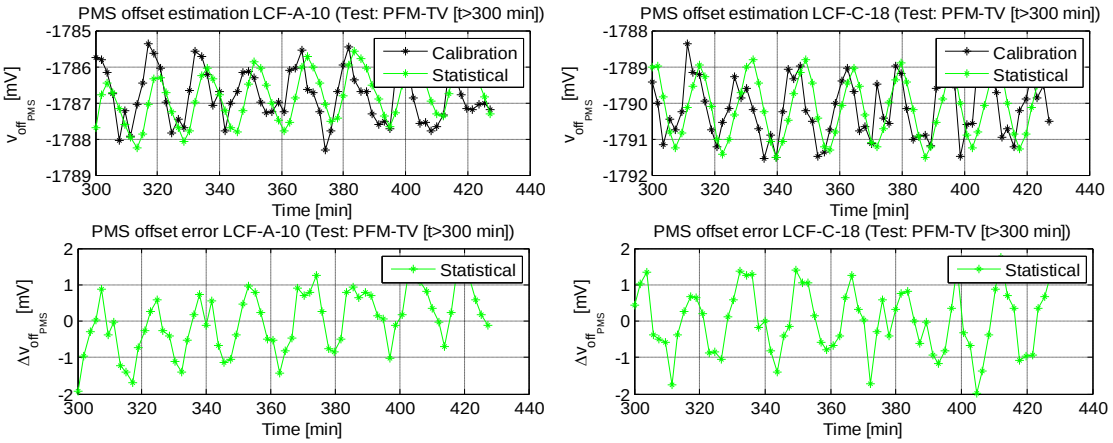

Fig. 6.4 Top: PMS offset tracking for the stabilized part using the sensitivity computed by Statistical method. Bottom: PMS offset error.

6.2.3. Estimation with offset Linear regression in stabilized part sensitivity

The sensitivity used to track the offset is computed by Linear regression in stabilized part of the dataset (section 5.3.4).

Some examples are presented in Fig. 6.5. Note that in this case the offset jumps correction is lower than the abrupt jumps in the offset measurements (top plots). Also there is some misalignment that produces an error greater than the offset thermal noise (bottom plots). As conclusion, this offset tracking is also ruled out for not conforming to the requirements.

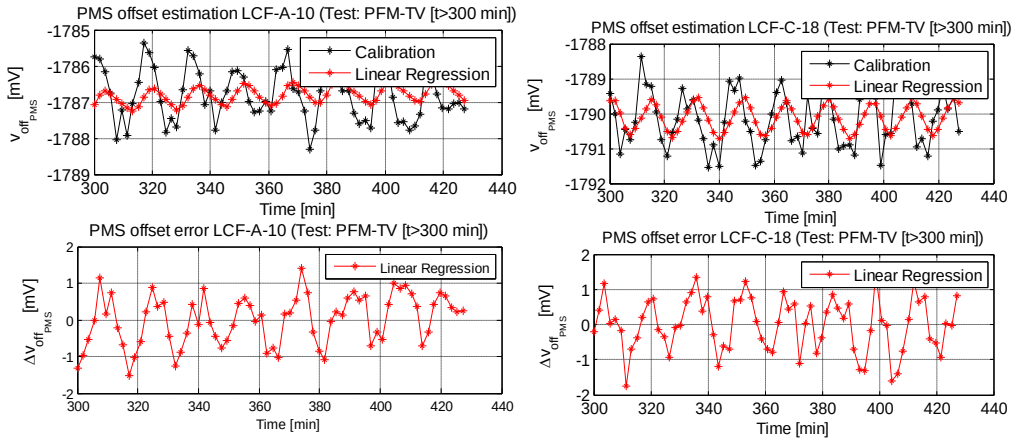

Fig. 6.5 Top: PMS offset tracking for the stabilized part using the sensitivity computed by Linear regression in stabilized part method. Bottom: PMS offset error.

6.2.4. Preliminary conclusions

To determinate the PMS offset sensitivity correctly at least a variation in physical temperature drift of a few degrees is required, something that is not possible in the stabilized part of the test *PFM-TV* used in the Statistical method and the Linear regression in stability part. The PMS offset second order sensitivity has been correctly calculated but the abrupt variations in the absolute offset values have been caused by the switching-on and switching-off of the heaters.

6.3. PMS offset track with heaters correction

During the investigation a way to predict the PMS offset using the state of the heaters has been tried to find. It is supposed that the offset has a high value when the heater is in state off and has a low value when the heater is in state on, but the offset has an unexpected and unknown delay of approximately one calibration time respect to the bit of the heater.

To study the heaters effect, every receiver has been assigned to a single heater. In the case of the receivers in the arms, the correlation between the change in the heater signal and the offset effect is clearer than the receivers in the hub. The Table 6.1 presents the correspondence between the heater number and the CMN segment.

	Heater
CMN-H1	1
CMN-A1	2
CMN-A2	3
CMN-A3	4
CMN-H2	5
CMN-B1	6

	Heater
CMN-B2	7
CMN-B3	8
CMN-H3	9
CMN-C1	10
CMN-C2	11
CMN-C3	12

Table 6.1 Correspondence between the heater number and the CMN segment.

In the arms the heater assigned to each receiver is the heater that belongs to the same CMN. Instead of that, in the hub the assignment is more difficult because the corresponding heater is not pertaining to the same CMN as the receiver.

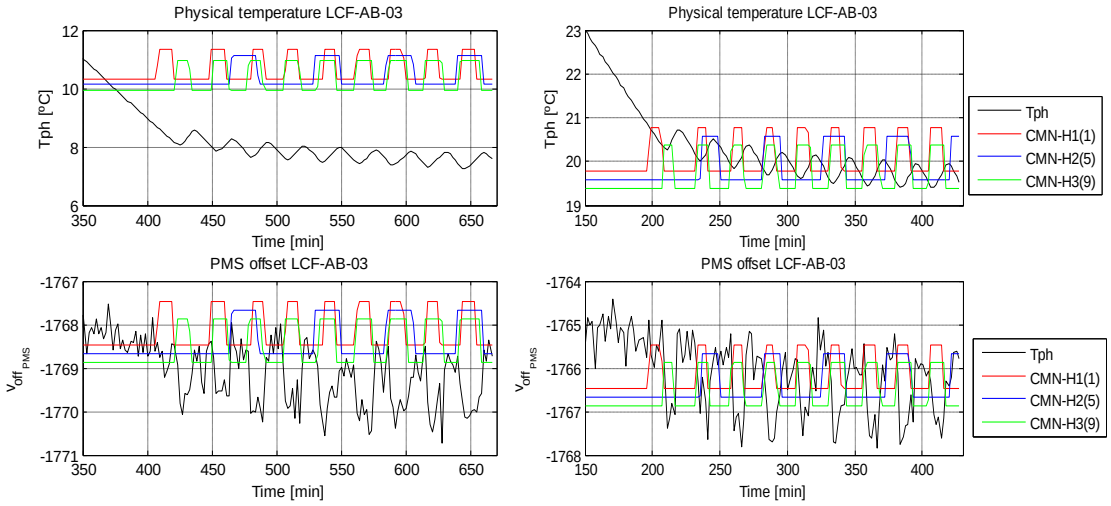

Fig. 6.6 LCF-AB-0 located in the segment H1. Left: dataset COLD. Right: dataset PFM-TV. Top: Physical temperature variation (black) and possible heater signals (red: heater 1 →H1; blue: heater 5 →H2; green: heater 9 → H3).

A preliminary assignment has been done using the dataset *COLD* and dataset *PFM-TV* with a detailed observation of the first switching-on of the heaters located in the hub and comparing with the offset jump and the physical temperature variation. Note that in this example (Fig. 6.6), the heater 5 (blue) is ruled out because the first signal change is after the offset jump and the temperature increase. The heater 1 (red) also is ruled out because the first signal change is much earlier in time (around 20 minutes) than the offset jump and the temperature increase. The heater 9 (green) is the assigned (heater located in the CMN-H3).

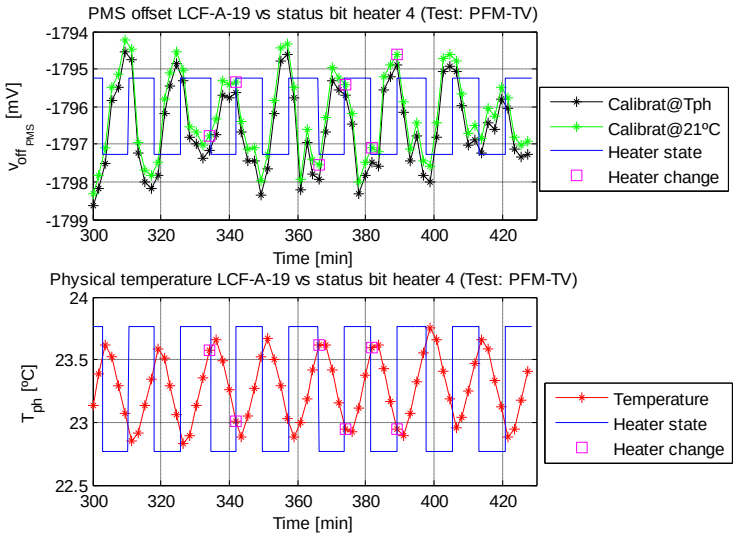

Fig. 6.7 Example of the delay in the PMS offset LCF-A-19 located in the segment A3.

Fig. 6.7 shows an example of the delay in the PMS offset. Note in the top plot that the effect of the heaters is most important that the temperature variation, because the offset represented at physical temperature (black color) oscillating between 22.8ºC and 23.6ºC and the offset represented at 21ºC (green color) differ in less than 0.5mV. The heater state (blue color) only marks on in high value (offset mean+1mV) and off in low value (offset mean-1mV). The delay respect to the heater state can be observed. The heater change (pink color) marks if during a calibration event steps in state on and steps in state off are mixed. In the bottom plot, the physical temperature (red color) has been represented with the heater state and the heater change similar as before.

6.3.1. Heaters correction on-ground

After the satellite launch, various heater offset corrections have been computed on-ground to find the better solution to remove the offset jumps effect. The first, without taking into account the delay between the offset jumps and the heater signal and the last using a delay of one long calibration sequence time (around 2 minutes) because in June 2009 datasets with only commanding the PMS calibration steps (with measurements closer in time) were not available.

6.3.1.1. Offset jumps without delay

Since the real cause of the delay between the offset jumps and heater signal state is unknown, the first estimation of the heater correction has been done without considering the delay, obtaining the offset jumps (Δv_{off_k}) for each *k*-receiver as follows:

$$\Delta v_{off_k} = v_{off_k}(HEATER_{ON}) - v_{off_k}(HEATER_{OFF}) \qquad \textit{Eq. 6.1}$$

where $v_{off_k}(HEATER_{ON})$ corresponds to the offset average value when the heater during this calibration is only in state on and $v_{off_k}(HEATER_{OFF})$ is the offset average value when the heater is only in state off, discarding the calibration events with mixed states.

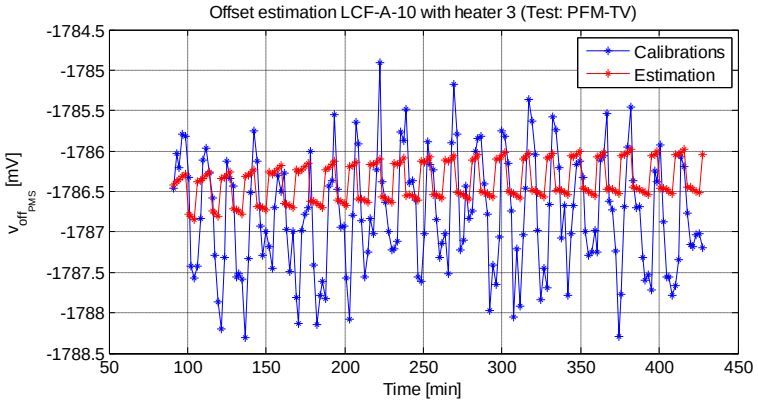

Fig. 6.8 On-ground PMS offset estimation LCF-A-10 using the offset jumps computed without delay and the second order sensitivity

One example is shown in Fig. 6.8. It has been represented using the offset jumps computed without delay and once the temperature correction has been applied. It can see clearly as the offset jumps are lower in magnitude than the real offset jumps from the calibrations. This estimation is not enough accurate to track the offset.

6.3.1.2. Offset jumps with delay

Note that the offset track is not possible without considering a delay. In this case the delay applied to the heater state is 1.9 minutes (the time between 2 long calibrations) due to the non availability of frequent calibrations in the datasets. The PMS offset jumps (Δv_{off_k}) can be obtained for each *k*-receiver as follows:

$$\Delta v_{off_k} = v_{off_k}(HEATER_{delayed_{ON}}) - v_{off_k}(HEATER_{delayed_{OFF}}) \qquad \text{Eq. 6.2}$$

where $v_{off_k}(HEATER_{delayed_{ON}})$ is the offset average value when the heater assigned is delayed and in state on and $v_{off_k}(HEATER_{delayed_{OFF}})$ being the offset average value when the heater delayed is off, discarding the calibration events with mixed states.

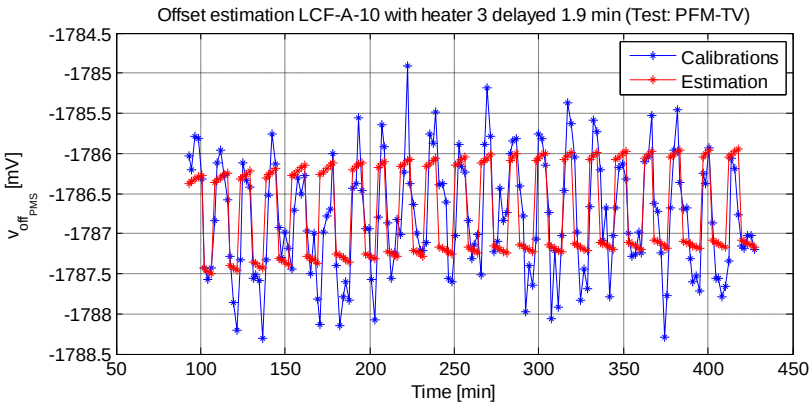

Fig. 6.9 Offset estimation LCF-A-10 on-ground using the offset jumps computed with delay of 1.9 minutes and the second order correction sensitivity.

The same example as before is presented in Fig. 6.9. Note that in this case, the offset jump in the correction is higher and the offset estimation tracks better the calibration measurements than in the previous case (without delay).

6.3.1.3. Preliminary conclusions

A delay between the offset jump and the heater state is present in the on-ground datasets but the cause is unknown at this moment and it is still unknown whether the delay is the same for all receivers.

The jumps in the offset are present due to the thermal control system that really takes a lot of power to heat the receivers and this should affect the polarization of the circuits. As there is a very critical interface for carrying the DC out of the PMS to the CMN it probably changes some mV in the offset when the heaters are switching on or off.

Then, it is necessary to wait for the datasets in-flight to check if the same circumstances occur and develop an algorithm to estimate the delay and the offset jumps.

6.3.2. Heaters correction in-flight

The main objective in 2010 is analyzing the PMS offset behavior related to the signal heater in datasets in-flight to estimate the delays and the offset jumps using the corresponding signal heater delayed.

The datasets used are PMS offset variation versus heater sequence dated the 9th of February 2010 from 03:00:32 to 12:59:55 and dated the 25th of April 2010 from 16:02:12 to 26th of April 2010 00:00:23. The special sequence contains the four steps with the injection of correlated odd noise required to compute the offset by the 4-points method in all receivers, except in the NIRs because the sequence does not work properly. The resulting sequence is detailed in Table 6.2.

PMS offset variation versus heater sequence				
Step	**Epochs**	**Correlated noise odd source**	**Attenuator**	**LICEF PMS**
1	1	WARM	L1	v_3^o
2	1	HOT	L1	v_4^o
3	1	WARM	L0	v_1^o
4	2	HOT	L0	v_2^o

Table 6.2 PMS offset special sequence steps.

For this reason, in the case of the NIRs the datasets used are *Short sequences* (with a longitude of eleven epochs) dated from the *24th of December 2009 0:00:25 to 25th of December 2009 15:56:40* and from the *20th of April 2010 06:00:25 to 21st of April 2009 22:00:03.*

6.3.2.1. Offset jumps and delay from PMS offset vs heater special sequence

For all *k*-receivers, the PMS offset delay has been estimated computing the correlation between the PMS offset and the signal heater [28][29] (using a method proposed by EADS-CASA Espacio):

$$c[\tau]_k = iFFT[FFT(v_{off_{PMS_k}}) \cdot FFT^*(heater)] \qquad \text{Eq. 6.3}$$

where $c[\tau]$ is the correlation, $FFT(v_{off_{PMS}})$ is the Fast Fourier Transform of the PMS offset, $FFT^*(heater)$ is the conjugate of the Fast Fourier Transform of the heater signal

associated with each LICEF in the central epoch of the sequence (for the offset special sequence is the third epoch (Table 6.2) and for the short sequence is the sixth epoch [13]) and *iFFT* corresponds to the inverse Fast Fourier Transform.

Using the correlation, the delay is the position [τ] of the first maximum in absolute value (because the PMS offset is negative). If the special sequence is used to compute the delay in epochs it is necessary to multiply the position by five (length of the special sequence in epochs). If short sequences are used the delay in epochs has been computed by multiplying the position by 0.56 minutes (the time between two short calibrations) and dividing by 0.02 minutes (the time of one epoch).

The delay for each receiver has been represented in Fig. 6.10 using the correction computed using the *dataset 09/02/2010* and the *dataset 25/04/2010*. For some receivers, the assigned delay is zero because the offset is not correlated with any heater signal.

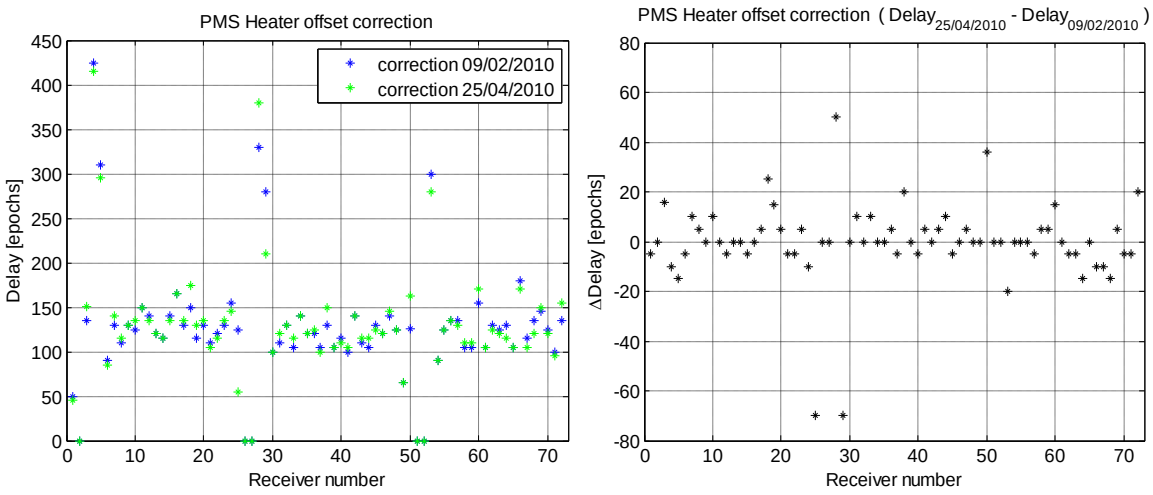

Fig. 6.10 Left: Delay in epochs with the correction values from 09-02-2010 (blue asterisks) and with the correction values from the 25-04-2010 (green asterisks). Right: Difference of the delay in epochs between both datasets.

To estimate the PMS offset jump for each *k*-receiver, the signal heater delayed is used and the offset jump is computed [28][29] as follows:

$$\Delta v_{off_{PMS_k}} = \overline{v_{off_{PMS_k}}}(heater_{delayed}^{ON}) - \overline{v_{off_{PMS_k}}}(heater_{delayed}^{OFF}) \qquad \textit{Eq. 6.4}$$

being $\Delta v_{off_{PMS}}$ the jump, $\overline{v_{off_{PMS_k}}}(heater_{delayed}^{ON})$ is the offset mean value of the calibrations when the heater delayed is on and $\overline{v_{off_{PMS_k}}}(heater_{delayed}^{OFF})$ corresponds to the offset mean value of the calibrations when the heater delayed is off. Note that the heater signal corresponds to the heater of the center epoch in the calibration sequence.

The jumps have been represented in Fig. 6.11. For those receivers which are not correlated with any heater signal, the PMS offset jump is set to zero.

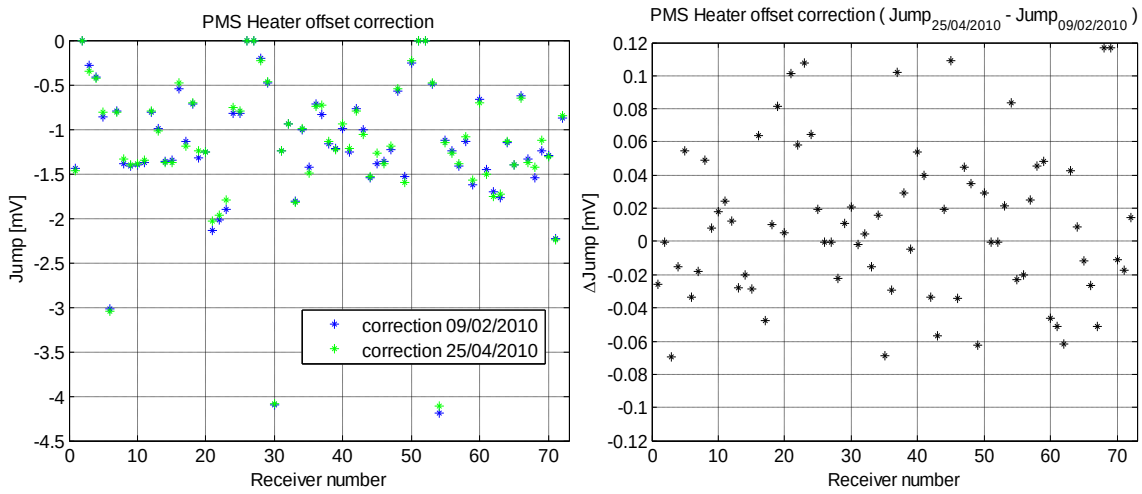

Fig. 6.11 Left: Jump in mV with the correction values from 09-02-2010 (blue asterisks) and with the correction values from the 25-04-2010 (green asterisks). Right: Difference of the jump in mV between both datasets.

To compare the application both PMS offset corrections, the rms error and the pk-to-pk error have been represented in Fig. 6.12 and in Fig. 6.13. In both plots, the standard deviation (left plots) with the correction values from the 09-02-2010 is very similar than the correction values from the 25-04-2010. The rms error decreases considerably when the heater offset correction is applied to the PMS offset special sequence and also for the long sequences, being in both cases around 1mV. The pk-to-pk error decreases a little in the long sequences and in the PMS offset special sequence increases.

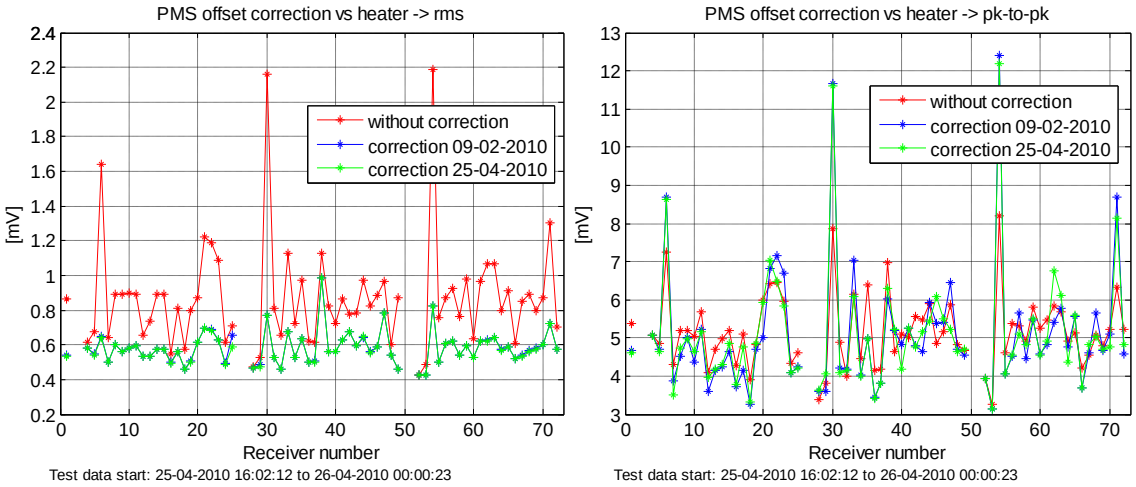

Fig. 6.12 PMS offset standard deviation (left) and pk-to-pk deviation (right) of the PMS offset special sequences without correction (red asterisks), with the correction values from 09-02-2010 (blue asterisks) and with the correction values from the 25-04-2010 (green asterisks).

When the Heater offset correction is applied there are two kinds of bad corrections:

- The offset jumps but correction is not applied yet: error = +Vjump
- The correction is applied but the jump has not occurred yet: error = -Vjump.

These effects are not appreciated in the long sequences because the time between calibrations is greater. However, since the performance of the instrument is based on its large capability for averaging errors (both in time and in direction), the plot to be considered is the one giving the rms error after the correction. This shows that the heater correction reduces rms error to the thermal noise level.

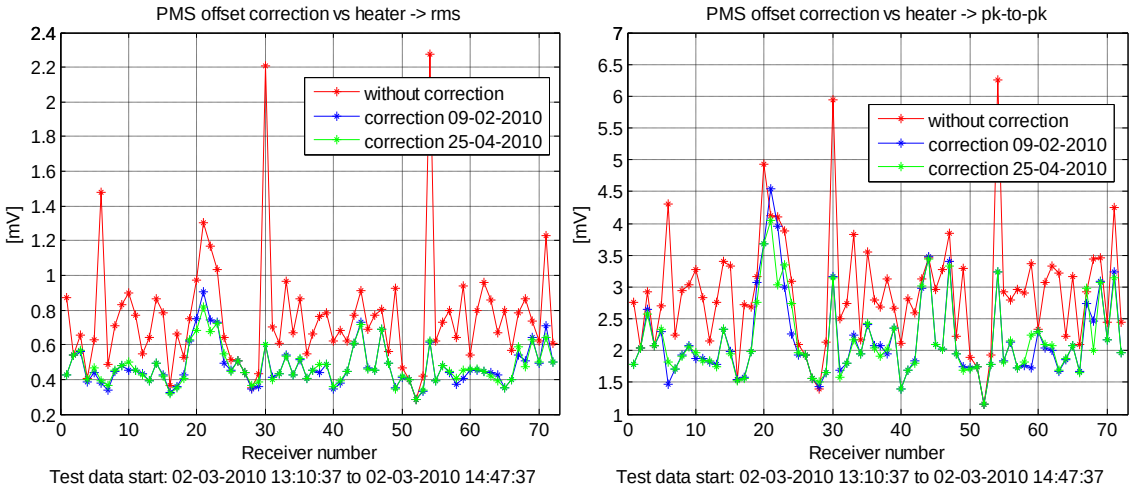

Fig. 6.13 PMS offset standard deviation (left) and pk-to-pk deviation (right) of the 45 long sequences without correction (red asterisks), with the correction values from 09-02-2010 (blue asterisks) and with the correction values from the 25-04-2010 (green asterisks).

In Fig. 6.14 two examples of PMS offset are shown: near 5000 offset special calibration sequences (top plots) and 45 long calibration sequences (bottom plots). The effects of the bad correction are not present in the long sequences due to the averaging of several epochs. However, in the special sequences it is present because it has only five epochs.

The application of this correction in the software to processing the datasets is done specifically at the PMS voltages level since the offset is computed from the PMS voltages and it is the same that apply the correction directly to the offset (v_{off_k}) :

$$v_{off_k} + \Delta v_{off_k} = \frac{(v_{2_k} + \Delta v_{off_k}) \cdot (v_{3_k} + \Delta v_{off_k}) - (v_{1_k} + \Delta v_{off_k}) \cdot (v_{4_k} + \Delta v_{off_k})}{(v_{2_k} + \Delta v_{off_k}) - (v_{4_k} + \Delta v_{off_k}) - (v_{1_k} + \Delta v_{off_k}) + (v_{3_k} + \Delta v_{off_k})} \qquad \textit{Eq. 6.5}$$

with v_{1_k} being the voltage for warm NS and no attenuator, v_{2_k} is the voltage for hot NS and no attenuator, v_{3_k} is the voltage for warm NS with attenuator, v_{4_k} is the voltage for hot NS with attenuator and Δv_{off_k} corresponds to the offset jump correction.

In conclusion, the heater correction is very stable in time. The differences between the two data sets in PMS offset rms error after the correction is negligible and rms deviation resulting after both corrections is in the level of thermal noise. The fact that pk-to-peak deviation increases in the special calibration sequences means that in punctual moments the error is large.

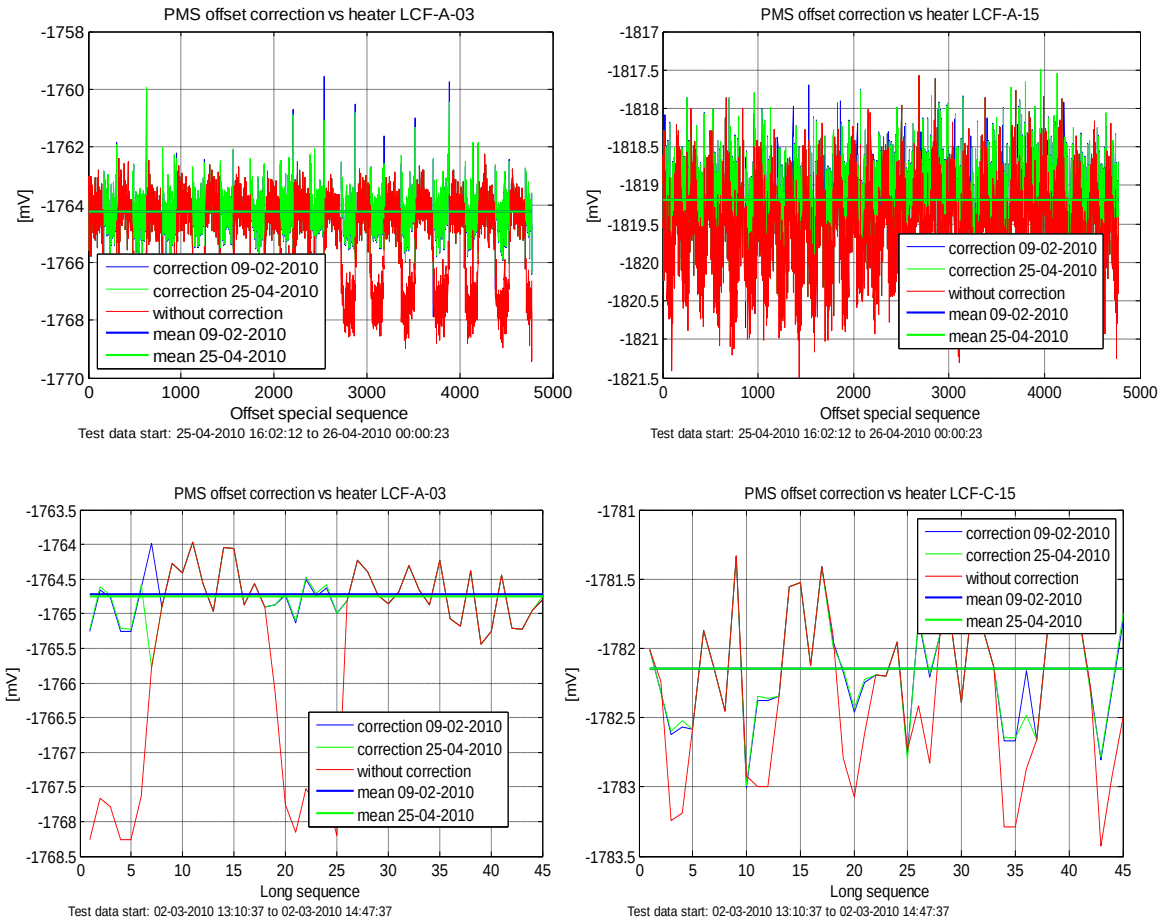

Fig. 6.14 PMS offset track along the special sequences (top) and 45 long sequences (bottom) for two receivers: LCF-A-03 that has a larger jump (left) and LCF-C-15 that has a lower jump (right).

6.3.2.2. Manual fine tuning adjustment

The dataset used to develop the manual fine tuning adjustment of the delay [30] is the PMS offset variation versus heater sequence dated from the *25th of April 2010 16:02:12 to 26th of April 2010 00:00:23*. The goal is the reduction of the pk-to-pk deviation to avoid high errors in the PMS offset in punctual moments because some epochs are affected by the heater delay misalignment.

The jump of the PMS offset has been calculated by averaging the values obtained in previous corrections in-flight (*Electrical Stability test 1* dated on *09-02-2010* and *Electrical Stability test 2* dated on *25-04-2010*).

The delay of the heater correction has been computed by an empirical method of trial and error from the values of the delay from previous estimations with the aim of reducing the pk-to-pk deviation in the offset. For the NIRs, the delay has been computed by averaging the value of the previous corrections because the data in the special sequence was corrupted.

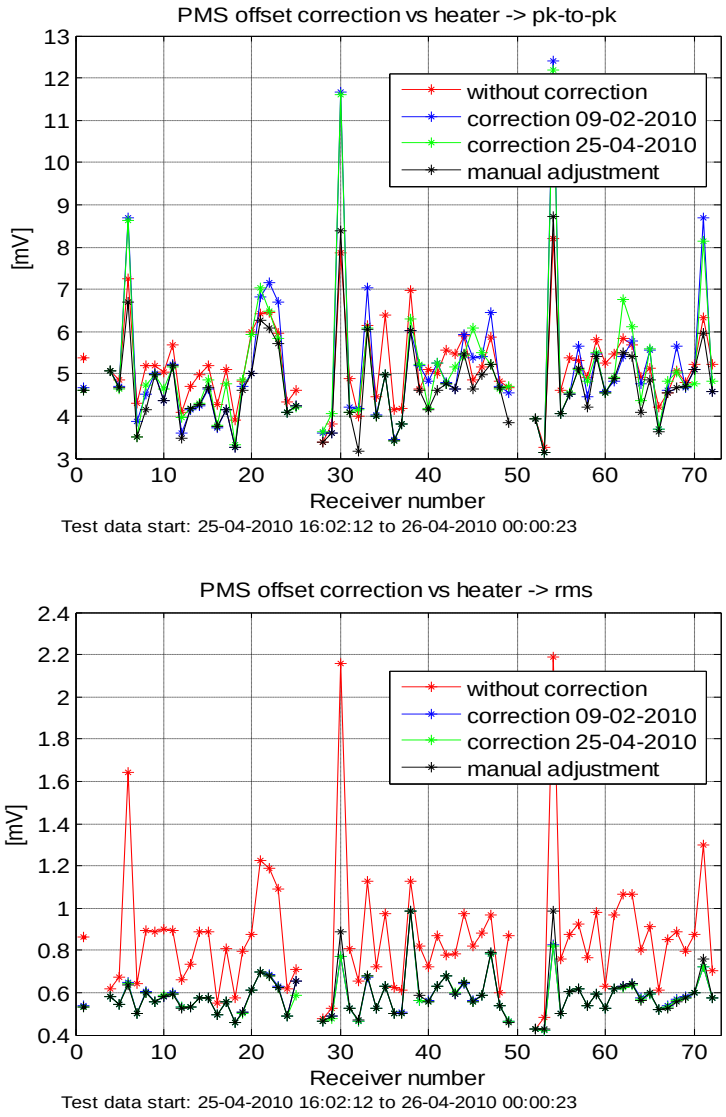

Fig. 6.15 Dataset offset special sequence dated in 25-04-2010. PMS offset standard deviation (bottom) and pk-to-pk deviation (top) without correction (red asterisks), with the correction values from 09-02-2010 (blue asterisks), with the correction values from the 25-04-2010 (green asterisks) and with the manual adjustment (black asterisks).

In Fig. 6.15 are presented PMS offset pk-to-pk and standard deviation. The top plot clearly shows that pk-to-pk deviation is lower with the manual adjustment for all receivers, except for the receivers LCF-B-03 and LCF-C-03. This good performance has not happened with the other corrections where most of receivers showed higher pk-to-pk deviation. It must be pointed out, that rms error (bottom plot) practically remains constant for all corrections. That is, the small delay misalignment affects a very reduced number of epochs in any case.

All the heater corrections have also been applied to the dataset PMS offset variation versus heater special sequence dated the *9th of February 2010 from 03:00:32 to 12:59:55* to check the behavior of the offset standard deviation and pk-to-pk deviation.

Fig. 6.16 shows that pk-to-pk deviation is also reduced in this case in many of the receivers. The standard deviation also remains constant.

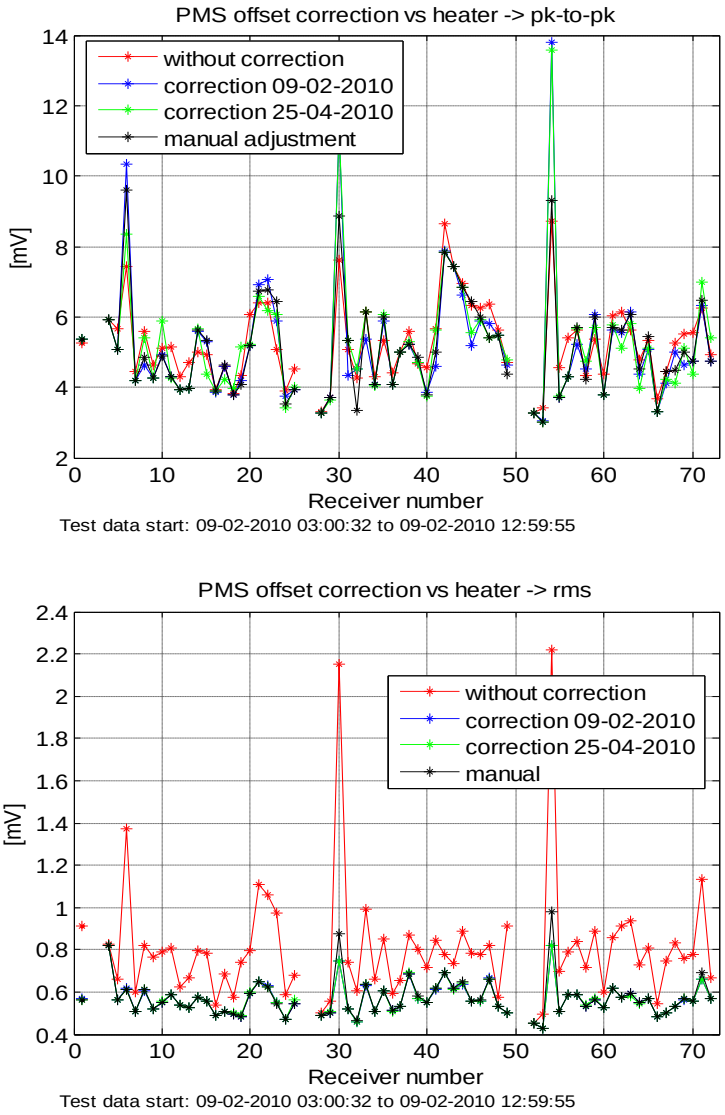

Fig. 6.16 Dataset offset special sequence dated in 09-02-2010.PMS offset standard deviation (bottom) and pk-to-pk deviation (top) without correction (red asterisks), with the correction values from 09-02-2010 (blue asterisks), with the correction values from the 25-04-2010 (green asterisks) and with the manual adjustment (black asterisks).

In conclusion, the objective of the pk-to-pk deviation reduction in the corrected PMS offset to minimize the number of epochs affected by delay misalignment is accomplished.

6.4. Conclusions of PMS offset track analysis

The definitive heater delay parameter has been tuned by means of a trial and error procedure. This yields a better performance of the corrected PMS offset since pk-to-pk error is very much reduced with relation to the previous values, thus minimizing the number of epochs affected by heater delay misalignment. In any case, rms error remains

practically constant in all cases, since the number of epochs affected by heater delay misalignment is low.

Currently, in the official SMOS Level 1 data processing, the PMS offset track is being performed using a combination of temperature correction (using only the alpha term of the second order sensitivity) and the heater correction (jumps and delays) computed by manual fine tuning adjustment. The definitive values are summarized in Appendix Table II (Appendix II: Heater offset correction values).

CHAPTER 7

7. PMS gain track

The main objective of this chapter is to analyze the PMS gain behavior with respect to the physical temperature, both on-ground and in-flight measurements, using different gain sensitivities to track the PMS gain.

In the end, an alternative PMS gain track is performed using the measures of the PMS voltages when the uncorrelated noise is injected.

7.1. Effects of the thermal noise in the PMS gain

The dataset used to study how the thermal noise affects PMS gain on-ground tests is the *PFM-TV* because the measurements have been acquired in the LSS and the environmental conditions (the thermal vacuum and the 22ºC temperature of stabilization) are similar to the space.

Fig. 7.1 presents the pk-to-pk and the standard deviation of the physical temperature (left plot) and of the PMS gain computed by *4-points calibration method* at C-plane (right plot) in the stabilized part of the test. Observing the standard deviation (red asterisks) the temperature value (left plot) is around 0.25ºC and the gain value (right plot) is around 0.25%. The conclusion is that there is very low gain sensitivity with relation to the physical temperature because the most of PMS holds the sensitivity near 1%/ºC. Also the pk-to-pk deviation (blue asterisks) shows that the mean value of the gain sensitivity is near the 1%/ºC because the pk-to-pk deviation of the gain is around 1.5% (right plot) and the pk-to-pk deviation in temperature is around 1.5ºC (left plot) too.

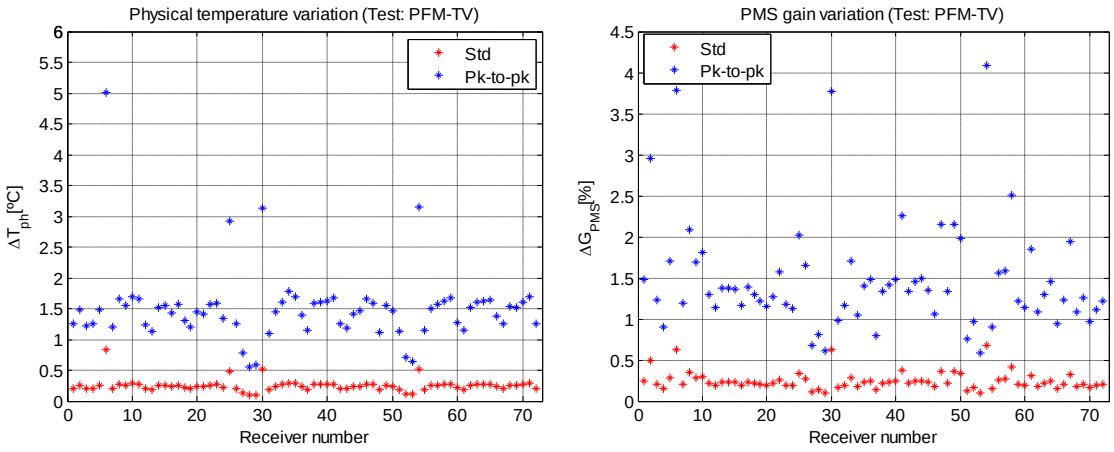

Fig. 7.1 Left: Physical temperature variation pk-to-pk and standard deviation. Right: PMS gain variation pk-to-pk and standard deviation in percent before temperature correction at C-plane.

The measured gain uncertainty due to thermal noise (finite PMS integration time), is computed at C-plane from the difference between consecutive gain calibrations as:

$$\sigma_{G_k^C} = \frac{1}{\sqrt{2}}\sigma_{\Delta G_k^C} \qquad \textit{Eq. 7.1}$$

being $\sigma_{G_k^C}$ the standard deviation for each k-receiver and $\sigma_{\Delta G_k^C}$ the standard deviation of the difference between two consecutive long calibrations. It is divided by $\sqrt{2}$ because two measures are taking into account.

The result is shown in Fig. 7.2, presenting an -ground thermal noise level of around 0.16%. This value is the minimum error that should present the gain estimation on-ground, without considering the physical temperature drift.

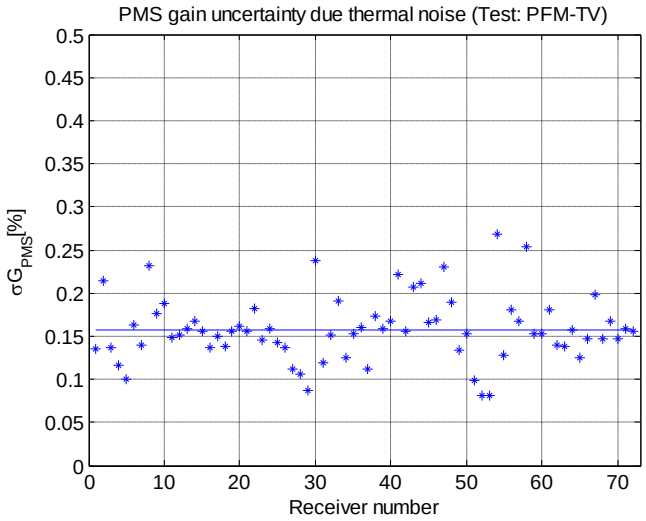

Fig. 7.2 PMS gain standard deviation due to thermal noise computed from the gain difference between two consecutive long calibrations.

To assess the effect of the thermal noise in-flight measurements, the measured gain uncertainty has been computed using Eq. 7.1 and the in-flight dataset starting the *24th December 2009 00:44:39 to the 25th of December 00:05:14* [31] .

Fig. 7.3 shows that the measured gain uncertainty due to the thermal noise in-flight around 0.25%, computed from the difference between two consecutive calibrations along 14 orbits. It is logical that the value is slightly above than the value on-ground. Note that a small increase along the arms is motivated by the distributed calibration.

In conclusion, the gain uncertainty due to the thermal noise is consistent (in a first guess) with PMS noise in the measured voltages in-flight (near 0.18%) because the standard deviation of the subtraction of the PMS voltages is around the 0.254% ($\sqrt{2}\cdot$ 0.18%).

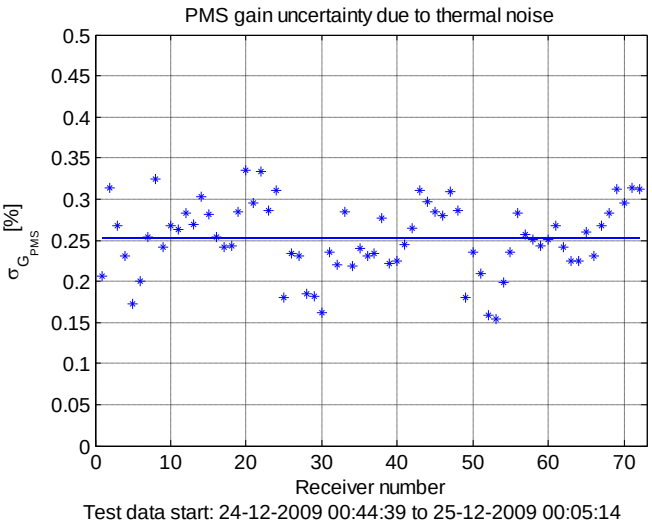

Fig. 7.3 PMS gain standard deviation due to thermal noise computed from the gain difference between two consecutive short calibrations.

7.2. PMS gain four-points versus gain one-point

To compare the PMS gain computed by *4-points calibration method* and the PMS gain computed by *1-point calibration method* it is necessary to obtain all the gain values in the same plane, since the gain computed by the first method is at CIP plane and in the second one is considered at the antenna plane.

If the C-plane is considered to represent all the gains, only a translation of the PMS $\text{gain}_{\text{1-point}}$ from the plane of antenna to the calibration plane is necessary, using the switch S-parameters (S_{LC_k}, S_{LH_k}, S_{LV_k}) and the antenna efficiency (η_{H_k}, η_{V_k}) as follows:

$$G_{1P_k}^{C} = G_{1P_k}^{H} \cdot \frac{\left|S_{LC_k}\right|^2}{\left|S_{LH_k}\right|^2 \cdot \eta_{H_k}} \qquad \textit{Eq. 7.2}$$

$$G_{1P_k}^{C} = G_{1P_k}^{V} \cdot \frac{\left|S_{LC_k}\right|^2}{\left|S_{LV_k}\right|^2 \cdot \eta_{V_k}} \qquad \textit{Eq. 7.3}$$

In Fig. 7.4 there are two examples of the PMS gain values computed using the stabilized part of the dataset *PFM-TV*. Note that the differences between the gain values computed by different methods compared at calibration plane are around than 5.5% (bottom left plot) or 5.75% (bottom right plot). Observing the gain variations (top plot), the oscillations are very similar; the differences are due to an upward shift.

These differences are shown for each receiver in Fig. 7.5 with a mean of 5.1%. The causes of this shift are the S-parameters in the CAS and the NIR calibration has been

done on-ground instead of with the deep sky views. To correct these differences, a detailed study has been done to develop the CAS correction [25].

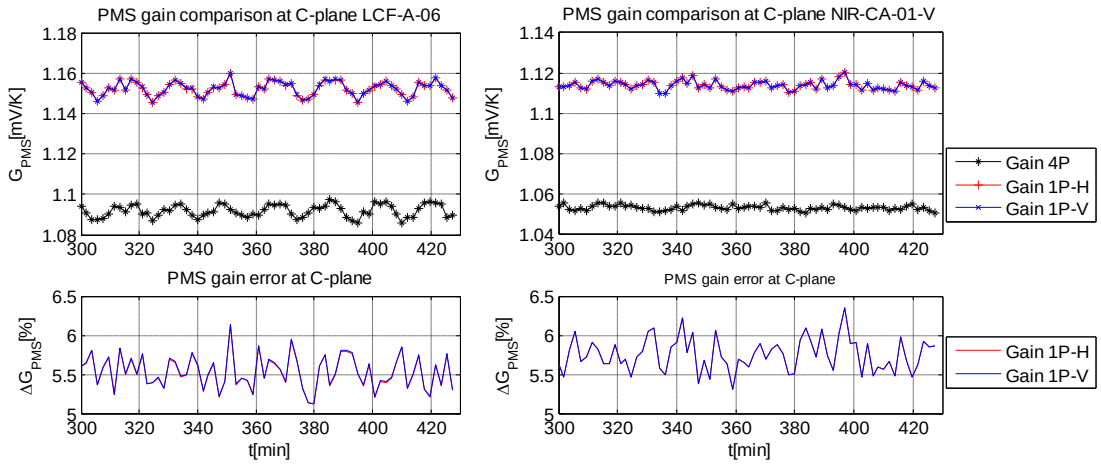

Fig. 7.4 Top: PMS gain comparison at calibration plane. Gain computed by the 4-points calibration method (black) and the gain computed by the 1-points calibration method (red horizontal and blue vertical). Bottom: One point gain error in percent respect to the gain computed by the 4-points calibration method. Left: LCF-A-06. Right: NIR-CA-01-V.

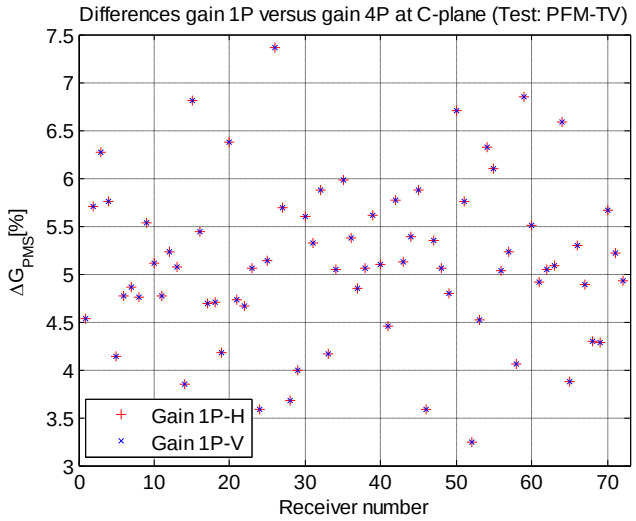

Fig. 7.5 PMS gain error between the gain computed by the 1-point calibration method and the gain computed by the 4-points calibration method.

From now the gain computed by the *4-points calibration method* will be used to track the PMS gain with temperature correction in all cases.

7.3. PMS gain track with temperature correction

The PMS gain has been tracking along the temperature variations using different sensitivity corrections computed in chapter 5, both on-ground and in-flight.

7.3.1. Temperature correction on-ground

The dataset *PFM-TV* is used to track the PMS gain on-ground, but only the stabilized part of the test because it simulates the thermal vacuum of the space conditions.

During the 2009, the sensitivity used to track the gain is computed using a second order polynomial (section 5.4.2) and estimated at the middle physical temperature (for more details see section 5.1.2).

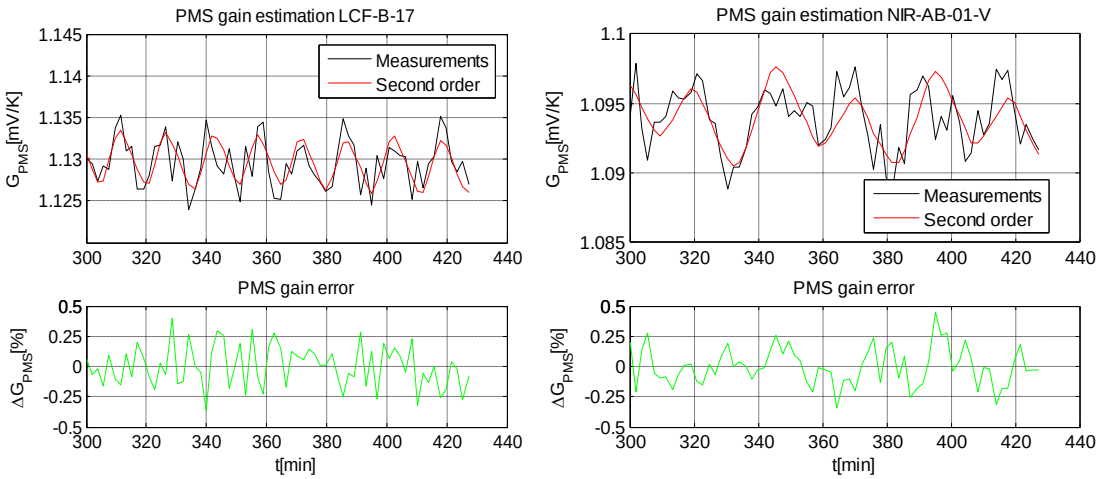

Fig. 7.6 Examples of the PMS gain track (top) and the PMS gain error (bottom) using the second order sensitivity. Left: LCF-B-17. Right: NIR-AB-01-V.

Two examples showing the stabilized part of the test, from the minute 300 from the start of the test to the end, are in Fig. 7.6. The second order sensitivity tracks very well the oscillations in the measurements (top plot) and the gain errors are below than the 0.5% (bottom plot).

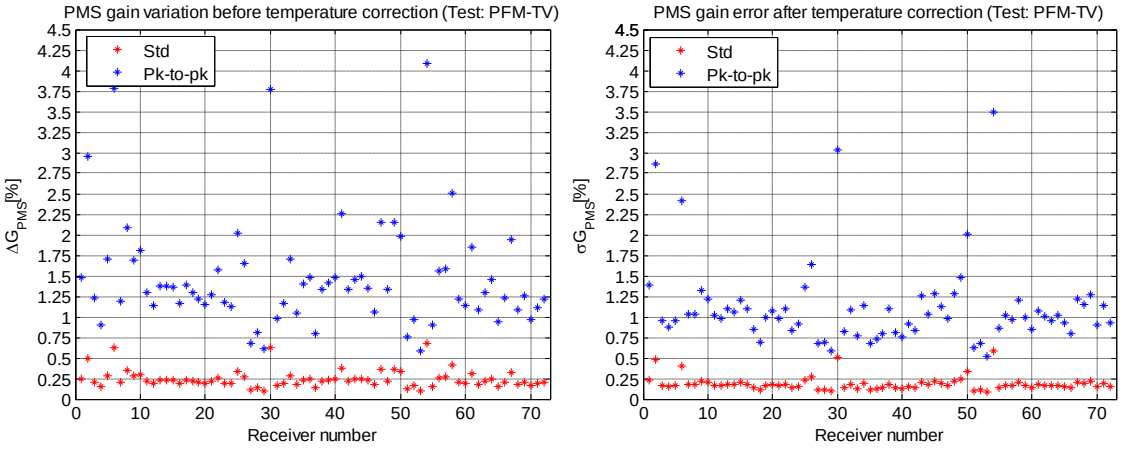

Fig. 7.7 PMS gain variation pk-to-pk and standard deviation in percent before temperature correction (left) and after temperature correction (right).

Fig. 7.7 shows the standard deviation and the pk-to-pk deviation before the temperature correction from the calibration measurements (left plot) and after the temperature

correction from the estimation with temperature track gain (right plot). Observing the right plot, the standard mean error is near 0.19% and the pk-to-pk mean error is around 1%. Note that the improvement respect to the left plot without temperature correction is not very large (from 0.25% in the standard deviation and from 1.5% in the pk-to-pk deviation) because the error is dominated by the thermal noise uncertainty (with a level of 0.16% on-ground as seen previously in Fig. 7.2).

Since the systematic PMS gain drift due to temperature is slightly larger than the PMS gain uncertainty due to thermal noise, the best approach for tracking the PMS gain in-flight is to compute a mean PMS gain for the whole set of orbits at their mean temperature. Then, PMS gain is tracked by using this mean PMS gain and the PMS gain sensitivity.

7.3.2. Temperature correction in-flight

The PMS gain tracking in-flight has been performed using different gain sensitivities. First of all, it is necessary to know the in orbit physical temperature drift.

Fig. 7.8 shows the standard and pk-to-pk temperature drift for the test starting the *24th December 2009 00:44:39 to the 25th of December 00:05:14*. The mean standard deviation of temperature drift in this test is 0.3ºC, the mean pk-to-pk of temperature drift is around 1.2ºC and the largest pk-to-pk variation is 3.3ºC. The temperature drift in orbit is similar to the temperature drift on-ground (Fig. 7.1 left).

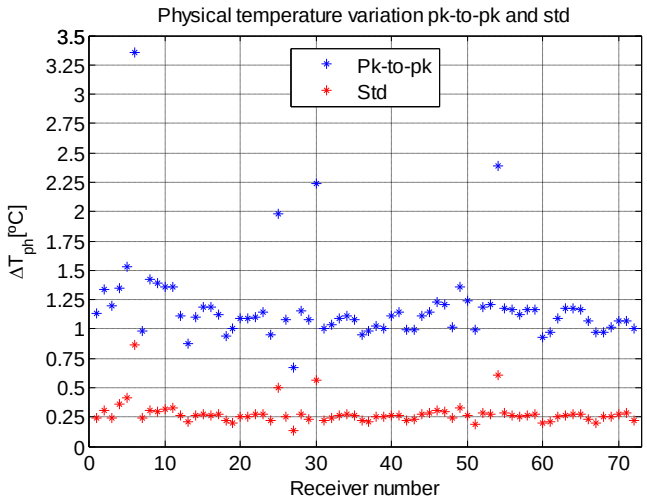

Fig. 7.8 Physical temperature variation pk-to-pk and standard deviation for the dataset 24th December 2009 00:44:39 to the 25th of December 00:05:14.

Although the thermal noise is slightly higher in orbit, the errors expected in the PMS gain after the temperature correction are within the order of magnitude than on-ground, i.e., slightly higher than the reference thermal noise in-flight.

7.3.2.1. Estimation with gain second order sensitivity

In 2010, the first in-flight PMS gain estimation has been computed using the dataset starting the *24th December 2009 00:44:39 to the 25th of December 00:05:14* that includes 14 orbits with only short calibration events [31].

For these dates, the computation of PMS gain sensitivity out of the flight data has not been concluded since a large set of calibration events is required due to the noise in the estimations and the low range of physical temperatures.

As the physical temperature drift in an orbit is small enough (between 1ºC and 3ºC) and close to 21ºC, the sensitivity used to track the gain is only the alpha term of the gain second order sensitivity computed on-ground (section 5.4.2).

Some examples are shown in Fig. 7.9 with a small set of drift periods to better observe the performance of the gain track. Note that both plots have a very good agreement between the temperature track estimations and the calibrations for each short calibration event. There is some degree of hysteresis in the behavior of PMS gain under fast and/or large temperature swings (LCF-A-03, LCF-B-03 and LCF-C-03), as it is shown in the right plot. In these cases, the gain when the temperature is increasing is different to the gain when the temperature is decreasing. However, the error is well below the requirement (1%).

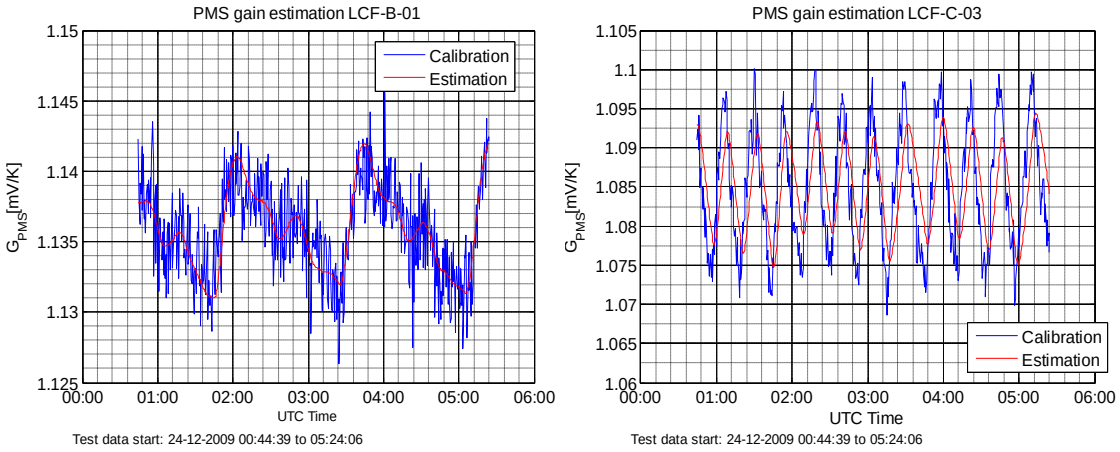

Fig. 7.9 PMS gain track from calibrations in-flight using only the alpha term of the gain second order sensitivity computed on-ground. Left: LCF-B-01. Right: LCF-C-03.

Fig. 7.10 shows the standard deviation and the pk-to-pk deviation in percent, before the temperature correction from the calibration measurements (left plot) and after the temperature correction from the estimation with temperature track gain (right plot). The statistics have been computed taking into account all the samples in the dataset. Observing in detail the right plot, the standard mean error is near 0.29% and the pk-to-pk mean error is around 2%. Note that the improvement respect the left plot without temperature correction is not very large (from 0.34% in the standard deviation and from 2.2% in the pk-to-pk deviation) as already happened on-ground. The reason is that in

orbit the thermal noise also is the most important uncertainty (with a level of 0.25% on-ground as seen previously in Fig. 7.3).

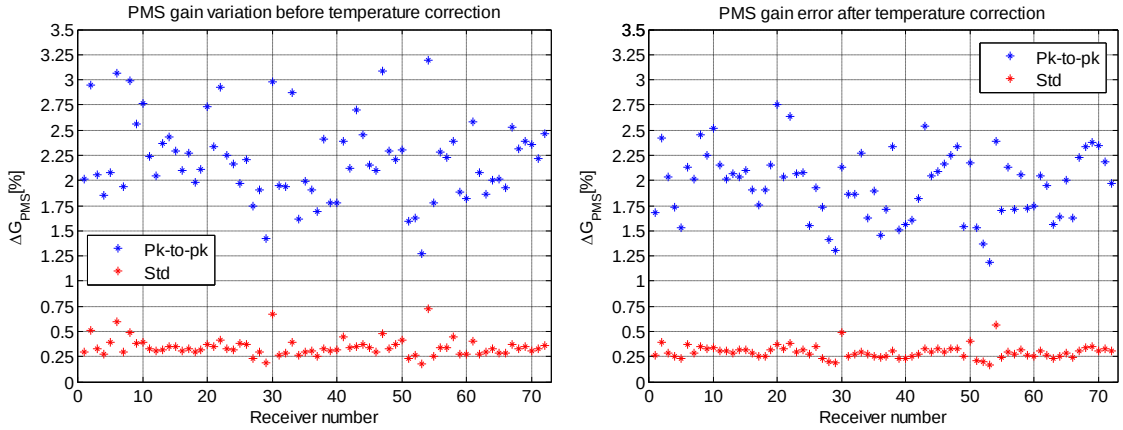

Fig. 7.10 PMS gain variation pk-to-pk and standard deviation in percent before temperature correction (left) and after temperature correction (right). Dataset: 24th December 2009 00:44:39 to the 25th of December 00:05:14.

7.3.2.2. Estimation with gain first order sensitivity

In June 2010, the PMS gain has been estimated in-flight using the dataset from *20th of April 2010 06:00:25 to 23rd April 2010 13:02:08* with two different sensitivities computed in-flight (*gain sensitivity from 25-12-2009* and *gain sensitivity from 23-04-2010*, for details see section 5.4.3). Moreover, the PMS gain track using only the alpha term of the gain second order sensitivity computed on-ground is presented in next graphics (section 5.4.2) [27].

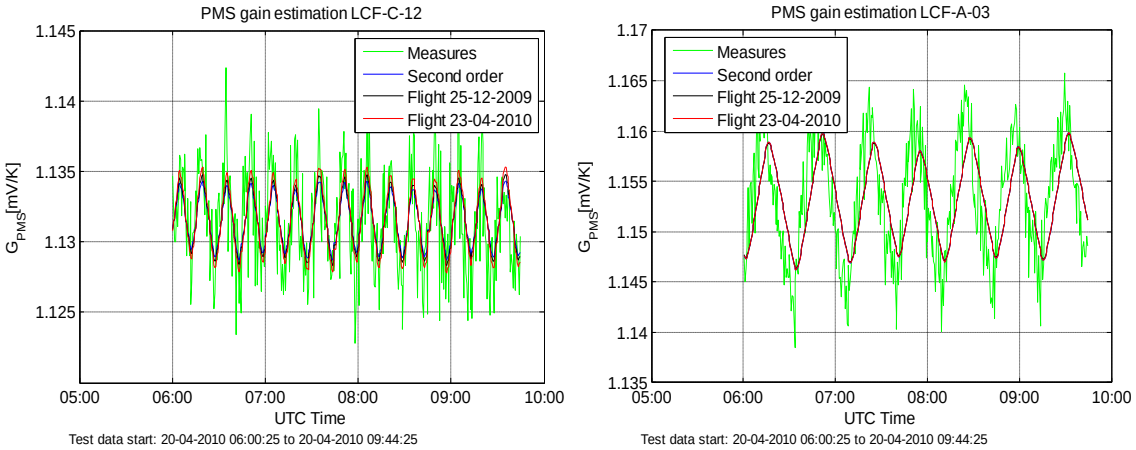

Fig. 7.11 PMS gain track from calibrations measures in-flight (green) using only the alpha term of the gain second order sensitivity computed on-ground (blue) and the sensitivity in flight from the 25-12-2009 (black) and 23-04-2010 (red) . Left: LCF-C-12. Right: LCF-A-03.

Two examples are represented in Fig. 7.11. The plots only represent a small set of drift periods to better show the performance of the gain track. As in the previous case, both plots have a very good agreement between the temperature track estimations and the

calibrations for each short calibration event. Also, there is some hysteresis in the LCF-A-03, LCF-B-03 and LCF-C-03), as it is shown in the right plot.

The mean square error in the estimations of the PMS gain has been represented in percent in Fig. 7.12. Clearly the plots show how the most of the LICEFs have an error about the same regardless of the sensitivity used and the mean around 0.27% is near the margins of thermal noise level (with a level of 0.25% on-ground as seen previously in Fig. 7.3).

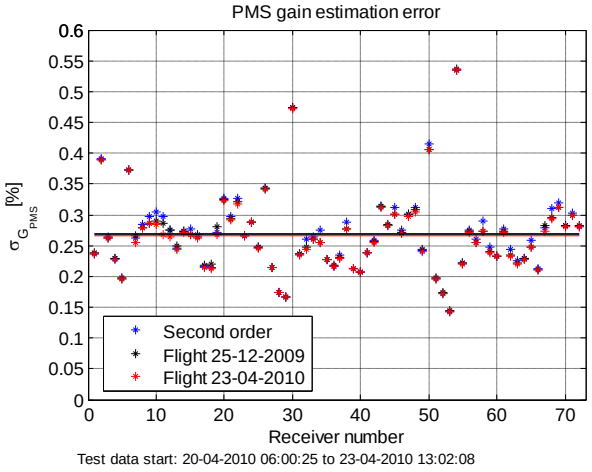

Fig. 7.12 Comparison of the PMS gain estimation error with the alpha term of the second order sensitivity computed on ground (blue asterisks) and with the sensitivity in-flight from 25-12-2009 (black asterisks) and 23-04-2010 (red asterisks).

7.3.2.3. Stability of PMS gain calibration in-flight

In order to assess the stability of the PMS gain calibrations in a long period (around one month), five sets of PMS calibration events (Table 7.1) have been taken into account [31]:

Day 1: 8th December 2009	*Number of calibrations:* N_{cal} = 46
Day 2: 22nd December 2009	*Number of calibrations:* N_{cal} = 8
Day 3: 23rd December 2009	*Number of calibrations:* N_{cal} = 47
Day 4: 24th December 2009	*Number of calibrations:* N_{cal} = 2499
Day 5: 7th January 2010	*Number of calibrations:* N_{cal} = 47

Table 7.1 Sets of PMS calibration events to assess the stability of the PMS gain.

For each of these PMS gain calibration sets, each gain has been translated to 21ºC and then the mean gain for each receiver in each data set has been computed. Fig. 7.13 (top) shows the gain of the different data sets and Fig. 7.13 (bottom) shows the fractional difference (in percent) of each gain for each LICEF, with relation to the mean gain of the five days. It is concluded that the PMS mean gain is stable within 1.2% pk-to-pk in a period of one month, and about 0.4% mean drift.

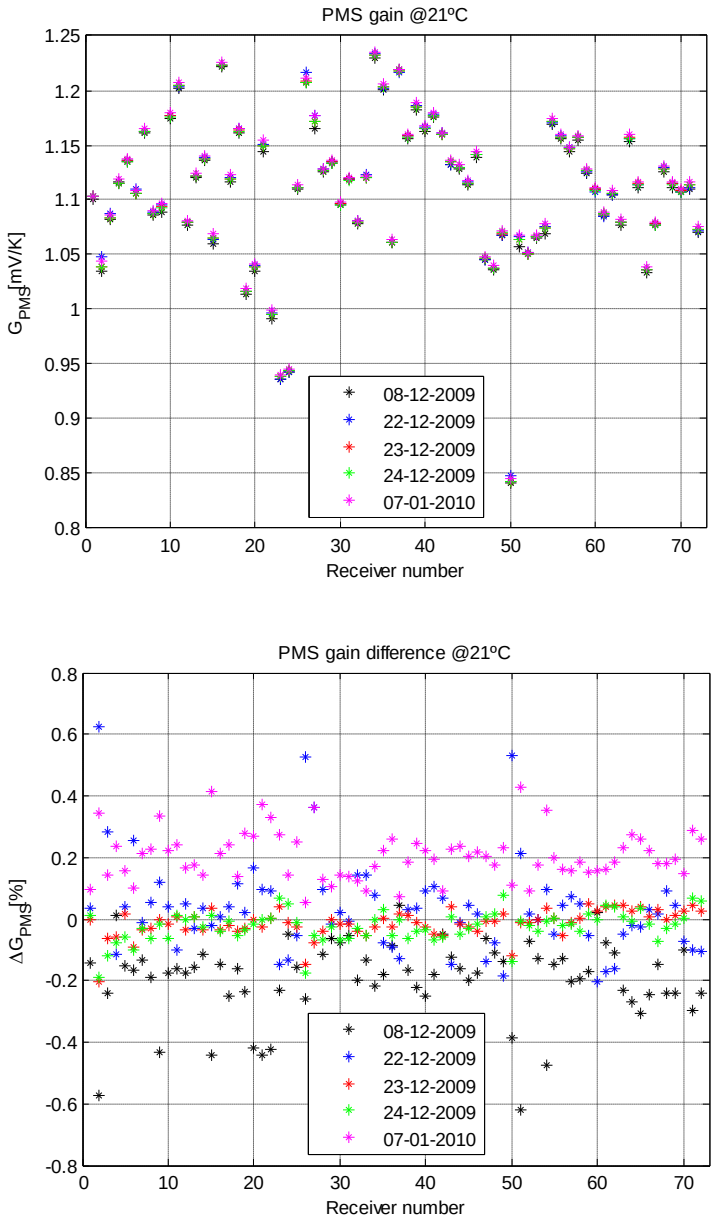

Fig. 7.13 Top: PMS gain of different test at 21ºC. Bottom: PMS gain difference at 21ºC with respect to the mean of the different test.

7.3.3. Conclusions of PMS gain track analysis with temperature correction

PMS gain presents a moderate orbital drift due to both, low PMS gain sensitivity to temperature and low pk-to-pk temperature swing. The absolute PMS gain excursion is slightly above (1-2%) the required PMS amplitude accuracy requirement (1%) thus requiring a moderate correction to fulfill SMOS system requirements.

The PMS mean gain remains fairly constant over one month (0.4% mean drift and 1.2% maximum drift). It must be taken into account that the sensor has been driven down to 18ºC and back to 22ºC. Additionally some sky views have also been undertaken.

Moreover, this small drift can also be caused by the calibration system and not the PMS units, since apparently affects to all LICEFs, to be further assessed.

According to the high stability of the mean PMS gain, and the moderate need for temperature correction (close to thermal noise) the best approach consists of computing the mean PMS gain, at the mean temperature to average thermal noise and apply the temperature correction over these means.

Only for some receivers (LCF-A-03, LCF-B-03 and LCF-C-03) the measurements of the gain have a peculiar behavior that produces a distribution showing memory effects (hysteresis) on the calibration measurement points. In these cases, the gain when the temperature is increasing is different to the gain when the temperature is decreasing. However, the error is well below the 1% requirement.

7.4. PMS gain track by periodic U-noise injection

This method has been devised as an alternative PMS gain estimation to be used in the case that periodic inter-orbit amplitude calibration was required. All the tests on-ground and in-flight revealed some degree of hysteresis in the behavior of PMS gain under fast and/or large temperature swings. This effect is more important in the receivers LCF-A-03, LCF-B-03 and LCF-C-03.

Since receiver noise temperature showed a better behavior, in-orbit internal calibration was foreseen by periodically switching the receiver to the internal matched load (*one point calibration method* with uncorrelated noise). In this case, for each k-receiver the PMS gain at the calibration physical temperature T_{phi_k} is given by (for more details see section 4.1.1.2):

$$G_k^A\left(T_{ph_{ik}}\right)=\frac{v_{U_k}-v_{off_k}\left(T_{ph_{ik}}\right)}{T_{R_k}^A\left(T_{ph_{ik}}\right)+T_{ph_{ik}}} \qquad \textit{Eq. 7.4}$$

Where v_{U_k} is the PMS voltage [V] when the U-noise is injected, $v_{off_k}\left(T_{ph_{ik}}\right)$ is the offset [V] from the internal calibration once the temperature correction has been applied, $T_{R_k}^A\left(T_{ph_{ik}}\right)$ corresponds to the receiver noise temperature [K] at the antenna plane after external calibration with the deep sky views, also corrected in temperature and $T_{ph_{ik}}$ is the physical temperature of the receiver [K].

In Fig. 7.14 there is an example at horizontal plane of the LCF-A-03, which is one of the outlier units presenting the largest temperature swing. The instrument was in calibration mode during a few orbits to assess the behavior in temperature of several calibration parameters. Observing the left plots, the black line gives PMS gain calibrations performed every 30 s. The blue line shows the estimation of PMS gain by means of temperature correction. The reference gain has been computed as the mean value for all the orbits, whereas the orbital drift is tracked by using the temperature

measurements from a thermistor placed at the front end in each unit and the 25-12-2009 gain sensitivity values. On the other hand, the red line represents spline interpolation from PMS gain estimations by 1-point calibration every 6.16 minutes (top plot), 8.96 minutes (middle plot) and 11.76 minutes (bottom plot).

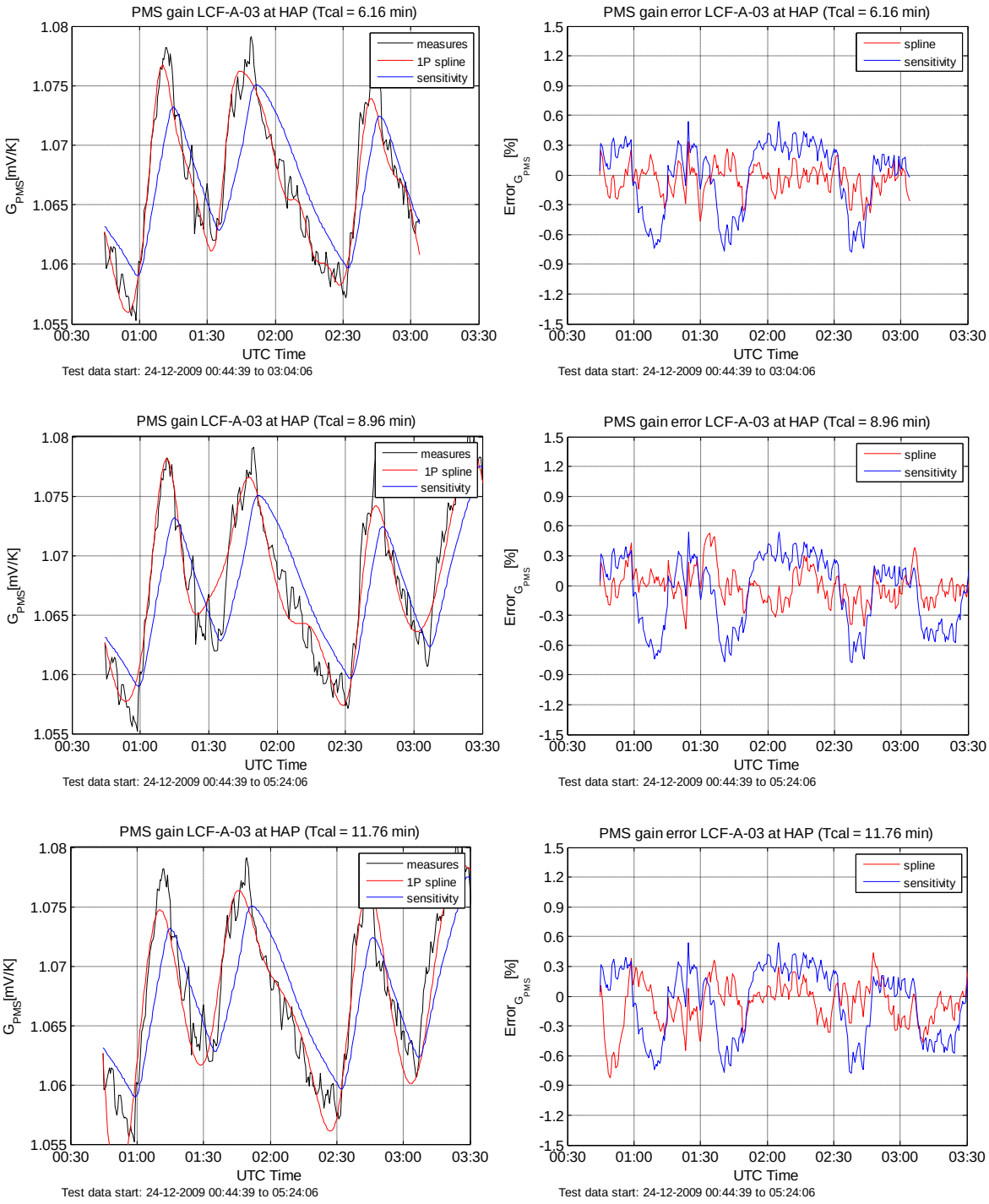

Fig. 7.14 Left: PMS gain measures from calibration (black), gain estimations using one-point and spline interpolation (red) every 6.16 minutes (top), 8.96 minutes (middle) and 11.76 minutes (bottom) and gain estimation using the temperature correction (blue). Right: Errors in percent of the PMS gain estimations.

The effect of a certain amount of hysteresis is clearly seen in the comparison of the two plots (black and blue lines). Note in the right plots that the error performed by spline interpolation in 1P is lower than the error performed with sensitivity correction in the top plot, while in middle plot and bottom plot the error increases to consider similar between the two estimations.

Considering only the spline interpolation from 1P calibration PMS gain estimations every 6.16 minutes, the rms error for all receivers is shown in Fig. 7.15. The study is done for the three methods analyzed from flight data during an entire day of the first months of the commissioning phase:

a) PMS gain constant as the mean value computed from several orbits in calibration mode (black stars). In this case, the error is caused by orbital temperature swing.

b) PMS gain estimation using the last calibration (more than one orbit apart) and temperature swing compensation by means of the PMS sensitivity to temperature (blue stars).

c) Inter-orbit PMS estimation by means of periodic (around 6 min) measurements of the matched load (U-noise injection) (red stars).

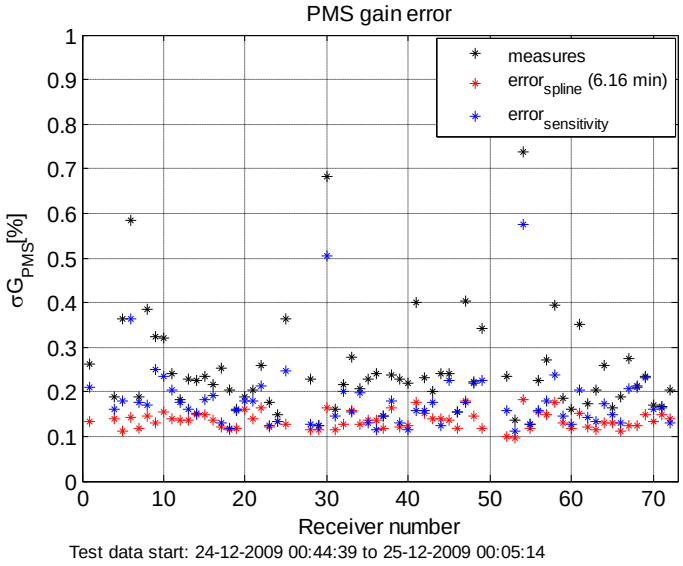

Fig. 7.15 PMS error comparison between the three methods analyzed (calibration, spline interpolation from 1P calibration and temperature correction).

7.4.1. Conclusions of PMS gain track analysis by periodic U-noise injection

Although method c) is the most accurate, method b) has been selected. **PMS gain estimation using the last calibration (more than one orbit apart) and temperature swing compensation by means of the PMS sensitivity to temperature gives an error well below 1% rms system gain error requirement and minimizes the loss of snap shots (maximum observation mode configuration).**

CHAPTER 8

8. Local Oscillator phase track

The Local Oscillator (LO) phase is a calibration parameter that has a very important impact in the visibility phases and therefore in the imaging reconstruction because the visibility phase in a baseline contains the image phase and the LO phases contribution of the involved receivers in the baseline. So, the main objective of this chapter is to analyze several strategies to track the LO phases, first using the temperature correction and next testing different methods based on interpolation.

8.1. LO phase track with temperature correction

The LO phase track analysis with temperature correction has been performed using both datasets on-ground and in-flight.

8.1.1. Temperature correction on-ground

A preliminary study of the correlation phase drift had been carried out in February 2009 using the LSS measurements. From this analysis some interesting conclusions about the LO phase tracking with temperature correction can be pointed out [32]:

- The correlation phase drift can be analyzed in a receiver basis (in separable phases), but phase unwrap and memory track is required to retrieve a smooth and continuous phase drift assigned to each receiver (as shown in section 4.2.1.1). It is confirmed that the phase drift is given in a CMN basis (LO phase drift) because the differences in individual receivers drift within a segment can be considered almost negligible.

- An estimation on the LO phase sensitivity to physical temperature can be retrieved from receiver phase drift grouped by segments. However, since the physical temperature readings are not sufficient accurate (not close enough to the LO), phase tracking errors are slightly above the required accuracy (1 degree) for some segments, mainly in the hub.

8.1.2. Temperature correction in-flight

Although visibility phase sensitivity to physical temperature is not good enough to predict with the required accuracy the evolution of the LO phase drift, it provides a first rough estimation of the in-orbit expected behavior. This analysis will give a first guess on the in-flight LO phase track strategy.

To track the baseline phase segments using the physical temperature sensitivity phase it is only necessary to take the measurements of the power divider physical temperatures (in case of segments located in the hub, the physical temperature of the last receiver in the segment) [33][34]. The phase sensitivity used is shown in Table 8.1**Error! Reference source not found.**. It was computed on ground using the LSS measurements [32].

Power divider segment	Phase sensitivity [deg/°C]
PD_H1	2.1701
PD_A1	5.9616
PD_A2	4.7143
PD_A3	2.0366
PD_H2	-1.7932
PD_B1	1.2629
PD_B2	5.7031
PD_B3	1.7106
PD_H3	1.7983
PD_C1	0.7021
PD_C2	2.0104
PD_C3	2.2568

Table 8.1 Retrieved sensitivity using all segments measured G_{kj} phases for those sets of baselines which have a common noise source.

Therefore, the 12-equations system to predict the phase is:

$$\begin{pmatrix} \alpha_{A1,H1} \\ \alpha_{H2,H1} \\ \alpha_{H3,H1} \\ \alpha_{A2,A1} \\ \alpha_{A3,A2} \\ \alpha_{B1,H2} \\ \alpha_{H3,H2} \\ \alpha_{B2,B1} \\ \alpha_{B3,B2} \\ \alpha_{C1,H3} \\ \alpha_{C2,C1} \\ \alpha_{C3,C2} \end{pmatrix} = \begin{pmatrix} \Delta T_{H1} & -\Delta T_{A1} & 0 & 0 & 0 & 0 & 0 & 0 & 0 & 0 & 0 & 0 \\ \Delta T_{H1} & 0 & 0 & 0 & -\Delta T_{H2} & 0 & 0 & 0 & 0 & 0 & 0 & 0 \\ \Delta T_{H1} & 0 & 0 & 0 & 0 & 0 & 0 & 0 & -\Delta T_{H3} & 0 & 0 & 0 \\ 0 & \Delta T_{A1} & -\Delta T_{A2} & 0 & 0 & 0 & 0 & 0 & 0 & 0 & 0 & 0 \\ 0 & 0 & \Delta T_{A2} & -\Delta T_{A3} & 0 & 0 & 0 & 0 & 0 & 0 & 0 & 0 \\ 0 & 0 & 0 & 0 & \Delta T_{H2} & -\Delta T_{B1} & 0 & 0 & 0 & 0 & 0 & 0 \\ 0 & 0 & 0 & 0 & \Delta T_{H2} & 0 & 0 & 0 & -\Delta T_{H3} & 0 & 0 & 0 \\ 0 & 0 & 0 & 0 & 0 & \Delta T_{B1} & -\Delta T_{B2} & 0 & 0 & 0 & 0 & 0 \\ 0 & 0 & 0 & 0 & 0 & 0 & \Delta T_{B2} & -\Delta T_{B3} & 0 & 0 & 0 & 0 \\ 0 & 0 & 0 & 0 & 0 & 0 & 0 & 0 & T_{H3} & -\Delta T_{C1} & 0 & 0 \\ 0 & 0 & 0 & 0 & 0 & 0 & 0 & 0 & 0 & \Delta T_{C1} & -\Delta T_{C2} & 0 \\ 0 & 0 & 0 & 0 & 0 & 0 & 0 & 0 & 0 & 0 & \Delta T_{C2} & -\Delta T_{C3} \end{pmatrix} \cdot \begin{pmatrix} S_{T_{PH}}^{\alpha_{H1}} \\ S_{T_{PH}}^{\alpha_{A1}} \\ S_{T_{PH}}^{\alpha_{A2}} \\ S_{T_{PH}}^{\alpha_{A3}} \\ S_{T_{PH}}^{\alpha_{H2}} \\ S_{T_{PH}}^{\alpha_{B1}} \\ S_{T_{PH}}^{\alpha_{B2}} \\ S_{T_{PH}}^{\alpha_{B3}} \\ S_{T_{PH}}^{\alpha_{H3}} \\ S_{T_{PH}}^{\alpha_{C1}} \\ S_{T_{PH}}^{\alpha_{C2}} \\ S_{T_{PH}}^{\alpha_{C3}} \end{pmatrix} \quad \textit{Eq. 8.1}$$

where $\alpha_{XN,YN}$ is the predicted baseline phase between the segment *XN* and the segment *YN* (being *XN* or *YN* the corresponding segments H1, H2, H3, A1, A2, A3, B1, B2, B3, C1, C2, C3), ΔT_{YN} and ΔT_{XN} are the physical temperatures, $S_{T_{PH}}^{\alpha_{XN}}$ and $S_{T_{PH}}^{\alpha_{YN}}$ are the sensitivities referred explicitly to the corresponding power divider, except for the hub. In case of segment H1 the physical temperature of the receiver LCF-A-03 is used, for the segment H2 is the receiver LCF-B-03 and for the segment H3 is the receiver LCF-C-03. Temperatures and phases are incremental from the first measurement.

In order to reduce the number of measurements, an averaging of every 8 samples has been applied before the resolution of the system of equations described in Eq. 8.1. So, SMOS satellite takes 100 minutes to make one orbit around the Earth and the temperature measurements are taken every 0.02 minutes. Therefore, 5000 measurements are available in one orbit and 625 after averaging, more than enough measurement to predict the phase drift.

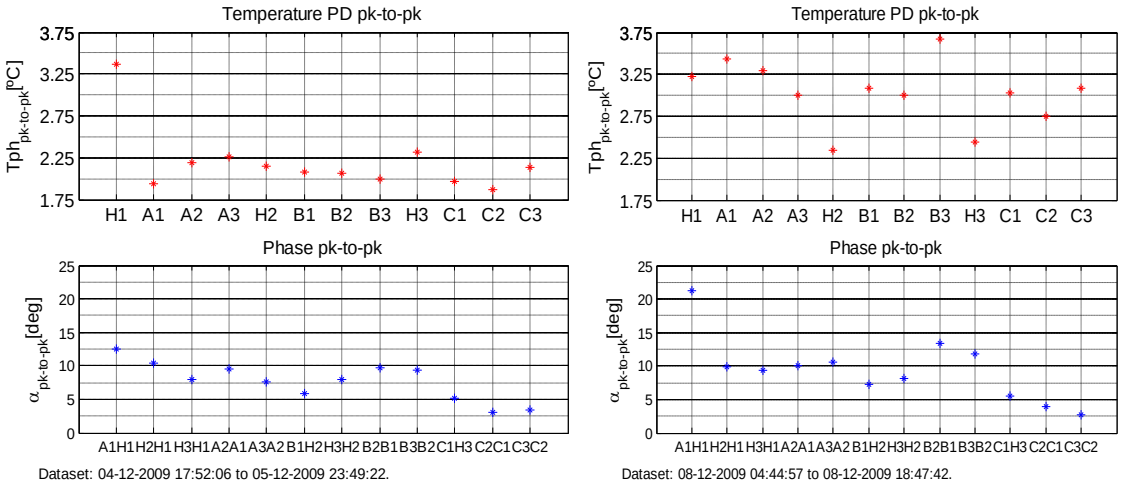

Fig. 8.1 PD physical temperature pk-to-pk deviation (top) and phase pk-to-pk deviation (bottom). Left: dataset from 4th to 5th December 2009. Right: dataset from 8th December 2009.

Fig. 8.1 presents some statistic results using the *dataset from 4th December 2009 17:52:06 to 5th December 2009 23:49:22* (left) and the *dataset from 8th December 2009 04:44:57 to 18:47:42* (right). The temperature drift is lower and the phase drift is grouped in segments.

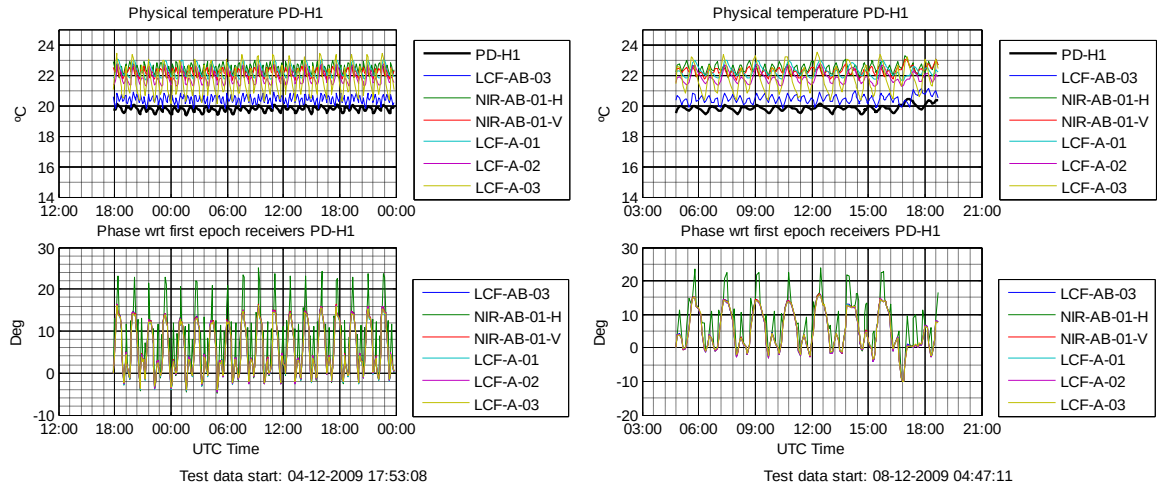

Fig. 8.2 Top: Physical temperature of segment H1 and PD-H1. Bottom: Incremental phase drift from first calibration for all receivers in the segment H1 (reference receiver: LCF-C-06, segment C1). Left: dataset from 4th December 2009. Right: dataset from 8th December 2009.

The physical temperatures of the six receivers of the CMN (solid line) and the physical temperature of the corresponding power divider (black line) are shown in Fig. 8.2 (top) for the segment H1 and in Fig. 8.3 (top) for the segment C3. The phase drift is represented for different receivers included in the same segments in Fig. 8.2 (bottom) and Fig. 8.3 (bottom), respectively.

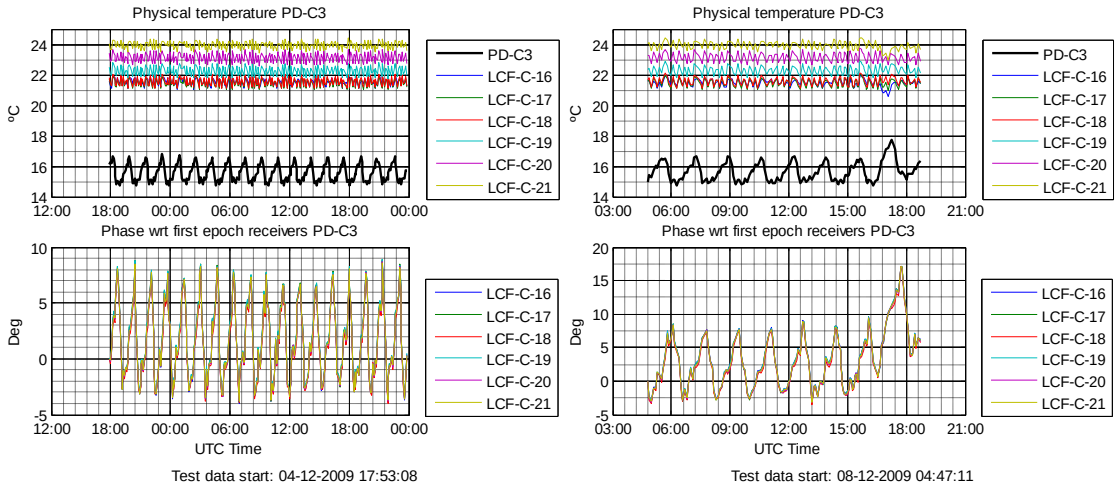

Fig. 8.3 Top: Physical temperature of segment C3 and PD-C3. Bottom: Incremental phase drift from first calibration for all receivers in the segment H1 (reference receiver: LCF-C-06, segment C1). Left: dataset from 4th December 2009. Right: dataset from 8th December 2009.

The phase drift of each receiver respect to the mean value of all receiver phases in the CMN are plotted in Fig. 8.4 and Fig. 8.5.

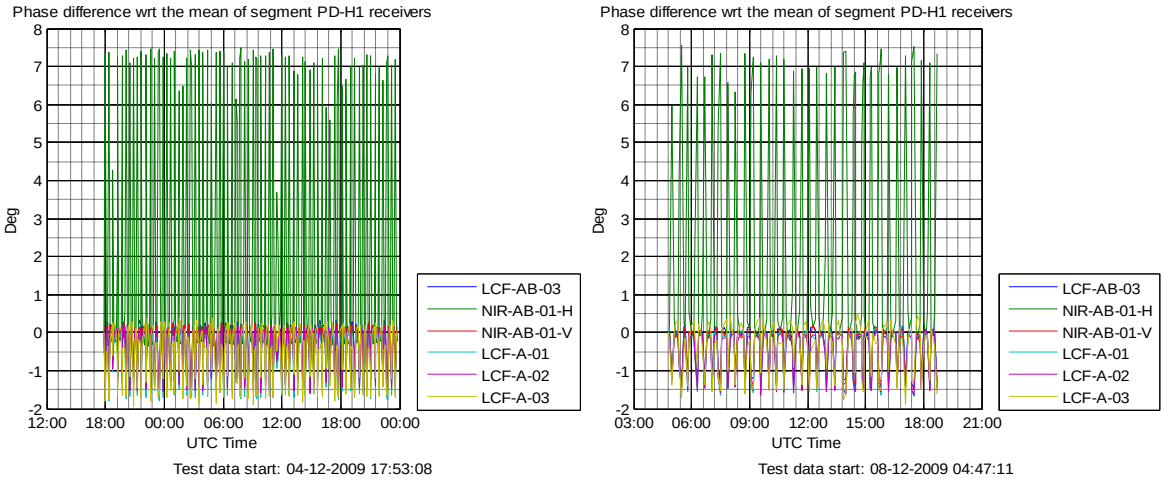

Fig. 8.4 Phase difference with respect to the mean value of segment H1receivers. Left: dataset from 4th December 2009. Right: dataset from 8th December 2009.

From the result shown in Fig. 8.4, it must be pointed out the oscillations NIR-AB-01-H, in segment H1. The rest of segments have a very good behavior because the phase differences with respect to the mean value in the segment are in all cases below 0.6 degrees as shown in Fig. 8.5.

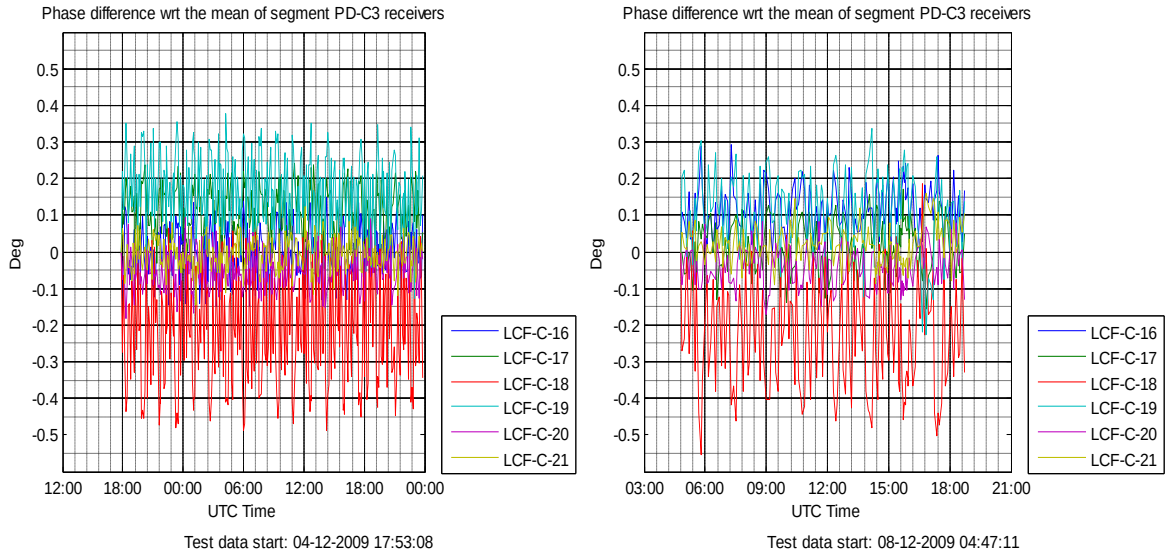

Fig. 8.5 Phase difference with respect to the mean value of segment C3 receivers. Left: dataset from 4th December 2009. Right: dataset from 8th December 2009.

In conclusion, the instrument presents robust and well behaved phase at CIP plane:

- **Phase drift per segments (CMNs) related to LO temperature drift.**
- **Very low, but no negligible phase drift in temperature at LICEF level.**
- **LICEF phase drift grouped in segments (12 CMNs) gives a simple way to monitor LO phase behavior and drift: drift, jumps, unlocks, etc.**

The LO phase track with temperature correction has been dismissed as a strategy for track the LO phase and only has been used to predict the phases during the measurements after the launch of the satellite.

8.2. LO phase track based on interpolation

This part of the work consists of assessing the G_{kj} phase to determine how long is possible to accurately track the correlation phase without the need for frequent instrument calibration. The required accuracy is 1 degree in the standard deviation of the error. Different methods are tested and compared in order to find out the best phase tracking method based on interpolation.

8.2.1. Interpolation on-ground

The data used for the LO phase track analysis on-ground take into account the dataset *PFM-TV* and dataset *COLD* [35].

The physical temperature variation can be observed in Fig. 8.6 (left plot). The pk-to-pk deviation of the physical temperature is slightly higher for some receivers in the test *COLD*, but for the rest of receivers is similar in both tests, although the stabilized temperature is different for each one (the stabilized temperature for the test *COLD* is

10ºC whereas that in the test *PFM-TV* the stabilized temperature is 22ºC). In relation to the right plot, it can clearly be seen that the test *COLD* has a higher standard deviation of the correlation phase than the *PFM-TV* test.

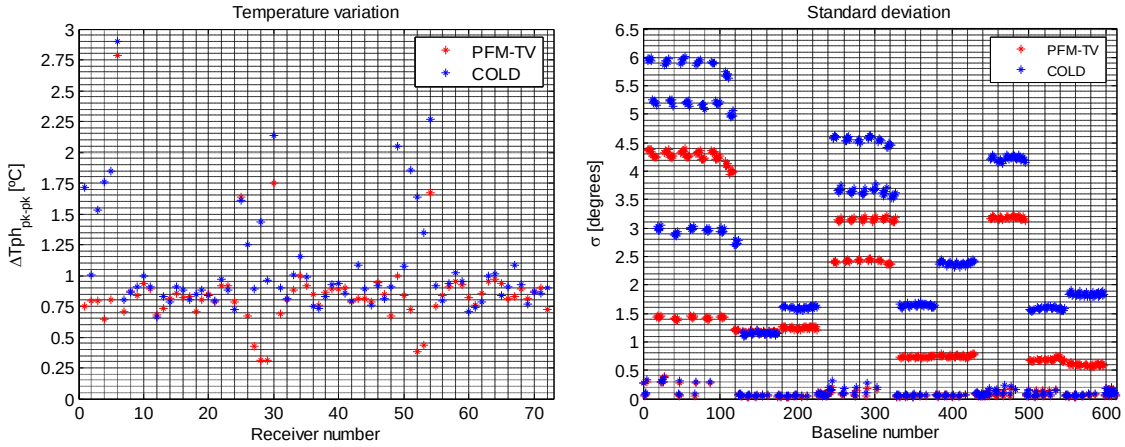

Fig. 8.6 Left: Comparative of the temperature variation for both tests in the stabilized part. Right: Correlation phase standard deviation for both tests in the stabilized part.

The analyzed methods to be used in the correlation phase interpolation are: Linear, Spline and Fourier interpolation.

8.2.1.1. Linear interpolation

In this method, the baseline phases can be estimated taking one of every *n* samples (*n=2, 3, 4, 5)* from the measurements, which are separated one calibration time (t_{cal}) and the rest of values are computed by linear interpolation:

$$\alpha_{kj_{linear}}[t] = \alpha_{kj}[t] \qquad If\ t = t_0 + m^* n^* t_{cal} \qquad where\ m=0, 1, 2, 3\ldots \qquad Eq.\ 8.2$$

$$\alpha_{kj_{linear}}[t] = \alpha_{kj}[t_0 + m\cdot n\cdot t_{cal}] + \left(\frac{t-(t_0+m\cdot n\cdot t_{cal})}{(t_0+(m+1)\cdot n\cdot t_{cal})-(t_0+m\cdot n\cdot t_{cal})}\right)\cdot\left(\alpha_{kj}[t_0+(m+1)\cdot n\cdot t_{cal}]-\alpha_{kj}[t_0+m\cdot n\cdot t_{cal}]\right)$$

where t_0 is the time of the initial calibration, t is the time at the calibration instant and t_{cal} is the time between calibrations.

Moreover, the separable phases can be estimated in the same way as before taking one of every *n* samples *(n=2, 3, 4, 5)* from the measurements and the rest of values are computed by linear interpolation. For $\alpha_{k_{linear}}$:

$$\alpha_{k_{linear}}[t] = \alpha_{k}[t] \qquad If\ t = t_0 + m^* n^* t_{cal} \qquad where\ m=0, 1, 2, 3\ldots \qquad Eq.\ 8.3$$

$$\alpha_{k_{linear}}[t] = \alpha_{k}[t_0 + m\cdot n\cdot t_{cal}] + \left(\frac{t-(t_0+m\cdot n\cdot t_{cal})}{(t_0+(m+1)\cdot n\cdot t_{cal})-(t_0+m\cdot n\cdot t_{cal})}\right)\cdot\left(\alpha_{k}[t_0+(m+1)\cdot n\cdot t_{cal}]-\alpha_{k}[t_0+m\cdot n\cdot t_{cal}]\right)$$

where t_0 is the time of the initial calibration, t is the time at the calibration instant and t_{cal} is the time between calibrations. $\alpha_{j_{linear}}$ is computed similarly.

Another possible estimation of the baseline phases can be performed from the interpolated linearly separable phases in this way:

$$\hat{\alpha}_{kj_{linear}}[t] \approx \alpha_{j_{linear}}[t] - \alpha_{k_{linear}}[t] \qquad \textit{Eq. 8.4}$$

where $\alpha_{k_{linear}}$ and $a_{j_{linear}}$ are the linearly interpolated separable phases and t is the time at the calibration instant.

As shown in Fig. 8.7, the rms error has been represented for all the baselines that have common noise source (612 baselines) for two on-ground datasets, in the stabilized part of each test. It is clear that when *n* increases, the rms error increases for the two estimations and the two datasets. The legend shows the mean rms value for interpolated baseline phases (top) and the mean rms value for the estimation from the linearly interpolated separable phases (bottom). It can be observed that in the case of *n=5*, i.e. making a calibration every 9.5 minutes (because the time between calibrations, t_{cal}, is 1.9 minutes), the maximum rms error is 1.2 degrees at baseline level. At receiver level this error is divided by $\sqrt{2}$ (error below 1 degree) satisfying the required accuracy.

In Fig. 8.8, the maximum error has been represented for all baselines for both datasets. The maximum error increases when *n* increases. This error is greater when it has been used the estimation of the baseline phases from the linear interpolation of the separate phases instead of the estimation directly from the linear interpolation of the baseline phases. The legend shows the mean maximum error for interpolated baseline phases (top) and the mean maximum error for the estimation from the linearly interpolated separable phases (bottom). The maximum error in a given baseline for *n=5* is in the order of 3 degrees, that implies a maximum error at receiver around 2.12 degrees.

However, if the mean error is represented, it can be clearly seen how the error of the estimation from the linear interpolation of the baseline phases increases with *n* while the error of the estimation from the linear interpolation of the separable phases remains almost constant, as shown in Fig. 8.9.

From the results presented in Fig. 8.7, Fig. 8.8 and Fig. 8.9, the conclusion is that the estimation from the linear interpolation of the separable phases produces an error in the resolution of the system of equations.

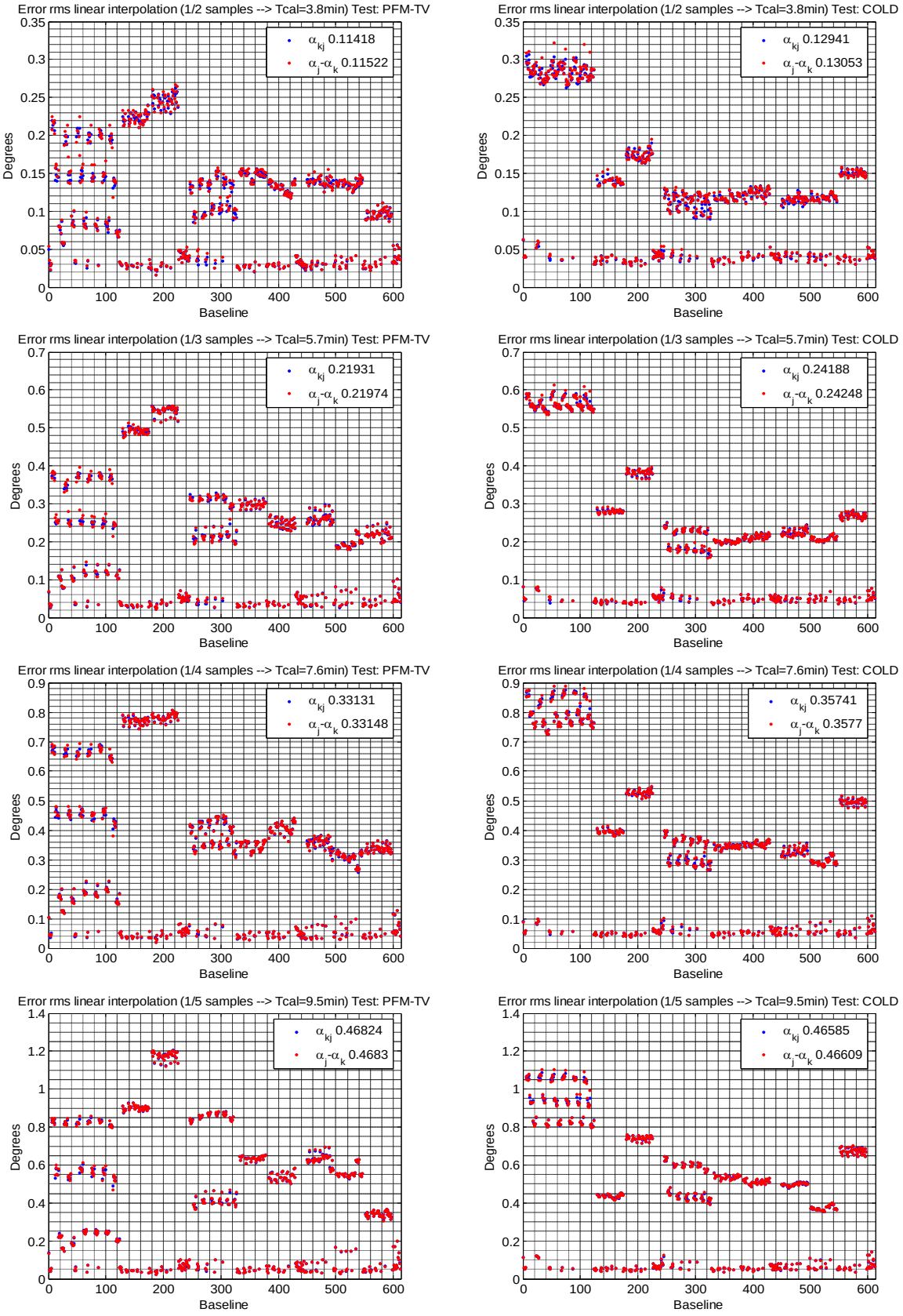

Fig. 8.7 RMS error of the linear interpolation for the $\alpha_{kj_{linear}}$ *(blue color) and the estimation* $\hat{\alpha}_{kj_{linear}} \approx \alpha_{j_{linear}} - \alpha_{k_{linear}}$ *(red color). Left plots: dataset PFM-TV. Right plots: dataset COLD. Interpolation with n=2 (first row), n=3 (second row), n=4 (third row) and n=5 (fourth row).*

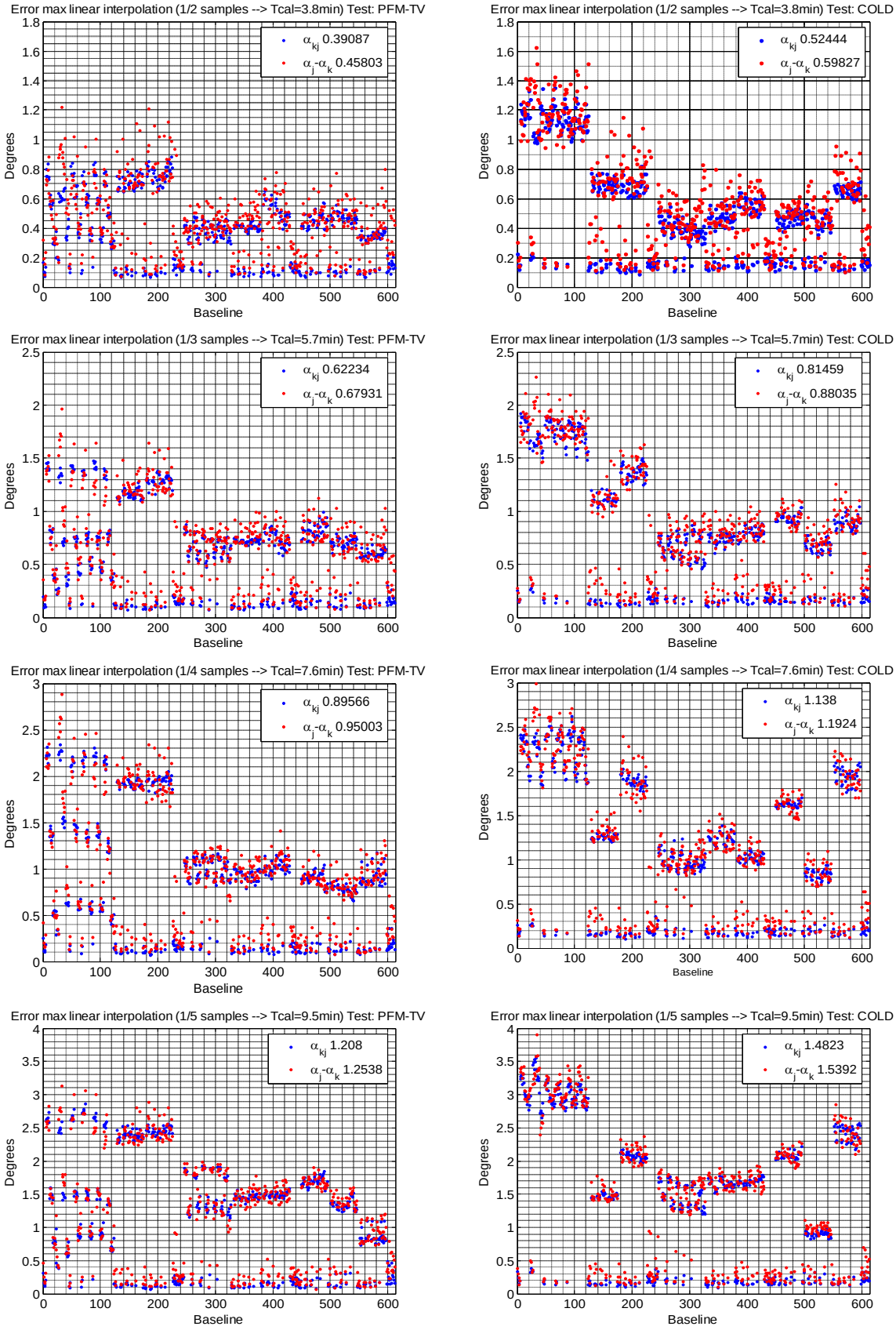

Fig. 8.8 Maximum error of the linear interpolation for the $\alpha_{kj_{linear}}$ *(blue color) and the estimation* $\hat{\alpha}_{kj_{linear}} \approx \alpha_{j_{linear}} - \alpha_{k_{linear}}$ *(red color). Left plots: dataset PFM-TV. Right plots: dataset COLD. Interpolation with n=2 (first row), n=3 (second row), n=4 (third row) and n=5 (fourth row).*

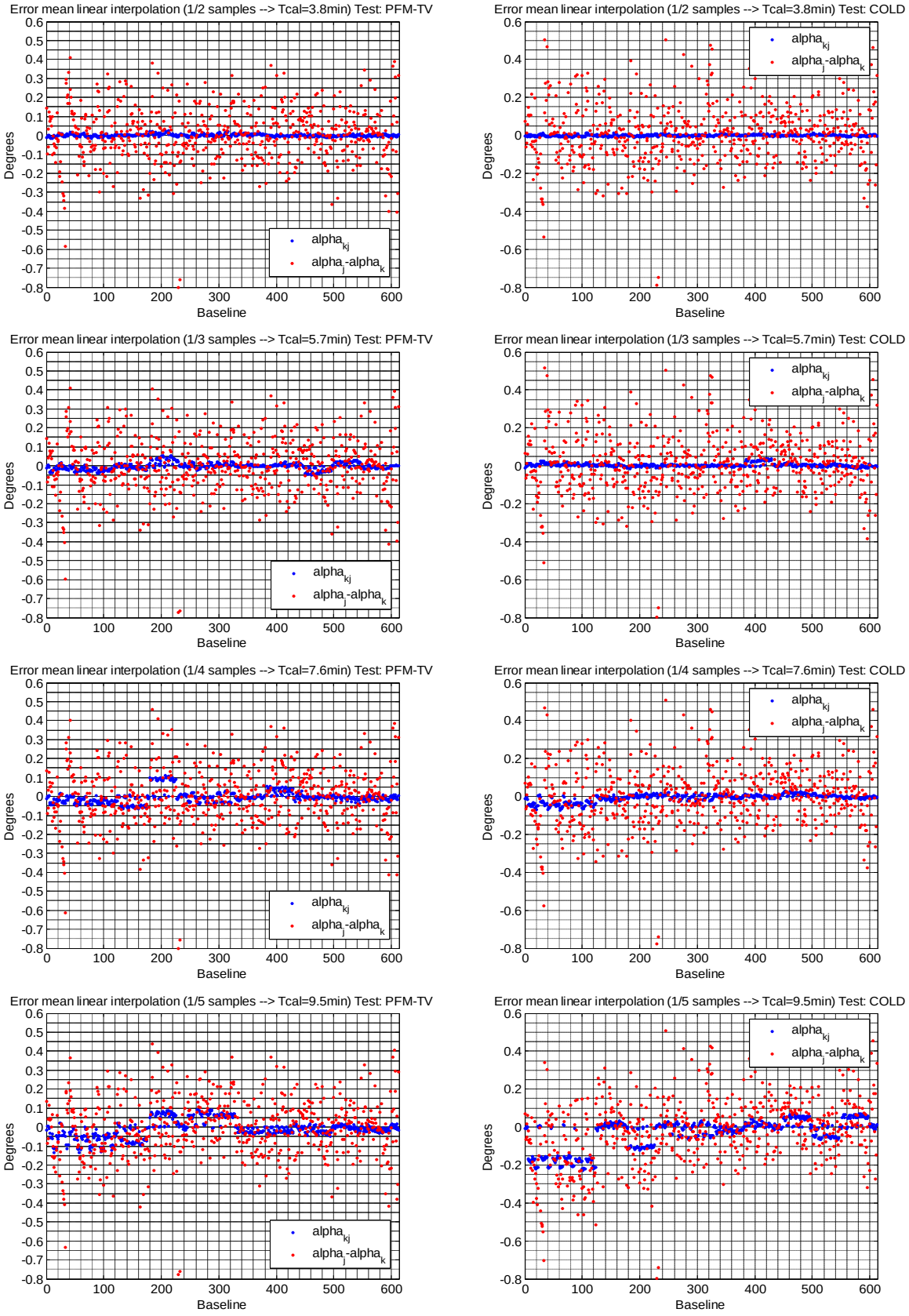

Fig. 8.9 Mean error of the linear interpolation for the $\alpha_{kj_{linear}}$ *(blue colour) and the estimation* $\hat{\alpha}_{kj_{linear}} \approx \alpha_{j_{linear}} - \alpha_{k_{linear}}$ *(red colour). Left plots: dataset PFM-TV. Right plots: dataset COLD. Interpolation with n=2 (first row), n=3 (second row), n=4 (third row) and n=5 (fourth row).*

To study the impact of the resolution of the system the equations, a comparison between the baseline phases measured (α_{kj}) and the baseline phases estimated from the separable phases ($\hat{\alpha}_{kj}$) has been carried out.

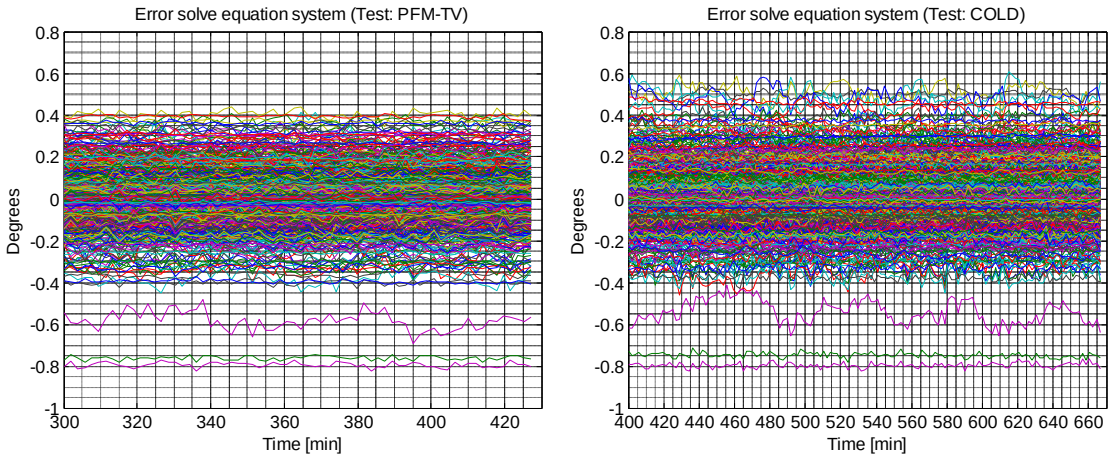

Fig. 8.10 Error between $\hat{\alpha}_{kj} \approx \alpha_j - \alpha_k$ estimation and α_{kj} measurement.
Leftt: dataset PFM-TV. Right: dataset COLD.

The estimation respect to the measures has an error produced by the resolution of the system of equations and the arbitrary constant phase term, shown in Fig. 8.10. In some baselines, this error is lower than 0.4 degrees, but in other cases the error reaches the 0.8 degrees.

In conclusion, it is better to interpolate the baseline phases (α_{kj}) directly because the resolution of the system produces a reference phase term that remains undetermined. The evolution of each phase includes the drift of this reference constant and therefore single phase drift is masked with this constant drift. This error is not constant in the different calibrations and it is impossible to remove [32] [35].

8.2.1.2. Spline and Fourier interpolation

In this section other different methods to interpolate the baseline phases (α_{kj}) have been studied: the Spline interpolation and the Fourier interpolation.

- ***Spline interpolation***

The baseline phases can be estimated using the spline interpolation taking one of every *n* samples (*n=2, 3, 4, 5)* from the measurements, which are separated one calibration time (t_{cal}) and the rest of the values are computed by cubic spline interpolation.

$$\alpha_{kj_{spline}}[t] = \alpha_{kj}[t] \qquad \text{If } t = t_0,\ t_0 + n*t_{cal},\ t_0 + 2n*t_{cal},\ \ldots \qquad \text{Eq. 8.5}$$

$$\alpha_{kj_{spline}}[t] = S[t] \qquad \text{Cubic spline interpolation in the rest of values}$$

where $S[t]$ is the independent segmental estimation with a polynomial of degree 3 with this form:

$$s_i[t] = a_i \cdot (t-(t-n\cdot t_{cal}))^3 + b_i \cdot (t-(t-n\cdot t_{cal}))^2 + c_i \cdot (t-(t-n\cdot t_{cal})) + d_i \qquad \text{Eq. 8.6}$$

If $t_0 < t < t_0 + n*t_{cal}$, $t_0 + n*t_{cal} < t < t_0 + 2n*t_{cal}$,... $t_0 + (m-2)*n*t_{cal} < t < t_0 + (m-1)*n*t_{cal}$

$$S[t] = \begin{Bmatrix} s_1[t] \\ s_2[t] \\ s_3[t] \\ \vdots \\ s_{m-1}[t] \end{Bmatrix} \qquad \text{Eq. 8.7}$$

being *m* the number of measurement in the original sequence and the spline interpolation is continuous.

- ***Fourier interpolation***

The baseline phases have been estimated taking one of every *n* samples (*n=2, 3, 4, 5)* from the measurements, which are separated one calibration time (t_{cal}) and the rest of the values are computed by Fourier interpolation:

$$\alpha_{kj_{fourier}}[t] = \alpha_{kj}[t] \qquad \text{If } t = t_0,\ t_0 + n*t_{cal},\ t_0 + 2n*t_{cal},\ \ldots \qquad \text{Eq. 8.8}$$

Interpolation using the FFT method (Fast Fourier Transformation) in the rest of values

The rms error for all interpolation methods has been represented in Fig. 8.11. The Fourier method has a different behavior when the dataset is taken at a lower temperature, such as the *COLD* test. In this case, the Fourier approximation has an error well above the rest, even being an order of magnitude above. Only for *n=3* the order is similar although the reason is unknown. The Spline method has a slightly worse performance at low temperatures, but the difference is really small. Moreover, for *n=5* the *COLD* dataset has a lower error than the *PFM-TV* dataset. The Linear interpolation has almost the same behavior in both tests.

The Fourier method would not be chosen due to it is complexity and the high rms error. The Spline method and the Linear method both would be a good choice.

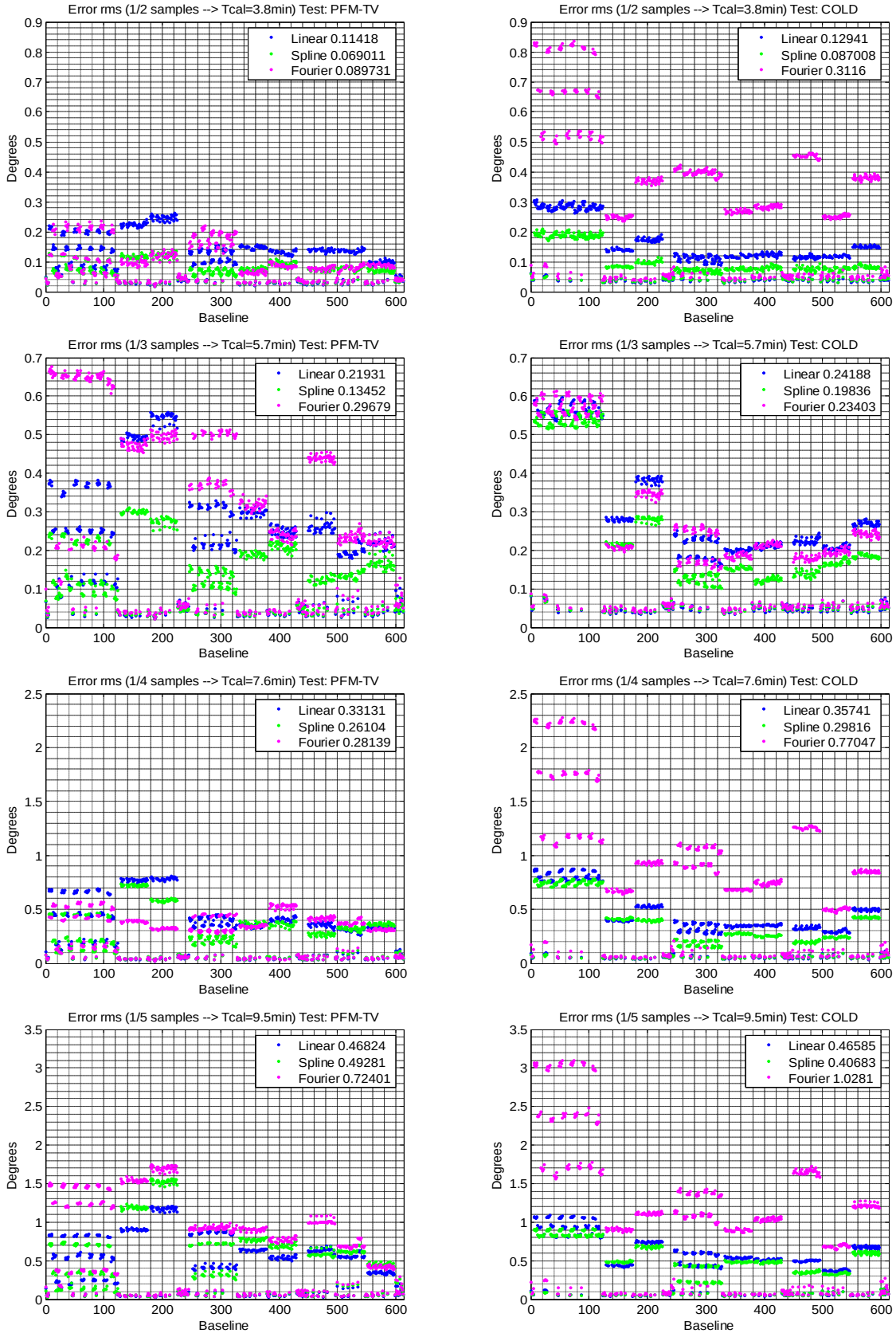

Fig. 8.11 RMS error in baseline phases (α_{kj}) by Linear interpolation (blue color), Spline interpolation (green color) and Fourier interpolation (pink colour). Left: dataset PFM-TV. Right: dataset COLD. Interpolation with n=2 (first row), n=3 (second row), n=4 (third row) and n=5 (fourth row).

8.2.1.3. Interpolation with a group correction

Analyzing the right plot obtained in Fig. 8.6, it must be pointed that the standard deviation has shape of groups. The values of the standard deviation are lower when the pair of receivers in a baseline belongs to the same segment. Instead of that, if the pair of receivers in a baseline belongs to different segment, the standard deviation is higher.

Taking into account this observation, it has been considered to apply a group correction using the mean of these groups after the interpolation of the baseline phases, and the results are presented in Fig. 8.12. It shows that the group correction does not get a lower rms error, so it is not interesting to apply it.

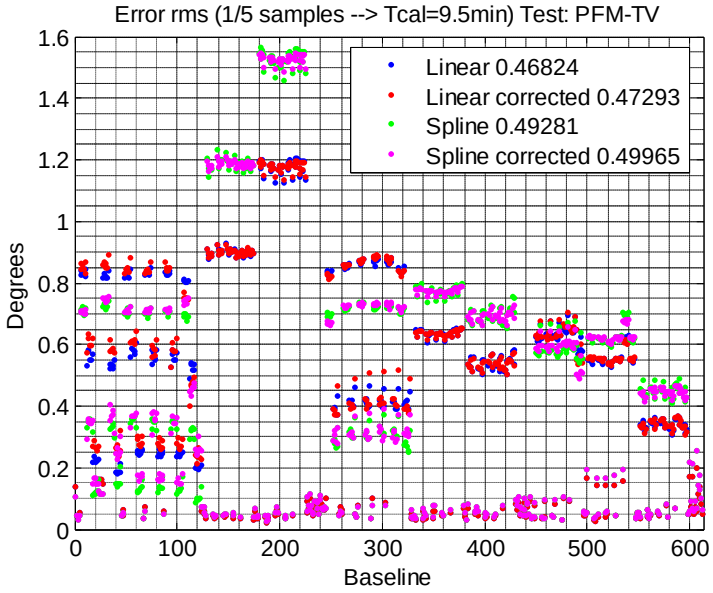

Fig. 8.12 RMS error with n=5 by Linear method and Spline method and their respective group correction.

8.2.1.4. Preliminary conclusions

Phase track interpolation performs better at baseline level that at receiver level. This is due to the small non-separable phase term that includes an offset error if interpolation is performed at receiver level and baseline phases constructed from the difference.

In order to maximize the LO phase track intercalibration period, several cases have been taken into account:

- Different calibration times: Tcal=1.9 minutes, 3.8 minutes, 5.7 minutes, 7.6 minutes and 9.5 minutes.
- In order to have a low estimation error, at least 3-4 samples per period are required to oversample phase drift. **This means that the intercalibration period is around Tcal=5.7 min if the interpolation error is to be kept below 1 deg for all baselines (case 1/3 samples).**

- **Spline interpolation performs better than linear interpolation since it uses a cubic interpolation (3 points) that better tracks the pseudo-sinusoidal behaviour of phase drift.**

Phase track interpolation by segments (group of LICEF units related to the same CMN) does not produce significant improvements in the phase tracking error and it is discarded.

8.2.2. Spline interpolation in-flight

This analysis is devoted to assess the validity of *spline interpolation* method already studied on-ground. The datasets used are the *5th of December 2009 from 10:41:00 to 19:41:00* and the *8th of December 2009 from 04:47:11 to 14:47:11*.

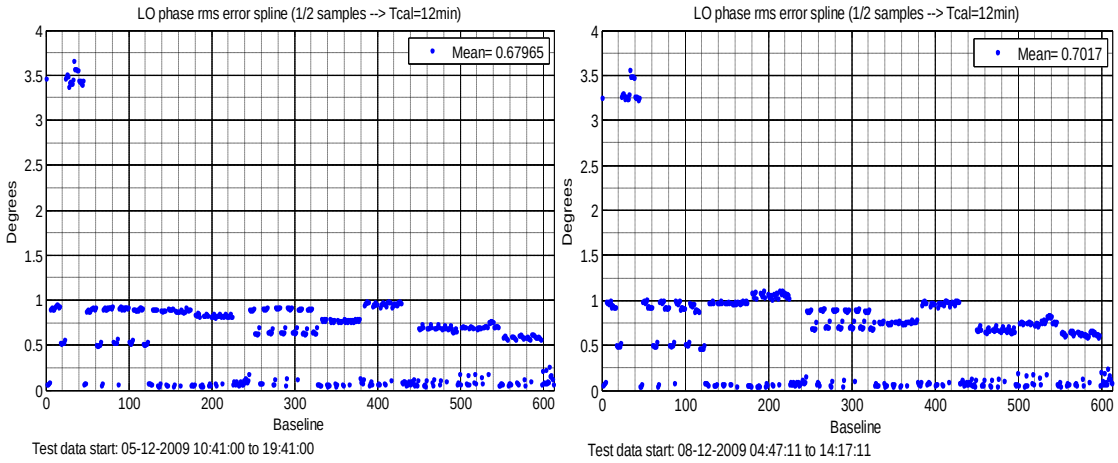

Fig. 8.13 RMS error in baseline phases for two real datasets

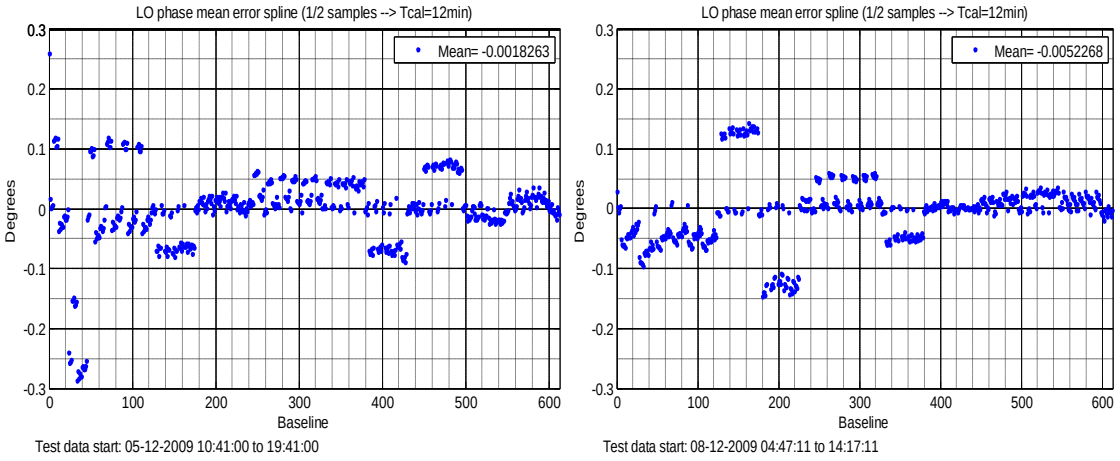

Fig. 8.14 Mean error in baseline phases for two real datasets

The rms error has been represented in Fig. 8.13. In both tests, the time between calibrations corresponds to 6 minutes. The errors in the baselines which contain the receiver NIR-AB-01-H are higher due to the oscillations in this receiver. In the rest of baselines, the rms error is approximately 1 degree. At receiver level, this error is divided by $\sqrt{2}$, (rms error lower than 1 degree), satisfying the required accuracy.

The mean error has also been represented (**Error! Reference source not found.**). This mean error is due to the resolution of the system of equations and it is below 0.3 degrees. The maximum error has been represented in Fig. 8.15. At baseline level it is around 4 degrees that implies a maximum error at receiver level around 2.83 degrees, except for those baselines formed by the receiver NIR-AB-01-H**.**

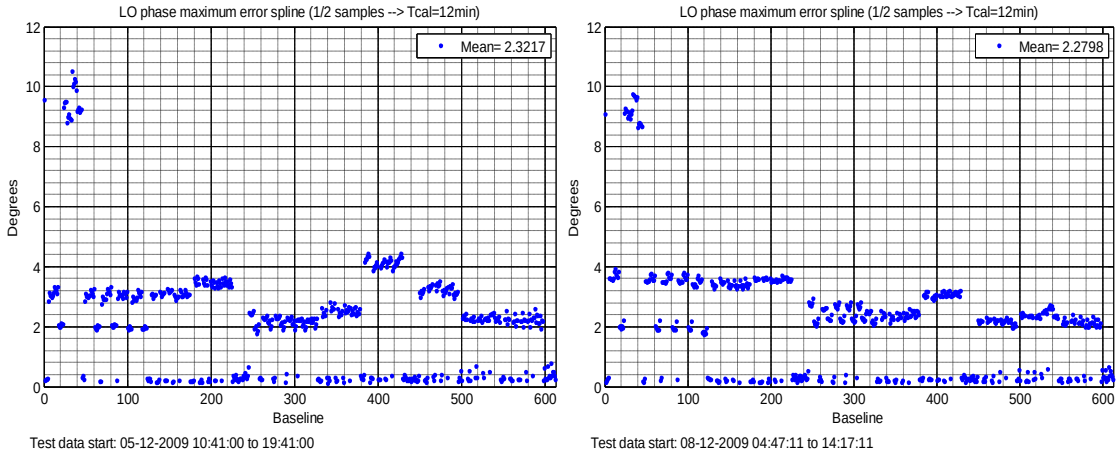

Fig. 8.15 Maximum error in baseline phases for two real datasets

.As a conclusion, the spline interpolation works very well in-flight datasets.

8.3. Conclusions LO phase track analysis

The current phase calibration baseline strategy in the official SMOS Level 1 data processor is done by LO phase tracking by frequent calibrations by noise injection. The frequency of calibrations is 10 minutes (LO phase tracking) and spline interpolation is used between calibrations in measurement mode.

CHAPTER 9

9. Conclusions and further work

This chapter is devoted to explain the conclusions of this Final Project and the future work which could be done.

9.1. Conclusions

The main objective of this Final Project has been the characterization of the PMS located in each receiver over the physical temperature**.** After the sensitivity analysis of the instrument there are some conclusions:

- **The physical temperature in orbit is really closed to 21ºC. The physical temperature drifts are between 1-3ºC, small enough to perform only a first order correction in the PMS calibration parameters.**

- **PMS gain sensitivity values at calibration plane are computed from linear regression using a dataset in-flight dated on 23rd April 2010. These values are the most current and are being used in the official SMOS Level 1 data processor.**

- **PMS offset sensitivity values at calibration plane are computed from a second order regression using a dataset on-ground from the LSS measurements. Due to the small temperature drift only the alpha term (which does not depend on the temperature) is used and the beta term (which is temperature dependent) is considered negligible. The reason of using a ground test is that it is the only estimation that is not affected by the heaters behavior. These values are considered the most accurate and are being used in the official SMOS Level 1 data processor.**

- **The receiver noise temperature sensitivity values at calibration plane provided by MIER Communications are considered as ground truth.**

During the sensitivity analysis, it has been discovered that PMS offset voltages showed small jumps linked to the signal controlling the heaters in the thermal control system. In summary:

- **A delay between the offset jumps and the heater state is present both on-ground and in-flight datasets, being the cause unknown.**

- **The jumps in the offset could be due to the thermal control system that really takes a lot of power to heat the receivers and this affect the polarization of the circuits. As there is a very critical interface for carrying the DC out of the PMS to the CMN it probably changes some mV in the offset when the heaters are switching on or off.**

To cancel this undesired variation, a correction using a delay in the signal heater and a jump in the PMS offset has been developed:

- **The correction is based on an accurate characterization carried out with the data acquired during tests sequence specifically designed for it and, at first time, using a correlation method between the offset voltage and the heater signal.**

- **The definitive heater delay parameter has been tuned by means of a trial and error procedure (manual fine tuning adjustment). This yields a better performance of the corrected PMS offset, thus minimizing the number of epochs affected by heater delay misalignment. The definitive offset jump has been obtained by average of the previous correlation methods. The heater offset correction (delay and jump) applied in the PMS voltages was implemented in the official SMOS Level 1 data processor**.

ESA decided that the PMS calibrations were done periodically by internal calibration. The long calibration sequence is performed once every eight weeks, which is enough to track the small variation of the retrieved parameters. This provides a total of 45 individual measurements of PMS gain and offset. All of them are averaged to obtain a calibration product.

Another objective of this Final Project was to track the PMS gain and offset parameters during the measurement mode of the instrument:

- **PMS gain is tracking from the calibration product corrected in temperature using the temperature gain sensitivity coefficients. Most of the receivers have gain variations below 0.5% rms and all of them are well below the requirement 1%.**

- **PMS offset is tracked from the calibration product corrected in temperature using the offset temperature sensitivity coefficients and the correction of the heater signal. The residual offset rms error is well below 1 mV specification**

The errors resulting of applying all the corrections in the PMS calibrations parameters are dominated by the thermal noise inherent to the measurements due to the limited integration time.

Regarding the correlation phase, the **LO calibration sequence is repeated once every ten minutes by internal calibration** and it consists of injecting correlated noise just to record the phase of the correlation, which is equal to the phase of the Fringe Washing term. During science measurement mode:

- **LO phase is estimated by spline interpolation between calibrations. This produces that all baselines have below 1 degree in the rms error, satisfying the required accuracy.**

9.2. Further work

The limited numbers of calibrated data sets that have been analyzed so far show a small mean value drift that may have an impact on the mean value of the brightness temperature retrievals. This drift needs further assessment to:

- **Assess the feasibility to develop additional correction techniques.**
- **Systematic and periodic analysis of all calibrations to check for correlation between instrument and physical parameter drifts/changes.**
- **Monitoring the PMS sensitivity coefficients and update if it is necessary.**
- **Verification of the PMS offset with heater signal (heater offset correction).**
- **Verification of the re-locks (whether onto the right frequency or not), specially in the NIR-AB-01-H.**

Appendix I: Sensitivity values

In this appendix there are summarized the sensitivity values (PMS offset sensitivity, PMS gain sensitivity and receiver noise temperature sensitivity) at calibration plane used in the SMOS Level 1 data processor.

		PMS offset sensitivity (*Second order)* $S_{v_{offk}} = \alpha_{v_{offk}}$ $(\beta_{v_{offk}} \cong 0)$	**PMS gain sensitivity** *(Flight data 23-04- 2010)* $S^C_{G_k} = \alpha^C_{G_k}$	**Receiver noise temperature sensitivity** *(MIER Communications)* $S^C_{T_{R_k}} = \alpha^C_{T_{R_k}}$
Receiver number	Receiver name	$\alpha_{v_{offk}}$ [V/ºC]	$\alpha^C_{G_k}$ [(V/K)/ºC]	$\alpha^C_{T_{R_k}}$ [K/ºC]
1	LCF_AB_03	2.1478E-04	8.1437E-06	0.5771
2	NIR_AB01_H	-1.8429E-04	1.0551E-05	0.6875
3	NIR_AB01_V	1.9852E-04	8.2222E-06	0.5750
4	LCF_A_01	-3.5175E-04	-2.5490E-06	0.6434
5	LCF_A_02	-1.4369E-04	9.5756E-06	0.7686
6	LCF_A_03	1.1995E-04	6.2324E-06	0.7668
7	LCF_A_04	2.3415E-05	7.0041E-06	0.6938
8	LCF_A_05	3.9718E-04	1.3030E-05	0.8937
9	LCF_A_06	1.0907E-04	9.0384E-06	0.6875
10	LCF_A_07	3.0041E-04	1.1207E-05	0.7563
11	LCF_A_08	-3.1199E-04	8.8490E-06	0.6938
12	LCF_A_09	1.7221E-04	6.0248E-06	0.8312
13	LCF_A_10	-2.0175E-04	1.0922E-05	0.8188
14	LCF_A_11	9.6138E-05	8.2177E-06	0.7000
15	LCF_A_12	-3.4024E-04	7.0514E-06	0.8188
16	LCF_A_13	-4.9260E-04	6.0932E-06	0.7625
17	LCF_A_14	-2.6603E-04	1.0203E-05	0.7687
18	LCF_A_15	-2.6620E-04	1.1355E-05	0.8312
19	LCF_A_16	-2.2215E-04	6.1954E-06	0.7687
20	LCF_A_17	-3.1937E-04	3.8997E-06	0.6938
21	LCF_A_18	3.3778E-04	7.8166E-06	0.8125
22	LCF_A_19	-1.4911E-04	8.4286E-06	0.6938
23	LCF_A_20	-2.3591E-04	4.9012E-06	0.7563
24	LCF_A_21	-3.6828E-05	2.9703E-06	0.7625
25	LCF_BC_03	2.2158E-04	7.0477E-03	0.7053
26	NIR_BC01_H	2.0449E-04	5.1603E-06	0.7563
27	NIR_BC01_V	-1.2448E-04	2.8333E-06	0.7000
28	LCF_B_01	4.1717E-04	1.2157E-05	0.9752
29	LCF_B_02	7.2649E-04	3.2273E-06	0.6420
30	LCF_B_03	5.3798E-05	9.7819E-06	0.7563
31	LCF_B_04	1.0464E-04	6.0266E-06	0.6375
32	LCF_B_05	4.1770E-05	6.1693E-06	0.6938
33	LCF_B_06	1.5300E-04	1.1878E-05	1.0250

34	LCF_B_07	-2.3102E-04	4.1682E-06	0.8312
35	LCF_B_08	-2.7355E-05	8.8729E-06	0.7625
36	LCF_B_09	5.7988E-04	1.0112E-05	0.7062
37	LCF_B_10	4.2488E-04	2.2312E-06	0.7000
38	LCF_B_11	-3.6395E-04	7.6468E-06	0.5750
39	LCF_B_12	5.4024E-04	9.4837E-06	0.7563
40	LCF_B_13	4.4354E-04	9.5133E-06	0.8312
41	LCF_B_14	4.8868E-04	1.6876E-05	0.3875
42	LCF_B_15	4.1574E-04	1.2406E-05	0.7563
43	LCF_B_16	4.2045E-04	8.8480E-06	0.6938
44	LCF_B_17	3.7091E-04	9.8535E-06	0.8250
45	LCF_B_18	-1.0250E-04	5.3614E-06	0.6938
46	LCF_B_19	-1.3916E-04	8.3186E-07	0.7750
47	LCF_B_20	-4.6144E-04	1.4581E-05	0.7625
48	LCF_B_21	1.5422E-04	6.1059E-06	0.7563
49	LCF_CA_03	-8.0403E-05	1.0522E-05	0.8905
50	NIR_CA01_H	1.2590E-04	1.8547E-06	0.6938
51	NIR_CA01_V	1.0496E-04	4.4504E-06	0.7563
52	LCF_C_01	3.1040E-04	9.3902E-06	0.7775
53	LCF_C_02	-3.5728E-05	5.1962E-06	0.7021
54	LCF_C_03	3.5194E-04	9.2319E-06	0.8317
55	LCF_C_04	-7.4731E-05	3.7359E-06	0.6813
56	LCF_C_05	7.9739E-05	9.1884E-06	0.7687
57	LCF_C_06	-4.5850E-04	1.0542E-05	0.8256
58	LCF_C_07	5.3651E-04	1.6298E-05	0.6944
59	LCF_C_08	4.0773E-04	5.8194E-06	0.7581
60	LCF_C_09	-1.4736E-04	6.0873E-06	0.5675
61	LCF_C_10	1.1013E-04	1.5698E-05	0.6375
62	LCF_C_11	-1.5572E-04	5.5716E-06	0.7631
63	LCF_C_12	-2.7735E-04	8.6068E-06	0.8250
64	LCF_C_13	1.6677E-04	1.0583E-05	0.7625
65	LCF_C_14	3.9683E-04	3.9261E-06	0.8419
66	LCF_C_15	-3.7131E-04	7.6011E-06	0.7613
67	LCF_C_16	1.6786E-05	1.5953E-05	0.7563
68	LCF_C_17	-2.5040E-04	3.2097E-06	0.6988
69	LCF_C_18	-3.5294E-04	2.7486E-06	0.6275
70	LCF_C_19	1.5969E-04	3.4149E-06	0.7631
71	LCF_C_20	2.8034E-04	1.8782E-06	0.6969
72	LCF_C_21	1.7381E-04	1.0386E-05	0.7613

Appendix Table I: PMS sensitivity values used in the SMOS Level 1 data processor.

Appendix II: Heater offset correction values

In this appendix there are summarized heater offset correction values (delay and jump) used in the SMOS Level 1 data processor.

Receiver number	Receiver name	Heater assignment	Manual adjustment	
			Offset correction [mV]	Delay [epochs]
1	LCF_AB_03	9	-1.454214811	45
2	NIR_AB01_H	Not assigned	0	0
3	NIR_AB01_V	9	-0.316954149	143
4	LCF_A_01	5	-0.425016849	400
5	LCF_A_02	5	-0.831016448	295
6	LCF_A_03	5	-3.032379593	87
7	LCF_A_04	2	-0.805518007	140
8	LCF_A_05	2	-1.357660187	112
9	LCF_A_06	2	-1.407405008	130
10	LCF_A_07	2	-1.398821671	125
11	LCF_A_08	2	-1.364485777	150
12	LCF_A_09	2	-0.796881015	137
13	LCF_A_10	3	-1.010304762	120
14	LCF_A_11	3	-1.366954945	115
15	LCF_A_12	3	-1.3643909	140
16	LCF_A_13	3	-0.51023011	165
17	LCF_A_14	3	-1.162907939	130
18	LCF_A_15	3	-0.710284159	150
19	LCF_A_16	4	-1.280522043	115
20	LCF_A_17	4	-1.255725468	130
21	LCF_A_18	4	-2.08341589	112
22	LCF_A_19	4	-1.997006884	117
23	LCF_A_20	4	-1.853299204	132
24	LCF_A_21	4	-0.792589576	150
25	LCF_BC_03	1	-0.810444974	125
26	NIR_BC01_H	Not assigned	0	0
27	NIR_BC01_V	Not assigned	0	0
28	LCF_B_01	9	-0.216813873	385
29	LCF_B_02	1	-0.475010829	280
30	LCF_B_03	1	-4.089792193	65
31	LCF_B_04	6	-1.237718611	120
32	LCF_B_05	6	-0.939957888	105
33	LCF_B_06	6	-1.816252661	115
34	LCF_B_07	6	-1.001797106	140
35	LCF_B_08	6	-1.458778246	120
36	LCF_B_09	6	-0.734152656	122
37	LCF_B_10	7	-0.778244278	105

38	LCF_B_11	7	-1.149516318	130
39	LCF_B_12	7	-1.225163857	122
40	LCF_B_13	7	-0.968244588	110
41	LCF_B_14	7	-1.235497000	110
42	LCF_B_15	7	-0.785065115	140
43	LCF_B_16	8	-1.036655894	110
44	LCF_B_17	8	-1.535968761	115
45	LCF_B_18	8	-1.328367152	127
46	LCF_B_19	8	-1.373277684	125
47	LCF_B_20	8	-1.206922956	145
48	LCF_B_21	8	-0.556973493	125
49	LCF_CA_03	9	-1.568155947	60
50	NIR_CA01_H	9	-0.241160176	144
51	NIR_CA01_V	Not assigned	0	0
52	LCF_C_01	Not assigned	0	0
53	LCF_C_02	1	-0.486761176	290
54	LCF_C_03	1	-4.148881461	50
55	LCF_C_04	10	-1.134459659	125
56	LCF_C_05	10	-1.259122756	135
57	LCF_C_06	10	-1.401877057	130
58	LCF_C_07	10	-1.109856318	107
59	LCF_C_08	10	-1.601643611	105
60	LCF_C_09	10	-0.684198075	170
61	LCF_C_10	11	-1.481345111	105
62	LCF_C_11	11	-1.731315885	130
63	LCF_C_12	11	-1.753785335	100
64	LCF_C_13	11	-1.145924647	122
65	LCF_C_14	11	-1.400986082	115
66	LCF_C_15	11	-0.633760053	175
67	LCF_C_16	12	-1.355607246	102
68	LCF_C_17	12	-1.492204032	118
69	LCF_C_18	12	-1.18852002	147
70	LCF_C_19	12	-1.307191088	125
71	LCF_C_20	12	-2.235705618	69
72	LCF_C_21	12	-0.861599148	135

Appendix Table II: PMS offset correction in mV and delay in epochs for all receivers with its corresponding heater associate used in the SMOS Level 1 data processor.

	Heater
CMN-H1	1
CMN-A1	2
CMN-A2	3
CMN-A3	4
CMN-H2	5
CMN-B1	6

	Heater
CMN-B2	7
CMN-B3	8
CMN-H3	9
CMN-C1	10
CMN-C2	11
CMN-C3	12

Appendix III: Publications

In this appendix some publications which contain part of the work developed during the development of this Final Project are presented.

Poster SMOS-BEC

Remote Sensing Laboratory — UPC

One point calibration in interferometric radiometers: MIRAS/SMOS preliminary results

F. Torres[1], I. Corbella[1], N. Duffo[1], V. González-Gambau[1], I. Durán[1], M. Pablos[1] and M. Martín-Neira[2]
[1]Remote Sensing Laboratory, Universitat Politècnica de Catalunya, SMOS Barcelona Expert Centre. xtorres@tsc.upc.edu
[2]European Space Agency, European Space Research and Technology Centre (ESTEC), Noordwijk, Holland

INTRODUCTION. After the successful launch of the SMOS satellite, on November 2009 at 02:50 CET (01:50 UT) from the Plesetsk Cosmodrome in northern Russia, a preliminary evaluation of the payload calibration strategy has been undertaken in order to assess the instrument performance and fix the operational measurement and calibration configuration. This work presents the performance of the amplitude calibration strategy, a key issue in achieving a stable and accurate operation of the sensor.

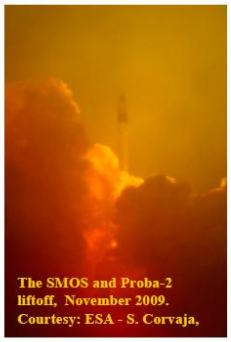

Calibrated visibility at the antenna plane

$$V_{kj}^{A} = \frac{\sqrt{T_{sys\_ak} T_{sys\_aj}}}{G_{kj}^{A}} M_{kj}$$

FWF at t=0 — Normalized correlation

System temperature at the antenna plane is measured by means of the Power Measurement System (PMS):

$$T_{sys\_ak} = \frac{v_{Ak} - v_{offk}}{G_k^A}$$

PMS gain orbital drift correction

$$G_k^A(T_{ph_i}) = G_k^A(T_{ph_0})\left(1 + S_{Tph}^{G}\left(T_{ph_i} - T_{ph_0}\right)\right)$$

Meas T_{ph} — Cal T_{ph} — Gain sensitivity

SMOS baseline amplitude calibration approach by internal noise injection

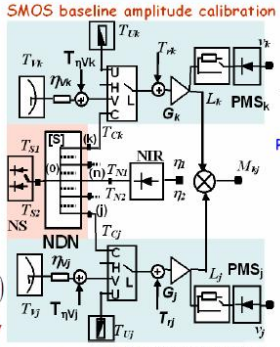

PMS calibration: 2-level 4-point method

$$v_{1k} = v_{offk} + G_k^C T_{sysC_k}^{WARM} \qquad v_{2k} = v_{offk} + G_k^C T_{sysC_k}^{HOT}$$

$$v_{3k} = v_{offk} + \frac{G_k^C}{L_k} T_{sysC_k}^{WARM} \qquad v_{4k} = v_{offk} + \frac{G_k^C}{L_k} T_{sysC_k}^{HOT}$$

PMS offset from the 4 point PMS voltages

$$v_{offk} = \frac{v_{2k}v_{3k} - v_{1k}v_{4k}}{(v_{2k} - v_{4k}) - (v_{1k} - v_{3k})}$$

PMS gain calibrated at plane C relative to the NIR reference radiometer

$$G_k^C = \frac{v_{2k} - v_{1k}}{T_{N2} - T_{N1}} \frac{|S_{n0}|^2}{|S_{k0}|^2}$$

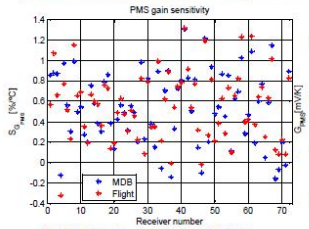

The 72 PMS gains show low sensitivity to temperature drift: a mean value of 0.6 %/°C.

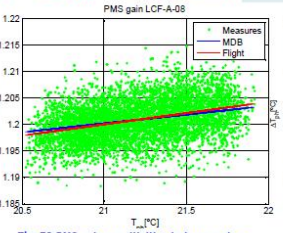

The 72 PMS gain sensitivities to temperature drift measured in-flight along several orbits in calibration mode show good agreement with the on-ground values

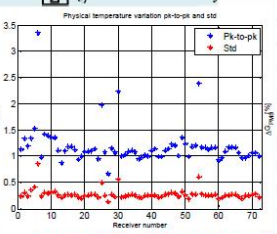

The orbital temperature swing of the 72 receivers is well constrained by the thermal control.

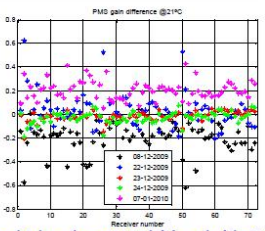

The plot shows the mean gain drift for each of the 72 PMS gains wrt to their mean value along the one month intercalibration period. Pk-to-pk residual drift below ±0.6%, well within mission requirements

ONE POINT CALIBRATION: 1) Used to correct CAS S-parameter residual errors during deep sky calibration.
2) Alternative method to correct PMS orbital drift by means of U-noise injection: Risk mitigation approach.

1) CAS 4P and external 1P PMS gains must be equal during deep sky calibration

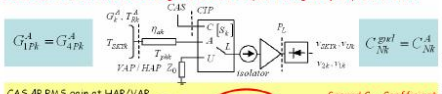

$$G_{1Pk}^{A} = G_{4Pk}^{A} \qquad C_{Nk}^{gwl} = C_{Nk}^{A}$$

CAS 4P PMS gain at HAP/VAP — Ground C_{Uk} Coefficient

$$G_{4Pk}^{A} = \frac{v_{2k} - v_{1k}}{T_{CAS\_H}^{2} - T_{CAS\_C}^{1}} \frac{|S_{LA_k}|^2 |S_{N0}|^2}{|S_{LC_k}|^2 |S_{k0}|^2} \eta_{A_k} \qquad C_{Nk}^{gwl} = \frac{|S_{LA_k}|^2 |S_{N0}|^2}{|S_{LC_k}|^2 |S_{k0}|^2} \eta_{A_k}$$

External 1P PMS gain at HAP/VAP — Deep sky C_{Uk} Coefficient

$$G_{1Pk}^{A} = \frac{v_{Uk} - v_{SKYk}}{T_{phk} - T_{SKYk}} \qquad C_{Nk}^{A} = \frac{T_{CAS\_H}^{2} - T_{CAS\_H}^{1}}{v_{2k} - v_{1k}} \frac{v_{Uk} - v_{SKYk}}{T_{Uk} - T_{SKYk}}$$

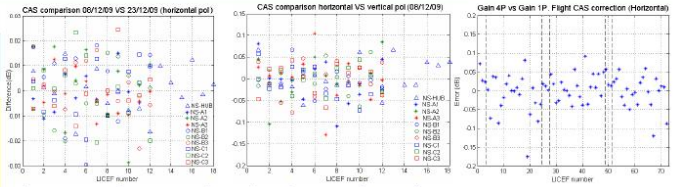

The CAS correction factors, measured at VAP/HAP, show very good one-month intercalibration stability (left) and low dependency on polarization configuration. LICEF numbers correspond to receivers within the HUB (18) or arm segments (12)

After CAS correction by means of external calibration PMS 1P gain and internal 4P gain match to 0.046 dB RMS

2) PMS 1P gain orbital drift correction by periodic U-noise injection (backup method)

$$G_k^A(T_{ph_i}) = \frac{v_{Uk} - v_{offk}}{T_{Rk}^A(T_{ph_i}) + T_{ph_i}} \qquad T_{Rk}^A(T_{ph_i}) = T_{Rk}^A(T_{ph_0})\left(1 + S_{Tph}^{TR}\left(T_{ph_i} - T_{ph_0}\right)\right)$$

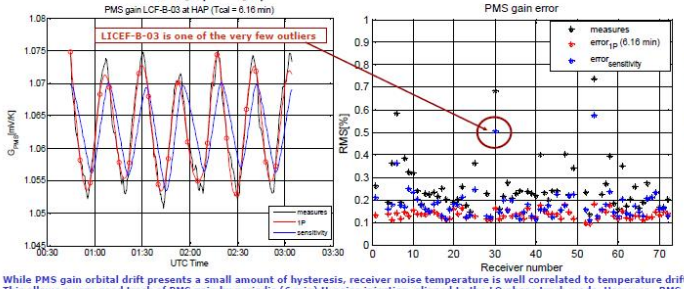

While PMS gain orbital drift presents a small amount of hysteresis, receiver noise temperature is well correlated to temperature drift. This allows a very good track of PMS gain by periodic (6 min) U-noise injection, aligned to the LO phase track mode. However, RMS residual error well within specifications and correction by means of sensitivity has been selected to maximize observation mode.

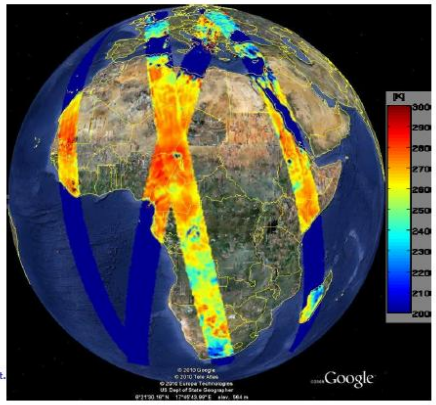

CONCLUSIONS

- In-orbit MIRAS/SMOS amplitude calibration performs well within expectations. Low temperature swing, very good stability and careful temperature compensation keeps PMS gain estimation well below the 1% RMS system error requirement.

Acknowledgments: This work was supported by the European Space Agency and EADS-CASA Space Division in the frame of the SMOS project. This work has been partially funded by the Spanish Ministry of Science and Innovation and FEDER under project TEC2008-06764-C02-01.

Geoscience and Remote sensing Symposium: MICRORAD 2010 (article I)

FIRST RESULTS ON MIRAS CALIBRATION AND OVERALL SMOS PERFORMANCE

Ignasi Corbella[(1)], Francesc Torres[(1)], Nuria Duffo[(1)], Verónica González-Gambau[(1)], Miriam Pablos[(1)], Israel Duran[(1)], Manuel Martín-Neira[(2)]

(1) Remote Sensing Laboratory, Universitat Politècnica de Catalunya (UPC).
C/ Jordi Girona 1-3. 08034 Barcelona, Spain.
(2) European Space Agency (ESA-ESTEC) Noordwijk. The Nederlands
contact e-mail: corbella@tsc.upc.edu

ABSTRACT

After the successful launching of the SMOS satellite, the first continuous streams of data are being processed and carefully analyzed in the frame of the SMOS In-Orbit Commissioning phase. Results regarding instrument calibration parameters retrieval, both internal and external, and brightness temperature imaging are presented. Images of ocean, ice and land are given as examples.

Index Terms— SMOS, interferometric synthetic aperture radiometry

1. INTRODUCTION

SMOS (acronym of Soil Moisture and Ocean Salinity) is a European Space Agency (ESA) mission designed to provide global maps of soil moisture over land and sea surface salinity over oceans [1]. It consists of a satellite in a sun-synchronous orbit at about 770 km height carrying a passive L-band sensor called MIRAS (Microwave Imaging Radiometer with Aperture Synthesis) [2]. The satellite was successfully launched the 2nd November 2009 from the Plesestz cosmodrome in northern Russia and the payload was switched on on 17th November 2009. Since then, continuous data is regularly received by the ground segment data acquisition station located in Villafranca del Castillo, near Madrid (E).

The SMOS In-Orbit Commissioning Phase (IOCP) started just after the 3-week long Switch-On and Data Acquisition Phase (SODAP), which was mainly focused at testing low level processes for data acquisition and handling. The IOCP has an overall duration of 6 months and the first half part comprises the characterization, calibration, validation and verification of the instrument [3]. The main goal is to provide a "fine tune" of MIRAS by means of: - Systematic check of all instrument modes - Retrieval of internal and external calibration parameters - Computation of temperature sensitivity coefficients - Assessment on imaging capability - Assessment on calibration rate requirement and - Instrument overall performance evaluation: Stability, Radiometric sensitivity, Radiometric accuracy and Absolute accuracy .

Most of the goals are being successfully achieved on time thanks to the combined effort of a team formed by EADS-CASA Espacio (E) as instrument manufacturer; Deimos Enginheria (P) developer of the Level 1 Prototype Processor (L1PP); the ESA Calibration Expert Center (CEC) dedicated to analyze the quality of the calibration data; and the Universitat Politecnica de Catalunya (UPC) responsible of the definition and implementation of calibration and processing algorithms. All of them are efficiently led by the ESA's principal engineer of the instrument.

The following sections provide a brief description of the activities carried out by UPC in the frame of the SMOS IOCP and shows the main results achieved, including determination of calibration parameters and their stability, as well as retrieval of brightness temperature images of ocean, ice and land. Everything has been processed using the MIRAS Testing Software, an independent software tool developed by UPC, capable of producing geolocated brightness temperature out of the raw data downloaded from the payload [4].

2. INTERNAL CALIBRATION

The procedures for MIRAS internal calibration are fully described in [5]. Essentially, calibration is carried out by injecting two-levels of correlated noise into all receivers [6] using a distributed approach to simplify the internal noise distribution network. The outcomes of the calibration procedure are three parameters: the power measurement system (PMS) gain (G_k) and offset (v_{off}) and the correlation complex gain (G_{kj}). Once these parameters are known, the calibrated visibility during scene observation is computed as

$$V_{kj} = \frac{M_{kj}\sqrt{T_{sys_k}T_{sys_j}}}{G_{kj}} \quad \text{where} \quad T_{sys_k} = \frac{v_k - v_{off_k}}{G_k} \quad (1)$$

This work was supported by the European Space Agency and EADS-CASA Space Division under ESTEC contract 17950/03/NL/FF-SMOS; and by the Spanish Ministry of Science and Technology (MCYT) under project TEC2008-06764-C02-01.

where v_k is the measured PMS voltage and M_{kj} the normalized correlation. Calibration parameters are measured at different times than when used during target observation. In order to accurately predict their values at measurement times, it is important to carefully assess their stability and temperature dependance. The following subsections show the main results obtained in specific tests carried out during the IOCP in order to measure the calibration parameters and their stability [3].

2.1. PMS gain

Figure 1 shows the relative PMS gain variation in percentage with respect to the average value. It has been computed after analyzing a total of 2499 samples measured during more than 24 hours with the instrument continuously in calibration mode. As seen, most of the receivers have PMS gain variations below 0.5% rms and all of them are well below the specified 1%. The plot at the right shows the long-term stability of the gain. It represents the difference in measured gain for 6 different calibration events separated more than one month. The result is that the PMS mean gain is stable within 1.2% peak to peak in a period of one month, and about 0.6% mean drift.

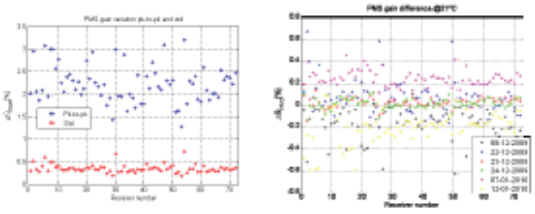

Fig. 1. Relative PMS gain variation in 24 hours continuous measurements (left) and between separated calibration events

Nevertheless, there is still a small dependance of the PMS gain with temperature. To characterize this behavior, plots of PMS voltages as a function of temperature have been produced and sensitivity coefficients computed from linear regression. An example of such plots is given in figure 2 along with a comparison between the measured gain and the one predicted from the temperature measurement. Two values of sensitivity are shown, one in blue corresponding to on ground measurement [7] and other in red obtained from flight data in the frame of the IOCP.

2.2. PMS offset

The PMS offset voltages showed unexpected jumps linked to the signal controlling the heaters in the temperature stabilization circuitry. Some receivers are more affected than others, but the effect is general. A correction has been implemented so as to estimate the offset using its mean value, the physical temperature and the heater signals. Figure 3 shows the comparison between the estimated offset and the measured one for

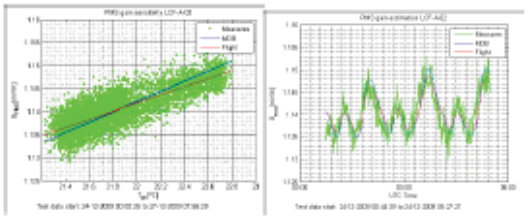

Fig. 2. PMS Gain sensitivity and estimation from physical temperature.

two particular receivers. The periodical variation corresponds to the heater signal frequency. It is apparent that the procedure devised is able to follow the actual value of the offset.

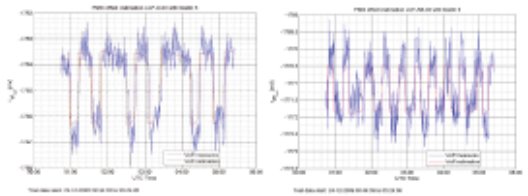

Fig. 3. PMS offset compared with its estimation using the temperature and the heater signal. Plots correspond to two sample receivers

2.3. Correlator gain

The correlator gain G_{kj} is a complex valued parameter. Its amplitude is always around unity and has small variation with time. On the other hand its phase depends on the local oscillator phases which in turn depend on the physical temperature variation with time. To account for this dependance, frequent phase calibration events are carried out interspersed with the normal measurement operation. Several strategies are being studied within the commissioning phase in order to decide the best phase calibration rate. To this end the payload has been programmed to acquire data with different LO calibration rates, ranging from 2 minutes to 14 minutes. The final value will be fixed after a complete analysis of the data acquired, bearing in mind that the final goal is to provide the maximum quality of the geophysical parameters retrievals. Figure 4 shows examples of amplitude and phase of G_{kj}. In this last case, the estimation based on a spline interpolation is also shown. As for the amplitude, in this particular case the variation is as small as 0.05% and in general most baselines present a ripple below 0.3% rms.

2.4. Internal calibration strategy

Once in a month a whole orbit is dedicated to internal calibration. Then, all measurements of PMS gain and offset as

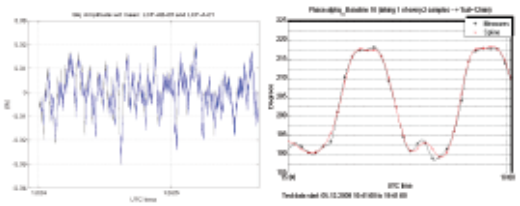

Fig. 4. Sample figures of the amplitude and phase of G_{kj} showing the phase variation due to local oscillator phase drift

well as amplitude of correlator gain are averaged and saved as reference. During science measurement operation, the PMS gain is estimated from this reference corrected using the temperature sensitivity coefficients. The offset is estimated using both the temperature sensitivity coefficient and the correction linked to the heater signal. The amplitude of the correlator gain is used just as measured and finally, the phase of this parameter is estimated by spline interpolation between interspersed measurements.

3. EXTERNAL CALIBRATION

Also once every month the platform rotates in order to point to the cold sky and acquire data for external calibration. The most important effect that must be corrected is the term of the PMS gain not included in the internal calibration procedure, namely the overall loss between the antenna plane and the switch, including the antenna ohmic efficiency. Figure 5 shows the difference in percentage between the PMS gain retrieved using internal calibration and by an independent procedure using the cold sky and the internal resistor [8]. At left, the original results are shown, which have been used to devise a procedure to correct for this inconsistency. At right the gain difference is shown after applying the correction factor. All differences remain below than ± 0.035 dB.

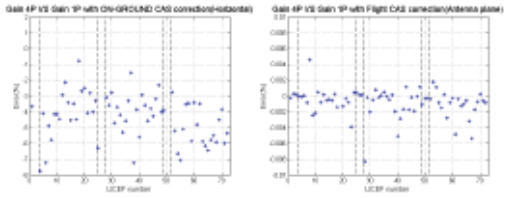

Fig. 5. Comparison between PMS gain retrieved with internal calibration and with external calibration. Left: without correction. Right: after correction

4. BRIGHTNESS TEMPERATURE IMAGES

Once the instrument is fully calibrated, the visibility is injected into the inversion algorithms in order to retrieve brightness temperature images. Examples have been produced for ocean, land and ice using the inversion approach number 3 defined in [9]. Figure 6 shows the average of horizontal and vertical brightness temperature for incidence angles below 30° for a region of the south pacific overlaying a map of salinity available from NOAA climatological data. According to the expected results the brightness temperature decreases for regions with higher salinity. At the right of the figure, the horizontal and vertical brightness temperature for the stable region of lower latitudes is shown. The consistency with the theoretical values computed using the Fresnel reflection coefficient, plot as solid lines, is remarkable, especially in vertical polarization.

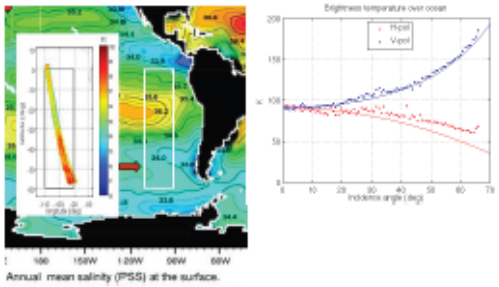

Fig. 6. Brightness temperature images over ocean. Left: map of $(T_H + T_V)/2$ for incidence angles below 30°. Right: Incidence angle dependance and comparison with Fresnel theoretical predictions

Figure 7 shows the retrieved brightness temperature over Antarctica. The figure at the left is a map of the average of horizontal and vertical brightness temperature. The small star marks the location of the Concordia Station in the Dome-C area. At right, there is a plot of the incidence angle dependence for this same area and a comparison with the data measured in the frame of the DOMEX campaign [10]. The general trend is clearly followed, but there is a small bias between both results.

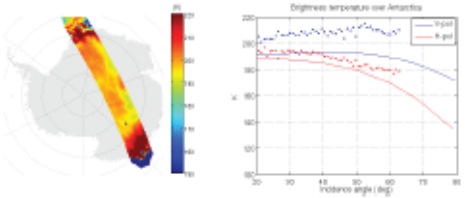

Fig. 7. Brightness temperature images over the Antarctica. Left: map of $(T_H + T_V)/2$. Right: Incidence angle dependance (dots) and comparison with experimental results of [10] (solid lines)

Finally, figure 8 shows again the average of horizontal and vertical brightness temperature for incidence angle lower than

30° in an overpass over South America. The image is superimposed to a map downloaded from Google Earth in order to show the extent of the Amazonian forest matching very well with the area of higher brightness temperature due to the shielding effect of the dense vegetation. The Amazon river itself is perfectly visualized in the image as a zone with lower brightness temperature. Other structures are seen corresponding to different terrains and humidities.

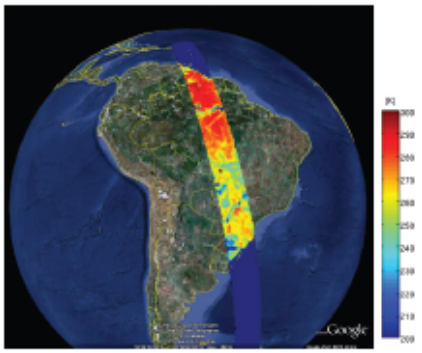

Fig. 8. Map of $(T_H + T_V)/2$ over South America and the Amazonian forest

5. CONCLUSIONS

MIRAS is already providing accurately calibrated visibility measurements as a result of using internal calibration corrected with external calibration. All parameters have been measured and found consistent with the on-ground characterization, showing high stability both in short- and long terms. Quality Brightness Temperature images are then ready to be retrieved, especially in the alias-free field of view and also in the extended part, although with some already expected degradation. Examples over sea, ice and land are given after processing data using the UPC's MIRAS testing software, an independent processing chain from raw data to geo-located brightness temperature. As a general conclusion: SMOS mission is a success and good global maps of Soil Moisture and Ocean Salinity are expected to be produced in the years to come

6. REFERENCES

[1] H. Barré, B. Duesmann, and Y. Kerr, "SMOS. the mission and the system," *IEEE Transactions on Geoscience and Remote Sensing*, vol. 46, no. 3, pp. 587–593, March 2008.

[2] K. McMullan, M. Brown, M. Martín-Neira, W. Rits, S. Ekholm, J. Marti, and J. Lemanzyk, "SMOS: The payload," *IEEE Transactions on Geoscience and Remote Sensing*, vol. 46, no. 3, pp. 594–605, March 2008.

[3] I. Corbella, F. Torres, N. Duffo, V. González-Gambau, A. Camps, and M. Vall-llossera, "On-flight characterization of the SMOS payload during the commissioning phase," in *International Geoscience and Remote Sensing Symposium, IGARSS 2009*, vol. 5. Cape Town, South Africa: IEEE, 12 - 17 July 2009, pp. V–180 – V–183.

[4] I. Corbella, F. Torres, N. Duffo, V. González, A. Camps, and M. Vall-llossera, "Fast processing tool for SMOS data," in *International Geoscience and Remote Sensing Symposium, IGARSS 2008*. Boston(Ma), USA: IEEE, 7 - 11 July 2008.

[5] M. Brown, F. Torres, I. Corbella, and A. Colliander, "SMOS calibration," *IEEE Transactions on Geoscience and Remote Sensing*, vol. 46, no. 3, pp. 646–658, March 2008.

[6] I. Corbella, F. Torres, A. Camps, A. Colliander, M. Martín-Neira, S. Ribó, K. Rautiainen, N. Duffo, and M. Vall-llossera, "MIRAS end-to-end calibration. Application to SMOS L1 processor," *IEEE Transactions on Geoscience and Remote Sensing*, vol. 43, no. 5, pp. 1126–1134, May 2005.

[7] I. Corbella, F. Torres, N. Duffo, M. Martín-Neira, V. González-Gambau, A. Camps, and M. Vall-llossera, "On-ground characterization of the SMOS payload," *IEEE Transactions on Geoscience and Remote Sensing*, vol. 47, no. 9, pp. 3123–3133, September 2009.

[8] F. Torres, V. González-Gambau, and C. González-Haro, "One-point calibration in interferometric radiometers devoted to earth observation," in *Proceedings of SPIE Europe Remote Sensing 2008*. Cardiff. Wales, United Kingdom: SPIE Europe Remote Sensing 2008. Sensors, Systems, and Next-Generation Satellites XII., 15-18 september 2008.

[9] I. Corbella, F. Torres, A. Camps, N. Duffo, and M. Vall-llossera, "Brightness temperature retrieval methods in synthetic aperture radiometers," *IEEE Transactions on Geoscience and Remote Sensing*, vol. 47, no. 1, pp. 285–294, January 2009.

[10] G. Macelloni, M. Brogioni, P. Pampaloni, A. Cagnati, and M. R. Drinkwater, "DOMEX 2004: An experimental campaign at Dome-C antarctica for the calibration of spaceborne low-frequency microwave radiometers," *IEEE Transactions on Geoscience and Remote Sensing*, vol. 44, no. 10, pp. 2642–2653, October 2006.

Geoscience and Remote sensing Symposium: MICRORAD 2010 (article II)

ONE POINT CALIBRATION IN INTERFEROMETRIC RADIOMETERS: MIRAS/SMOS PRELIMINARY RESULTS

F. Torres[(1)], I. Corbella[(1)], N. Duffo[(1)], V. González-Gambau[(1)], I. Durán[(1)], M. Pablos[(1)] and M. Martín-Neira[(2)]

[(1)]Remote Sensing Laboratory, Universitat Politècnica de Catalunya, Barcelona
SMOS Barcelona Expert Centre. e-mail: xtorres@tsc.upc.edu
[(2)]European Space Agency, European Space Research and Technology Centre, Noordwijk, Holland

ABSTRACT

After the successful launch of the SMOS satellite, on November 2009 at 02:50 CET (01:50 UT) from the Plesetsk Cosmodrome in northern Russia, a preliminary evaluation of the payload calibration strategy has been undertaken in order to assess the instrument performance and establish the operational measurement and calibration configuration. With this objective in mind, this work presents a preliminary study on the performance of the amplitude calibration strategy, a key issue in achieving a stable and accurate operation of the sensor.

Index Terms— radiometer, interferometer, aperture synthesis, amplitude calibration, error assessment.

1. INTRODUCTION

This work has been conducted in the framework of a project devoted to assess the performance of the MIRAS (Microwave Imaging Radiometer with Aperture Synthesis) instrument [1], the single payload of the ESA-SMOS mission [2]. The MIRAS consists of a Y-shape interferometric radiometer basically formed by 72 receivers called LICEF (Lightweight Cost Effective Front End) placed along the three arms. Cross-correlations of the signals collected by each receiver pairs "k,j" give the samples of the so-called visibility function, V_{kj}, which develops into a brightness temperature map by means of a Fourier synthesis technique. Amplitude calibration has a major impact in the final performance since amplitude errors in the visibility samples are directly translated into image distortion (the so-called pixel bias) through this Fourier synthesis process.

MIRAS measures normalized correlations M_{kj} by means of 1-bit digital correlators. As detailed in [3], these measurements are denormalized according to

$$V_{kj} = \frac{\sqrt{T_{sys_{Ak}} T_{sys_{Aj}}}}{G_{kj}} M_{kj}\,,\; T_{sys_{Ak}} = \frac{v_{Ak} - v_{offk}}{G_k^A} \qquad (1)$$

A PMS (Power Measuring System) in each LICEF is used to measure the equivalent system temperature T_{sysAk} (A=V,H) at each antenna plane. The PMS gain at the antenna plane G_k^A and the offset v_{offk} are calibrated by means of the so-called *two-level four-point method* [3]. This calibration procedure makes use of two-level (HOT and WARM) noise sources (CAS=Calibration System) that injects the signals to the LICEF C port by means of the a noise distribution network. A switch placed at the LICEF front end is used to select the measurement mode.

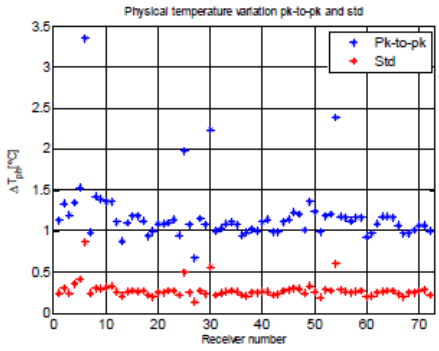

Figure 1. The physical temperature of the 72 LICEF/PMS receivers is well constrained by means of the thermal control.

2. IN-FLIGHT AMPLITUDE CALIBRATION PERFORMANCE

The orbital temperature drift of the 72 receivers is well constrained by the thermal control (fig. 1). However, this small temperature swing produces a non-negligible PMS gain drift that must be corrected for. In this sense, PMS gain in measurement mode at a physical temperature T_{phi} is estimated as

$$G_k^A(T_{ph_i}) = G_k^A(T_{ph_0})\left(1 + S_{Tph}^G\left(T_{ph_i} - T_{ph_0}\right)\right) \qquad (2)$$

PMS gain at the calibration temperature $G_k^A(T_{ph_0})$ is estimated by means of the 4P method during an orbit in calibration mode to be performed, tentatively, every month. PMS gain sensitivity to temperature drift has been measured on-ground and in-flight showing good agreement (fig. 2).

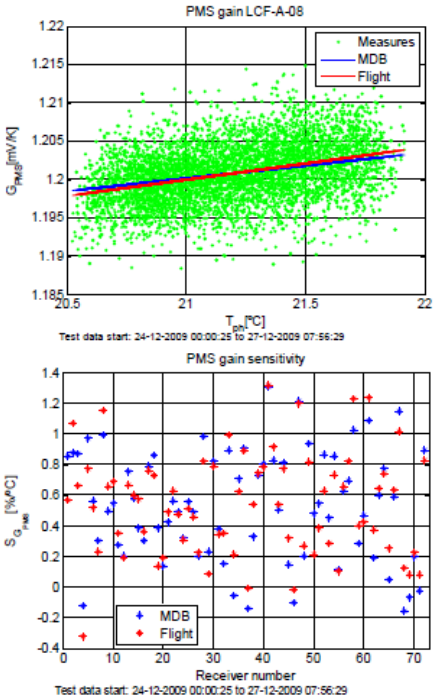

Figure 2. PMS gain sensitivity to physical temperature has been measured both on-ground and in-orbit, showing a high degree of consistency (top). The PMS gain presents low sensitivity to temperature drift (bottom).

PMS gain is foreseen to be calibrated periodically, with an estimated intercalibration period of about two weeks to be frozen by the end of the commissioning phase. Currently, more frequent calibration events during commissioning phase are showing PMS gain pk-to-pk residual drift constrained to ± 0.6 % with relation to the mean value of each PMS in an one month period, well within mission requirements (fig. 3).

3. ONE POINT CALIBRATION

The so-called "one-point calibration" [4][5] is an alternative PMS calibration method that has been developed, as a risk mitigation approach, with two objectives:

- Evaluate (and correct if required) CAS S-parameter residual errors during deep sky calibration.
- Alternative method to track PMS orbital gain drift by means of periodic U-noise injection

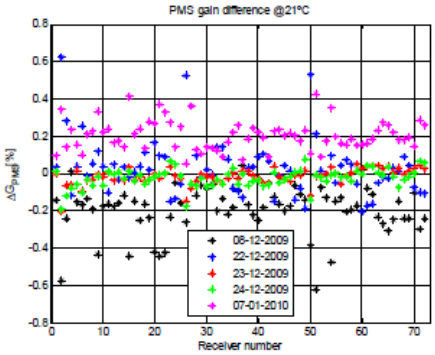

Figure 3. Mean gain drift for each of the 72 PMS gains with relation to their mean value along the one month intercalibration period. Pk-to-pk residual drift below ±0.6%, well within mission requirements.

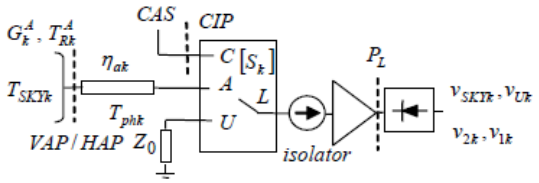

Figure 4. LICEF/PMS front-end scheme to illustrate the one-point calibration scheme.

3.1 Validation of CAS coefficients

Figure 4 gives the block diagram of the PMS front end, showing the main "1P calibration" magnitudes. During periodic (one month) deep sky views, the PMS is simultaneously calibrated by means of the internal 4P CAS system at the calibration plane CIP and by means of the external 1P calibration at the antenna plane. This last is given by

$$G_{1Pk}^A = \frac{v_{Uk} - v_{SKYk}}{T_{phk} - T_{SKYk}} \tag{3}$$

On the other hand, when translated to the antenna plane, the internal PMS 4P gain is given by [3]:

$$G_{4Pk}^A = \frac{v_{2k} - v_{1k}}{T_{CAS_N}^2 - T_{CAS_N}^1} \frac{\left|S_{LA_k}\right|^2}{\left|S_{LC_k}\right|^2} \frac{\left|S_{N0}\right|^2}{\left|S_{k0}\right|^2} \eta_{A_k} \tag{4}$$

As these two gains are computed at the same plane and at the same temperature, they must be equal:

$$G_{1Pk}^A = G_{4Pk}^A \tag{5}$$

In order to evaluate the error and compute a correction coefficient, the magnitudes are rearranged in the so-called C_{Nk} coefficients. One is computed from the on-ground parameters. The other uses the flight measurements and can be computed during each external calibration (deep sky views) if required:

$$C_{Nk}^{gnd} = \frac{\left|S_{LA_k}\right|^2}{\left|S_{LC_k}\right|^2}\frac{\left|S_{N0}\right|^2}{\left|S_{k0}\right|^2}\eta_{A_k} \qquad (6)$$

$$C_{Nk}^{A} = \frac{T_{CASN}^{2} - T_{CASN}^{1}}{v_{2k} - v_{1k}}\frac{v_{Uk} - v_{SKYk}}{T_{Uk} - T_{SKYk}^{A}} \qquad (7)$$

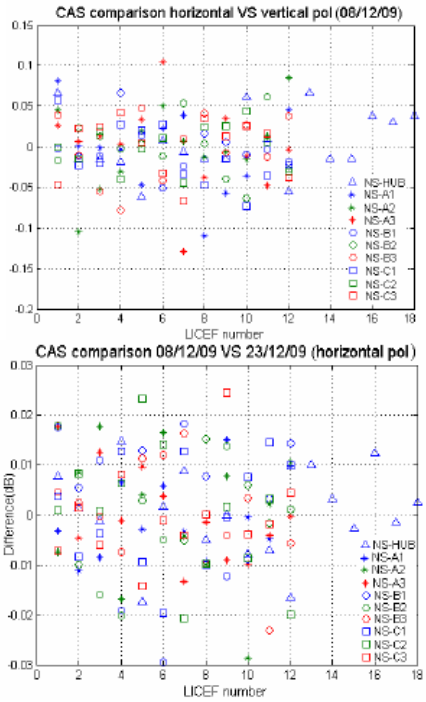

Figure 5. The CAS correction factors, measured at the antenna plane, show low dependency on polarization configuration (top) and very good one-month intercalibration stability (bottom). LICEF numbers correspond to receivers within the HUB (18) or arm segments (12).

The error in the C_{Nk} coefficients can be assigned to a CAS correction factor to force $G_{1Pk}^{A} = G_{4Pk}^{A}$. In order to check the consistency of this correction, some analysis has been undertaken. First, it has been shown that the CAS correction factor presents low dependency on the polarization configuration of the receiver (horizontal or vertical), proving that the dominant error mainly comes from the noise distribution network (fig. 5, top). In second place, the CAS correction factor shows a good repeatability between one-month external calibration events (fig. 5, bottom). After applying the external CAS correction factors the internal 4P PMS gain and the external 1P PMS gain match to 0.023 dB rms error (fig. 6).

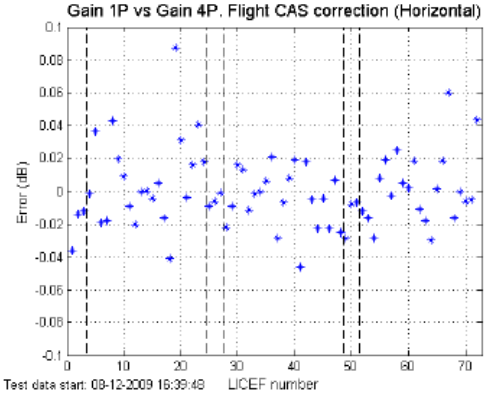

Figure 6. After CAS correction by means of external calibration PMS 1P gain and internal 4P gain match to 0.023 dB RMS

3.2 PMS gain correction by periodic U-noise injection

This method was been devised as an alternative PMS gain estimation to be used in the case that periodic inter-orbit calibration was required. On-ground tests revealed some degree of hysteresis in the behaviour of PMS gain under fast and/or large temperature swings [5]. Since receiver noise temperature showed a better behaviour, in-orbit internal calibration was foreseen by periodically switching the receiver to the internal matched load (U-noise). In this case, PMS gain at the calibration physical temperature T_{phi} is given by

$$G_k^A\left(T_{ph_i}\right) = \frac{v_{Uk} - v_{offk}}{T_{Rk}^A\left(T_{ph_i}\right) + T_{ph_i}} \qquad (8)$$

Where, receiver temperature at T_{phi} is estimated as

$$T_{Rk}^A\left(T_{ph_i}\right) = T_{Rk}^A\left(T_{ph0}\right)\left(1 + S_{Tph}^{TR}\left(T_{ph_i} - T_{ph0}\right)\right) \qquad (9)$$

The reference receiver temperature $T_{Rk}^A\left(T_{ph_0}\right)$ is estimated by means of the 4P method during external calibration (deep sky views) at physical temperature T_{ph0}. Their sensitivity to temperature (about 0.75 K/ºC) was measured during the on-ground characterization when the instrument was tested at the Large Space Simulator (LSS) in Nordwijk, Holand (ESA) [5].

Figure 7 (top), shows an example of this calibration approach applied to unit 30 (LCF-B-03), which is one of the

four outlier units presenting larger temperature swing (fig. 1). The instrument was in calibration mode during a few orbits to assess the behaviour in temperature of several calibration parameters. The black line gives PMS gain calibrations performed every 30 s. The blue line shows the estimation of PMS gain by means of (2). The reference gain has been computed as the mean value for all the orbits, whereas the orbital drift is tracked by using the temperature measurements from a thermistor placed in the front end of each unit, and the sensitivity measured in flight (fig. 2). The effect of hysteresis is clearly seen in the comparison of the two plots (black and blue lines).

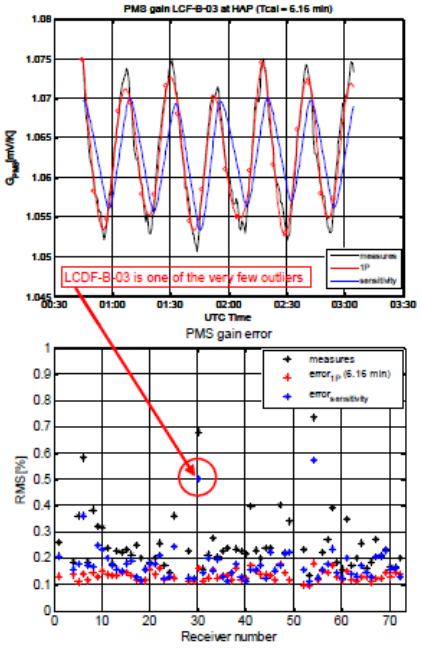

Figure 7. While PMS gain orbital drift presents a small amount of hysteresis, receiver noise temperature is well correlated to temperature drift. This allows a very good track of PMS gain by periodic (6 min) U-noise injection, aligned to the LO phase track mode (Top). However, RMS residual error well within specifications and correction by means of sensitivity has been selected to maximize observation mode (bottom).

On the other hand, the red line presents spline interpolation from 1P calibration PMS gain estimations every 6 min (red dots). In this case, since receiver temperature shows lower hysteresis [5], PMS gain can be tracked by periodic measures of the internal matched load (U-noise injection). Figure 6, bottom, shows the PMS rms gain error for the three methods analyzed from flight data during the first months of the commissioning phase:

a) PMS constant value as the mean value computed from several orbits in calibration mode (black stars). In this case, the error is caused by orbital temperature swing.
b) PMS estimation using the previous value and temperature swing compensation by means of the PMS sensitivity to temperature (blue stars).
c) PMS estimation by means of periodic (6 min) measurements of the matched load (U-noise injection).

Although method c) is the more accurate, method b) has been selected since gives an error well below the 1% PMS system gain error requirement and minimizes the loss of snap shots (maximum observation mode configuration)

4. CONCLUSIONS

In-orbit MIRAS/SMOS amplitude calibration performs well within expectations. Preliminary results during the commissioning phase show that low orbital temperature swing, very good stability and careful temperature compensations keeps PMS gain estimation well below the 1% system error requirement.

5. ACKNOWLEDGMENT

This work was supported by the European Space Agency and EADS-CASA Space Division in the frame of the SMOS project "SMOSops Receiver Technology Study" and by the Spanish Ministry of Science and Innovation and FEDER under project TEC2008-06764-C02-01.

6. REFERENCES

[1] M. Martín-Neira and J. M.Goutoule, "A two-dimensional aperture synthesis radiometer for soil moisture and ocean salinity observations ESA bulletin, no. 92 pp 95-104, November 1997.
[2] Y. Kerr, J. Font, P. Waldteufel, M. Berger. (2000). The Second of ESA's Opportunity Missions: The Soil Moisture and Ocean Salinity Mission–SMOS, ESA Earth Observation Quart. 66, 18f.
[3] I. Corbella, F. Torres, A. Camps, A. Colliander, M. Martín-Neira, S. Ribó, K. Rautiainen, N. Duffo and M. Vall-llossera. "MIRAS end-to-end calibration. Application to SMOS L1 processor." IEEE Transactions on Geoscience and Remote Sensing. Vol. 43, May 2005, pp:1126-1134.
[4] F. Torres, I. Corbella, A. Camps, N. Duffo, M. Vall-llossera, S. Beraza, C. Gutiérrez and M. Martín-Neira. "Denormalization of visibilities for in-orbit calibration of interferometric radiometers". IEEE Transactions on Geoscience and Remote Sensing. Vol. 44, No. 10, pp 2679- 2686. Oct. 2006.
[5] F. Torres, V. Gonzàlez-Gambau, C. Gonzàlez-Haro. "One-point calibration in interferometric radiometers devoted to Earth observation". Proceedings SPIE Europe Remote Sensing 2008. Sensors, Systems, and Next-Generation Satellites XII. Cardiff. Wales, United Kingdom. 15-18 September 2008.

Geoscience and Remote sensing Symposium: IGARSS 2010 (article I)

SOME RESULTS ON SMOS-MIRAS CALIBRATION AND IMAGING

Ignasi Corbella[(1)], Francesc Torres[(1)], Nuria Duffo[(1)], Verónica González-Gambau[(1)], Israel Duran[(1)], Miriam Pablos[(1)], Manuel Martín-Neira[(2)]

(1) Remote Sensing Laboratory, Universitat Politècnica de Catalunya (UPC).
C/ Jordi Girona 1-3. 08034 Barcelona, Spain.
(2) European Space Agency (ESA-ESTEC) Noordwijk. The Nederlands
contact e-mail: corbella@tsc.upc.edu

ABSTRACT

After the six-month long In-Orbit Commissioning Phase (IOCP) the SMOS satellite started to work in its fully operational mode. During the IOCP, the payload MIRAS was completely characterized, both in short- and long-term, and the optimum calibration rate for in-flight operation was established. The results show that the amplitude of the visibility is very stable, thus allowing a very low calibration rate, and that the phase has a systematic and periodic variation, easily tracked with short but frequent internal calibration sequences. Absolute calibration for antenna temperature is carried out by external maneuvers to account for drift in the reference Noise Injection Radiometer. Brightness temperature images of good quality are obtained by inverting the calibrated visibility. The images show features compatible with ocean salinity over ocean and soil moisture over land.

1. INTRODUCTION

SMOS (acronym of Soil Moisture and Ocean Salinity) is an European Space Agency (ESA) mission aimed at providing global maps of soil moisture over land and sea surface salinity over oceans [1]. The mission payload is the Microwave Imaging Radiometer with Aperture Synthesis (MIRAS) [2, 3], an L-band, Y-shape 2D interferometric radiometer manufactured by EADS-CASA Espacio (ES) and integrated to a generic PROTEUS platform manufactured by Thales Alenia Space. SMOS was successfully launched on 2nd November 2009 from the Plesestz cosmodrome by a launcher from Eurockot. The payload was switched on on 17th November and since then raw data measurements are being received regularly by the ground segment data acquisition station, located near Madrid (ES). After due processing, they provide the first-ever global brightness temperature maps at L-band.

The work was supported by the European Space Agency and EADS-CASA Space Division under ESTEC contract 17950/03/NL/FF-SMOS; and by the Spanish Ministry of Science and Innovation and FEDER under projects TEC2008-06764-C02-01 and MIDAS-5 ESP2007-65667-C04-0

The first six months of operation were dedicated to make a complete and systematic check of the payload, including the retrieval of all calibration parameters and their temperature dependance [4]. Good brightness temperature images can be produced by inverting the calibrated visibility, which is a good indicator of the quality of the calibration. This paper shows some of the results, especially those dealing with the main calibration parameters and their stability; and the brightness temperature imaging. All the results have been obtained using the MIRAS testing software [5], developed by the UPC team.

2. CALIBRATION

Calibration is needed to provide accurate values of visibility for all receiver pairs and antenna temperature for at least one element. Besides, image reconstruction algorithms [6, 7] need the fringe washing function shape and the flat target response [8]. MIRAS uses a combination of both external and internal calibration to estimate all the time varying parameters [9]. Stable parameters such as antenna patterns, S-parameters of noise distribution network and others, are directly used from on-ground characterization [10].

The outcome of the MIRAS calibration system consists of the following parameters: the PMS (power monitoring system) gain G_k and offset v_{off}, the correlation complex gain G_{kj} in amplitude and phase, the NIR source noise temperature T_{NA} and the the normalized fringe washing function [11]. All of them are periodically updated during the mission to account for instrumental drifts. Additionally, the Flat Target Response [8] is also considered a calibration parameter.

2.1. Internal and External calibration

External calibration is performed by commanding the platform to go into inertial attitude. In this case, the instrument starts to rotate with respect to the earth-fixed coordinate system until the earth disappears from the field of view of the antenna. At this point, the radiometer is measuring the brightness temperature of a fixed point of the sky, which is chosen

to be near the galactic pole to avoid influence from the Galactic emission. Since the sky brightness temperature at L-band is known [12], the calibration parameters of the instrument are adjusted so as to match the measurements to this absolute reference. External calibration provides the best quality of calibration and it is the only way to obtain the absolute accuracy of the instrument. However, the pointing maneuvers cannot be performed too often and the impact in terms of percentage of time dedicated to calibration is high.

Internal calibration is carried out by periodically injecting noise to all receivers using an internal source and a distribution network [11]. It tracks fast variations of parameters, but for those requiring a known calibration standard, it cannot provide their absolute values. In this case, the accuracy of the internal calibration relies on the quality of a secondary standard, which has to be previously calibrated using the external view. On the other hand, noise injection is very fast and is easily interspersed between normal measurement operation.

The calibration method utilized for each of the parameters is the following

- PMS gain: External calibration with periodic tracking by internal calibration
- PMS offset: Internal calibration.
- Correlator gain (amplitude and phase): Internal calibration.
- NIR internal noise temperature: External calibration
- Fringe washing function parameters: Internal calibration

2.2. Calibration rate

Most of the calibration procedures and measurement sequences were precisely defined during the on-ground characterization of the instrument [10]. Then, the in-orbit commissioning phase has been essential to adjust the timing of calibration events in accordance with the real in-flight instrument operation [4]. Particularly, the following general trends have been observed:

- Flat Target Response: Stable, to be corrected only twice a year.
- Fringe washing function shape: The same stability as the Flat Target Response
- Visibility amplitude: To be updated once every 8 weeks
- Antenna temperature: Needs to be calibrated every 2 weeks
- Visibility phase. A calibration is needed every 10 minutes.

Some parameters, as the PMS gain and offsets have been accurately characterized in terms of temperature variation though the computation of sensitivity parameters. This, in combination with a very low physical temperature drift of the whole instrument, has allowed to reduce the need for their frequent calibration updates. New sensitivity parameters have been derived during the in-orbit commissioning phase and they are very well in agreement with the ones obtained during the ground characterization.

As a general rule, the percentage of total time devoted to calibration must be the minimum, just to ensure that the quality of the measurements is according to the requirements. In SMOS, about one percent of the time is used in calibration. This has been achieved by minimizing the number of external calibration maneuvers, using accurate thermal characterization and agreeing a compromise value for the parameters changing the fastest (phase of visibility).

2.3. Calibration parameters trend

Figure 1 shows a plot of the long-term stability of the amplitude of correlator gain (G_{kj}), along with the short-term variation of its phase for a baseline having two different local oscillators. As seen, the amplitude has negligible variation from one calibration event to another. On the other hand, the phase variation is large, but can be easily tracked by frequent internal calibration sequences: every ten minutes a short burst of correlated noise is injected during 1.2 seconds to all receivers to measure this phase.

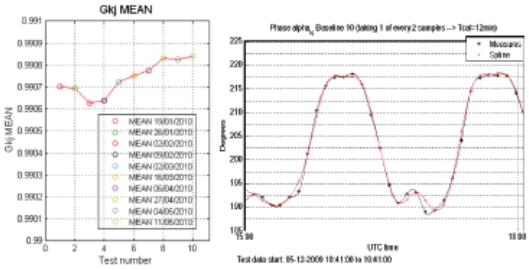

Fig. 1. Left: Stability of the amplitude of G_{kj} along time. Right: phase of G_{kj} variation due to local oscillator phase drift

Figure 2 shows the measurements of PMS gain during a specific test carried out to derive its thermal sensitivity. The figure shows a comparison between the measured gain and the one derived from the physical temperature and the sensitivity, demonstrating that the gain can be accurately tracked just by measuring the temperature sensors.

Figure 3 shows the long-term stability of both PMS gain and offset. It shows the difference of the averaged values retrieved during ten calibration events distributed regularly between 12th January to 11th May 2010. It turns out that the long-term drift is lower than 0.5 mV for the offset and 0.2% for the gain, which has led the the proposal of a PMS intercalibration period of eight weeks to be conservative.

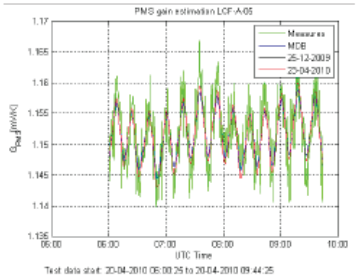

Fig. 2. PMS gain tracking using the sensitivity parameter

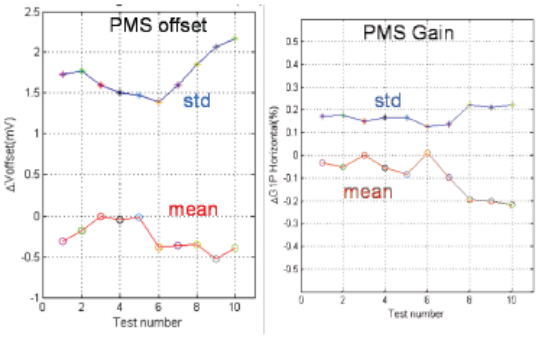

Fig. 3. Long term PMS calibration. The test numbers correspond to different calibration events carried out in a 4-month span, from 19th January 2010 to 11th May 2010. Left: Offset, Right: Gain

3. IMAGING

Figure 4 shows an example of several snapshots in a pass over Australia in dual polarization mode. Since the polarization is mixed in the field of view, the definitions Horizontal and Vertical refer to the sub-satellite track. These images were obtained just two weeks after the payload switch-on with still uncomplete calibration. Nevertheless, they already show that the instrument is capable of producing good brightness temperature images. Improved images were obtained after the instrument was fully characterized and calibrated. Figure 5 shows two images corresponding to four-day cumulated data over Australia acquired in January 2010 and in February 2010. Between both dates there were strong rain events in the eastern part of Australia due to the pass of the tropical storm "Olga". This is clearly visible in the images, where lower britghtness temperatures are measured after the pass of the storms.

Over the ocean the brightness temperature is lower than in land and has also a much smaller dynamic range than in land. On the other hand its spatial variation is much smoother, allowing to perform spatial averages. Figure 6 shows the averages of 150 consecutive snapshots over the ocean both

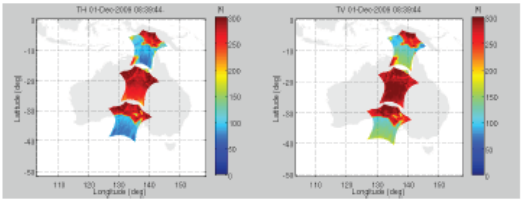

Fig. 4. L-Band brightness temperature maps at instrument reference frame retrieved over Australia in a descending orbit Left: H-polarization at satellite track. Right: V-polarization at satellite track

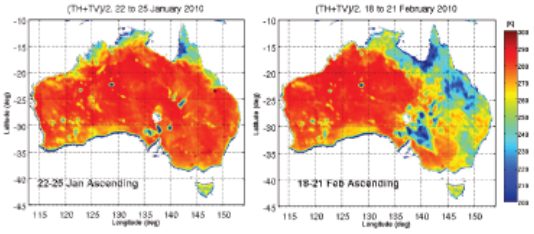

Fig. 5. Average of horizontal and vertical L-Band brightness temperature. Four-day cumulated data for ascending orbits. Left: 22nd to 25th January 2010. Right 18th to 21th February 2010.

for horizontal and vertical channel. The strong dependance with the incidence angle, characteristic of the ocean brightness temperature is clearly visible in these images. Also, some artifacts can be seen in the extended alias-free zone, in which a model is used to estimate the brightness temperature of the sky alias zone and the result subtracted to the images. This procedure is not eliminating all the errors in the sky alias zone. To assess the instrument capability of making brightness temperature images, only the strict alias-free zone has been considered in subsequent processing.

As an example, figure 7 shows the image of four-day cumulated first Stokes parameter over the Atlantic. As expected, it has lower values in those regions where the salinity is known to be larger according to the NOAA climatological data.

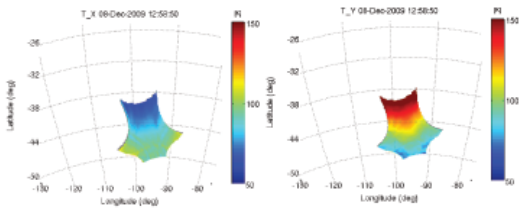

Fig. 6. Average of 150 snapshots in for a region of pure ocean. Left: Horizontal polarization. Right: Vertical polarization.

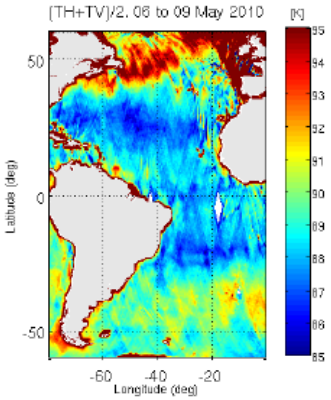

Fig. 7. Image of cumulated first Stokes parameter ($(T_H + T_V)/2$) over the Atlantic for 6th to 9th May 2010. The variation is compatible with the global maps of salinity available from NOAA climatological data.

4. CONCLUSIONS

SMOS is producing high quality brightness temperature images thanks to the accurate characterization and calibration of the instrument MIRAS, which was performed first on ground and later in flight conditions during the In-Orbit Commissioning phase. Most of the calibration parameters have very small drift with time and temperature, while the others are accurately tracked using sensitivity coefficients or specially designed internal calibration sequences. The overall time dedicated to calibration is slightly larger that 1% of the measurement time, in agreement with the mission requirements. Images of first Stokes parameter over land and ocean show geophisical features compatible with soil moisture and salinity respectively.

5. REFERENCES

[1] Hubert Barré, Berthyl Duesmann, and Yann Kerr, "SMOS. the mission and the system," *IEEE Transactions on Geoscience and Remote Sensing*, vol. 46, no. 3, pp. 587–593, March 2008.

[2] Manuel Martín-Neira and Jean Marie Goutoule, "MIRAS a two-dimensional aperture-synthesis radiometer for soil moisture and ocean salinity observations," *ESA Bulletin*, , no. 92, pp. 95–104, November 1997.

[3] Kevin McMullan, Michael Brown, Manuel Martín-Neira, W Rits, S Ekholm, J Marti, and Jerzky Lemanzyk, "SMOS: The payload," *IEEE Transactions on Geoscience and Remote Sensing*, vol. 46, no. 3, pp. 594–605, March 2008.

[4] Ignasi Corbella, Francesc Torres, Nuria Duffo, Verónica González-Gambau, Miriam Pablos, Israel Duran, and Manuel Martín-Neira, "First results on MIRAS calibration and overall SMOS performance," in *11th Specialist Meeting on Microwave Radiometry and Remote Sensing of the Environment - μRad 2010*, Washington DC, USA, 1-4 March 2010, pp. 1–4.

[5] Ignasi Corbella, Francesc Torres, Nuria Duffo, Verónica González, Adriano Camps, and Mercè Vall-llossera, "Fast processing tool for SMOS data," in *International Geoscience and Remote Sensing Symposium, IGARSS 2008*, Boston(Ma), USA, 7 - 11 July 2008, number II, pp. 1152–1155, IEEE.

[6] Ignasi Corbella, Francesc Torres, Adriano Camps, Nuria Duffo, and Mercè Vall-llossera, "Brightness temperature retrieval methods in synthetic aperture radiometers," *IEEE Transactions on Geoscience and Remote Sensing*, vol. 47, no. 1, pp. 285–294, January 2009.

[7] Adriano Camps, Mercè Vall-llossera, Ignasi Corbella, Nuria Duffo, and Francesc Torres, "Improved image reconstruction algorithms for aperture synthesis radiometers," *IEEE Transactions on Geoscience and Remote Sensing*, vol. 46, no. 1, pp. 146–158, January 2008.

[8] Manuel Martín-Neira, Martin Suess, and Juha Kainulainen, "The flat target transformation," *IEEE Transactions on Geoscience and Remote Sensing*, vol. 46, no. 3, pp. 613–620, March 2008.

[9] Michael Brown, Francesc Torres, Ignasi Corbella, and Andreas Colliander, "SMOS calibration," *IEEE Transactions on Geoscience and Remote Sensing*, vol. 46, no. 3, pp. 646–658, March 2008.

[10] Ignasi Corbella, Francesc Torres, Nuria Duffo, Manuel Martín-Neira, Verónica González-Gambau, Adriano Camps, and Mercè Vall-llossera, "On-ground characterization of the SMOS payload," *IEEE Transactions on Geoscience and Remote Sensing*, vol. 47, no. 9, pp. 3123–3133, September 2009.

[11] Ignasi Corbella, Francesc Torres, Adriano Camps, Andreas Colliander, Manuel Martín-Neira, Serni Ribó, Kimmo Rautiainen, Nuria Duffo, and Mercè Vall-llossera, "MIRAS end-to-end calibration. Application to SMOS L1 processor," *IEEE Transactions on Geoscience and Remote Sensing*, vol. 43, no. 5, pp. 1126–1134, May 2005.

[12] David M. Le Vine and Saji Abraham, "Galactic noise and passive microwave remote sensing from space at L-band," *IEEE Transactions on Geoscience and Remote Sensing*, vol. 42, no. 1, pp. 119–129, January 2004.

Geoscience and Remote sensing Symposium: IGARSS 2010 (article II)

ONE POINT CALIBRATION IN INTERFEROMETRIC RADIOMETERS: MIRAS/SMOS PRELIMINARY RESULTS

F. Torres[(1)], I. Corbella[(1)], N. Duffo[(1)], V. González-Gambau[(1)], M. Pablos[(1)], I. Duran[(1)] and M. Martín-Neira[(2)]

[(1)] Remote Sensing Laboratory, Universitat Politècnica de Catalunya
SMOS Barcelona Expert Centre, Spain. xtorres@tsc.upc.edu
[(2)] European Space Agency, European Space Research and Technology Centre (ESTEC), The Netherlands

ABSTRACT

After the successful SMOS launch on November 2009 a comprehensive evaluation of the payload calibration strategy has been undertaken during a six months commissioning phase. In the frame of the activities devoted to assess the instrument performance and to establish the operational measurement and calibration configuration, this work presents a study on the performance of the so called "one-point" method, an alternative calibration scheme developed as a risk mitigation approach.

1. INTRODUCTION

This work has been conducted in the framework of a project devoted to assess the performance of the MIRAS (Microwave Imaging Radiometer with Aperture Synthesis) instrument [1], the single payload of the ESA-SMOS mission [2]. The MIRAS consists of a Y-shape interferometric radiometer basically formed by 72 receivers called LICEF (Lightweight Cost Effective Front End) placed along the three arms. Cross-correlations of the signals collected by each receiver pairs "k,j" give the samples of the so-called visibility function, V_{kj}, which develops into a brightness temperature map by means of a Fourier synthesis technique. Amplitude calibration has a major impact in the final instrument performance since amplitude errors in the visibility samples are directly translated into image distortion (the so-called pixel bias) through this Fourier synthesis process.

MIRAS measures normalized correlations M_{kj} by means of 1-bit/2-level digital correlators. As detailed in [3], these measurements are denormalized according to

$$V_{kj} = \frac{\sqrt{T_{sys_{Ak}} T_{sys_{Aj}}}}{G^A_{kj}} M_{kj}\,,\; T_{sys_{Ak}} = \frac{v_{Ak} - v_{offk}}{G^A_k} \quad (1)$$

A PMS (Power Measuring System) in each LICEF is used to measure the equivalent system temperature $T_{sys,Ak}$ (A=V,H) at each antenna plane. The fringe-wash term G^A_{kj}, PMS gain at the antenna plane G^A_k and PMS offset v_{offk} are currently calibrated by means of the so-called *two-level four-point (4P) method* [3]. This calibration procedure makes use of the CAS (CAlibration System) based on two-level noise sources (hot and warm) that inject the signals to the LICEF calibration port C by means of a noise distribution network. A highly stable radiometer called NIR (Noise Injection Radiometer) measures the hot and warm signals at the CAS output port N, to be used as references to calibrate the PMS units. A switch placed at the LICEF front end is used to select the instrument operating configuration: measurement mode (V/H) or calibration mode (C/U).

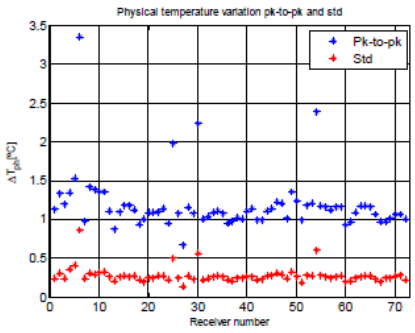

Figure 1. The physical temperature of the 72 LICEF units is well constrained by means of thermal control.

The orbital temperature drift of the 72 receivers is well constrained by the thermal control (fig. 1). However, this small temperature swing produces a non-negligible orbital PMS gain drift that must be corrected for. At each snap shot, PMS_k gain in measurement mode is estimated as

$$G^A_k(T_{phi_k}) = G^A_k(T_{ph0_k})\left(1 + S^{G_k}_{Tph}\left(T_{phi_k} - T_{ph0_k}\right)\right) \quad (2)$$

Where T_{phi_k} is the measurement physical temperature, $G^A_k(T_{ph0_k})$ is PMS gain at the calibration temperature T_{ph0_k} which is estimated by means of the *two-level four-point* method during an orbit in calibration mode to

be performed every two months. Finally, $S_{Tph}^{G_k}$ is PMS gain sensitivity to temperature drift, which has been measured both on-ground and in-flight for each LICEF, showing good agreement.

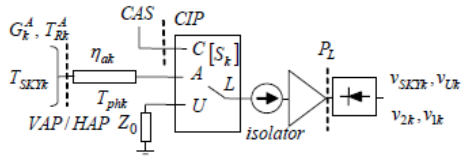

Figure 2. LICEF/PMS front-end scheme to illustrate the one-point calibration scheme.

2. ONE POINT AMPLITUDE CALIBRATION

The so-called *one-point (1P) calibration* [4][5] is an alternative PMS calibration method that has been developed, as a risk mitigation approach, with two main objectives:

- Evaluate (and correct if required) ground CAS S-parameter residual errors, during deep sky calibration.
- Alternative method to track PMS orbital gain drift by means of periodic U-noise injection

As an exploratory option, the instrument has also been tested to operate in the so-called "all-LICEF" mode. In this mode, the *one-point method* is used to estimate the antenna temperature (zero baseline visibility) as the mean value given by the 72 LICEF units.

2.1. Validation of CAS coefficients

Fig. 2 gives the block diagram of the PMS front end, showing the main 1P calibration magnitudes. During periodic (e.g. one month) deep sky views, the PMS is simultaneously calibrated by means of the internal 4P CAS system at the calibration plane CIP and by means of the external 1P calibration at the antenna planes (VAP/HAP). For a perfectly matched passive front end at a constant temperature T_{phk}, [4] shows that switching the instrument to the internal matched load (U port) is equivalent to place an absorber at the same physical temperature in front of the antenna. In this way, 1P PMS_k gain at the antenna plane is given by

$$G_{1Pk}^{A} = \frac{v_{Uk} - v_{SKYk}}{T_{phk} - T_{SKYk}} \qquad (3)$$

On the other hand, when translated to the antenna plane, the internal PMS 4P gain is given by [3]:

$$G_{4Pk}^{A} = \frac{v_{2k} - v_{1k}}{T_{CAS\,N}^{2} - T_{CAS_N}^{1}} \frac{\left|S_{LA_k}\right|^2 \left|S_{N0}\right|^2}{\left|S_{LC_k}\right|^2 \left|S_{k0}\right|^2} \eta_{A_k} \qquad (4)$$

Where $T_{CAS\,N}^{1,2}$, are the CAS hot and warm temperatures as measured by the reference radiometer (NIR) at CAS port N, S_{N0}, S_{k0} are the CAS s-parameters from the noise source to the reference radiometer and PMS_k calibration ports, respectively, η_{A_k} is the antenna efficiency (A=V/H) and, finally, S_{LA_k}, S_{LC_k} are the switch s-parameters. As the 1P and 4P gains are computed at the same plane and at the same temperature, an error free instrument would yield:

$$G_{1Pk}^{A} = G_{4Pk}^{A} \qquad (5)$$

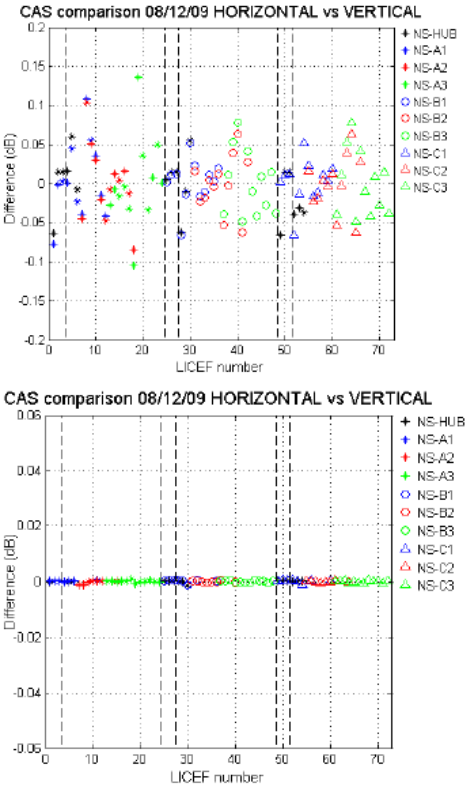

Figure 3. Comparison of CAS correction factors computed from horizontal and vertical amplitude calibrations by using ground antenna efficiencies (top) and flight antenna efficiencies (bottom).

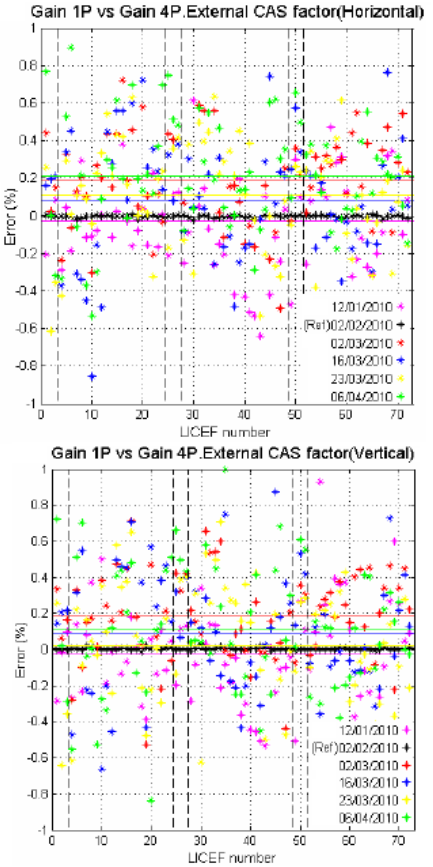

Figure 4. Matching between 1P and 4P PMS calibration after CAS and antenna efficiency correction (02/02/2010) for a number of calibration events. Matching well below the 1% RMS error requirement in a three months period.

In order to evaluate the error and compute a correction coefficient, the parameters in (5) are rearranged in the so-called C_{Nk} coefficients. One of them is computed from the on-ground parameters.

$$C_{Nk}^{gnd} = \frac{\left|S_{LA_k}\right|^2}{\left|S_{LC_k}\right|^2}\frac{\left|S_{N0}\right|^2}{\left|S_{k0}\right|^2}\eta_{A_k} \qquad (6)$$

The other one uses the flight measurements and is computed during each external calibration (deep sky views):

$$C_{Nk}^{A} = \frac{T_{CAS\,N}^{2} - T_{CAS_N}^{1}}{v_{2k} - v_{1k}}\frac{v_{Uk} - v_{SKYk}}{T_{phk} - T_{SKYk}} \qquad (7)$$

The error in the C_{Nk} coefficients can be assigned to a CAS correction factor to be applied to the CAS ground coefficients. In order to check the consistency of this correction, some analysis has been undertaken and presented hereafter.

The C_{Nk} coefficients can be computed from horizontal and vertical PMS gains. Both magnitudes should be equal, since each LICEF has a single CAS coefficient related to its calibration port CIP. Fig. 3 (top) shows that the ground characterization of the PMS front end is quite good since vertical and horizontal CAS coefficients match to ± 0.14 dB. However, when using antenna efficiencies computed from the external deep sky views, the match is almost perfect (fig. 3, bottom). That is, external calibration decouples the ground characterization errors in antenna efficiency (two values per PMS) from the CAS ground errors (one value per PMS). The good consistency of CAS coefficients computed from horizontal and vertical calibration reveals both the good quality of the measurements and the front-end model.

In second place, the CAS correction factors have shown very good repeatability in a three months period. In Fig. 4 the external antenna efficiency and external CAS factors have been computed from the calibration event on 02/02/2010 (reference calibration). These coefficients have then been used to calibrate the internal 4P gain in different calibration events from 12/01/2010 to 06/04/2010 to be compared with new 1P external calibrations. In this period, the match between internal and external gains remains within ± 1% pk-to-pk, well below the system requirement of 1% RMS error. There is a small 0.2% bias in the error that requires further assessment. In any case, this bias is corrected by the periodic external calibration events.

2.2. PMS gain correction by periodic U-noise injection

This method has been devised as an alternative PMS gain estimation to be used in the case that periodic inter-orbit amplitude calibration was required. On-ground tests revealed some degree of hysteresis in the behaviour of PMS gain under fast and/or large temperature swings [5]. Since receiver noise temperature showed a better behaviour, in-orbit internal calibration was foreseen by periodically switching the receiver to the internal matched load (U-noise). In this case, PMS_k gain at the calibration physical temperature T_{phi_k} is given by

$$G_k^A\left(T_{phi_k}\right) = \frac{v_{Uk} - v_{offk}}{T_{Rk}^A\left(T_{phi_k}\right) + T_{phi_k}} \qquad (8)$$

Where, receiver temperature at T_{phi} is estimated as

$$T_{Rk}^{A}(T_{phi_k}) = T_{Rk}^{A}(T_{ph0_k}) + S_{Tph}^{TR}\left(T_{phi_k} - T_{ph0_k}\right) \quad (9)$$

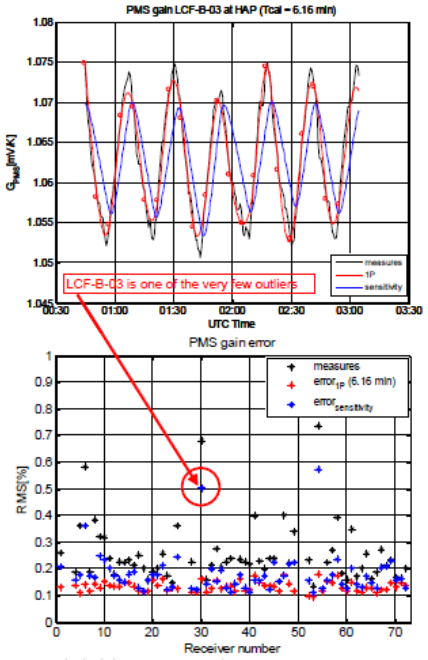

Figure 5. PMS receiver noise temperature is well correlated to temperature drift. This allows a very good track of PMS gain by periodic (6 min) U-noise injection, aligned to the LO phase track mode (Top). However, the 4P PMS gain calibration method has been selected since RMS residual error is well within the 1% rms error requirement (bottom).

The reference receiver temperature $T_{Rk}^{A}(T_{ph0_k})$ is estimated by means of the 1*P* method [5] during external calibration (deep sky views) at the calibration physical temperature T_{ph0_k}. T_{Rk}^{A} sensitivity to temperature (about 0.75 K/ºC) was measured during the on-ground characterization when the instrument was tested at the Large Space Simulator (LSS) in Nordwijk, Holland (ESA) [5].

Figure 5 (top), shows an example of the 1P calibration approach applied to unit 30 (LCF-B-03), which is one of the four outlier units presenting the largest temperature swing (fig. 1). The instrument was in calibration mode during a few orbits to assess the behaviour in temperature of several calibration parameters. The black line gives PMS gain calibrations performed every 30 s. The blue line shows the estimation of PMS gain by means of (2). The reference gain has been computed as the mean value for all the orbits, whereas the orbital drift is tracked by using the temperature measurements from a thermistor placed at the front end in each unit. The effect of a certain amount of hysteresis is clearly seen in the comparison of the two plots (black and blue lines), yielding a moderate rms error (red circle in fig. 5, bottom).

On the other hand, the red line presents spline interpolation from 1P calibration PMS gain estimations every 6 min (red dots). In this case, since receiver temperature shows lower hysteresis [5], PMS gain can be tracked by periodic measures of the internal matched load (U-noise injection). Figure 5, bottom, shows the PMS rms gain error for the three methods analyzed from flight data during the first months of the commissioning phase:

a) PMS gain constant as the mean value computed from several orbits in calibration mode (black stars). In this case, the error is caused by orbital temperature swing.
b) PMS gain estimation using the last calibration (more than one orbit apart) and temperature swing compensation by means of the PMS sensitivity to temperature (blue stars).
c) Inter-orbit PMS estimation by means of periodic (E.g. 6 min) measurements of the matched load (U-noise injection).

Although method c) is the most accurate, method b) has been selected since gives an error well below the 1% RMS system gain error requirement and minimizes the loss of snap shots (maximum observation mode configuration).

2.3. All-LICEF antenna temperature

Fig. 6 shows SMOS antenna temperature -V(0,0)- computed as the mean antenna temperature estimated by the 66 LICEF units. For each LICEF, antenna temperature at the antenna plane is computed as

$$\hat{T}_{Ak} = \frac{v_{Ak} - v_{offk}}{\hat{G}_k^A} - \hat{T}_{Rk}^{A} \quad (10)$$

Where PMS gain $\hat{G}_k^A$, offset v_{offk} and receiver temperature $\hat{T}_{Rk}^{A}$ are computed by means of the external PMS cold sky calibration directly at VAP/HAP, and corrected in physical temperature T_{phk} for each snap shot, as given in (9).

All-LICEF antenna temperature is compared in H/V to the mean antenna temperature measured by the three NIR units. The plots show antenna temperature evolution (horizontal and vertical polarizations) within

an orbit on 02/02/2010. As shown in fig. 6, the coarse behaviour given by the NIR units and the All-LICEF mode is very similar. Some additional analysis reveals that the performance of each single LICEF unit yields a moderate error in the estimation of antenna temperature, however, the average of the 66 LICEF estimations gives a performance similar to the NIR units. Fig. 6 shows the capability of both, the NIR and the all-LICEF mode to track antenna temperature orbital evolution. However, further analysis is still required to fully assess the absolute accuracy of the measurements.

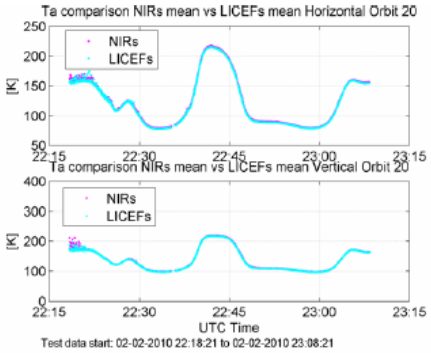

Figure 6. Comparison of antenna temperature (horizontal and vertical polarizations) measured by the all-LICEF mode and by the NIR units on 02/02/2010, showing similar performance.

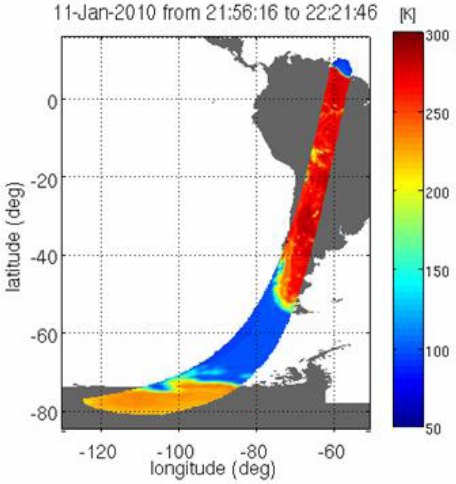

Figure 7. Brightness temperature map retrieved from one orbit in all-LICEF configuration (11-01/2010 all-LICEF test).

In order to illustrate the capability of the one-point calibration method in retrieving V(0,0), fig. 7 presents the brightness temperature retrieval from data collected on January 2010 within the "all-LICEF" test.

3. CONCLUSIONS

In-orbit MIRAS/SMOS amplitude calibration performs well within expectations. First analysis performed during the commissioning phase show that low orbital temperature swing, very good stability and careful temperature compensations keep PMS gain estimation well below the 1% rms system error requirement.

The one point method has proved to work properly both to check (and fine tune) the performance of the current *four point two level* amplitude calibration method and as a risk mitigation alternative to be used, if required, to retrieve the antenna temperature (all-LICEF mode) or to track orbital PMS gain drift.

4. ACKNOWLEDGMENT

Work supported by the European Space Agency and EADS-CASA Space Division in the frame of the SMOS project and by the Spanish Ministry of Science and Innovation and FEDER under projects TEC2008-06764-C02-01 and MIDAS-5 ESP2007-65667-C04-0

6. REFERENCES

1. Martín-Neira, M. and Goutoule, J. M. "A two-dimensional aperture synthesis radiometer for soil moisture and ocean salinity observations *ESA bulletin*, no. 92 pp 95-104, November 1997.
2. Kerr, Y.; Font, J.; Waldteufel, P. & Berger, M. (2000). The Second of ESA's Opportunity Missions: The Soil Moisture and Ocean Salinity Mission–*SMOS, ESA Earth Observation Quart.* 66, 18f.
3. Corbella, I.; Torres, F.; Camps, A.; Colliander, A.; Martín-Neira, M.; Ribó, S.; Rautiainen, K.; Duffo, N & Vall-llossera, M. "MIRAS end-to-end calibration. Application to SMOS L1 processor." *IEEE Transactions on Geoscience and Remote Sensing*. Vol. 43, May 2005, pp:1126-1134.
4. Torres, F.; Corbella, I.; Camps, A.; Duffo, N. Vall-llossera, M.; Beraza, S.; Gutiérrez, C. & Martín-Neira, M. "Denormalization of visibilities for in-orbit calibration of interferometric radiometers". *IEEE Transactions on Geoscience and Remote Sensing*. Vol. 44, No. 10, pp 2679- 2686. Oct. 2006.
5. Torres, F.; Gonzàlez-Gambau, V. & Gonzàlez-Haro, C. "One-point calibration in interferometric radiometers devoted to Earth observation". *Proceedings SPIE Europe Remote Sensing 2008. Sensors, Systems, and Next-Generation Satellites XII. Cardiff*. Wales, United Kingdom. 15-18 September 2008.

ESA's Living Planet Symposium in Bergen (June 2010)

SMOS-MIRAS CALIBRATION AND PERFORMANCE

Ignasi Corbella[1], Francesc Torres[1], Veronica Gonzalez-Gambau[1], Nuria Duffo[1], Miriam Pablos[1], Israel Duran[1], Josep Closa[2], and Manuel Martin-Neira[3]

[1]*Remote Sensing Laboratory, Universitat Politècnica de Catalunya (UPC). C/ Jordi Girona 1-3. 08034 Barcelona, Spain.*
[2]*EADS-CASA Espacio*
[3]*ESA-ESTEC, 2200 AG Noordwijk, The Netherlands*

ABSTRACT

An intense activity has been carried out during the in-orbit commissioning phase of the SMOS (Soil Moisture and Ocean Salinity) mission. Concerning the payload MIRAS (Microwave Imaging Radiometer with Aperture Synthesis) it has been fully characterized using specific orbits dedicated to check all instrument modes. The procedures, already defined during the on-ground characterization, have been repeated so as to obtain realistic temperature characterization and updated internal calibration parameters. External calibration maneuvers have been tested for the first time and have provided absolute instrument calibration, as well as corrections to improve the internal calibration data.

Key words: SMOS; MIRAS; Interferometric Radiometers; Calibration; Imaging.

1. INTRODUCTION

The ESA SMOS satellite was successfully launched on the 2nd November 2009. The six-month long in-orbit commissioning phase started just after launch and included a complete and systematic check of the payload MIRAS, the retrieval of all calibration parameters and a thorough thermal characterization. The mission is now in the operational phase and data products are continuously being generated by the data processing ground segment using the selected algorithms and payload modes of operation.

This paper is focused on the work performed during the payload commissioning. It describes some tests carried out during this phase and the results obtained. All results have been obtained using the MIRAS-Testing Software (MTS) [1], an independent processing tool able to ingest SMOS raw data and produce calibration parameters, calibrated visibility (compatible with level 1A SMOS data) and geolocated brightness temperature (equivalent to the SMOS level 1C).

2. MIRAS CALIBRATION OVERVIEW

A complete description of the MIRAS calibration system can be found in [2]. In general, calibration of an interferometric radiometer such as MIRAS is needed to provide accurate values of visibility for all receiver pairs and antenna temperature (zero baseline visibility) for at least one element. Besides, image reconstruction algorithms [3, 4] need additional calibration parameters, such as the fringe washing function shape and the flat target response [5]. MIRAS uses a combination of both external and internal calibration procedures to estimate all the time varying parameters. On the other hand, stable parameters such as antenna patterns, S-parameters of noise distribution network and others, are directly used from on-ground characterization.

The visibility is derived by the level 1 processor using the following equation

$$V_{kj} = \frac{M_{kj}\sqrt{T_{sys_k}T_{sys_j}}}{G_{kj}} \quad \text{where} \quad T_{sys_k} = \frac{v_k - v_{off_k}}{G_k} \quad (1)$$

where v_k is the measured voltage of the PMS (power measurement system) and M_{kj} the normalized correlation measured by the on-board digital correlator. On the other hand, antenna temperature is measured by three noise-injection radiometers (NIR's) [6] located near the center of the array using

$$T_A = T_U - \eta T_{NA} \quad (2)$$

where T_U is the physical temperature in kelvin measured by a sensor placed in a reference resistor near the antenna, η is the measured Dicke pulse fraction (raw NIR measurement) and T_{NA} the noise equivalent temperature of the internal noise source.

The brightness temperature is computed out of the calibrated visibility (1) by inverting the visibility equation [7].

$$V_{kj} = \iint_{\xi^2+\eta^2\leq 1} T'_{kj}(\xi,\eta)\,\overline{r}_{kj}\left(-\tfrac{u\xi+v\eta}{f_0}\right) e^{-j2\pi(u\xi+v\eta)} d\xi d\eta \quad (3)$$

where $\overline{\overline{r}}_{kj}(\ )$ is the fringe washing function normalized to its value at the origin and T'_{kj} the *modified* brightness temperature:

$$T'_{kj}(\xi,\eta) = \frac{\sqrt{D_k D_j}}{4\pi} \frac{T_B(\xi,\eta) - T_r}{\sqrt{1-\xi^2-\eta^2}} F_{n_k}(\xi,\eta) F^*_{n_j}(\xi,\eta) \tag{4}$$

where T_B is the brightness temperature to be retrieved. In this equation, the only parameter that has eventually to be updated is the normalized fringe washing function, which is approximated by the following analytical expression.

$$\overline{\overline{r}}_{kj} \approx A\,\mathrm{sinc}(B(\tau - C))\, e^{j(D\tau^2 + E\tau)} \tag{5}$$

In summary, the outcome of the MIRAS calibration procedure is made of the following parameters: the PMS gain G_k and offset v_{off}, the correlation complex gain G_{kj} in amplitude and phase, the NIR source noise temperature T_{NA} and the five parameters A to E of the fringe washing function. All calibration parameters are planned to be periodically updated during the mission to account for possible instrumental drifts. Additionally, the Flat Target Response, which is essentially the calibrated visibility measured when the instrument is pointing to the cold sky, is also considered a calibration parameter.

3. INTERNAL AND EXTERNAL CALIBRATION

External calibration is performed by commanding the platform to go into inertial attitude. In this case, the instrument starts to rotate with respect to the earth-fixed coordinate system until the earth disappears from the field of view of the antenna. At this point, the radiometer is measuring the brightness temperature of a fixed point of the sky, which is chosen to be near the galactic pole to avoid influence from the Galactic emission. Since the sky brightness temperature at L-band is known [8], the calibration parameters of the instrument are adjusted so as to match the measurements to this absolute reference.

External calibration provides the best quality of calibration and it is the only way to obtain the absolute accuracy of the instrument. However, the pointing maneuvers cannot be performed too often and the impact in terms of percentage of time dedicated to calibration is high.

Internal calibration, on the other hand, is carried out by periodically injecting noise to all receivers using an internal source and a distribution network [9]. It tracks fast variations of parameters, but for those requiring a known calibration standard, it cannot provide their absolute values. In this case, the accuracy of the internal calibration relies on the quality of a secondary standard, which has to be previously calibrated using the external view. On the other hand, noise injection is very fast and is easily interspersed between normal measurement operation.

The calibration method utilized for each of the parameters is the following

- PMS gain: External calibration with periodic tracking by internal calibration
- PMS offset: Internal calibration.
- Correlator gain (amplitude and phase): Internal calibration.
- NIR internal noise temperature: External calibration
- Fringe washing function parameters: Internal calibration

4. CALIBRATION RATE

Most of the calibration procedures and measurement sequences were precisely defined during the on-ground characterization of the instrument [10]. The in-orbit commissioning phase has been essential to adjust the timing of calibration events in accordance with the real instrument operation. Particularly, the following general trends have been observed:

- Flat Target Response: Stable, to be corrected only twice a year.
- Fringe washing function shape: The same stability as the Flat Target Response
- Visibility amplitude: To be updated once every 8 weeks
- Antenna temperature: Needs to be calibrated every 2 weeks
- Visibility phase. A calibration is needed every 10 minutes.

Some parameters, as the PMS gain and offsets have been accurately characterized in terms of temperature variation though the computation of sensitivity parameters. This, in combination with a very low physical temperature drift of the whole instrument, has allowed to reduce the need for their frequent calibration updates. New sensitivity parameters have been derived during the in-orbit commissioning phase and they are very well in agreement with the ones obtained during the ground characterization.

As a general rule, the percentage of total time devoted to calibration must be the minimum, just to ensure that the quality of the measurements is according to the requirements. In SMOS, about one percent of the time is used in calibration. This has been achieved by minimizing the number of external calibration maneuvers, using accurate thermal characterization and agreeing a compromise value for the parameters changing the fastest (phase of visibility)

5. CORRELATOR CALIBRATION

Calibrating the corrrelator gain means measuring the complex parameter G_{kj} and its evolution with time and

temperature. This is achieved by processing the internal calibration data using a straightforward method described in [9, 11]. The absolute value of G_{kj} is nearly one by definition and it has been observed having negligible variation from one calibration event to the other. However, the phase of G_{kj} for some baselines shows large and relatively fast variations with time that must be tracked by frequent calibration events. The reason is that the G_{kj} phase for two receivers not sharing a common local oscillator is roughly equal to the phase difference between the signals generated by the oscillators, which vary independently as a function of their local temperature variation. This effect is the main driver for the intercalibration period: every ten minutes a short burst of correlated noise is injected during 1.2 seconds to all receivers just to compute this phase. Figure 1 shows a plot of the amplitude stability of G_{kj} and the large phase variation in a baseline having two different local oscillators.

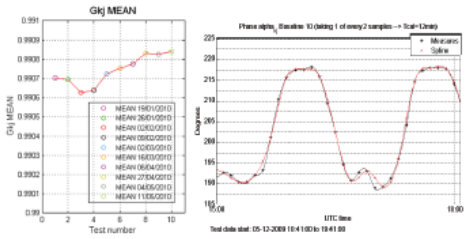

Figure 1. Left: Stability of the amplitude of G_{kj} along time. Right: phase of G_{kj} variation due to local oscillator phase drift

6. PMS CALIBRATION

According to (1), the PMS parameters (gain and offset) are directly responsible of the amplitude of the calibrated visibility. For this reason, accurate PMS calibration has a strong impact on the quality of the final brightness temperature image. In general, errors in the PMS gains and offsets increase the pixel bias, defined as the spatial standard deviation of an image in the director cosines coordinates [12, 13].

The measurements carried out during the commissioning phase have shown that the PMS offset has a periodic variation linked to a control signal used to drive the heaters of the instrument thermal control system. This effect is general but particularly noticeable in some receivers, and has been solved by applying a software correction based on a meticulous process of characterization. The results are given in figure (2) where plots of the offset and the heater signal are drawn superimposed to demonstrate this effect. At the right the same plot after applying the software correction is given. The effect of the correction is apparent.

On the other hand, the PMS gain is extremely stable and very well characterized in temperature. In fact, several

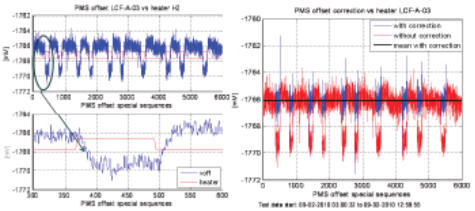

Figure 2. Effect of heater signal in the PMS offset and its correction

retrievals made in different calibration events show high consistency among them. It is calibrated by external calibration using the sky as cold standard and an internal resistor at known physical temperature as hot standard [11]. Independently, their values are monotored by internal calibration using the method described in [9, 11, 14], based on using the NIR, working in a specific mode of operation, to measure the noise power injected to the receivers. This implies that the NIR has to be previously calibrated during the cold sky views. One key result of the in-orbit payload characterization is the computation of correction factors to be applied to internal noise distribution network parameters and antenna efficiencies so as to make these two PMS gain measurements consistent with each other.

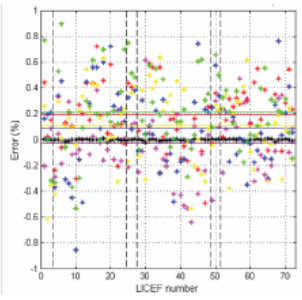

Figure 3. PMS gain calibration. Difference between external and internal calibrations once correction factors applied. The results are for H-pol and for six calibration events spanning three months

Figure 3 shows the difference in percentage between gain retrievals from both external and internal calibration, once the correction factors have been applied. The different traces correspond to six calibration events carried out respectively on 12th January, 2nd February, 2nd, 16th and 23rd March, and 6th April 2010, that is spanning about three months. The peak to peak differences in individual gains is always lower than $\pm 1\%$ and the drift of the average values is as low as 0.2%.

The PMS gain variation between calibration events is very well tracked by means of the measured physical temperature and the sensitivity parameter derived during the in-orbit commissioning phase. Figure 4 shows the measurements of gain during a specific test carried out to

derive this sensitivity. During this test, several orbits of continuous gain retrievals using internal calibration were commanded. The gain sensitivity parameter to temperature was computed by using linear regression of the data acquired. The figure shows a comparison between the measured gain and the one derived using the sensitivity parameter and the physical temperature, so demonstrating that the gain can be accurately tracked just by measuring the temperature sensors, and there is no need for frequent calibration updates.

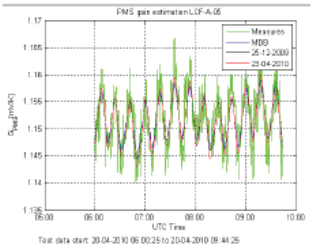

Figure 4. PMS gain tracking using the sensitivity parameter

Finally, figure 5 shows the long-term stability of both PMS gain and offset. It shows the difference of the averaged values retrieved during ten calibration events distributed regularly between 12th January to 11th May 2010. It turns out that the long-term drift is lower than 0.5 mV for the offset and 0.2% for the gain, which has led the the proposal of a PMS intercalibration period of eight weeks to be conservative.

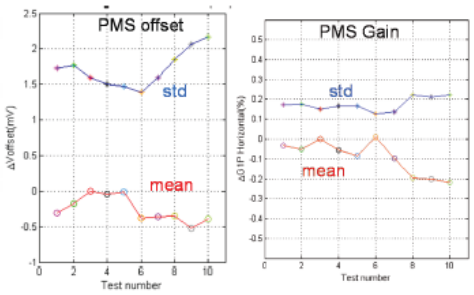

Figure 5. Long term PMS calibration. The test numbers correspond to different calibration events carried out in a 4-month span, from 19th January 2010 to 11th May 2010. Left: Offset, Right: Gain

7. CONCLUSIONS

Calibration and performance of MIRAS, the SMOS payload, has been accurately assessed during the in-orbit commissioning phase. By careful analysis of the measurements performed in specific tests, all the parameters related to internal and external calibration have been retrieved and found to be very well in consistency with the ones obtained during the on-ground characterization. The rate of calibration events, both internal and external, has been established as a result of the analysis made during the commissioning phase.

ACKNOWLEDGMENTS

The work was supported by the European Space Agency and EADS-CASA Space Division under ESTEC contract 17950/03/NL/FF-SMOS; and by the Spanish Ministry of Science and Innovation and FEDER under projects TEC2008-06764-C02-01 and MIDAS-5 ESP2007-65667-C04-0

REFERENCES

1. I. Corbella, F. Torres, N. Duffo, V. González, A. Camps, and M. Vall-llossera, "Fast processing tool for SMOS data," in *International Geoscience and Remote Sensing Symposium, IGARSS 2008*, no. II. Boston(Ma), USA: IEEE, 7 - 11 July 2008, pp. 1152–1155.

2. M. Brown, F. Torres, I. Corbella, and A. Colliander, "SMOS calibration," *IEEE Transactions on Geoscience and Remote Sensing*, vol. 46, no. 3, pp. 646–658, March 2008.

3. I. Corbella, F. Torres, A. Camps, N. Duffo, and M. Vall-llossera, "Brightness temperature retrieval methods in synthetic aperture radiometers," *IEEE Transactions on Geoscience and Remote Sensing*, vol. 47, no. 1, pp. 285–294, January 2009.

4. A. Camps, M. Vall-llossera, I. Corbella, N. Duffo, and F. Torres, "Improved image reconstruction algorithms for aperture synthesis radiometers," *IEEE Transactions on Geoscience and Remote Sensing*, vol. 46, no. 1, pp. 146–158, January 2008.

5. M. Martín-Neira, M. Suess, and J. Kainulainen, "The flat target transformation," *IEEE Transactions on Geoscience and Remote Sensing*, vol. 46, no. 3, pp. 613–620, March 2008.

6. A. Colliander, L. Ruokokoski, J. Suomela, K. Veijola, J. Kettunen, V. Kangas, A. Aalto, M. Levander, H. Greus, M. T. Hallikainen, and J. Lahtinen, "Development and calibration of SMOS reference radiometer," *IEEE Transactions on Geoscience and Remote Sensing*, vol. 45, no. 7, pp. 1967–1977, July 2007.

7. I. Corbella, N. Duffo, M. Vall-llossera, A. Camps, and F. Torres, "The visibility function in interferometric aperture synthesis radiometry," *IEEE Transactions on Geoscience and Remote Sensing*, vol. 42, no. 8, pp. 1677–1682, August 2004.

8. D. M. Le Vine and S. Abraham, "Galactic noise and passive microwave remote sensing from space at L-band," *IEEE Transactions on Geoscience and Remote Sensing*, vol. 42, no. 1, pp. 119–129, January 2004.

9. I. Corbella, F. Torres, A. Camps, A. Colliander, M. Martín-Neira, S. Ribó, K. Rautiainen, N. Duffo, and M. Vall-llossera, "MIRAS end-to-end calibration. Application to SMOS L1 processor," *IEEE Transactions on Geoscience and Remote Sensing*, vol. 43, no. 5, pp. 1126–1134, May 2005.

10. I. Corbella, F. Torres, N. Duffo, M. Martín-Neira, V. González-Gambau, A. Camps, and M. Vall-llossera, "On-ground characterization of the SMOS payload," *IEEE Transactions on Geoscience and Remote Sensing*, vol. 47, no. 9, pp. 3123–3133, September 2009.

11. F. Torres, I. Corbella, A. Camps, N. Duffo, M. Vall-llossera, S. Beraza, C. Gutierrez, and M. Martín-Neira, "Denormalization of visibilities for in-orbit calibration of interferometric radiometers," *IEEE Transactions on Geoscience and Remote Sensing*, vol. 44, no. 10, pp. 2679–2686, October 2006.

12. F. Torres, A. Camps, J. Bará, and I. Corbella, "Impact of receiver errors on the radiometric resolution of large 2d aperture synthesis radiometers. study applied to MIRAS," *Radio Science*, vol. 32, no. 2, pp. 629–642, March-April 1997.

13. I. Corbella, F. Torres, A. Camps, J. Bará, N. Duffo, and M. Vall-llossera, "L-band aperture synthesis radiometry: hardware requirements and system performance," in *International Geoscience and Remote Sensing Symposium, IGARSS 2000*, vol. 7. Honolulu (Hw), USA: IEEE, 24-28 July 2000, pp. 2975 – 2977.

14. F. Torres, A. Camps, J. Bará, I. Corbella, and R. Ferrero, "On-board phase and modulus calibration of large aperture synthesis radiometers: Study applied to MIRAS," *IEEE Transactions on Geoscience and Remote Sensing*, vol. GRS-34, no. 4, pp. 1000–1009, July 1996.

15. A. Camps, "Application of interferometric radiometry to Earth observation," Ph.D. dissertation, Universitat Politècnica de Catalunya, November 1996.

IEEE Transactions on Geoscience and Remote Sensing (Submitted)

IEEE TRANSACTIONS ON GEOSCIENCE AND REMOTE SENSING VOL. ##, NO. #, MM YYYY

MIRAS Calibration and Performance. Results From the SMOS In-Orbit Commissioning Phase

Ignasi Corbella, *Senior Member, IEEE,* Francesc Torres, *Senior Member, IEEE* Nuria Duffo, *Member, IEEE,* Verónica González-Gambau, Miriam Pablos, Israel Duran, Manuel Martín-Neira, *Senior Member, IEEE,*

Abstract

After the successful launching of the SMOS satellite in November 2009, continuous streams of data started to be regularly downloaded and made available to be processed. The first six months of operation were fully dedicated to the In Orbit Commissioning Phase, with an intense activity aimed at bringing the satellite and instrument into a fully operational condition. Concerning the payload MIRAS (Microwave Imaging Radiometer with Aperture Synthesis) it was fully characterized using specific orbits dedicated to check all instrument modes. The procedures, already defined during the on-ground characterization, were repeated so as to obtain realistic temperature characterization and updated internal calibration parameters. External calibration maneuvers were tested for the first time and provided absolute instrument calibration, as well as corrections to internal calibration data. Overall performance parameters, such as stability, radiometric sensitivity and radiometric accuracy were evaluated. The main results of this activity are presented in this paper, showing that the instrument delivers stable and well calibrated data thanks to the combination of external and internal calibration and to an accurate thermal characterization. Finally, the quality of the visibility calibration is demonstrated by producing brightness temperature images in

The work was supported by the European Space Agency and EADS-CASA Space Division under ESTEC contract 17950/03/NL/FF-SMOS; and by the Spanish Ministry of Science and Innovation and FEDER under projects TEC2008-06764-C02-01 and MIDAS-5 ESP2007-65667-C04-0

I. Corbella, F. Torres, N. Duffo V. González-Gambau, I. Duran and M. Pablos are with the Remote Sensing Laboratory, Universitat Politècnica de Catalunya and with the SMOS Barcelona Expert Centre. Barcelona-Spain (e-mail: corbella@tsc.upc.edu).

M. Martín-Neira, is with the European Space Agency (ESA-ESTEC) Noordwijk. The Nederlands (e-mail: Manuel.Martin-Neira@esa.int)

the alias-free field of view using standard inversion techniques. Images of ocean, ice and land are given as examples.

Index Terms

SMOS, interferometric synthetic aperture radiometry, calibration, imaging

I. INTRODUCTION

SMOS (acronym of Soil Moisture and Ocean Salinity) is a European Space Agency (ESA) mission designed to provide global maps of soil moisture over land and sea surface salinity over oceans [1]. It consists of a satellite in a sun-synchronous orbit at about 770 km height carrying a passive L-band sensor called MIRAS (Microwave Imaging Radiometer with Aperture Synthesis) [2], [3]. The satellite was successfully launched the 2nd November 2009 from the Plesestz cosmodrome in northern Russia and the payload was switched on on 17th November 2009. Since then, continuous data is regularly received by the ground segment data acquisition station located in Villafranca del Castillo, near Madrid (E).

The SMOS In-Orbit Commissioning Phase (IOCP) started just after the 3-week long Switch-On and Data Acquisition Phase (SODAP), which was mainly focused at testing low level processes for data acquisition and handling. The IOCP had an overall duration of 6 months and the first half part comprised the characterization, calibration, validation and verification of the instrument. The main goal was to provide a fine tune of MIRAS by means of: Systematic check of all instrument modes, retrieval of internal and external calibration parameters, computation of temperature sensitivity coefficients, assessment on imaging capability, assessment on calibration rate requirements, and instrument overall performance evaluation: Stability, Radiometric sensitivity, Radiometric accuracy and Absolute accuracy.

Most of the goals were successfully achieved on time thanks to the combined effort of a team formed by EADS-CASA Espacio (E) as instrument manufacturer; Deimos Enginheria (P) developer of the Level 1 Prototype Processor (L1PP); the ESA Calibration Expert Center (CEC) dedicated to analyze the quality of the calibration data; and the Universitat Politecnica de Catalunya (UPC) responsible of the definition and implementation of calibration and processing algorithms. All of them were efficiently led by the ESA's principal engineer of the instrument.

The following sections provide a brief description of the activities carried out by UPC in the frame of the SMOS IOCP and shows the main results achieved, including determination of calibration parameters and their stability, as well as retrieval of brightness temperature images of ocean, ice and land. Everything has been processed using the MIRAS Testing Software, an independent software tool developed by UPC, capable of producing geolocated brightness temperature out of the raw data downloaded from the payload [4].

II. MIRAS CALIBRATION

A complete description of the MIRAS calibration system can be found in [5]. In general, calibration of an interferometric radiometer such as MIRAS is needed to provide accurate values of visibility for all receiver pairs and antenna temperature (zero baseline visibility) for at least one element. Besides, image reconstruction algorithms [6], [7] need additional calibration parameters, such as the fringe washing function shape and the flat target response [8]. MIRAS uses a combination of both external and internal calibration to estimate all the time varying parameters. On the other hand, stable parameters such as antenna patterns, S-parameters of noise distribution network and others, are directly used from on-ground characterization.

The visibility is derived by the level 1 processor using the following equation

$$V_{kj} = \frac{M_{kj}\sqrt{T_{sys_k}T_{sys_j}}}{G_{kj}} \text{ where } T_{sys_k} = \frac{v_k - v_{off_k}}{G_k} \tag{1}$$

where v_k is the measured voltage of the PMS (power measurement system) and M_{kj} the normalized correlation measured by the on-board digital correlator. On the other hand, antenna temperature is measured by three noise-injection radiometers (NIR's) [9] located near the center of the array using

$$T_A = T_U - \eta T_{NA} \tag{2}$$

where T_U is the physical temperature in kelvin measured by a sensor placed in a reference resistor near the antenna, η is the measured Dicke pulse fraction (raw NIR measurement) and T_{NA} the noise equivalent temperature of the internal noise source.

The brightness temperature is computed out of the calibrated visibility (1) by inverting the visibility equation [10].

$$V_{kj} = \iint_{\xi^2+\eta^2\leq 1} T^{'}_{kj}(\xi,\eta)\,\overline{r}_{kj}\left(-\tfrac{u\xi+v\eta}{f_0}\right) e^{-j2\pi(u\xi+v\eta)} d\xi d\eta \tag{3}$$

where $\overline{r}_{kj}(\ )$ is the fringe washing function normalized to its value at the origin and T'_{kj} the *modified* brightness temperature:

$$T'_{kj}(\xi,\eta) = \frac{\sqrt{D_k D_j}}{4\pi} \frac{T_B(\xi,\eta) - T_r}{\sqrt{1-\xi^2-\eta^2}} F_{n_k}(\xi,\eta) F^*_{n_j}(\xi,\eta) \tag{4}$$

with T_B is the brightness temperature to be retrieved. In this equation, the only parameter that needs eventually to be updated is the normalized fringe washing function, which is approximated by the following analytical expression.

$$\overline{r}_{kj} \approx A\,\mathrm{sinc}(B(\tau - C))\, e^{j(D\tau^2 + E\tau)} \tag{5}$$

In summary, the outcome of the MIRAS calibration procedure is made of the following parameters: the PMS gain G_k and offset v_{off}, the correlation complex gain G_{kj} in amplitude and phase, the NIR source noise temperature T_{NA}, and the five parameters A to E of the fringe washing function. All calibration parameters are planned to be periodically updated during the mission to account for possible instrumental drifts. Additionally, the Flat Target Response, which is essentially the calibrated visibility measured when the instrument is pointing to the cold sky, is also considered a calibration parameter.

III. INTERNAL CALIBRATION

Internal calibration is carried out by periodically injecting noise to all receivers using an internal source and a power distribution network. Two-levels of power are injected so as to cancel the internal noise coming from the distribution network [11], [12]. Also, in order to simplify this network, a distributed approach is used [13].

Internal calibration is used to monitor the power measurement system (PMS) (gain G_k and offset v_{off}), the correlator complex gain (G_{kj}), both in amplitude and phase and the fringe washing function parameters. It is also used to measure the residual visibility offset by switching all receivers' inputs to internal resistors, so producing uncorrelated noise injection. This offset is very small and was very well characterized on ground [14].

A. PMS gain

Figure 1 shows the relative PMS gain variation in percentage with respect to the average value for all 72 receivers. Both the standard deviation and the peak to peak deviation are shown. It

is computed after analyzing a total of 2499 samples measured during more than 24 hours with the instrument continuously in internal calibration mode. Most of the receivers have PMS gain variations below 0.5% rms and all of them are well below the specified 1%. These variations are dominated by the thermal noise inherent to the measurements due to the limited integration time.

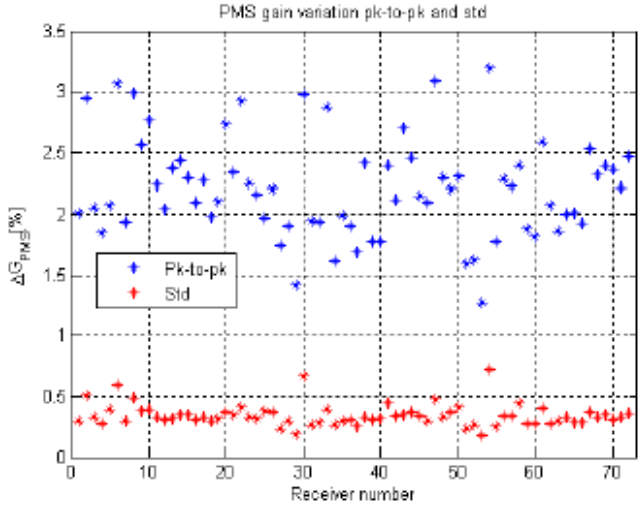

Fig. 1. Relative PMS gain variation in 24 hours of continuous measurements

Nevertheless, there is still a small dependance of the PMS gain with temperature. To characterize this behavior, plots of PMS gains as a function of temperature have been produced and sensitivity coefficients have been computed from linear regression. An example of such plots is given in figure 2 along with a comparison between the measured gain and the one predicted from the temperature measurement. Two values of sensitivity are shown, one in blue corresponding to on ground measurement [14] and other in red obtained from flight data in the frame of the In Orbit Commissioning Phase.

Figure 3 shows the long-term stability of the gain. It represents the difference in the measured gain at six different calibration events spanning more than three months. At each event, the gain is computed by averaging 45 individual retrievals, saving the result as a calibration product to be used during the measurement mode (see section III-D). To make the plot of figure 3 all

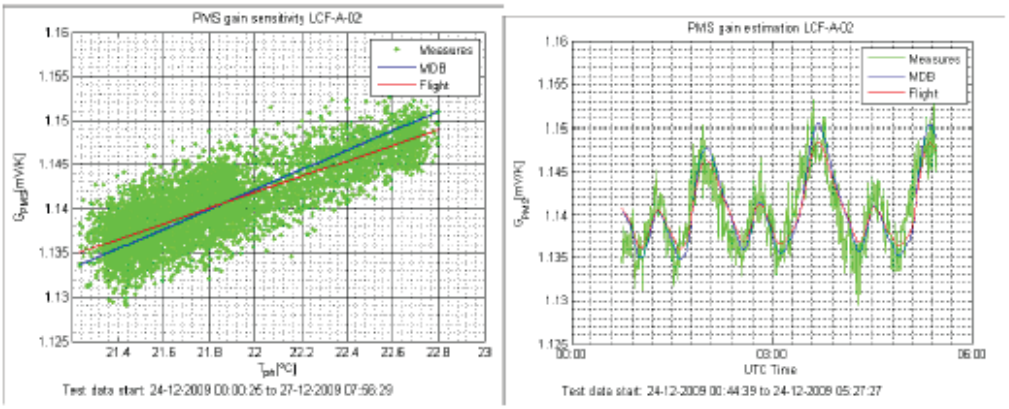

Fig. 2. PMS Gain sensitivity and estimation from physical temperature.

gains were corrected in temperature as described above. The main result is that the overall PMS gain is stable within 0.4% peak to peak in a period of three months, provided the temperature correction is applied.

B. PMS offset

The PMS offset voltages showed small jumps linked to the signal controlling the heaters in the payload temperature stabilization circuitry. Some receivers are more affected than others, but the effect is general. Plots of the offset voltage and the heater signal are drawn superimposed in figure 4 (left) to demonstrate this effect. To cancel this variation, a software correction was implemented based on an accurate characterization carried out with the data acquired during a test sequence specifically designed for it. It consisted of continuously driving the voltage detectors at four levels, so as to make continuous measurements of PMS offsets using the four-point technique [15]. The result is seen in the plot at the right of figure 4, showing the offset once the correction is applied. There are still some points where it is not perfect, but in general most of the points show only the random fluctuation due to thermal noise. A better insight on the quality of this correction is given in figure 5 where for all the receivers, the standard deviation of the measured offset is plot as a function of the receiver number. Three traces are given: without heater correction and with two different retrievals of the correction parameters measured at two different operations of the special sequence of calibration. The correction clearly reduces the

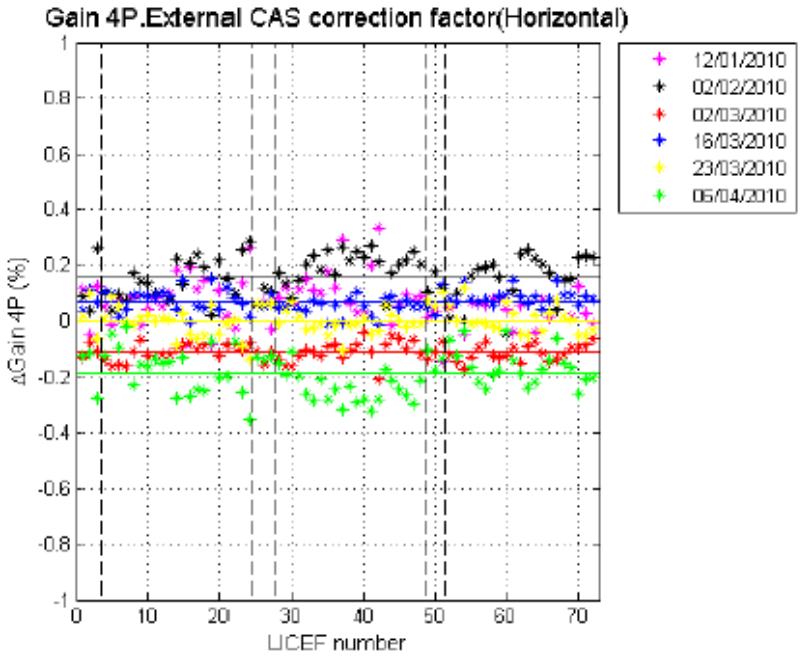

Fig. 3. PMS gain differences between separated calibration events

rms values of the offset and the results are very consistent with each other for both retrievals. The residual offset rms error is well below the 1 mV specification.

C. Correlator complex gain

The correlator gain G_{kj} is a complex valued parameter. Its amplitude is always around unity and very stable: only a negligible variation with time has been detected (see the plot at the left of figure 6). On the other hand, in baselines formed by two receivers not sharing a common local oscillator, the phase of G_{kj} has a significant variation. This phase is roughly equal to the phase difference between the signals generated by the oscillators, which vary independently as a function of their local temperature variation [16]. To account for this dependance, frequent phase calibration events must be carried out interspersed with the normal measurement operation. Several strategies were studied within the commissioning phase in order to decide the best phase calibration rate. To this end the payload was programmed to acquire data with different LO

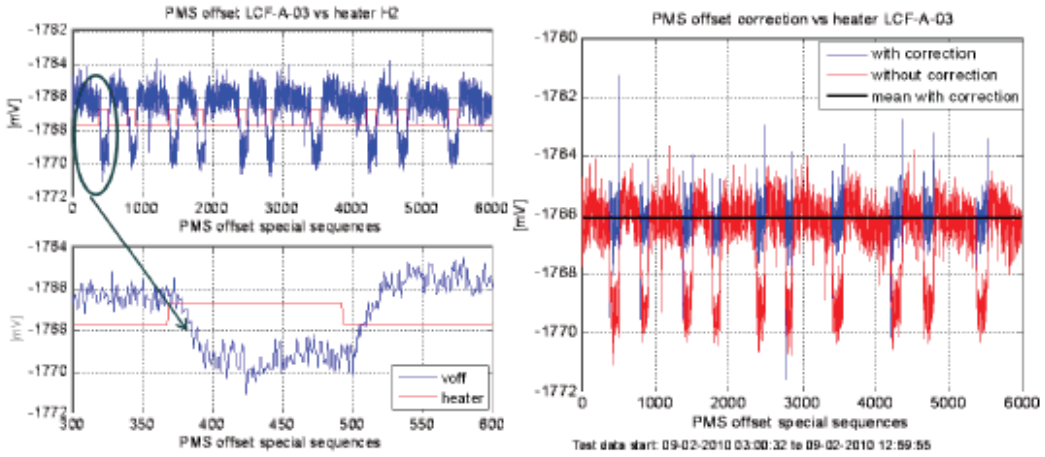

Fig. 4. Left: PMS offset and heater signal showing the high correlation between both. Right: Offset voltage after correction for heater signal dependance.

calibration rates, ranging from 2 minutes to 14 minutes. The final value was fixed after a complete analysis of the data acquired, bearing in mind that the final goal is to provide the maximum quality of the geophysical parameters retrievals. It was finally established in ten minutes to keep residual rms phase error below the 1 deg requirement. Figure 6 shows an example of the phase of G_{kj} along with its estimation based on a spline interpolation.

D. Internal calibration strategy

Two different sequences are used for internal calibration purposes. The so-called "LOcal" consists of injecting a short burst of noise (1.2s duration) just to record the phase of the correlation, which is equal to the phase of G_{kj}. Due to the distributed approach of the network [13], this is actually done twice, one with the "even" sources and other with the "odd" sources. For baselines not sharing noise source, their phases are estimated by solving a system of equations. The LOcal sequence is repeated once every ten minutes and has a total duration of 6 seconds to allow for signals to stabilize after changing the input power so drastically. This is the main contribution to an overall ratio of calibration to measurement slightly above 1%.

The second internal calibration sequence is the "Long-cal". As described in [17] it uses a whole orbit (actually two half-orbits) continuously dedicated to internal calibration alternating between

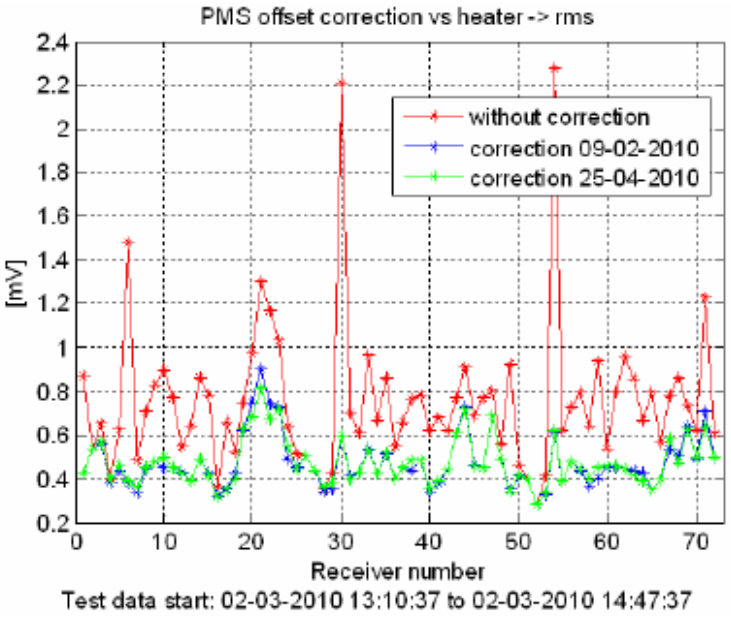

Fig. 5. PMS offset standard deviation of all receivers. After correction, the RMS is reduced well below the 1 mV specification.

two-level correlated noise and uncorrelated noise injection. Figure 7 shows the schematic time line of this sequence. The whole orbit of 5000 seconds is divided into 15 segments of about 400 seconds each. Each one includes three subsegments of correlated noise injection and a longer one of uncorrelated noise injection (abbreviated "U-noise"). This provides a total of 45 individual measurements of PMS gain, offset and amplitude of G_{kj} (its phase is ignored). All of them are averaged to obtain a calibration product that is saved and used later for correcting the science measurements as explained below. All the U-noise measurements are averaged together to estimate the visibility offset to be subtracted to all the subsequent measurements. Finally, using part of the correlated noise injection with time delays, the parameters of the fringe washing function are estimated. The long calibration sequence is performed once every eight weeks, which is enough to track the small variation of the retrieved parameters.

During science measurement operation, the PMS gain is estimated from the calibration product just described but corrected in temperature using the temperature sensitivity coefficients derived during the commissioning phase (see figure 2). The offset is estimated from the calibration product and the correction of the heater signal. The amplitude of the correlator gain is just the

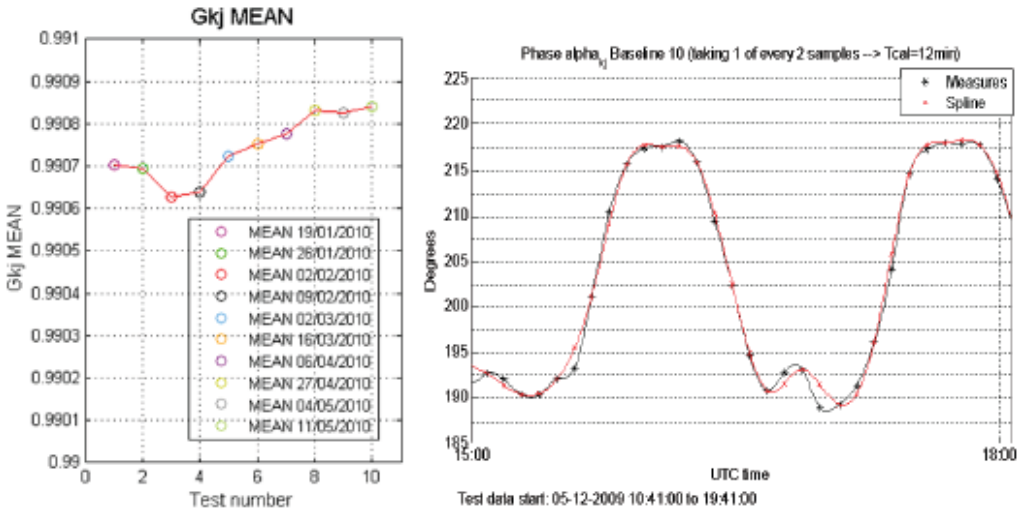

Fig. 6. Correlator complex gain G_{kj}: left: Stability of amplitude along time showing high stability in four-month span. Right: Fast phase variation due to local oscillator phase drift

one measured and its phase is estimated by spline interpolation between measurements of the LOcal sequence.

IV. External Calibration

External calibration is performed by commanding the platform to go into inertial attitude. When this command is received, the instrument starts to rotate with respect to the earth-fixed coordinate system until the earth disappears from the field of view of the antenna. At this point, the radiometer is measuring the brightness temperature of a fixed point of the sky, which is chosen to be near the galactic pole to avoid influence from the Galactic emission. Since the sky brightness temperature at L-band is known [18], the calibration parameters of the instrument are adjusted so as to match the measurements to this absolute reference.

External calibration is used to calibrate the Noise Injection Radiometers (NIRs), which means computing the equivalent noise temperature of their internal source [9]. For each NIR, two parameters are obtained (T_{NA} and T_{NR}), the first one used in equation (2) to measure the antenna temperature and the second one as a secondary standard for the PMS gain calibration in the internal calibration procedure [12].

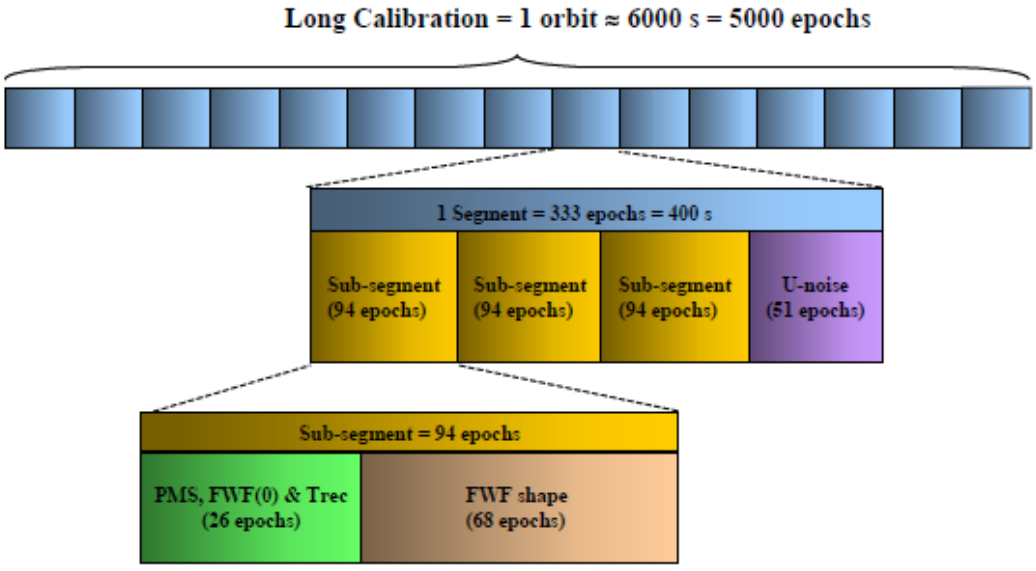

Fig. 7. Long calibration sequence

External calibration is also used to correct for the term of the PMS gain not included in the internal calibration, namely the overall loss between the antenna plane and the noise input port. This is achieved by comparing the PMS gain derived from internal calibration with the one obtained using the one-point approach described in [12], [19] and using the sky as cold standard and an internal resistor at known physical temperature as hot standard. Figure 8 shows the measured difference in percentage between both PMS gains. The comparison is made by translating the internal gain to the antenna reference plane using the S-parameters of the switches measured on ground and a rough estimation of the antenna ohmic efficiencies. The plot shows that the gains have a discrepancy of about 4%, which is completely out of requirements.

Correction factors were computed during the in-orbit payload characterization to be applied to internal noise distribution network parameters, switches and antenna efficiencies so as to make these two PMS gain measurements consistent with each other. The correction factors were computed once for a particular external calibration data set and saved as fixed parameters to use in subsequent calibrations. Eventually, during the mission lifetime these parameters could be updated. Figure 9 shows the difference in percentage between gain retrievals from both

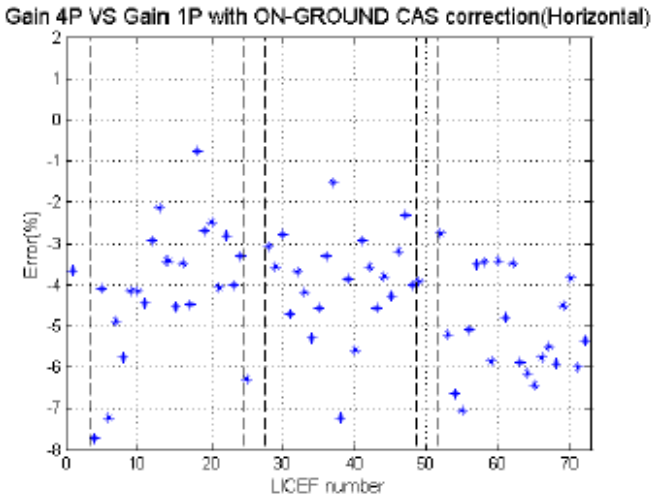

Fig. 8. Comparison between PMS gain retrieved with internal calibration and with external calibration.

external and internal calibration, once the correction factors have been applied. The different traces correspond to eight calibration events carried out at the dates specified in the figure, that is spanning about five months. The peak to peak differences in individual gains is always lower than $\pm 1\%$ and the drift of the average values is as low as 0.6%.

The gain derived from external calibration is more accurate than the one from internal calibration since it uses directly well known standards. The gain from internal calibration is based on using the NIR working in a specific mode of operation to measure the noise power injected to the receivers, which is then used as a secondary standard. This implies that the NIR has to be previously calibrated during the cold sky views. Figure 14 shows the long term stability of the PMS gain derived from external calibration using the one-point approach.

V. System Performance

Two parameters have been used to define the overall system performance of the instrument [20]. The first is the radiometric sensitivity, defined as the temporal standard deviation of the brightness temperature, a function of the spatial direction. The second is the pixel bias, defined as the spatial standard deviation across the image in the director cosines coordinates. Both of them have been obtained after analyzing in detail the data retrieved from ocean scenes. Figure

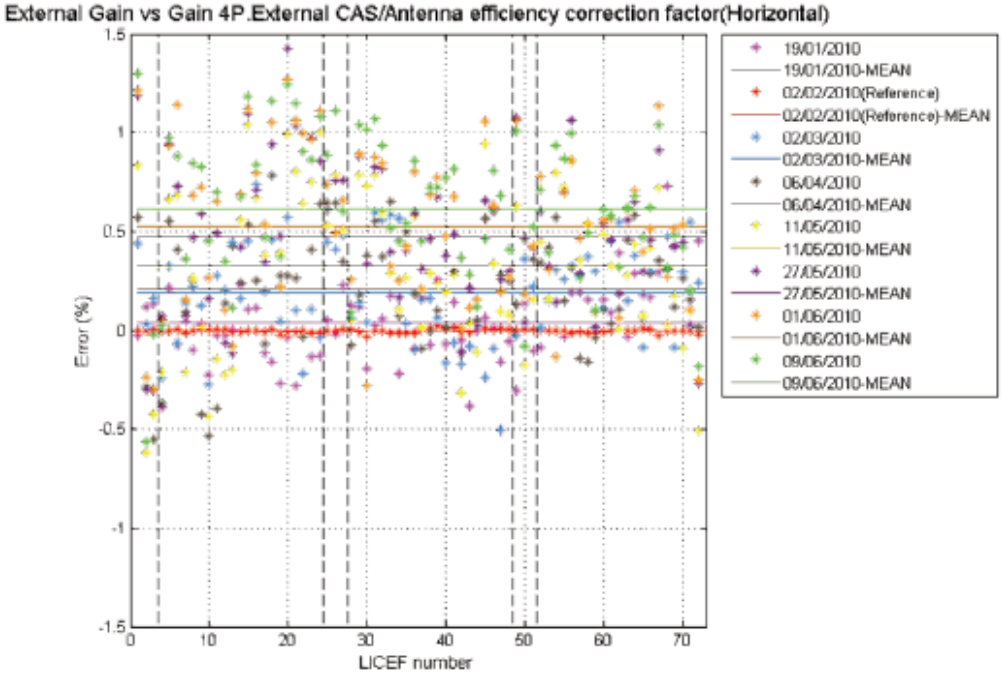

Fig. 9. PMS gain calibration. Difference between external and internal calibrations once correction factors applied. The results are for H-pol and for six calibration events spanning three months

(11) at the left shows an image of the radiometric sensitivity as a function of the director cosines coordinates. At the right of the figure there is a plot of a cut for $\xi = 0$ and a comparison between the measured values and those predicted by the following theoretical formula derived in [21]:

$$\Delta T_B(\xi,\eta) = \frac{\sqrt{3}d^2}{2}\frac{T_A + T_R}{\sqrt{B\tau_{eff}}}\frac{\Omega_a}{t(\xi,\eta)}\sqrt{1-\xi^2-\eta^2}\alpha_w\sqrt{N} \tag{6}$$

where T_A is the antenna temperature measured by the NIRs, T_R is the average receiver noise temperature measured while in external calibration, B is the noise equivalent bandwidth measured through the B parameter of the fringe washing function, τ_{eff} is the effective integration time taking into account the one-bit correlator [20], α_w is a coeficient that depends on the window used in the inversion process (0.45 for Blackmann window), Ω_a is the antenna equivalent solid angle and $t(\xi,\eta)$ is the normalized antenna power pattern, these last two obtained from the accurate antenna measurements carried out on ground. The plot shows an excellent agreement between

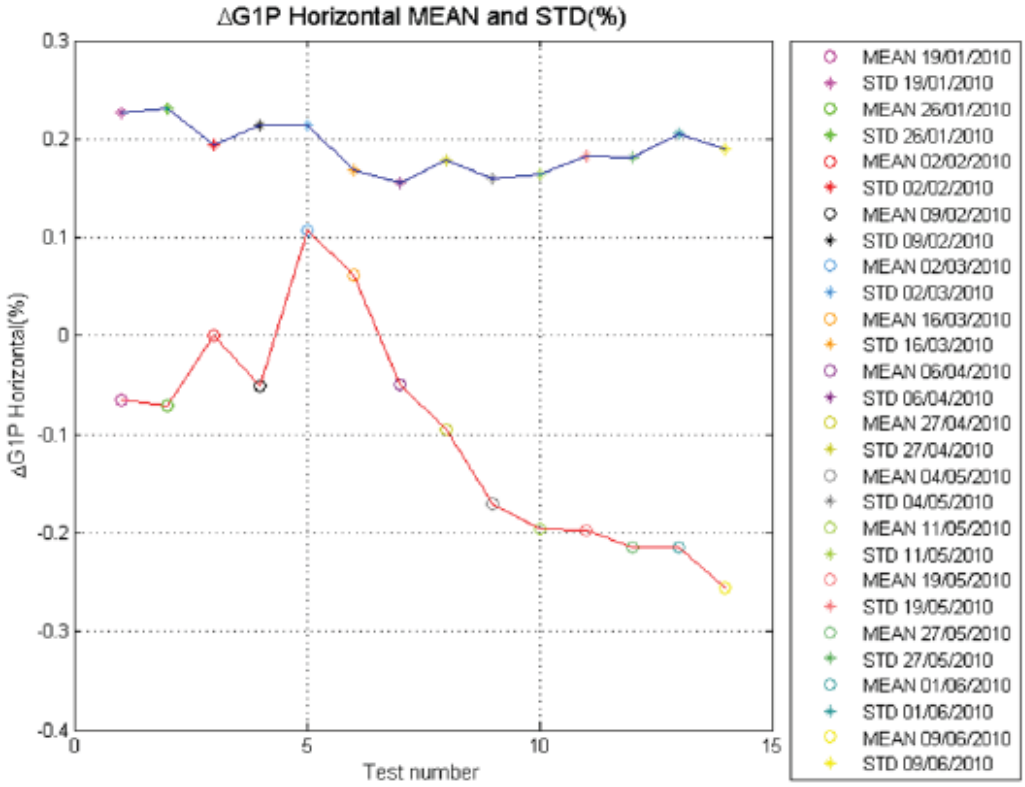

Fig. 10. Stability of the PMS gain derived from external calibration.

the measurement results and the theoretical predictions.

Figure 12 gives the same results but for the measurement of the cold sky during an external calibration maneuver. The agreement is also good, although not as perfect as for the ocean scenes. One of the reasons for this discrepancy might be associated to the back lobes of the antennas that when the instrument is looking upwards are collecting the power emitted by the Earth and are thus contaminating the measurements.

Figure (13) shows an image corresponding to the average of about 60 consecutive snapshots of pure ocean after compensating for the incidence angle dependance. The pixel bias is estimated by the spatial standard deviation of this image in a circle of radius 0.3 inside the alias-free field of view. According to the labels of the images, this turns out to be 1.2 K and 1.35 K respectively

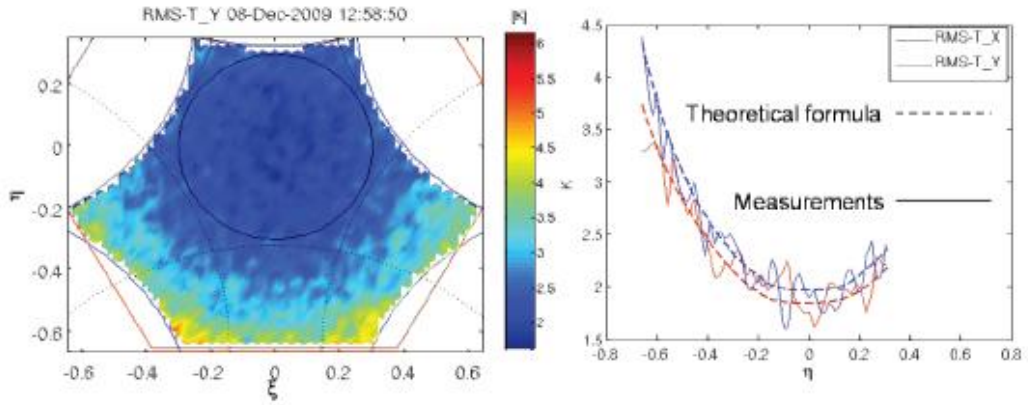

Fig. 11. Radiometric sensitivity in ocean scenes. Left: as a function of pixel position for H-pol. Right: comparison with theoretical formula

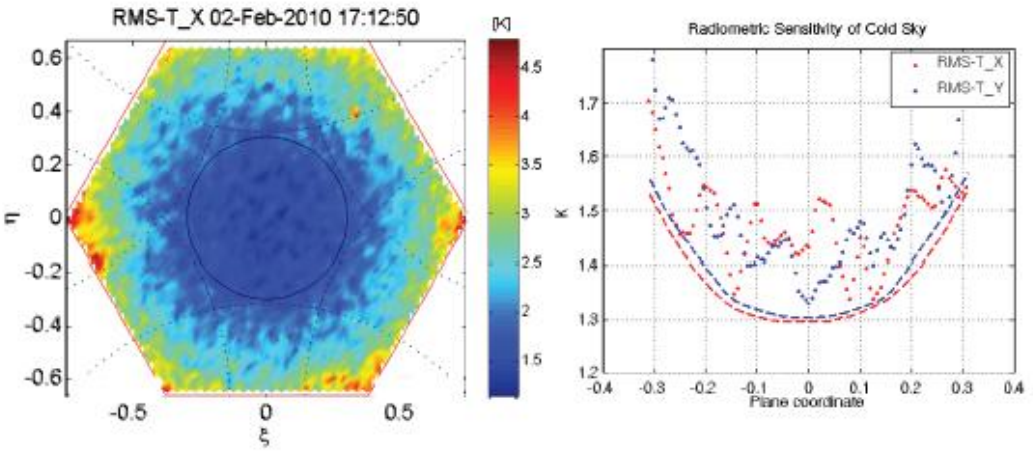

Fig. 12. Radiometric sensitivity during sky looks. Left: as a function of pixel position for H-pol. Right: comparison with theoretical formula

for horizontal and vertical polarization. It should be noted that the predicted value given in [20] was of 1.8K in the worst case, well in line with the values obtained with the real instrument, and it is a good indicator of the quality of the calibration and the inversion. The structure of the image and thus the corresponding standard deviation, is highly increased if the extended alias-free region is considered, although it is not shown here.

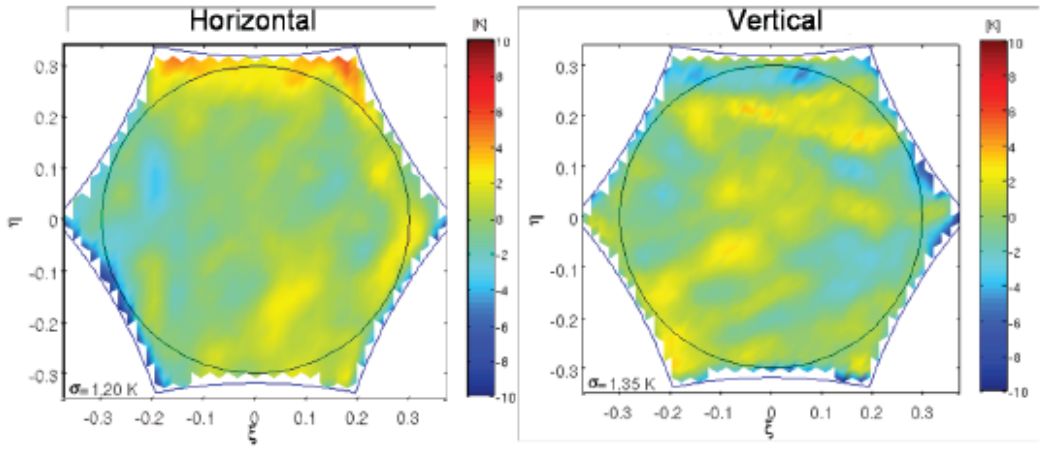

Fig. 13. Pixel bias derived from the brightness temperature of the ocean corrected to compensate the incidence angle dependency

VI. Brightness temperature images

Brightness temperature images are obtained by inverting the calibrated visibility using equation (5). Examples are presented here for ocean, land and ice using the inversion approach number 3 defined in [6] and implemented in the MIRAS Testing software [4]. The images correspond to maps of half the first Stokes parameter, that is $(T_H + T_V)/2$ to make them independent of the rotation angles between the instrument frame at each pixel and the ground frame. In the case of ocean images, the theoretical variation due to specular reflection, directly computed from the fresnel reflection coefficients, has been compensated so as to obtain fairly constant images in all the field of view. Only the data in the true alias-free zone is considered since it is the one of which its quality depends only on the quality of the visibility calibration.

Figure (14) shows a four-days cumulated image over ocean corresponding to data from 6th to 9th June 2010 using both ascending and descending orbits. The image shows low brightness temperature values on the Atlantic compatible with a known increase of salinity in this area. Other stable spatial structures are observed at certain locations over the globe, particularly at high latitudes, although no scientific assessment has been made about them in the frame of this work. They could be caused by RFI sources, particularly in Southern Greenland and North of Canada. What is apparent from this figure is the increase of brightness temperature at the Amazon river plume, which is due to the mixing of fresh water. This is confirmed by a zoom

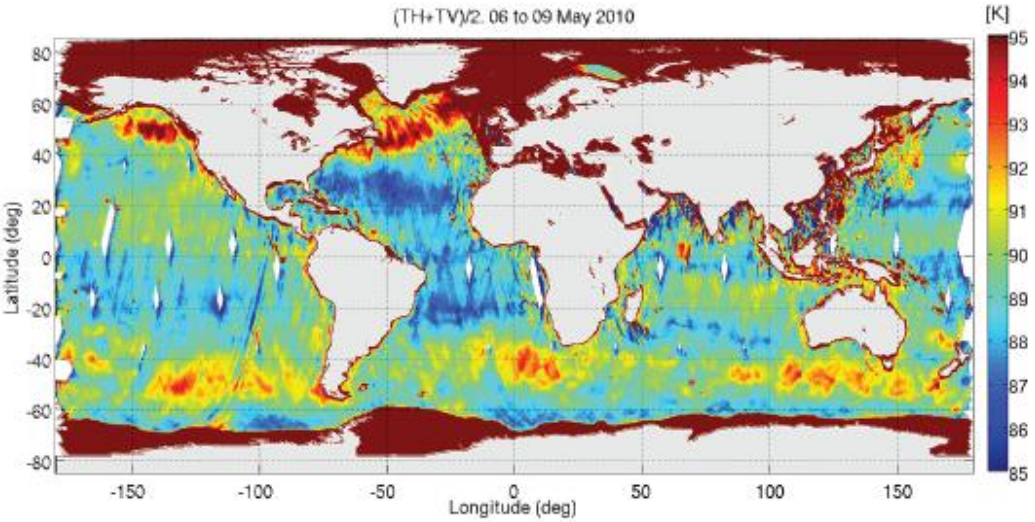

Fig. 14. Cumulated brightness temperature in ocean from 6th to 9th May 2010 for both ascending and descending orbits

of the image shown in figure 15. There is a clear negative gradient of brightness temperature that enters to the ocean just at the point where the river Amazon flows into the Atlantic ocean.

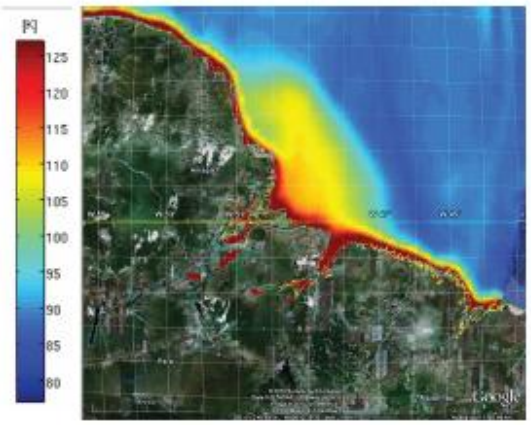

Fig. 15. Zoom of the Amazon river plume showing the influence of higher brightness temperature of fresh water entering into the ocean.

Figure 16 shows the retrieved brightness temperature over Antarctica. A fairly constant value of about 200K is seen at the right of the image and in particular at the Dome-C area, but higher

values are measured in other zones.

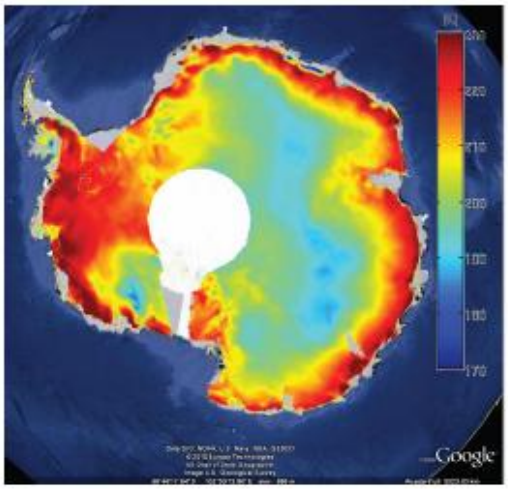

Fig. 16. Brightness temperature image over the Antarctica in 9th May 2010

Brightness temperature over land is expected to be more variable in time since it depends on the amount of water in the soil, which can have important variations when strong rain events are present. Also, differences from ascending to descending orbits are expected since they correspond respectively to the dawn and dusk times of the day. In any case, in order to have a global view of the L-band brightness temperature of the land areas, Figure 17 shows the cumulated brightness temperature for the same four days (6th to 9th May 2010), but separating ascending and descending orbits. Clear features are observed, which in general coincide with the zones of the planet where there are changes in soil moisture. However, there are zones of the planet, particularly in Europe and Asia, that are highly contaminated by RFI, making the brightness temperature images to saturate.

VII. Conclusions

MIRAS provides accurately calibrated visibility as a result of using a combination of internal and external calibration. During the in-orbit commissioning phase, all calibration parameters were measured and found consistent with the ones obtained during the on-ground characterization of the instrument. The visibility amplitude shows a high degree of stability both in short- and long terms, which allows to space apart the external calibration events. On the other hand, the

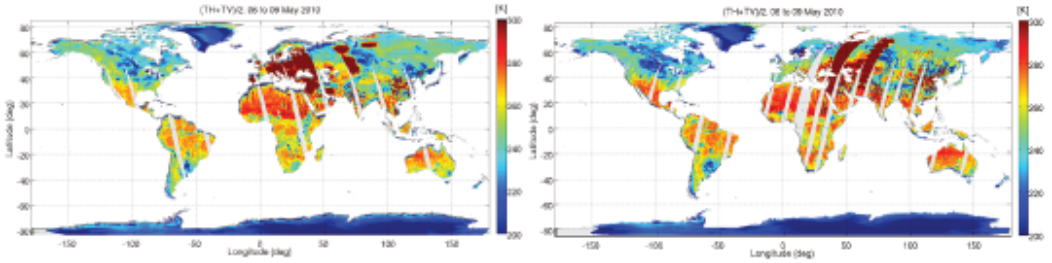

Fig. 17. Global brightness temperature for land regions in ascending (left) and descending (right) orbits

phase has significant variations, requiring to perform updates every ten minutes using internal calibration. The main overall system performance parameters, such as radiometric accuracy and pixel bias have been found well in accordance with the expected values. Brightness Temperature images of good quality in the alias-free field of view have been demonstrated using the UPC's MIRAS testing software, an independent processing tool able to ingest SMOS raw data and provide calibrated visibility and geo-located brightness temperature. Examples over sea, ice and land are given. As a general conclusion: SMOS mission is a success and good global maps of Soil Moisture and Ocean Salinity are expected to be produced in the years to come

REFERENCES

[1] H. Barré, B. Duesmann, and Y. Kerr, "SMOS. the mission and the system," *IEEE Transactions on Geoscience and Remote Sensing*, vol. 46, no. 3, pp. 587–593, March 2008.

[2] M. Martín-Neira and J. M. Goutoule, "MIRAS a two-dimensional aperture-synthesis radiometer for soil moisture and ocean salinity observations," *ESA Bulletin*, no. 92, pp. 95–104, November 1997.

[3] K. McMullan, M. Brown, M. Martín-Neira, W. Rits, S. Ekholm, J. Marti, and J. Lemanzyk, "SMOS: The payload," *IEEE Transactions on Geoscience and Remote Sensing*, vol. 46, no. 3, pp. 594–605, March 2008.

[4] I. Corbella, F. Torres, N. Duffo, V. González, A. Camps, and M. Vall-llossera, "Fast processing tool for SMOS data," in *International Geoscience and Remote Sensing Symposium, IGARSS 2008*, no. II. Boston(Ma), USA: IEEE, 7 - 11 July 2008, pp. 1152–1155.

[5] M. Brown, F. Torres, I. Corbella, and A. Colliander, "SMOS calibration," *IEEE Transactions on Geoscience and Remote Sensing*, vol. 46, no. 3, pp. 646–658, March 2008.

[6] I. Corbella, F. Torres, A. Camps, N. Duffo, and M. Vall-llossera, "Brightness temperature retrieval methods in synthetic aperture radiometers," *IEEE Transactions on Geoscience and Remote Sensing*, vol. 47, no. 1, pp. 285–294, January 2009.

[7] A. Camps, M. Vall-llossera, I. Corbella, N. Duffo, and F. Torres, "Improved image reconstruction algorithms for aperture synthesis radiometers," *IEEE Transactions on Geoscience and Remote Sensing*, vol. 46, no. 1, pp. 146–158, January 2008.

[8] M. Martín-Neira, M. Suess, and J. Kainulainen, "The flat target transformation," *IEEE Transactions on Geoscience and Remote Sensing*, vol. 46, no. 3, pp. 613–620, March 2008.

[9] A. Colliander, L. Ruokokoski, J. Suomela, K. Veijola, J. Kettunen, V. Kangas, A. Aalto, M. Levander, H. Greus, M. T. Hallikainen, and J. Lahtinen, "Development and calibration of SMOS reference radiometer," *IEEE Transactions on Geoscience and Remote Sensing*, vol. 45, no. 7, pp. 1967–1977, July 2007.

[10] I. Corbella, N. Duffo, M. Vall-llossera, A. Camps, and F. Torres, "The visibility function in interferometric aperture synthesis radiometry," *IEEE Transactions on Geoscience and Remote Sensing*, vol. 42, no. 8, pp. 1677–1682, August 2004.

[11] I. Corbella, F. Torres, A. Camps, A. Colliander, M. Martín-Neira, S. Ribó, K. Rautiainen, N. Duffo, and M. Vall-llossera, "MIRAS end-to-end calibration. Application to SMOS L1 processor," *IEEE Transactions on Geoscience and Remote Sensing*, vol. 43, no. 5, pp. 1126–1134, May 2005.

[12] F. Torres, I. Corbella, A. Camps, N. Duffo, M. Vall-llossera, S. Beraza, C. Gutierrez, and M. Martín-Neira, "Denormalization of visibilities for in-orbit calibration of interferometric radiometers," *IEEE Transactions on Geoscience and Remote Sensing*, vol. 44, no. 10, pp. 2679–2686, October 2006.

[13] F. Torres, A. Camps, J. Bará, I. Corbella, and R. Ferrero, "On-board phase and modulus calibration of large aperture synthesis radiometers: Study applied to MIRAS," *IEEE Transactions on Geoscience and Remote Sensing*, vol. GRS-34, no. 4, pp. 1000–1009, July 1996.

[14] I. Corbella, F. Torres, N. Duffo, M. Martín-Neira, V. González-Gambau, A. Camps, and M. Vall-llossera, "On-ground characterization of the SMOS payload," *IEEE Transactions on Geoscience and Remote Sensing*, vol. 47, no. 9, pp. 3123–3133, September 2009.

[15] F. Torres, N. Duffo, I. Corbella, A. Camps, M. Vall-llossera, and L. Sagués, "Dynamic range and linearity tradeoff in detectors for interferometric radiometers," *IEE Electronics Letters*, vol. 39, no. 25, pp. 1852–1854, 11th December 2003.

[16] V. González-Gambau, F. Torres, and N. Duffo, "Phase calibration temperature track in interferometric radiometers devoted to earth observation," in *Proceedings of SPIE Europe Remote Sensing 2008*. Cardiff. Wales, United Kingdom: SPIE Europe Remote Sensing 2008. Sensors, Systems, and Next-Generation Satellites XII., 15-18 september 2008.

[17] I. Corbella, F. Torres, N. Duffo, A. Camps, M. Vall-llossera, and V. González, "MIRAS in-orbit calibration," in *International Geoscience and Remote Sensing Symposium, IGARSS 2007*, no. ISBN DVD-ROM: 1-4244-1212-9. Barcelona, Spain: IEEE, 23 - 27 July 2007, pp. 3622–3625.

[18] D. M. Le Vine and S. Abraham, "Galactic noise and passive microwave remote sensing from space at L-band," *IEEE Transactions on Geoscience and Remote Sensing*, vol. 42, no. 1, pp. 119–129, January 2004.

[19] F. Torres, V. González-Gambau, and C. González-Haro, "One-point calibration in interferometric radiometers devoted to earth observation," in *Proceedings of SPIE Europe Remote Sensing 2008*. Cardiff. Wales, United Kingdom: SPIE Europe Remote Sensing 2008. Sensors, Systems, and Next-Generation Satellites XII., 15-18 september 2008.

[20] I. Corbella, F. Torres, A. Camps, J. Bará, N. Duffo, and M. Vall-llossera, "L-band aperture synthesis radiometry: hardware requirements and system performance," in *International Geoscience and Remote Sensing Symposium, IGARSS 2000*, vol. 7. Honolulu (Hw), USA: IEEE, 24-28 July 2000, pp. 2975 – 2977.

[21] A. Camps, "Application of interferometric radiometry to Earth observation," Ph.D. dissertation, Universitat Politècnica de Catalunya, November 1996.

Bibliography

[1] European Space Agency web: http://www.esa.int/esaLP/LPsmos.html

[2] Remote sensing laboratory group web: http://www.tsc.upc.edu/rslab/index.php?option=com_content&view=article&id=79&Itemid=165

[3] Camps, A., "*Application of Interferometric Radiometry to Earth Observation*"; PhD Thesis. Barcelona November 1996. Universitat Politècnica de Catalunya.

[4] Ulaby, F.T.; Moore, R.K.; Fung, A.K; "*Microwave Remote Sensing Active and Passive Vol. I Fundamentals and Radiometry"*; Norwood, MA: Artech House, 1981.

[5] Eurorockot Launch Service Provider web: http://www.eurockot.com/alist.asp?cnt=20040811&main=3&subm=97

[6] Barcelona Expert Centre on Radiometric Calibration and Ocean Salinity web: http://www.smos-bec.icm.csic.es

[7] McMullan. K.D.; Brown. M.A.; Martín-Neira. M.; Rits. W.; Ekholm. S.; Martí. J.; Lemanczyk. J.; "*SMOS: The payload*". Geoscience and Remote Sensing. vol. 46. Pages: 594-605. IEEE Transactions March 2008.

[8] González-Gambau. V.; "*Caracterización y calibración de radiómetros interferométricos por Síntesis de Apertura*"; Final Project. Barcelona June 2006. Universitat Politècnica de Catalunya.

[9] Camps. A.; Corbella. I.; Duffo. N.; "*Temas de formación SMOS*". Training course for INDRA Espacio. San Fernando de Henares March 2006. Universitat Politècnica de Catalunya.

[10] Corbella. I.; "*Interferometric aperture synthesis radiometry for Earth Observation*". Seminar. Estec January 2008. Universitat Politécnica de Catalunya.

[11] Sanz. J.A.; Rubiales. P.; Lamela. F.; Liozondo. J.L.; Borges. A.; "*Heater Controls Law Definition*". Ref: SO-TN-CASA-PLM-0657. January 2007. EADS Casa Espacio.

[12] Brown. M.A.; Torres. F.; Corbella. I.; Colliander. A.; "*SMOS Calibration*". Geoscience and Remote Sensing. vol. 46. Pages: 646-658. IEEE Transactions March 2008.

[13] Corbella. I.; Torres. F.; Duffo. N.; Camps. A.; Vall-llossera. M.; González-Gambau. V.; "*MIRAS In-Orbit Calibration*". Geoscience and Remote Sensing Shymposium. IGARSS 2007. IEEE International. Universitat Politécnica de Catalunya.

[14] Corbella. I.; Torres. F.; Camps. A.; Colliander. A.; Martín-Neira. M.; Ribó. S.; Rautiainen. K.; Duffo. N.; Vall-llossera. M.; "*MIRAS End-to-End calibration: application to SMOS L1 Processor*". Geoscience and Remote Sensing. vol. 43. Pages: 1126-1134. IEEE Transactions May 2005.

[15] González-Haro. C.; "*Power detector of second order correction stydy applied to MIRAS/SMOS mission*". MERIT Master Thesis. Barcelona. February 2010. Universitat Politécnica de Catalunya.

[16] Torres. F.; Corbella. I.; Camps. A.; Duffo. N.; Vall-llossera. M.; Beraza. S.; Gutierrez. C.; Martín-Neira. M.; "*Denormalization of visibilities for in-orbit calibration of interferometric radiometers*". Geoscience and Remote Sensing. vol. 44. Pages: 2679-2686. IEEE Transactions October 2006.

[17] Torres. F.; González-Gambau. V.; González-Haro. C.; "*One point calibration in interferometric radiometers devoted to Earth observation*". SPIE Europe Remote Sensing 2008. Barcelona. Universitat Politècnica de Catalunya. SMOS Barcelona Expert Centre.

[18] Torres. F; Corbella. I.; Duffo. N.; González-Gambau. V.; "*One point calibration in interferometric radiometers: Error assessment*". Geoscience and Remote sensing Symposium. IGARSS 2009. IEEE International. Universitat Politécnica de Catalunya.

[19] Duffo. N.; Corbella. I.; Torres. F.; González-Gambau. V.; Martín-Neira. M.; "*Interferometric Radiometers: Fringe Washing Function Estimation*". Geocience and Remote Sensing Symposium. IGARSS 2008. IEEE International. Universitat Politécnica de Catalunya. SMOS Barcelona Expert Centre.

[20] Torres. F.; Corbella. I.; Duffo. N.; Camps. A.; Vall-llossera. M.; González-Gambau. V.; "*Analysis of PMS temperature correction on IVT test data*". Internal technical note. Ref: SO-TN-UPC-PLM-0061 v1.0. 18th September 2007. Universitat Politècnica de Catalunya.

[21] **Pablos. M.**; González-Gambau. V.; Duffo. N.; Torres. F.; Corbella. I.; "*Review of PMS sensitivity analysis in LSS tests*"; Internal technical note. Ref: SO-TN-UPC-PLM-0079 v1.1. 10th February 2009. Universitat Politècnica de Catalunya.

[22] **Pablos. M.**; González-Gambau. V.; Duffo. N.; Torres. F.; Corbella. I.; "*Review of PMS sensitivity analysis in LSS tests*"; Internal technical note. Ref: SO-TN-UPC-PLM-0079 v2.0. 10th February 2009. Universitat Politècnica de Catalunya.

[23] **Pablos. M.**; González-Gambau. V.; Duffo. N.; Torres. F.; Corbella. I.; "*Assessment of PMS offset track in LSS tests*"; Internal technical note. Ref: SO-TN-UPC-PLM-0084 v1.0. 15th May 2009. Universitat Politècnica de Catalunya.

[24] **Pablos. M.**; González-Gambau. V.; Duffo. N.; Torres. F.; Corbella. I.; "*Review of PMS offset calibration parameters*"; Internal technical note. Ref: SO-TN-UPC-PLM-0110 v1.0. 7th June 2010. Universitat Politècnica de Catalunya.

[25] Durán. I.; "*SMOS flight external calibration and monitoring*"; Final Project. Barcelona September 2010. Universitat Politècnica de Catalunya.

[26] **Pablos. M.**; González-Gambau. V.; Duffo. N.; Torres. F.; Corbella. I.; "*Estimation of PMS gain sensitivity of SMOS flight data*"; Internal technical note. Ref: SO-TN-UPC-PLM-0098 v1.1. 15th April 2010. Universitat Politècnica de Catalunya.

[27] **Pablos. M.**; González-Gambau. V.; Duffo. N.; Torres. F.; Corbella. I.; "*Electrical stability test 2: PMS gain sensitivity*"; Internal technical note. Ref: SO-TN-UPC-PLM-0104 v1.0. 7th May 2010. Universitat Politècnica de Catalunya.

[28] **Pablos. M.**; González-Gambau. V.; Duffo. N.; Torres. F.; Corbella. I.; "*PMS HEATER offset correction*"; Internal technical note. Ref: SO-TN-UPC-PLM-0102 v1.0. 10th May 2010. Universitat Politècnica de Catalunya.

[29] **Pablos. M.**; González-Gambau. V.; Duffo. N.; Torres. F.; Corbella. I.; "*Electrical stability test 2: PMS HEATER offset correction verification*"; Internal technical note. Ref: SO-TN-UPC-PLM-0103 v1.0. 12th May 2010. Universitat Politècnica de Catalunya.

[30] **Pablos. M.**; González-Gambau. V.; Duffo. N.; Torres. F.; Corbella. I.; "*Review of PMS offset calibration parameters*"; Internal technical note. Ref: SO-TN-UPC-PLM-0110 v1.0. 7th June 2010. Universitat Politècnica de Catalunya.

[31] **Pablos. M.**; González-Gambau. V.; Duffo. N.; Torres. F.; Corbella. I.; "*Preliminary assessment on PMS flight gain calibration*"; Internal technical note. Ref: SO-TN-UPC-PLM-0095 v1.0. 1st January 2010. Universitat Politècnica de Catalunya.

[32] González-Gambau. V.; Duffo. N.; Torres. F.; Corbella. I.; Camps. A.; Vall-llossera. M.; "*LO Phase track analysis*"; Internal technical note. Ref: SO-TN-UPC-PLM-0070 v1.1. 19th February 2009. Universitat Politècnica de Catalunya.

[33] **Pablos. M.**; González-Gambau. V.; Duffo. N.; Torres. F.; Corbella. I.; "*Rough prediction of visibility phase drift*"; Internal technical note. Ref: SO-TN-UPC-PLM-0092 v1.1. 20th November 2009. Universitat Politècnica de Catalunya.

[34] **Pablos. M.**; González-Gambau. V.; Duffo. N.; Torres. F.; Corbella. I.; "*LO phase track analysis of SMOS flight data*"; Internal technical note. Ref: SO-TN-UPC-PLM-0094 v1.0. 12th January 2010. Universitat Politècnica de Catalunya.

[35] **Pablos. M.**; González-Gambau. V.; Duffo. N.; Torres. F.; Corbella. I.; "*Assesment of LO phase tracking by interpolation on LSS*"; Internal technical note. Ref: SO-TN-UPC-PLM-0089 v1.0. 13rd November 2009. Universitat Politècnica de Catalunya.